Investigation to assess the feasibility of using the GRI+ Compton Camera for Radioactive Waste Characterisation

Thesis submitted in accordance with the requirements of the University of Liverpool for the degree of Doctor in Philosophy by

Jaimie Marie Platt

December 2020

Acknowledgements

These past four years have been an absolute whirlwind. Publishing this thesis has undoubtedly lifted the spirits of a particularly rubbish 2020, and there are numerous people whom I wish to give thanks to, for the opportunities and support which made this happen.

Firstly, to my supervisor, Prof. Andy Boston. You were always able to give me guidance and advice throughout my PhD, despite how overwhelmingly busy you were, and I appreciated all the support you gave me. To my secondary supervisor, Prof. Robert Page, whose door I could always knock on for a question. To Laura Harkness-Brennan and Paul Nolan. I wouldn't be where I am today if it wasn't for your help and support, and initially giving me the opportunity to do this PhD. A large thanks to the other members of staff in the Nuclear Physics department who provided guidance and support throughout my PhD, especially through the hardships I faced.

To Adam and Ellis, a particular thanks has to go to the two of you for the help you provided during the work on this project. I think I would have definitely fallen apart if it wasn't for the constant support, discussions and help when working late in the lab! To the others who worked on the Compton Camera with me as well, even those who worked on it for a small part, it was incredible to be involved in a project with you all (even if the cart was frustrating to work with!). To Dan Judson, the lab would fall apart without you, we are lucky to have you here to answer our detector questions and keep the cart ticking!

I'll be forever grateful for the friendships I have made during my time here from the nuclear physics group. Lucy, for the times we would show up the lads playing football. Ellis, my desk neighbour and someone to make the work days easier with chats of Liverpool FC or fantasy football. Andy, my fellow scouser and teammate. To everyone else I met, I'm sorry I can't list you all here (the acknowledgements would go on for forever), but please know that I love you all.

A shoutout to Popworld, I wouldn't have been able to get through University at all without your cheesy music and large partini glasses. The biggest Popworld party will be happening once we can all celebrate passing our vivas properly!

A large thank you to my family (even if you don't have a clue what any of this work is about), and for the friends outside of Uni, whose support and encouragement has helped me through these past 4 years.

And finally to my wonderful partner, Mikey. You sacrified so much in order for me to do this PhD, especially with me being self-funded, and I know there were many times you were patient with my stressed out head. I'll forever be grateful for your support, for your reassuring words (the numerous takeouts you ordered for me when I was working late), and for persuading me to get our Riley - having a golden retriever to cuddle when things weren't working for me helped massively! I love you so much, and I'm incredibly lucky to be spending the rest of my life with you.

Abstract

The work presented in this thesis examines key scenarios that a gamma-ray imaging system may face when characterising radioactive waste contamination. The aim of this project is to show that a mobile Compton Camera Gamma-Ray Imaging (GRI+) system developed by the University of Liverpool for medical and nuclear decommissioning applications, can quantitatively assess data collected from industrially relevant measurements. GRI+ consists of Si(Li) and HPGe planar, electrically segmented detectors, and a third coaxial HPGE detector. The three detectors are mounted onto a mobile cart system, along with their mechanical cooling systems, power supply and the digital data acquisition system. The mobility of the GRI+ system allowed for the first set of 'in situ' measurements to take place in a room with a significantly high-level of background radiation. A replication of a select few standard laboratory measurements showed no outstanding effect from the presence of the background radiation from analysis of the peak-to-total values. This could be significant in waste contamination scenarios where the influence of high-levels of background radiation could potentially affect the quality of the data. The imaging response of the detector system for a range of standoff distances was explored, with distances ranging from a minimum of 45 cm (the closest feasible distance the cart could achieve in measuring a source in a contamination scenario) to a maximum of 250 cm. ^{137}Cs point sources were measured in various positions across the detector's field of view at a standoff distance of 45 cm to assess its capability for measuring a non-uniform distributed sample. The average angular resolution across the range of 68 cm to 250 cm was determined to be 7.19 ± 0.26 degrees, a leading performance for a gamma-imaging system used today. The detector's sensitivity to concrete material has been examined to provide a better understanding of the influence of scattering material on coincidence energy spectra, with a view of utilising this in future to increase the number of useable imageable events. The peak-to-total ratio was determined for the 662 keV full-energy peak from a 15.6 MBq ^{137}Cs point source in each coincidence energy spectrum produced for differing thicknesses of concrete. A linear relationship is observed between the natural log of the peak-to-total ratio and the thickness of concrete, with a gradient of -0.066 obtained. These results indicate that GRI+ would be capable of waste characterisation measurements. However, further optimisation of the system is required, with the main focus being to overlay Compton images onto real photographic images. Potential improvements to GRI+ have been suggested and would be recommended before any future offsite measurements take place.

Contents

Chapter 1

Introduction

The UK has accumulated decades worth of radioactive waste originating from the nuclear industry. Some of this material will only become waste after several decades, and is mostly kept in interim storage. Other long-term facilities such as the First Generation Magnox Storage Pond (FGMSP) at the Sellafield Nuclear Site, Cumbria are producing large decommissioning challenges with problematic waste. The cost of decommissioning in the UK is approximately £3 billion a year [1], with the costs split between the UK government and private contracts.

The Nuclear Decommissioning Authority (NDA) acts on behalf of the UK government to clean up and decommission various sites across the UK. The long-term strategy for managing higher-activity waste is through disposal via a Geological Disposal Facility (GDF). This is overseen by Radioactive Waste Management (RWM), a subsidary of the NDA [1]. This method involves isolating radioactive waste in a well-engineered facility underground, with no waste or radioactivity reaching the surface.

Radioactive waste is classified during the decommissioning of a nuclear facility. Directly after operations cease at a nuclear facility, a *post-operational clean out* (POCO) takes place, which includes the safe removal of contaminated contents or structures with any residual activity and facilitates the decommissioning of the facility so that it is safely shut down. The current POCO timeline for Sellafield continues to 2032 [2]. The location and classification of radioactive waste account for the major costs in the decommissioning process.

The current method that is utilised uses non-destructive analysis of radioactive waste by using gamma-ray imaging systems. Current characterisation of waste is poor as it assumes a homogenous mixture, and does not account for variations. Also, along with chemical degradation of the waste bins, the current composition of the waste is largely unknown due to the decay of radioisotopes leading to various amounts of daughter nuclides. If waste is accurately char-

acterised and partitioned, radiological hazards could be minimised to workers and the total decommissioning time and costs could be reduced going forward [3].

The aim of the research project is to develop a portable gamma-imaging system to be used in nuclear decommissioning scenarios. Industrial partners would like a system that is able to check possible contamination in places such as a waste storage room, to see if there is any contamination on the walls or accumulation in the pipes. Problems arise in situations where there is a possible ingress of radioactive material through a wall or concrete. Determining the depth that this ingress has occurred is an additional challenge to be investigated.

This thesis will outline an investigation into the feasibility of the GRI+ Compton Camera for imaging radioactive waste in scenarios more akin to those found in waste sites.

1.1 Introduction to GRI+

GRI+ is the next stage to the ProSPECTus Compton Camera [4] at the University of Liverpool. The system consists of two planar double-sided strip semiconductor detectors, silicon and germanium, and a third tier coaxial germanium detector. All are mounted on a custom designed cart, which is self-contained with its electrical cooling systems, digital data acquisition electronics and power supply.

By analysing the interactions that take place within these detectors, the information provided by the energy deposited and the location of the interaction can allow for the location of the source of radiation to be determined using Compton kinematics. The excellent spectroscopic capabilities of semiconductor detectors, along with the increased sensitivity from electronic collimation, makes it ideal for possible in-situ measurements compared to current systems which utilise mechanical collimation in scintillator based detector systems.

The capability and performance of GRI+ for possible future in-situ measurements was investigated. The following objectives were assessed:

1) Measurements at industrially relevant standoff distances (up to 2.5 m).

2) Observing the influence of scattering material on the quality of Compton images.

3) Determining the possible ingress of radiation within a scattering medium.

4) Observing the influence of high-levels of background radiation on the quality of the data.

1.2 Thesis Outline

This thesis reviews the work undertaken to achieve the objectives described. The content of the chapters in this thesis is detailed below:

Chapter 2 - A description of current radioactive waste characterisation techniques, along with a comparison of current gamma-ray imaging systems used today.

Chapter 3 - Provides an outline to the fundamental physics relating to this thesis; including the interaction of gamma rays and the operation of gamma-ray detectors.

Chapter 4 - This chapter gives an in depth description of how GRI+ operates, along with describing the data aquisition process and image reconstruction algorithms.

Chapter 5 - This chapter presents the results from the data collected to achieve the above mentioned objectives.

Chapter 6 - A discussion of the results obtained in this thesis, along with comments on possible future measurements.

Appendices - Additional information regarding the data that was taken for this campaign, plus details on specific solid angle calculations.

Chapter 2

Radioactive Waste Characterisation

Radiological assessment of radioactive or nuclear material is done through quantifying the different amounts of alpha, beta and gamma-emitting radionuclides present in the material.

Radioactive material, if left unmonitored, could have a hazardous effect on life and the environment around it. By understanding the importance of the different quantities associated with radiation, such as the activity, dose or half-life, then it can be accurately characterised. This can aid with decommissioning purposes to enact the appropriate measures for disposal of radioactive material such as problematic waste.

Problematic waste is defined as waste for which safe, efficient and cost-effective methods for treatment and processing are not readily available [5], or if the waste type failed to meet acceptance critera. One of the key methods used for radioactive waste characterisation is gamma-ray spectrometry. Determining the level of exposure and dose from gamma radiation is crucial when trying to characterise radioactive material.

2.1 Radiation Exposure and Dose

A nucleus is defined by various characteristics such as its mass number, A, and atomic number, Z. Radioactive nuclides (radionuclides) are additionally characterised by their *half-life*. The half-life of a sample, $T_{\frac{1}{2}}$ describes how long it takes for the total number of radioactive nuclei to reduce by half.

The activity, A, of a particular radionuclide is measured as the number of decays per second, measured in SI units of the becquerel (Bq) [Relative to the

old unit of the Curie, 1 Bq = 2.703×10^{-11} Ci]. Laboratory standard sources are usually at a level of kilobecquerel (kBq), whereas radioactive waste produced from a nuclear facility could fall within the range of megabecquerels (MBq) to terabecquerels (TBq).

The relationship between the total number of radioactive nuclei of a particular radioisotope, N, and the half-life, $T_{\frac{1}{2}}$, can be represented by the fundamental law of radioactive decay:

$$A = \frac{dN}{dt} = -\frac{ln2}{T_{1/2}}N \tag{2.1}$$

Equation 2.1 expresses the rate of the number of atoms present decreasing with time. The term $\frac{ln2}{T_{1/2}}$ is also known as the decay constant, λ.

The specific activity of a sample relates a source's activity to its mass. It is defined as the activity per unit mass of the radioisotope.

$$\text{Specific Activity} = \frac{\text{Activity}}{\text{Mass}} = \frac{\lambda N}{NM/N_A} = \frac{\lambda N_A}{M} \tag{2.2}$$

Where M is the relative molecular mass of the sample, N_A is Avogadro's Number (6.02 x 10^{23} nuclei/mole), λ is the decay constant and N is the number of radioactive nuclei. Equation 2.2 relates to one specific radioactive atom of a given nuclide per molecule. If there are multiple radioactive atoms in a given molecule, then the activity would be increased. For example, the activity of tritium that is in a water molecule, ^3H_2O will be twice that of a standalone ^{3}H atom.

The decay law states that the number of atoms present at a particular time, t, follows the relationship of:

$$N(t) = N(0)e^{-\lambda t} \tag{2.3}$$

By combining Equations 2.1 and 2.3, we are able to get the following equation for the activity of sample:

$$A(t) = A(0)e^{-\lambda t} \tag{2.4}$$

Where *A(t)* is the activity of the sample at time *t*, and *A(0)* is the original activity.

Absorbed Dose is the quantity of ionising radiation energy absorbed by a body per unit mass. The units of absorbed dose is represented by 1 J/kg = 1 Gray (Gy).

$$\mathrm{D(Gy)} = \frac{\text{Energy Absorbed}}{\text{Mass}} \tag{2.5}$$

Other factors that affect the risk to people include the type of radiation that interacted with the body, the dose rate, or the sensitivity of a particular organ.

Equivalent Dose accounts for the different biological effects of radiation on the absorbed dose, by taking into account the radiation weighting factor, W_R. For photons and electrons, this weighting factor is equal to one.

$$\mathrm{H(Sv)} = W_R \times D \tag{2.6}$$

The unit of Sieverts (Sv) is a standard unit to describe the effects of ionising radiation on the human body. It is equivalent to 1 J/kg, unlike the Gray which is a physical quantity. Sieverts describes the biological effect that one joule of energy has to a kilogram of human tissue.

Effective Dose accounts for the sensitivity of different biological tissue to the effects of radiation. This is represented by the tissue weighting factor, W_T

$$\mathrm{E(Sv)} = W_T \times H \tag{2.7}$$

2.2 Sources of Contamination

2.2.1 Nuclear Facilities - Process of Nuclear Fission

In the UK, approximately 10 % of the energy generated is through nuclear power [6]. The main process in which energy is generated is through the fission of fissile nuclides in nuclear reactors.

Fissionable materials are those in which nuclear fission can occur through the capture of either a fast ($\backsim$ MeV) or thermal ($\backsim$ eV) neutron. Fissile materials are fissionable nuclides that can sustain a chain reaction from slow, thermal neutrons. ^{235}U or ^{239}Pu are common fissile materials due to their ability to maintain a chain reaction, as the fast neutrons released in the fission process can be thermalised by the moderators. Nuclides such as ^{238}U are fissionable, as they require high-energy neutrons ($\backsim$ 1 MeV) in order to produce a fission reaction, but they are not fissile. It is unable to sustain a chain reaction as it cannot be fissioned by the thermalised neutrons that are moderated during the fission process.

When a thermal neutron interacts with a nuclide, for example ^{235}U, the nuclide will undergo neutron capture, a process where the addition of a neutron creates a new unstable isotope, as shown by the equation below. This will produce the unstable ^{236}U isotope. It is energetically possible for heavy nuclides, such as ^{236}U, to decay via the fission process, rather than an alternative such as alpha decay.

$$\text{Example}: \ ^{235}U + n \rightarrow \ ^{144}Ba + \ ^{90}Kr + 2n + \text{Energy}\ (MeV) \tag{2.8}$$

In order to overcome the strong nuclear force, work must be done to remove a nucleon from its nucleus. This can be represented by the binding energy, the energy required to separate the nucleus into its constituent protons and neutrons.

A plot of the binding energy per nucleon (BEN) as a function of atomic number, A, is shown in Figure 2.1. This figure shows that higher values of the BEN lead to more stable nuclei, as shown by the peak at the mass of ^{56}Fe. ^{56}Fe is considered the most stable nuclide as it is the most efficiently bound and therefore it takes the most energy per nucleon to completely separate the nucleus.

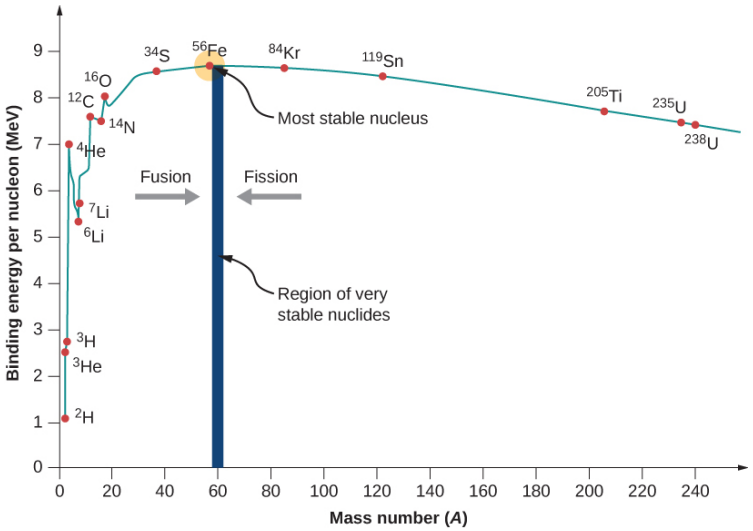

Figure 2.1: Graph showing the binding energy per nucleon for different atomic numbers, A [7]. The peak of the graph shows the masses of stable nuclei. Nuclei of low atomic mass can undergo fusion as the attractive strong nuclear force dominates. At high mass nuclei, the repulsive electrostatic forces causes nucleons to separate, leading the nucleus to undergo fission to return to stability.

The binding energy trend shown in Figure 2.1 [7] can be described by the semi-empirical mass formula (SEMF), which is derived from average nuclear properties established from the liquid drop model. These properties include the assumption of a spherical shape, and that the density is constant throughout the volume as the 'drop' is incompressible. The SEMF is described by Equation 2.9 [8, 9].

$$B(Z,A) = a_V A - a_S A^{\frac{2}{3}} - a_C \frac{Z^2}{A^{\frac{1}{3}}} - a_A \frac{(A-2Z)^2}{A} + \delta(Z,A) \tag{2.9}$$

B(Z, A) describes the nuclear binding energy, as a function of atomic mass number, A, and proton number, Z. The remaining terms can be described as:

- a_V - Volume term
  Each nucleon is bound by an attractive force, acting on a short range.

- a_S - Surface term
  Nucleons found at the surface have a lower binding energy, as they are less tightly bound.

- a_C - Coulomb term
  A long range, uniform electrostatic force.

- a_A - Asymmetry term
  Nuclides that have the same number of protons and neutrons have a higher binding energy compared to nuclides that have a differing number of protons and neutrons.

- $\delta(Z, A)$ - Pairing term
  Describes how the pairing of two protons or neutrons, is more strongly bound than one proton and one neutron together.

At high values of A, the repulsive electrostatic forces between protons dominate over the strong attractive nuclear forces. Therefore, the forces within the nucleus favour it to splitting into lighter nuclei. Fission causes a larger shift of A towards stability than alpha decay, and also releases more energy (hundreds of MeV). In some nuclei, this is why it is the more favourable process.

Referring back to the example shown in Equation 2.8, the SEMF can be used to calculate that the binding energy of ^{235}U will decrease by approximately 6 MeV when it undergoes neutron capture. This change in binding energy will increase the probability that ^{236}U will fragment via the fission process, compared to the probability of the spontaneous fission of ^{235}U governed by its decay branch.

How these heavier nuclides divide into smaller masses can also be estimated by Equation 2.9. The SEMF can predict which stable nuclides can be produced from the fission process, with the prediction that symmetric fission can sometimes occur, with the daughter nuclei relatively equal in mass. Other models however, such as the Nuclear Shell model [10], state it can be more energetically favourable for asymmetric fission to occur, producing *heavy* and *light* nuclei. This can be demonstrated in Figure 2.2.

2.2.2 Production of Radioactive Waste in Nuclear Facilities

Figure 2.2 shows the product yield from the thermal-induced nuclear fission of the common fissile products ^{235}U or ^{239}Pu. The figure demonstrates that following thermal-induced fission, rather than an equal mass distribution between the daughter products, an asymmetric distribution is observed. There

is always a *heavy* daughter product, with atomic masses distributed between 125 to 155, and a *light* daughter product with atomic masses between 80 and 115. An example of two daughter products produced from the fission of ^{236}U is shown in Equation 2.8.

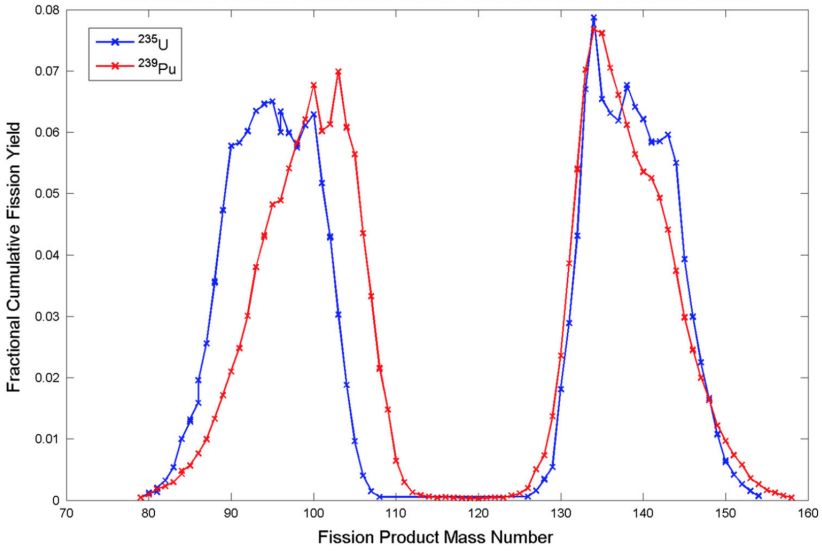

Figure 2.2: Graph to show the cumulative fission product yield from thermal-induced nuclear fission for ^{235}U and ^{239}Pu [11].

As can be seen from Figure 2.2, there is a wide spectrum of various fission products that can be produced for ^{235}U or ^{239}Pu fuels. Table 2.1 shows the percentage yields of the most abundant nuclides produced from the fission of ^{235}U fuel [12].

Table 2.1: Table showing the cumulative yields from thermal fission products produced from ^{235}U and ^{239}Pu fuel, or indirectly from the decay of other products [12].

Nuclide	Half-life	Percentage Yield (%)	
		^{235}U	^{239}Pu
^{135}Xe	9.1 hours	6.61	7.36
^{99}Mo	65.9 hours	6.13	6.19
^{131}I	8.0 days	2.89	3.72
^{90}Sr	28.9 years	5.73	2.01
^{137}Cs	30.2 years	6.22	6.59
^{99}Tc	211k years	6.13	6.19

^{135}Xe, whilst it has a half-life of 9.1 hours, decays to the radioactive ^{135}Cs, which has a half-life of approximately 2,300,000 years. ^{135}Xe is the product of the beta decay from ^{135}I, which has a half-life of 6.6 hours and is considered as a reactor poison. This is because it has a high probability of capturing thermal neutrons, and therefore reduces the efficiency of the reactor process.

^{99}Mo has a half-life of 65.9 hours and decays to technetium-99m, which is beneficial in the medical industry as a diagnostic radioisotope. ^{131}I decays with both beta and gamma radiation. Whilst it has a short half-life in comparison to the other fission products, the possible release of ^{131}I into the environment can be a concern as it can be readily uptaken in the thyroid, leading to an increased risk of cancer.

^{99}Tc is the longest-living fission product on the list, with a half-life of over 211,000 years. ^{99}Tc, ^{90}Sr, ^{99}Mo, ^{135}Cs and ^{137}Cs decay via beta emission. Excluding ^{137}Cs and ^{99}Mo, the remaining products are difficult to detect due to the absence of gamma rays, and the limited distance betas will travel in air.

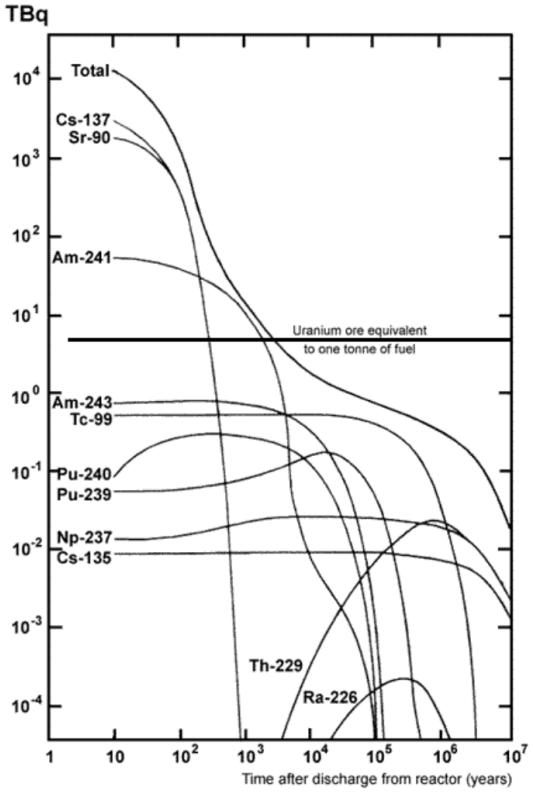

Figure 2.3: Graph showing the activity of waste products from one tonne of spent nuclear fuel with time [13].

A graph showing the activity of these various waste products produced from one tonne of spent ^{235}U fuel, and the activity of these products reducing over time after the reactor has been discharged is shown in Figure 2.3. As stated before, the fission products are predominantly beta and alpha emitters. After a few years, the build-up of these fission reaction products within the fuel increases the neutron absorption, and in turn reduces the efficacy of the fission process. It is at this point where the fuel needs to be removed and replaced. As explained earlier, nuclear fuel falls under the category of HLW, due to the fact the fuel continues to produce heat.

As well as waste originating from the fission of the nuclear fuel, other radioactive products can be produced from other mechanisms. Nuclei which capture a neutron but do not undergo fission are known as actinides, and these include plutonium isotopes and minor actinides such as isotopes of americium and neptunium. Radioactive waste can also be produced from neutron activation within the reactor. Cobalt-60 (^{60}Co) is an example of an activation product produced in nuclear waste.

One of the most abundent waste products is caesium-137 (^{137}Cs). ^{137}Cs is one of the more problematic waste products due to its relatively long half-life of 30.2 years [14]. ^{137}Cs decays via β^- emission to the isomer of barium-137 (^{137m}Ba). It is ^{137m}Ba which is responsible for emitting gamma rays, as ^{137m}Ba decays after 2.55 minutes to its ground state, emitting a 662 keV gamma ray in the process (Figure 2.4) via an M4 transition. As shown in Figure 2.4, the branching ratio for the 662 keV gamma ray is 85.1 %. The remaining 14.9 % is it returning to stability via internal conversion.

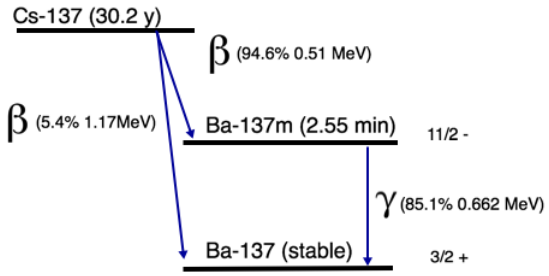

Figure 2.4: Decay scheme of ^{137}Cs. The spins and parities of the two ^{137m}Ba states show the production of the 662 keV gamma ray via an M4 transition.

Days after the initial incident from the Chernobyl disaster in 1986, radioactive material including ^{137}Cs and ^{131}I was found in surrounding territories (Figure 2.5). Gaseous fission products such as Xenon isotopes (^{137}Xe and ^{131}Xe), which

can decay via beta emission to ^{137}Cs and ^{131}I, were likely released into the air as a result of the incident and were subsequently carried by the wind.

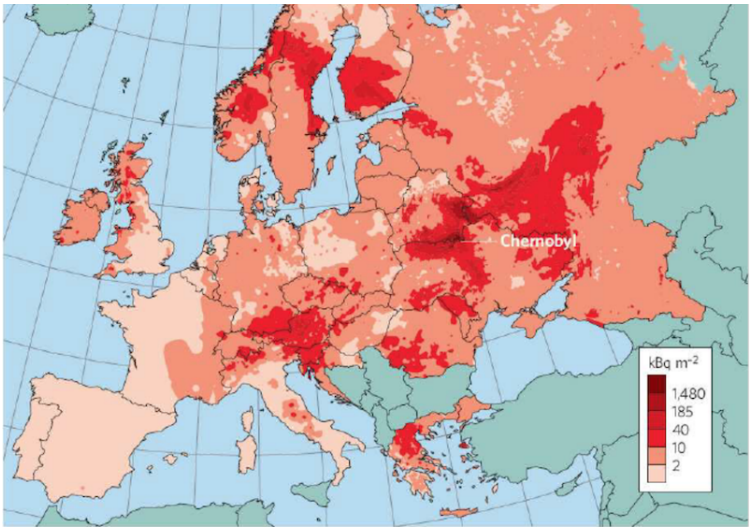

Figure 2.5: Ground deposition of ^{137}Cs across Europe after the Chernobyl nuclear disaster [15].

With the Fukushima Nuclear disaster in March 2011, ^{137}Cs and ^{131}I were released into the environment after an earthquake and tsunami destroyed the Fukushima Daiichi Nuclear Power Plant (FDNPP). Through the uptake of wind or rain, soils in nearby areas were contaminated. The chemical properties of ^{137}Cs are important to consider, as caesium is highly soluble in water, and it can remain on the surface layers of soil as it can strongly bond to soil particles. To prevent the harmful effects on agriculture and human life, it was necessary to try and remove the deposition of ^{137}Cs in the soil. Sporadic sampling of soil was undertaken to provide mapping of the deposition. However, this method was time-consuming and limitations were quickly discovered, with a lack of soil-sampling protocols set out for analysing large numbers of samples for gamma-emitting radionuclides [16]. With an urgency required to minimize the full impact of this contamination, there was a requirement for the use of gamma-imaging systems.

Challenges arise with radiation mapping inside buildings, such as within the FDNPP itself, as locations of contamination included walls, floors or pipes; fixed objects that cannot be easily removed for laboratory analysis. Figure 2.6 shows intensity mapping of gamma-radiation contamination in one of the buildings in the FDNPP with the data collected using a two-tiered Compton

Camera, utilising Ce-doped scintillator detectors [17]. The Compton Camera was able to successfully detect a region of high-dose-rate and visualise it in an image within a short measurement time (40 seconds), whilst being consistent with handheld survey meters.

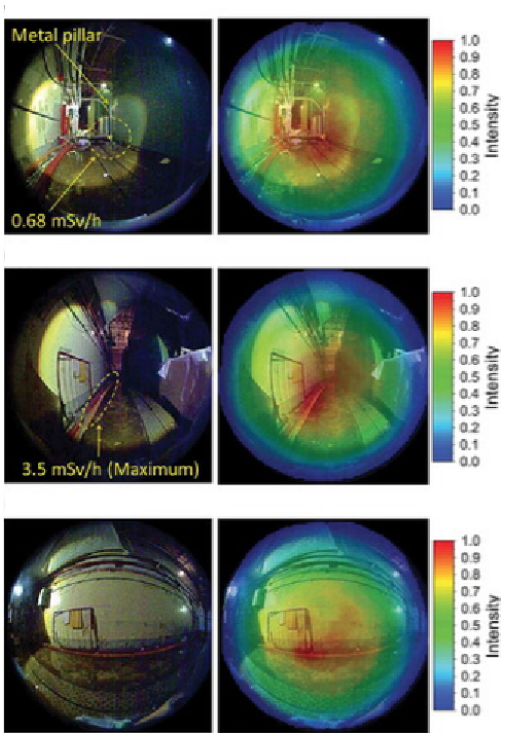

Figure 2.6: Measurements of gamma-radiation distribution inside the Fukushima Daiichi Nuclear Power Plant using a Compton Camera [17].

2.2.3 Waste Classification

Radioactive waste is usually treated based on its material, chemical and radiological composition. Different waste types require different ways of packaging, transportation, storage and disposal. Therefore, it is important that waste streams are characterised accurately to ensure the correct methods are used for the relevant waste, so that authorities or licensees know what they are receiving and need to dispose. Along with this, disposal, transportation or storage of the radioactive waste must comply with local and national regulations such as the Ionising Radiation Regulations 2017 (IRR17) for the UK, enforced by the Health and Safety Executive (HSE).

These regulations vary depending on the classification of the radioactive waste

stream. The main classification technique is to group radioactive waste into one of three groups depending on how hazardous it is to life and the environment, usually defining it by its activity or temperature:

- Low-Level Waste (LLW)
- Intermediate-Level Waste (ILW)
- High-Level Waste (HLW)

HLW, the most dangerous and difficult to process, is characterised in the UK as waste *'with levels of activity concentration high enough to generate significant quantities of heat by the radioactive decay process or waste with large amounts of long-lived radionuclides that need to be considered in the design of a disposal facility for such waste'* [18]. Reprocessed nuclear fuel such as that stored in the FGSMP fall under the category of HLW, and is usually in liquid form. Because of this, HLW has to undergo a process known as *vitrification*, which solidifies the waste and makes it suitable for long-term storage.

Waste is defined as LLW if its radioactive content is less than either 4 GBq per tonne of alpha activity or 12 GBq per tonne of gamma or beta activity [19]. Any waste that exceeds the upper-boundaries of LLW, but the heat production is low enough to not be taken into consideration for storage or disposal can be classified as ILW.

It is possible to classify radioactive waste to a level lower than the three main groups. Ideally, for anything lower than LLW, the free release of materials can be considered. Free release, or the clearance of radioactive material (usually classified as Very Low-Level Waste, VLLW), is defined by the International Atomic Energy Agency (IAEA) as the removal of radioactive materials or objects from any further regulatory control for radiation protection purposes.

For this to be achieved, the radioactivity of the waste must be sufficiently low to not pose a significant risk to individuals. If the effective dose is less than the recommended amount (10 μSv for a member of the public), then cleared waste may be treated as normal waste and can be disposed of as such in surface-type landfill facilities for example. However, for the clearance of a building, clearance levels are expressed as surface specific activity levels, which relate to the activity on and beneath a surface [20].

The Nuclear Decommissioning Authority (NDA) estimated how much radioactive waste would be produced in the UK over the next 100 years. Figure 2.7 shows that the largest amount of waste by volume is VLLW. Whilst HLW has

the smallest volume, this accounts for the majority of the radioactivity that is emitted from this waste.

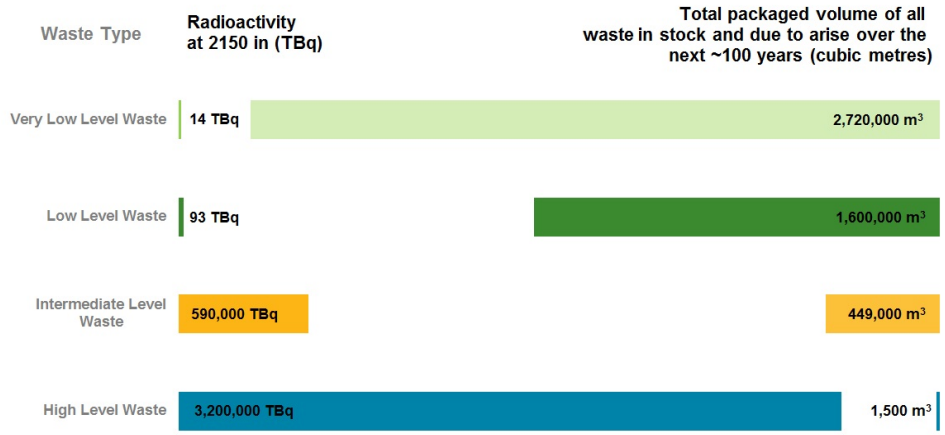

Figure 2.7: Chart showing how much of the different waste types are estimated to be produced in the UK over the next 100 years, by volume and levels of activity [21].

Currently, HLW and some ILW are being considered for storage in a geological disposal facility (GDF). This facility is an engineered facility situated deep underground for the long-term storage of waste, where the natural geological structure of the facility creates a natural barrier against the escape of radioactivity.

ILW is usually packaged in 500 litre or 3 m^3 stainless steel drums [22]. Before storage, the drums are commonly *grouted*, which means the gaps within the storage containers are filled with concrete (Figures 2.8 and 2.9), which limits the amount of radiation that can escape.

Figure 2.8: Image of a 500 litre waste drum containing grouted metallic waste [22].

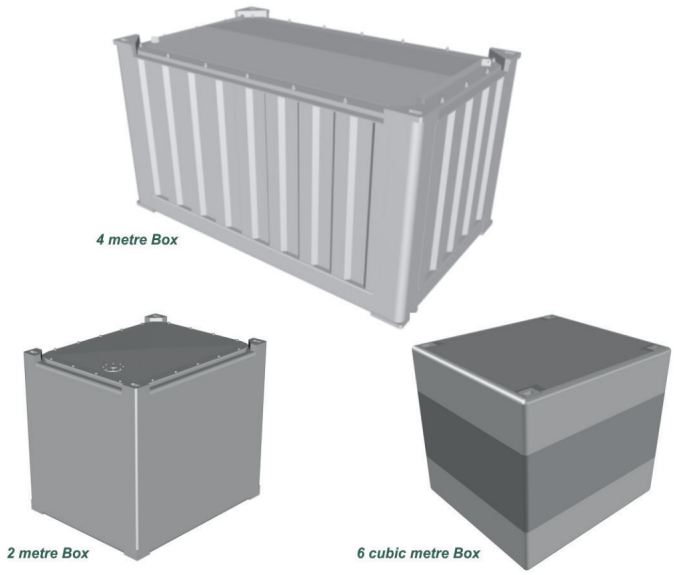

Figure 2.9: Diagrams of different storage containers which can be used for Intermediate Level Waste or Shielded Intermediate Level Waste [22].

LLW in the UK is usually disposed at the Low Level Waste Repository in Cumbria. Similiar to ILW, LLW is usually grouted before being placed within the storage facility. Alternative methods include incineration or disposal in an appropriate landfill site should they be classified at a low enough level.

Locating the radioactive waste can be a complicated process. Unlike waste drums, which can be easily identified from a visual inspection, the complications arise when radiation contamination is deposited on surfaces such as walls, or has accumulated within pipes. When legacy nuclear facilities were designed, it was not with decommissioning in mind, leaving complicated infrastructure that poses difficulties in decommissioning.

However, various methods for characterisation and clearance are used, including:

- Use of a dose meter
- Laboratory analysis methods
- Surface contamination monitors
- Wipe tests

- *In situ* Gamma spectrometry
- Non-Destructive Analysis techniques (NDA)[23]

Dose meters (Figure 2.10) and surface contamination monitors are advantageous as they can identify distributions of activity, and locate any areas of elevated activity, however they do not provide information on the nuclide composition. Different radionuclides have differing release levels, so it is important to determine the composition accurately.

Figure 2.10: Image of the RADIAGEM^{TM} 2000, a personal portable dose rate and survey meter [24].

Despite providing the most accurate insight, laboratory analysis methods hold the obvious disadvantage that samples would have to be collected and then processed in a laboratory set up, causing high exposure to workers if using samples such as spent nuclear fuel. This process also requires knowledge that the mixtures are homogenous.

The use of gamma-ray spectroscopy would be a Non-Destructive Analysis (NDA) technique used in order to characterise the waste stream. Radiological content can be defined with a high level of accuracy, and can help certify waste for transportation which would be important for waste being transferred to a GDF.

If an accurate gamma-ray spectroscopy system could be identified which would satisfy various conditions required such as identifying constituents within the waste stream, as well as their concentrations and various activities, whilst not requiring the waste to be homogenous, then a potentially cost-effective radioactive waste characterisation technique could provide invaluable benefits in the nuclear decommissioning industry.

2.2.4 Non-Destructive Analysis

As stated in its title, non-destructive analysis is a fundamental process in the science community for analysing a sample without dismantling it. Common contamination measurements in a nuclear decommissioning scenario include wipe testing, stationary measurements with a detector, or systematic scanning of a surface [13].

Various instruments are used for non-destructive analysis of radionuclides to assess the contents of waste. Scintillation detectors or Geiger-Muller counters can be used to survey alpha or beta radiation [25]. Environmental analysis of neutrons can be quite difficult due to their weak interaction with matter, with measurement techniques usually involving large detectors [26] or the use of the very expensive and rare helium-3 isotope. However, developments in liquid scintillation detectors have led to improvements in more portable detection technology [27]. Utilising this technique can lead to the simultaneous measurements of thermal neutrons and gammas.

The most common gamma-ray detector systems are usually scintillation based systems such as NaI. Systems that are used for imaging are commonly mechanically collimated high-purity germanium (HPGe) systems, where a single-sample spectrum is collected and analysed for results [28].

On-site measurement is necessary when there is an inability to take samples to a laboratory for further analysis. Varying factors such as the efficiency of the detector system used, the background activity levels, density and activity of the waste material and geometry of the container that it is stored in, will mean measurement times necessary for identifying and localising a weak radioactive source will differ.

Homogeneity

A lot of the characterisation techniques mentioned earlier require knowledge or an assumption that the waste stream being investigated is homogenous. Criteria can be developed for homogenous samples for appropriate treatment processes to take place. If key radionuclides can be identified along with non-radioactive elements, then a waste stream can be declared homogenous as long as NDA measurements of sources at different locations are with a 30 % relative interval [5].

If only a single measurement is made, then it is assumed that the contents being measured are relatively homogenous. By repeating measurements at

different angles, homogeneity can be investigated. Software can be used to plot peak-by-peak differential attenuation for selected nuclides to show the inhomogeneities.

2.3 Industrial systems

Since the Fukushima Daiichi nuclear accident, there has been an increase in the requirement of gamma-imaging systems for radioactivity monitoring or nuclear decommissioning scenarios. These systems need to have spectroscopic and imaging capabilities, and to be utilised in real-time in-situ measurements. Gamma imaging systems that are tested in active demonstrations of decommissioning scenarios have to be able to [29]:

- Be sensitive to gamma radiation.
- Be able to determine the direction of an emitted gamma ray.
- Display the above data as an image showing the spatial distribution and intensity of the gamma radiation.

If, in addition to these essentials, the intensity map can be overlaid onto an optical image in order to display the physical location of the radiation, then it can greatly help with real-world decommissioning scenarios. The aim of any gamma-imaging system is to provide a quantifiable measurement that not only identifies the location of the radioactive contamination, but also provide an accurate measurement of its activity or dose, and identify any radioisotopes present in the contamination.

A technology demonstration workshop held in Vienna, Austria in 2015 compared the capabilities of modern gamma-imaging systems to relevant IAEA applications, for both commercial and prototypes [30]. Generally, these systems included room-temperature semiconductors or scintillator-based detectors. They were compared in a series of experiments that included efficiency tests, extended source measurements, and measurements in a high-background location.

A 18.5 MBq source of ^{137}Cs and a 65 MBq source of ^{60}Co were measured at standoff distances of over 3 m for efficiency measurements. The geometry of extended sources and weak point sources had to be identified and localised, with a sufficient level of detail to be provided on the geometry of the extended source.

It was established that there is no one single best gamma camera which would satisfy every safeguarding scenario set out by the IAEA in preparation for geological repositories [31]. However certain systems may be better suited for specific scenarios (Section 2.3.2). It was also concluded that more work was needed before deployment in active field scenarios.

One of the key objectives for the GRI+ project discussed in this work, is to take in-situ measurements to check for possible radioactive contamination on walls or if there is any accumulation within pipes. The aim of these measurements would be to provide quantifiable information on the contamination, as well as identifying its location. Measurements that are collected in the presence of scattering material, such as concrete, are concentrated on identifying any activity on the surface [32].

Challenges

In order to quantify measurements of LLW items and to separate multiple gamma rays of different energies, or to have a sensitivity for the required detection limits, a detector will have to have certain spectroscopic capabilities such as good energy resolution and efficiency (see Section 3.2.3 - Properties of Radiation Detectors).

In certain environments it is important to have a system that is sensitive to what is being measured without interference from background radiation. With on-site measurements, it is not just the effects of environmental background radiation that can interfere with the measurements. Many radioactive items may be present in the near vicinity which will also contribute to the background radiation levels. Therefore in order to reduce the effect of background radiation, collimated detector systems are usually used.

A collimator, examples of which is shown in Figure 2.11, is used in conjunction with a detector and can define the angle of incidence of an incoming gamma ray, and therefore can be used to observe the distribution of radiation. The collimator is a thick, perforated amount of dense material with a high Z number, examples of such include lead and tungsten. Only gamma rays that pass through the perforations will be detected by the system, any other gamma rays will be absorbed by the collimator [33].

In a scenario of a room full of radioactive storage drums, a collimated system could be placed to focus on one particular drum, thus reducing any additional background radiation coming from the other drums from the measurement. This can be limiting however as it will reduce the efficiency of the system, and

increase the amount of counting time required to collect sufficient data.

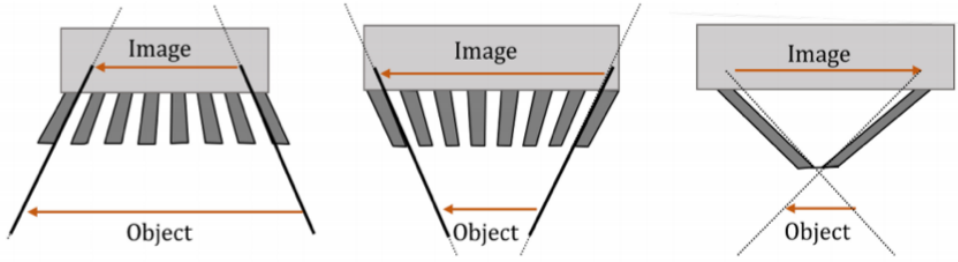

Figure 2.11: Schematic diagrams of different types of collimator used for gamma imaging systems, showing from left to right; diverging collimator, converging collimator, and a pinhole collimator [33].

As well as determining the contents of storage containers, gamma imaging is also used in identifying possible contamination within a room. Investigations take place to see if radiation hotspots are originating from the surface of a wall, or 'from waste from within a silo behind the wall' [32], and to measure the activity on a concrete wall's surface.

2.3.1 Other Gamma Imaging Systems

There are lots of different choices for detector materials to be used for gamma-imaging systems. Solid state scintillators and semiconductors are efficient choices for gamma-ray detectors, however there are limits to using the different detector crystals. Scintillator detectors, or room-temperature semiconductors are advantageous due to ease of transportation, however they have a poorer energy resolution in comparison to standard semiconductors.

Certain types of semiconductor detectors have extremely good spectroscopic capabilities, but it would have to be continuously cooled, either with liquid nitrogen or a mechanical cooling unit, limiting portability. They are also restricted to a particular thickness due to manufacturing limitations. A balance must be found between what is desirable and what is achievable.

In the UK, the majority of radioactive waste is stored at the British Nuclear Fuels Ltd (BNFL) Sellafield site, Cumbria. One of the imaging systems used at Sellafield is the Cavendish Nuclear RadScan®. This includes a scintillator detector and a 4 degree collimator (a more detailed description is found further

in this section). It is commonly used to determine if a wall is contaminated, situated at a large stand-off distance over a long period of time.

Sellafield Ltd. invited Radiometric suppliers of various gamma-imaging systems to an active demonstration test facility to exhibit their systems within a series of tests [29]. The tests included:

- Identifying the location of radiation sources by producing an image of the characterised area.
- Provide spectroscopic information, or isotopic composition of the radiation sources.
- Dose rates arising from the radiation sources.
- Quantification of the activity of the radiation sources.

As well as demonstrating imaging capabilities, different characterisation scenarios were included to see if true hotspots could be distinguished from a separate point source, or an identical source added to observe the effect of off-axis radiation.

The test shown in Figure 2.12 utilised an area within the active demonstration facility with known hotspots of extended radioactivity on the surface of a wall. The detectors would have to be placed at a standoff distance of more than 4m from the source of radioactivity.

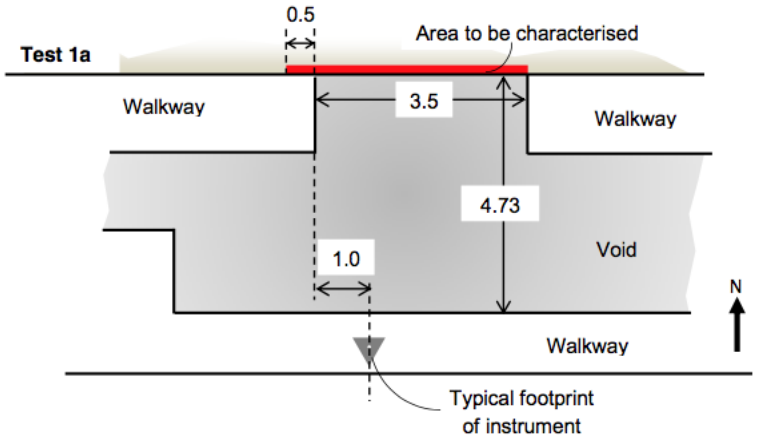

Figure 2.12: Test scenario at Sellafield, where a wall of known radiation contamination had to be characterised. Dimensions are in metres [29].

The different detector systems would have to accurately measure the hotspots found on the wall, and provide in their reports the items in the list detailed earlier. These systems are the current standard of gamma-imaging systems utilised in industrial scenarios, and therefore are the best comparison to the GRI+ imaging system for radioactive waste characterisation scenarios.

Cavendish Nuclear RadScan®:800 and RadScan®:900

The RadScan® is composed of scintillating material, either sodium iodide (NaI) for the RadScan®:800 model or cerium bromide ($CeBr_3$) for the RadScan® :900 model. Surrounding the detection crystal is a tungsten collimator, except for a narrow beam which can be altered to a size of 4°, 3°, 2° or 1° . The differing collimator sizes can lead to improved spatial resolution, but will greatly affect the efficiency of the system.

The RadScan is a collimated pan-and-tilt system, acquiring spectra at discrete pan-tilt angles. This means the orientation of the collimator can be precisely controlled and measured when it is left to count incident gamma rays for a determined 'dwell time'.

The intensity map is overlaid onto a conventional optical image from a charge-coupled device camera which is mounted on the detector head. It is also able to do background subtraction through spectra collected from radiation hitting outer shielding, rather than directly through the collimator.

The RadScan ®:800 model has been utilised at Sellafield previously, and is the main point of comparison for any new detector systems. The updated RadScan ®:900 model has an energy resolution of 9.5 % FWHM at 662 keV [34]. The gamma images produced of the Test 1a scenario (Figure 2.12) at Sellafield shown in Figure 2.13 show how well the RadScan is able to map the intensity of the radiation hotspots.

Figure 2.13: Gamma image produced by the Cavendish Nuclear RadScan ®:800 (left) and RadScan ®:900 (right) of the test scenario seen in Figure 2.12 [29].

N-Visage Gamma Imager

The N-Visage Gamma Imager includes a small cadmium zinc telluride (CZT) detector, surrounded by spherical tungsten shielding, with a slit collimator, and is able to cover a solid angle view of 4π steradians [29]. It was designed to be helpful for nuclear engineers, with a low mass and specifically designed to be deployed through small apertures [35]. It has an energy resolution of 3 % FWHM at 662 keV, and can take less than 3 hours to produce a gamma image [35].

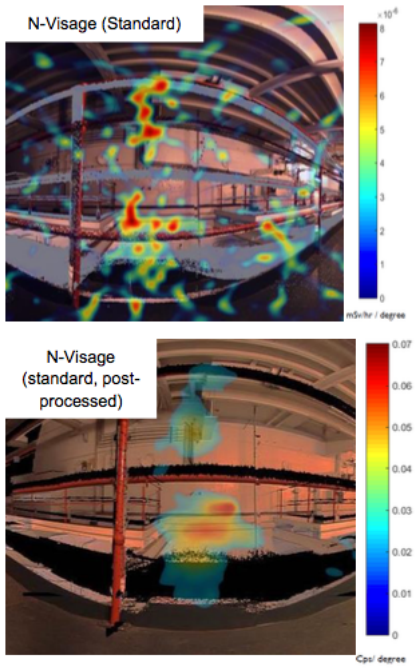

Figure 2.14: Gamma image produced from the N-Visage Gamma Imager at a test site at Sellafield [29].

As it can be seen from the top image in Figure 2.14, the N-Visage Gamma Imager's initial image is extremely inaccurate and the source intensity is not identified until after post-processing of the data to produce the bottom image in Figure 2.14. In comparison to Figure 2.15, which shows intensity mapping of contamination at a site at Fukushima from an initial image. It could be deduced that the N-Visage is more suitable to higher-activity scenarios (GBq) compared to lower-activity contamination.

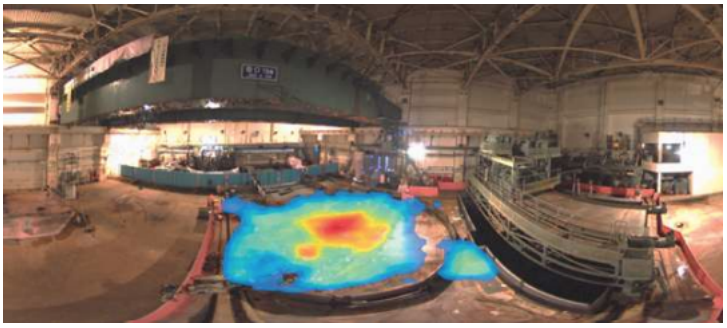

Figure 2.15: 2D Visualisation mapping of radioactive contamination at Fukushima using the N-Visage Gamma Imager [36].

ANTECH RadSearch Gamma Camera, G3050

Similar to the RadScan detector, the RadSearch Gamma Camera uses a collimated detector which is coupled to a laser rangefinder and a camera atop a pan-tilt unit which can give a total solid angle view of 4π steradians [37] . It was supplied by A. N. Technologies Ltd (ANTECH) through AMEC-Foster-Wheeler.

The gamma camera features a 1 inch x 1 inch Lanthanum tribromide ($LaBr_3$) scintillation detector, which offers an energy resolution that is of typically 2.5 % - 3 % for 662 keV energies [37], high detection sensitivity and a wide dose-rate range.

iPIX

Like the previously described gamma imager systems, the iPIX system, provided by Mirion Technologies UK through NNL, includes a collimator that can also be altered in order to improve efficiency. The collimator used is known as a 'coded mask'. It is a piece of specific shielding which has a particular pattern of holes which allow gamma rays to pass through.

Images can be produced from mathematical analysis and knowledge of the mask's pattern. However, it can be susceptible to off-axis radiation, leading to artefacts being produced in the final image.

The iPIX usually features a cadmium telluride (CdTe) detector. However the energy resolution of this is comparitively poor and not suitable for spectroscopy purposes. This can be seen in the spectrum shown in Figure 2.16 of a ^{137}Cs

measurement taken with the iPIX CdTe detector, and the difficulty observing the 662 keV full-energy peak.

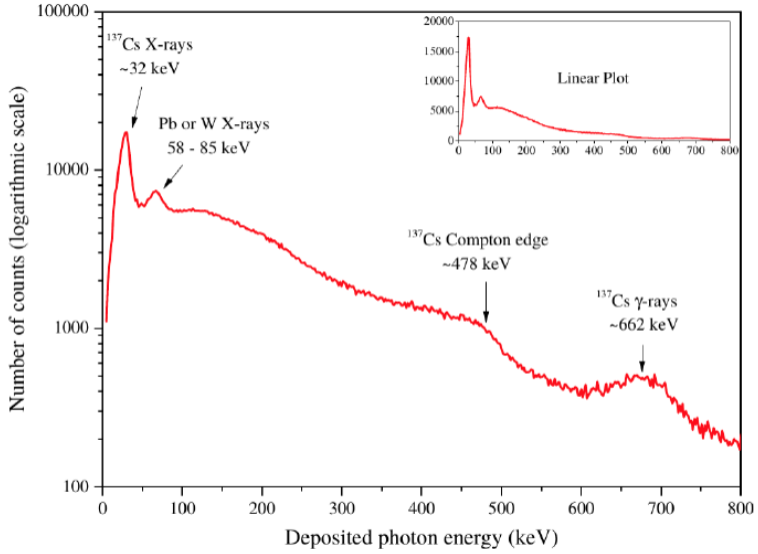

Figure 2.16: Energy spectrum from a ^{137}Cs collected with the iPIX CdTe detector, highlighting the poor spectroscopic performance of the CdTe [39].

Therefore, an alternative lead collimated 1 cm^3 CZT spectrometer, which has an energy resolution of 2.5 % for ^{137}Cs [38] was used, which is more suitable for gamma spectroscopy. It is a lightweight device (2.5 kg [38]), which can be easily deployed in a decommissioning or contamination scenario.

HSL-Lite

The HSL-Lite Plus model uses a casesium iodide (CsI) scintillator detector, along with a coded mask aperture similiar to that used by iPIX, and is supplied by Innovative Physics Limited (IPL) through REACT engineering.

To combat the interference from off-axis radiation which can be present from coded masks, the HSL-Lite features a rotating mask which was not present in previous models. It is a lightweight model (10 kg), with a 45^o gamma field of view [40], and is capable of collecting rapid measurements of low-level radiation, or detecting hotspots of radiation of approximately 2 mSv/h.

Polaris-H

Compared to the other systems, the Polaris-H detector, produced by H3D, consists of a larger, pixelated CZT detector crystal (6 cm^3). Polaris-H is able to achieve a higher efficiency as it does not require any additional shielding around the system. Rather than using a collimator, Polaris-H determines the direction of the incident gamma rays by using the *Compton Camera* technique, which will be detailed in Section 3.3.

It has excellent energy resolution for gamma spectroscopy measurements compared to other room-temperature semiconductors, achieving a 1.1 % FWHM at 662 keV [41], which is also the best energy resolution out of the seven systems detailed here. It has an angular resolution of 30 deg FWHM during real-time measurements, which improves to 20 deg FWHM post-processing [42]

The main benefits of the Polaris-H are portability, rapid measurement (a few minutes), a 360^o field of view and high efficiency combined with excellent energy resolution for gamma spectroscopy for a CZT detector.

Comparison

It is clear that gamma imaging systems require a balance between the efficiency of the system and the position resolution. Some measurements that collected a lot of events in a short period of time had a poorer performance in locating the distributed activity, and those with superior position resolution would have required long measurement times to collect a sufficient amount of data.

The GRI+ system's efficiency is not limited by physical collimators as the detectors are electrically segmented. The mechanically cooled semiconducter detectors used in GRI+ also have superior spectroscopic capabilities compared to the scintillator or room-temperature semiconductors currently used, meaning it would be able to distinguish between multiple gamma-ray energies or multiple radioisotopes. GRI+ is described in more detail in Section 4.1.

The gamma imagers included in this report were able to fulfil the requirements set out, with conclusions that the systems were able to agree on the location of distributed activity and the production of gamma images, as well as providing quantifiable information (not detailed in the report) on activities and dose rates. The images produced had the assumption that the contamination was only on the surface of the wall, with no calculations on the amount of ingress within the concrete.

Chapter 3

Principles of gamma-ray detection

3.1 Interaction of Gamma Rays

Gamma rays are uncharged, electromagnetic radiation that arise from the decay of excited nuclear states, which can be populated following radioactive decay. Compared to particulate radiation that can be emitted from atomic nuclei, gamma rays interact differently. Charged particles will interact via direct ionisation with matter, whilst gamma rays interact through indirect ionisation.

In a nuclear interaction with a target atom, a photon will interact via scattering or absorption. The transfer of the photon's energy can cause secondary processes to occur such as the ejection of orbital electrons, or production of electron-hole pairs. It is the outcome of these secondary reactions that can allow the original incoming photon to be detected.

The interactions of significance in this work will be photons that are Compton scattered and those that are photoelectrically absorbed. This is due to the characteristic energies of the radioisotopes that will be used, with various factors determining which process is more likely to occur.

3.1.1 Photoelectric Absorption

This process requires an incoming photon with a characteristic energy to be completely absorbed and is commonly observed with low-energy gamma rays. The interaction involves a photon incident on an atom, interacting with a bound atomic electron. The complete transfer of the photon's energy to a

bound electron produces an energetic photoelectron. If the energy transferred is larger than the binding energy, then the photoelectron will be ejected from the shell in which it resides. This can be represented by the following equation:

$$E_e = E_\gamma - E_b \tag{3.1}$$

Here, E_e represents the energy of the photoelectron, E_γ the characteristic energy of the incoming photon, and E_b the binding energy of the atomic electron.

The ejected photoelectron now leaves a vacancy in the atomic shell it has vacated. This vacancy commonly occurs in the tightly bound K-Shell, the lowest energy state of an atom. This causes an electron from a higher orbital state to drop down to fill this vacancy. This de-excitation process causes the emission of a characteristic X-ray, with the energy equalling the difference in binding energies between the two shell states.

The probability that photoelectric absorption will occur is defined as the cross-section, σ_{PA}, as shown in Equation 3.2.

$$\sigma_{PA} = K \times \frac{Z^n}{E_\gamma^{3.5}} \tag{3.2}$$

Z is the atomic number of the material with the exponent n falling between 4 and 5 [43]. K is a proportionality constant. Equation 3.2 shows that there is a large dependence on the probability of photoelectric absorption occurring and the Z-number of the material. The larger the Z-number, the more probable it is that photoelectric absorption will occur, which is why high-Z materials such as lead are beneficial for radiation shielding.

3.1.2 Compton Scattering

Compton scattering occurs when a photon inelastically collides with an electron in an outer-shell orbital of an atom. Instead of a complete transfer of energy like in photoelectric absorption, the photon will transfer a proportion of its energy to the electron and is then scattered in a particular direction in relation to its original trajectory. The incident gamma-ray energy, E_I, the

scattered gamma-ray energy, E_S, and the scattering angle θ are related via the Compton scattering formula:

$$E_S = \frac{E_I}{1 + \alpha(1 - cos\theta)} \tag{3.3}$$

Where $\alpha = \frac{E_I}{m_0 \times c^2}$, and m_0 is the rest mass of an electron.

The probability of Compton scattering per atom of the absorbing material, which can be described by the Compton cross section, σ_C, depends on the number of electrons available as scattering targets which increases linearly with Z number ($\sigma_C \backsim Z$). The angular distribution of scattered gamma rays can be described by the Klein-Nishina formula, Equation 3.4, for the differential cross section $\frac{d\sigma_C}{d\Omega}$.

$$\frac{d\sigma_C}{d\Omega} = Zr_0^2\Big(\frac{1}{1 + \alpha(1 - cos\theta)}\Big)^2\Big(\frac{1 + cos^2\theta}{2}\Big)\Big(1 + \frac{\alpha^2(1 - cos\theta)^2}{(1 + cos^2\theta)(1 + \alpha(1 - cos\theta))}\Big) \tag{3.4}$$

Where $\alpha = hv/m_0c^2$ and r_0 is the classical electron radius.

A visual representation of the Klein-Nishina formula is shown in the polar plot in Figure 3.1. The plot describes a gamma ray originating from the left-hand side of the figure, and the angle at which it may scatter is reflected in the polar plot.

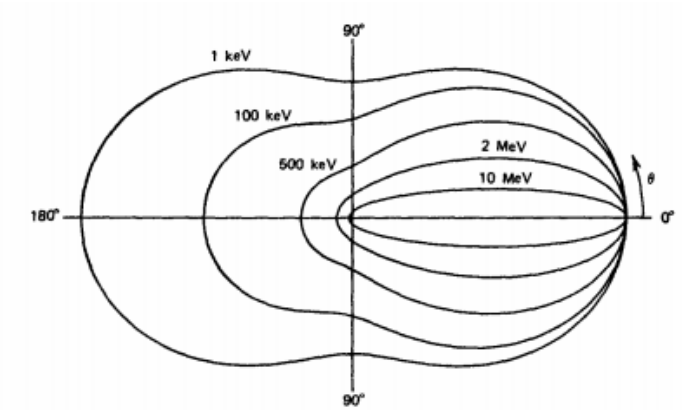

Figure 3.1: Polar plot representing the Klein-Nishina formula, which shows photons (incident from the left-hand side of the plot) Compton scattered at particular solid angles θ depending on the energy of the incoming photon [43].

Understanding the possible spread of scattering angles can help optimise the efficiency of measurements by enabling the positioning of detectors in the correct location. The plot illustrates a strong tendancy for forward scattering at high values of gamma-ray energy, which is relevant for this investigation when the energy of interest is 662 keV. This knowledge of forward scattering photons means the geometry of the Compton camera should be arranged with one detector directly behind the other for maximum efficiency.

3.1.3 Other interaction processes

Pair Production

If a photon energy exceeds 1.022 MeV, then it is energetically possible for pair production to take place. At this energy, the gamma ray is able to transform into matter in accordance with Einstein's equation (Equation 3.5) in the form of an electron-positron pair, as the 1.022 MeV equals twice the rest-mass of an electron, m.

$$E = mc^2 \tag{3.5}$$

This conversion only occurs within the Coulomb field of the nucleus in order to satisfy the conservation of energy and momentum. Any excess energy from the production of the electron-positron pair is shared between them as additional kinetic energy.

The positron will eventually thermalise within an absorbing medium and interact. When a particle and antiparticle meet, they annihilate to produce two directly opposing photons of energy 511 keV.

The relative probabilities of each interaction process (τ, σ and κ represent the probabilities per unit length of photoelectric, Compton or pair production interactions respectively) are shown in Figure 3.2 showing which gamma-ray interaction is most likely to dominate depending on the gamma-ray energy and the absorber atomic number; denser materials are more likely to lead to full absorption whereas low Z values will likely lead to scattering.

For lower energies, the photoelectric effect is the dominant process, and as the energy of the gamma ray increases, Compton scattering and eventually pair production become the dominant processes. The two additional solid lines shown in Figure 3.2, show where the interaction effects are equally probable

[44].

The detecting materials that are used for GRI+ include Silicon (Si) and Germanium (Ge). The atomic numbers of these elements are 14 and 32 respectively, and are shown on Figure 3.2 as additional dashed lines to show which interaction processes dominate as you increase the gamma-ray energy. The gamma-ray energy of interest in this thesis is 0.662 MeV from ^{137}Cs. As shown in Figure 3.2, Compton scatter events are the most likely to occur within both Si and Ge at this energy.

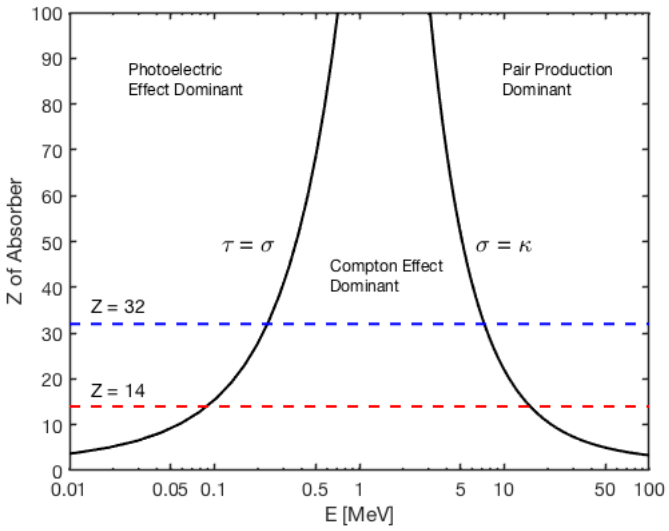

Figure 3.2: A graph displaying the importance of the three major types of gamma-ray interactions; Photoelectric absorption, Compton scattering and pair production. This is shown as a function of gamma-ray energy, and the solid black lines represent where neighbouring effects are equally probable. The dashed red and blue lines show what interaction processes are most likely for Si (Z = 14) and Ge (Z = 32).

Interaction of Charged Particles

Charged particles interact primarily through Coulomb forces between their own positive charge, and the negatively charged orbital electrons of the atoms within which they are interacting. When the charged particle interacts with a medium, the attractive Coulomb force has a large affect on the electrons in one of the following processes.

In *excitation*, the energy that is transferred to the electron can cause it to move to a higher-lying orbital state. If the energy is high enough, it can cause the electron to be ejected from the atom in *direct ionisation*. The atom then

becomes ionised due to the removal of the electron.

Charge carriers are usually defined as particles that are free to move within the material, which carry an electric charge. Within a given material, the differential energy loss, dE, for that material over a differential path length, dx, defines the *linear stopping power,* S of that material.

$$S = -\frac{dE}{dx} \tag{3.6}$$

For heavy particles (those which have an atomic mass unit of 1 or greater) that move through a material, the specific energy loss $(-\frac{dE}{dx})$ is represented by the Bethe-Bloch formula (Eq. 3.7). This shows that high-atomic number, high-density materials will have the greatest linear stopping power.

$$-\left\langle \frac{dE}{dx} \right\rangle = \frac{4\pi}{m_e c^2} \cdot \frac{nz^4}{\beta^2} \cdot \left(\frac{e^2}{4\pi\varepsilon_0}\right) \cdot \left[ln\left(\frac{2m_e c^2 \beta^2}{I \cdot (1-\beta^2)}\right) - \beta^2\right] \tag{3.7}$$

ε_0 is the vacuum permittivity, $\beta = \frac{v}{c}$, where c is the speed of light, and e and m_e are the electron charge and electron rest mass respectively. The electron density of the material, n, can be represented by Eq. 3.8.

$$n = \frac{N_A \cdot Z \cdot \rho}{A \cdot M_u} \tag{3.8}$$

In Equation 3.8, N_A is Avogadro's number, Z is the atomic number, ρ is the density of the material, A its relative atomic mass, , and M_u is the molar mass constant.

Specific energy loss of electrons can be divided into two different interactions. Collisional $-(\frac{dE}{dx})_c$ losses describe energy loss due to ionisation and excitation of electrons, and radiative losses $-(\frac{dE}{dx})_r$ describe losses such as *bremsstrahlung* radiation. When fast electrons interact with matter, part of their energy is converted into electromagnetic radiation as the electron decelerates within the material.

Both processes can be summised in Equation 3.9 with the total linear stopping power for electrons.

$$\frac{dE}{dx} = \left(\frac{dE}{dx}\right)_c + \left(\frac{dE}{dx}\right)_r \tag{3.9}$$

In ^{137}Cs, the energy loss can be described soley by collisional losses. As radiative losses dominate at higher energies (>3 MeV), and within absorber materials of a high atomic number (Z), they can therefore be considered negligible for the work in this thesis. The effect of radiative losses is low in comparison to collisional losses, as shown by the ratio of energy losses in Equation 3.10.

$$\frac{(dE/dx)_r}{(dE/dx)_c} \cong \frac{EZ}{700} \tag{3.10}$$

Whilst radiative losses can be considered negligible for this work, consideration of radiative losses may be required for any future in-situ environmental measurements. Environmental measurements can be influenced by the interactions of beta particles. Therefore the affect of bremmsstrahlung radiation must be considered, which contribute to radiative losses.

3.1.4 Attenuation of Gamma Rays

When gamma rays pass through a material, as well as undergoing the processes of photoelectric absorption and pair production, they can Compton scatter off atomic electrons and lose energy.

For a beam of mono-energetic photons, the change in intensity of the incoming photons through a certain material can be represented by the following equation:

$$dI(x) = -I_0(x) n \sigma dx \tag{3.11}$$

Where dI is the change in intensity through a material of thickness x, with dx being the incremental thickness the photon has travelled, after passing through with an initial intensity of $I_0(x)$. σ represents the microscopic cross-section, and is a proportionality constant which reflects the total probability that a photon is scattered (σ_C) or absorbed (σ_{PA}) in the material, with n being the number of atoms per cm^3.

This equation once integrated becomes:

$$I(x) = I_0 \, e^{(-n\sigma x)} \tag{3.12}$$

The values of n and σ are combined to become the linear attenuation coefficient, μ (cm^{-1}).

The linear attenuation coefficient is the probability that a photon will be attenuated per thickness of the attenuating material. This value decreases with increasing energy.

The total linear attenuation coefficient (μ_{tot}) is the sum of the individual coefficients corresponding to each type of interaction; i.e photoelectric absorption (μ_{PA}), Compton scattering (μ_{CS}) and pair production (μ_{PP}).

$$\mu_{tot} = \mu_{PA} + \mu_{CS} + \mu_{PP} \tag{3.13}$$

The average distance travelled by the photon in an attenuating material before a particular interaction takes place is represented by the mean free path, λ.

$$\lambda = \frac{\int_0^\infty x e^{-\mu x} dx}{\int_0^\infty e^{-\mu x} dx} = \frac{1}{\mu} \tag{3.14}$$

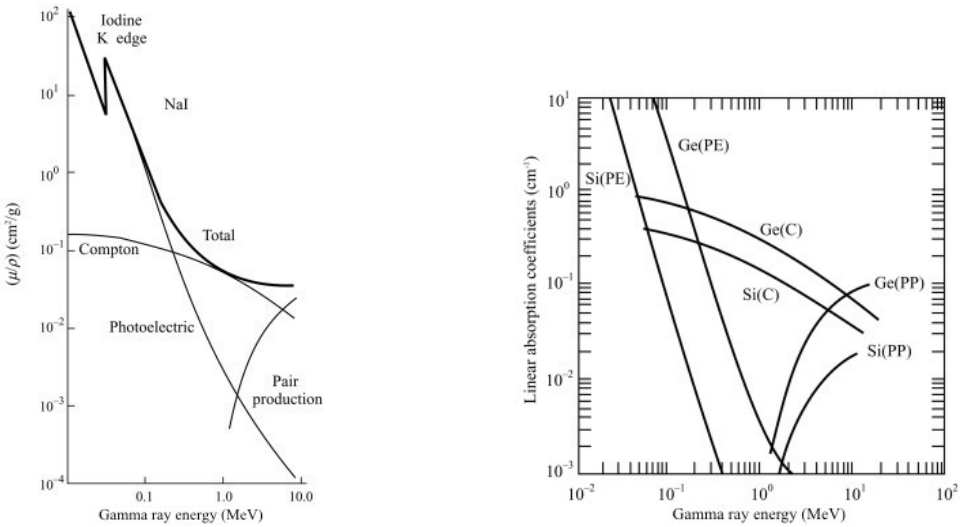

(a) (b)

Figure 3.3: (a) Graph showing the variation of mass attenuation coefficient against gamma-ray energies for various gamma-ray interaction processes in a sodium iodide crystal [45] (b) Graph showing the variation of linear attenuation coefficient against gamma-ray energies for various gamma-ray interaction processes in semiconductor crystals germanium (Ge) and silicon (Si) [45].

Figures 3.3a and 3.3b show the variation of mass attenuation and linear coefficients respectively for a range of gamma-ray energies within sodium iodide, germanium and silicon, and show how the density of different materials also effect the probability of interaction processes. Both show that as the gamma-ray energy increases, probability of Compton scattering processes decreases.

Mass Attenuation Coefficient

The probability of a gamma ray interacting in a material is dependent on the number of atoms that are present in a given area. Because of this, the linear attenuation coefficient is dependent on the density of the material. This can be represented by the mass attenuation coefficient, μ_m.

$$\mu_m = \frac{\text{Linear attenuation coefficient } (\mu)}{\text{Density } (\rho)} \tag{3.15}$$

The mass attenuation coefficients for elements up to Z = 92 can be found for different photon energies [46]. If the density of the material is known, then it can be converted to the linear attenuation coefficient to be used with the attenuation law (Equation 3.12).

3.2 Operation of Gamma-Ray Detectors

Through the interaction processes detailed earlier in this chapter, a detector is able to provide information on the incident photons. A suitable gamma-ray spectrometer must be able to carry out the following functions [47]:

- Act as a successful conversion medium, which means incident photons will interact with the medium to produce electrons.
- Must be functional in detecting these secondary electrons.

It is also ideal for the produced signal to be proportional to the energy deposited by the interacting photon, but this is not the case for all gamma-ray detectors.

This section details the difference between the operation of scintillation detectors, such as NaI, and semiconductor detectors, such as Si and Ge.

3.2.1 Scintillation Detectors

The principle of scintillation detectors relies on the material being able to emit light when ionising radiation interacts with the material. The energy lost by this ionising radiation is converted into a pulse of light, which can then be transformed into an electric signal.

The choice of material for scintillation detectors varies depending on what type of radiation is to be detected. These can be divided into *organic* or *inorganic* scintillators.

The main difference between the two is the scintillation mechanism. In organic materials, the fluorescence process arises from transitions between energy levels of the single molecule. This differs in comparison to inorganic materials where the fluorescence process relies on the structure of the crystal lattice.

In insulating, semiconducting or conducting materials, there consists a valence band and a conduction band. For insulators and semiconductors, there is an energy gap separating the two.

The valence band consists of outer-shell electrons that are bound to specific lattice sites within the material. The conduction band is where the electrons are free to move about, and is what contributes to the conductivity of the material.

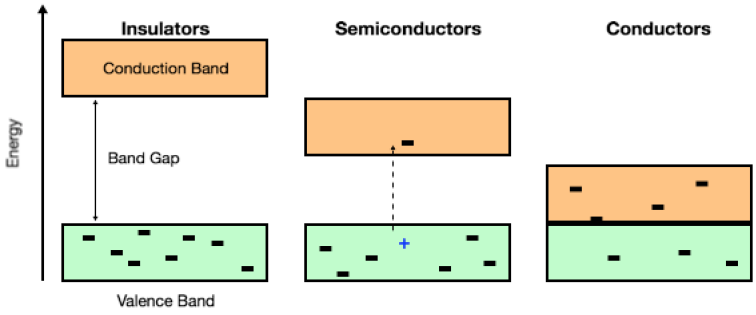

Figure 3.4: Diagram showing the different band gap energies for insulators, semiconductors and conducting materials.

.

The energy gap between the three materials varies as shown in Figure 3.4. For insulators, the energy is so high ($\backsim$ 6 eV) that it is near impossible for electrons to gain sufficient energy to excite from the valence band to the conduction

band. In conducting materials, the two bands overlap so that electrons can move freely.

When an electron is elevated to the conduction band, it leaves a hole in the valence band. A photon is usually emitted when an electron returns to the valence band. However, this is an inefficient process as an electron may not always return to the valence band. To account for this, impurities are added to the crystal lattice. These impurities are known as *activators*, and they are able to modify the band structure by creating special sites within the lattice. These additional energy states, as shown in Figure 3.5, allow electrons to de-excite back to the valence band, and give rise to a visible photon.

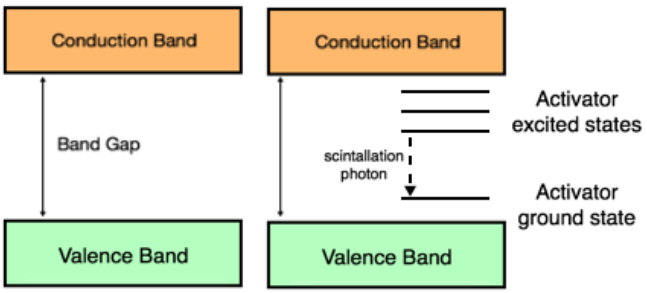

Figure 3.5: Diagram showing the addition of impurities to the crystal lattice to include additional activator excited states.

Whether organic or inorganic materials are chosen can also be down to their atomic number. A lower atomic number for organic scintillators makes it suitable for neutron or charged particle detection, whereas inorganic scintillators often have a higher atomic number, making it more suitable for gamma-ray detection [48].

The pulse of light can be converted into an electrical signal through a photodetector, such as a photomultiplier (PMT) tube. The PMT consists of a photocathode, which uses the photoelectric effect to convert light into a photoelectron. As shown by Figure 3.6, the initial electrons are accelerated towards a dynode by an electric field.

Upon contact with the first dynode, secondary electrons are emitted, which in turn are accelerated to the next dynode. This process repeats producing a cascade of photoelectrons, until they eventually reach the anode where the resulting charge is collected.

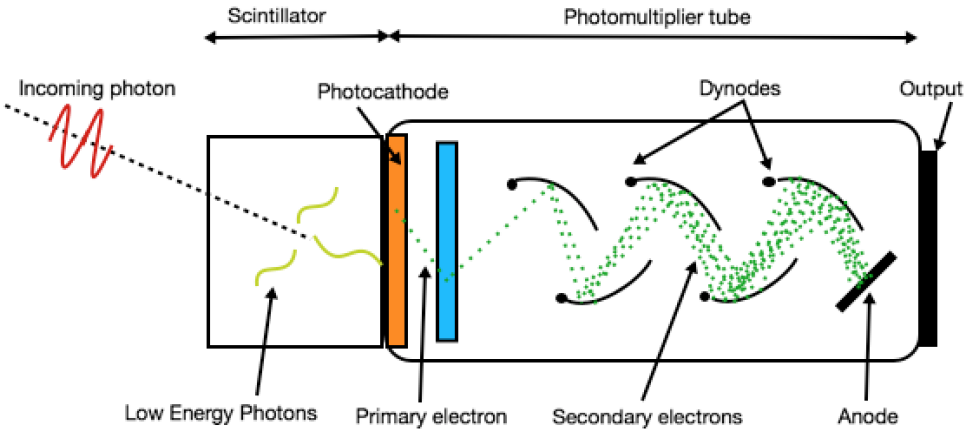

Figure 3.6: Schematic diagram showing the workings of a scintillator detector with a photomultiplier tube.

The current can be determined from a voltage-divider network. This consists of a series of resistors between the anode and cathode. By dividing the applied voltage by the resistance, the anode current can be determined. This can be compared to the internal current of electrons moving between dynodes. The ratio between the two output currents is proportional to the incident light level. The gain, or current amplification, observed between the two can describe the output charge per pulse. This can then be converted into an electrical signal to be analysed by the system electronics.

Properties of Scintillation Detectors

For a scintillation detector to be as efficient as possible, the largest possible fraction of light emitted from the ionising track deposited in the crystal is to be collected.

The quantum efficiency is a term that describes the sensitivity of the photocathode, and describes the probability of the conversion of light to an electric signal. This is represented by Equation 3.16. The average quantum efficiency is found to be between 20 - 30 % [49].

$$\text{Quantum Efficiency} = \frac{\text{Number of photoelectrons emitted}}{\text{Number of incident photons}} \tag{3.16}$$

NaI crystals are common materials for scintillation detectors, as its high atomic number of Z = 53 means that they have a very high intrinsic detection efficiency. Other materials used for scintillation spectrometers include cesium iodide (CeI), bismuth germanate (BGO), and lanthanum bromide ($LaBr_3$). These materials may hold advantages over NaI such as a greater detection efficiency, or a better energy resolution, however NaI is common for spectroscopy applications due to its balance to not just detector performance, but also its affordable cost and widespread availability [50].

3.2.2 Semiconductor Detectors

Operation of Semiconductors

At absolute zero, semiconductors will have a an idealised configuration in which the valence band is completely full and the conduction band is empty. Because of this, the semiconductor acts as a thermal insulator.

As the temperature increases from absolute zero, a finite amount of thermal energy will cause a valence electron to be excited to the conduction band, allowing it to leave its specific site and drift freely throughout the crystal. This excitation consequently leaves a 'hole' in the valence band from the excited electron. The combination of the excited electron and the vacancy left by the excited electron (*hole*) is known as an *electron-hole* pair. A potential-difference can be applied across the semiconducting material to induce an electric field, which can cause the holes and electrons to move freely.

Each energy level can only accommodate a limited number of electrons. The Fermi level, is any energy level found that has an equal probability to be exactly half-filled with electrons. This Fermi level will shift towards either the valence or conduction band if the concentration of electrons or holes changes.

Doping

In intrinsic (extremely pure) semiconductors, the number of electrons and holes that exist must be equal. This is because a hole can only be produced from the thermal excitation of an electron from the valence band to the conduction band.

In a pure intrinsic, elemental material such as silicon (Si) or germanium (Ge),

each nucleus forms four covalent bonds with its neighbours to form a crystal lattice, using their four valence electrons. However, not all semiconductors can be classed as intrinsic materials. In reality, chemical impurities are likely to exist in the lattice due to natural formation. These impurities can also be deliberately introduced to the material using a process known as doping. By doping a semiconducting material, the Fermi level energy can be shifted towards either the valence band or conduction band depending on the dopant concentration, as shown in Figure 3.7. Materials can be doped with either a p-type or n-type material, which will lead to the addition of free holes or electrons respectively.

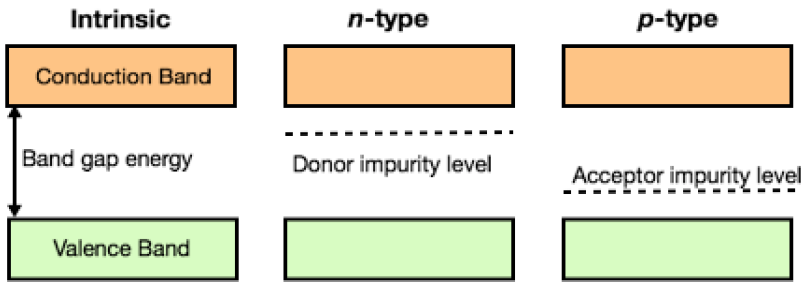

Figure 3.7: Diagram to show the shift in the Fermi level enegy by doping semiconducting material with either n-type or p-type material.

For Group IV n-type material semiconductors, such as Si and Ge, Group V elements are likely substitutions due to their additional valence electrons. Lithium is a Group I element that is commonly used for doping in Si and Ge detectors. The additional electron is not bound within the lattice and therefore is free to move about. This abundance of electrons means that they are the majority charge carriers.

Group III elements such as boron or gallium are likely substitutions for p-type material. Their three valence electrons lead to a hole in excess. In this case, holes become the majority charge carriers.

P-N Junction

If a n-type material was placed at a boundary to a p-type material, then a P-N junction forms when it is in contact under thermal equilibrium. When the two materials are in contact with each other, diffusion of charge occurs across the boundary due to the differences in concentration of electrons and holes. Electrons begin to diffuse from the n-type material to the p-type, and vice-versa for the holes. A region of space charge of opposite polarities is produced from the free charge carriers leaving their immobile ions.

A natural potential is establised at the P-N interface because of this space charge, preventing any further diffusion of electrons or holes across the junction. The region over which this takes place is called the depletion region. By applying a **reverse bias** to the P-N junction, the thickness of the depletion region increases, representing the active volume of the detector and which can be represented by the following equation [51]:

$$d \cong \left(\frac{2\varepsilon V}{eN}\right)^{\frac{1}{2}} \tag{3.17}$$

Here, ε is the dielectric constant, V is the applied voltage, e is the electric charge and N is the number of impurities.

If the number of impurities within the material is too high, these can create *electron traps* within the crystal. These traps can capture electrons during the ionisation process. These traps can therefore immobilise the mobile charges and can affect the number of majority charge carriers due to electrons and holes recombining, leading to a loss of electron-hole pairs produced from an event. Based on Equation 3.17, an increase in impurities, N, will limit the thickness of the depletion region.

Equation 3.17 also shows how the thickness of the semiconducting material is affected by the applied bias voltage. The bias voltage that is applied to the semiconductor must be high-enough for good charge collection, but not too high that a dielectric breakdown occurs (where an electrical insulating material suddenly becomes an electrical conductor if a significantly high voltage is applied), or that the surface leakage current becomes a significant problem.

Therefore, as there will be an upper limit on the bias voltage, this ultimately sets a limit on the thickness of the semiconducting material, restricting it to a maximum of just a few centimetres depending on the element.

Migration of charge carriers

In semiconducting materials, charge carriers refer to unbound electrons and holes. The probability that an electron-hole pair is thermally generated is represented by Equation 3.18.

$$p = CT^{\frac{3}{2}} \exp\left(-\frac{E_g}{2kT}\right) \tag{3.18}$$

Where T is the absolute temperature, E_g is the bandgap energy, k is the Boltzmann constant and C is a proportionality constant characteristic of the material. This relationship shows the importance of the bandgap energy to the absolute temperature. If a photon interacts with a semiconductor material via one of the interaction processes detailed earlier with sufficient energy, then an electron-hole pair can be produced.

The incident gamma rays first release a free electron based on the specific interaction process; in photoelectric absorption this is the released photoelectron, in Compton scattering this is the recoil electron, and in pair production it is the electron released from the electron-positron pair. These secondary electrons pass through the material, producing a cloud of electron-hole pairs along the particle track within the semiconducting material. If the incident photon carries sufficient energy to remove the loosely bound electrons and create an electron-hole pair, this is known as the *ionisation energy*.

Electrons and holes will naturally diffuse away from their point of origin at the site of a photon interaction, undergoing random thermal motion. However a migration of the electrons and holes in opposite directions can be induced by applying an electric field, $\vec{E}$ (Vcm^{-1}). The migration of these charge carriers will move parallel to the applied $\vec{E}$ field. Should the electric field be removed, the electron-hole pairs recombine. Recombination is the process in which the conduction band electron re-occupies the vacancy that was left in the valence band.

The 'movement' of a hole within the crystal is infact due to the repeated process of valence electrons leaving and filling holes. The site that was previously left vacant from the excited electron is filled by a neighbouring valence electron. This then causes another hole at the vacancy of this secondary electron. This movement of a hole, a net positive charge, induces a current in the crystal.

The concentration of electron-hole pairs can also be dependent on the abso-

lute temperature, as shown in Equation 3.18. If the material is cooled, the concentration will decrease.

When a reverse-bias potential difference is applied across the semiconductor crystal, the electrons and holes begin to drift to the positive and negative junctions respectively through the applied electric field. The acceleration of the electrons and holes induces an average speed defined as the drift velocity, as shown in the equations below:

$$v_e = \mu_e \vec{E} \tag{3.19}$$

$$v_h = \mu_h \vec{E} \tag{3.20}$$

Where $\vec{E}$ is the magnitude of the electric field, and μ represents the mobility of the electron and hole respectively.

The mobility of electrons and holes at 77 K and 300 K in Si and Ge can be seen in Table 3.1. In both materials, the mobility of electrons is larger than the mobility of holes. This is because electrons are able to traverse through the conduction band quite freely, whereas holes are restricted in the valence band. Ge has one of the highest electron mobilities observed in detector materials [52].

Table 3.1: Comparison of properties of intrinsic silicon and germanium [53].

Property	Si	Ge
Atomic Number	14	32
Density (300 K): g/cm^3	2.33	5.32
Band Gap Energy (0 K)	1.165	0.746
Band Gap Energy (300 K)	1.115	0.665
Dielectric constant	12	16
Electron Mobility (300 K) cm^2/V.s	1350	3900
Hole Mobility (300 K) cm^2/V.s	480	1900
Electron Mobility (77 K) cm^2/V.s	2.1×10^4	3.6×10^4
Hole Mobility (77 K) cm^2/V.s	1.1×10^4	4.2×10^4
Energy per E/H pair (77 K) eV	3.76	2.96

Table 3.1 compares other key properties of Si and Ge semiconductor detectors. Due to its low atomic number, Si is considered for applications in measuring low-energy X-rays or for charged particle spectroscopy.

Semiconductor Detector Geometry

The two main configurations of semiconductor detectors include planar and coaxial geometries.

A planar detector involves wafers of semiconducting material, where the electrical contacts are on opposite sides of the flat surfaces of the crystal. This is shown in the schematic diagram in Figure 3.8, which shows the positioning of the electrical contacts on opposite surfaces, and the movement of electrons and holes when a reverse bias is applied.

The planar configurations of the Si(Li) and Ge detectors in GRI+ allows segmentation which can improve the positional resolution of the system. Multiple electronic contact strips are incorporated on either face of each detector, situated orthoganal to each other using a process known as *lithography*. The separate orientations are labelled as the AC and DC sides of the detector.

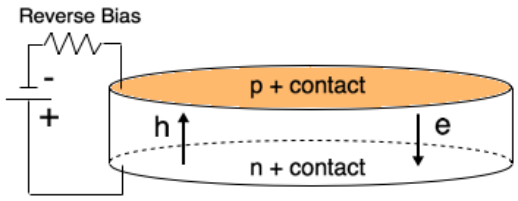

Figure 3.8: Schematic representation of a planar semiconductor detector, with electrical contacts on opposite flat surfaces, and the drifting of holes (h) and electrons (e) when a reverse bias is applied.

The AC and DC sides refer to the type of capacitive coupling between the electric contacts and the preamplifiers. Each individual strip can be connected to its own readout channel, providing a direct connection from the strip to the amplifier input (DC coupling). Alternatively, AC coupling filters the DC current over a capacitor as signals pass from the detector to the preamplifiers. In detector set-ups, the high voltage is applied to the AC side in order to isolate the preamplifiers from any direct leakage current induced.

The second Ge detector in the GRI+ set-up is of a coaxial configuration. Coaxial detectors are often preferred over planar due to the larger achievable active volume, as shown by Figure 3.9.

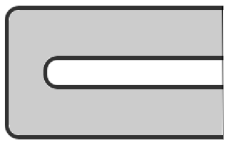

Figure 3.9: Cross-sectional view of one of the common coaxial detector shapes, Closed-ended Coaxial. The thick black line represents the electrical surface contact.

Part of the core of the crystal is removed, with the inner cylindrical surface being replaced by an electrical contact. The outer surface is the outer electrode, and extends across the whole outer surface of the detector. It was demonstrated that closed-end coaxial detectors can achieve good charge-collection properties by linearly increasing the impurity concentration from the open end to the closed end [54]. The closed-ended coaxial geometries are often selected over a true coaxial geometry (where the core is removed throughout the whole volume) to avoid issues with leakage current.

With this geometry, the inner or outer surface contact can be selected as the point in which the semiconductor junction is formed. Manufacturers usually choose the outer surface contact as a higher electric-field value is maintained at the outer regions of the crystal, where the majority of photon interactions are likely to take place.

The Ge planar detector used in GRI+ consists of bulk p-type material. As shown in Figure 3.8, the electrical contacts are provided onto two flat, opposite surfaces of germanium. One of the surface contacts is made from n-type material to create a p-i-n junction for the depletion region to be formed. The opposite contact is made of p-type material. Lithium may be drifted into p-type detectors to act as the n^+ contact, whilst boron implantation is utilised to create the p^+ contact. A P-N junction is formed at the side in which the lithium ions have been diffused. Under the influence of an electric field, these lithium ions will drift across the P-N junction to the p-type detector material.

The depletion thickness of a pure semiconducting material such as silicon can be limited to a fraction of a millimetre. As described by Equation 3.17, in order to obtain a thicker detector, either the number of impurities, N has to be reduced, or the applied voltage, V, can be increased up to a limit.

In order to reduce the impurity level in high-purity germanium detectors, a *zone-refining* technique [55] is applied. This can allow the bulk Ge material to be made several centimeters thick. This technique can not be utilised with

silicon however, so an alternative process is required.

In order to obtain thicker silicon detectors, lithium is added in bulk to silicon across the region to compensate for impurities in a process known as *Lithium Drifting*. This compensated region now acts as the active volume of the detector, and is known as lithium-drifted silicon (Si(Li)).

A perfect compensation region would mean the applied voltage would be consistent throughout the bulk of the high-purity material. This compensated region of intrinsic material creates a newly defined *p-i-n* diode. This new compensated region, i, is throughout the volume of the detector. The presence of the space charge leads to a non-uniform electric-field however, which results in a maximum $\vec{E}$ field strength within the p-i-n junction.

The applied voltage needed to achieve a depletion region throughout the bulk of a germanium detector is significantly higher compared to silicon. The operating voltage of the detectors is higher than what is applied to fully deplete the crystal. This is in order to keep the electric field uniform over the large thickness of the detector, and to increase the efficiency of the collection of electrons and holes by reducing recombination. This will have an important affect on the energy resolution of the detector, as described in Section 3.2.3.

Detector Dead Layers

The active volume of a semiconductor detector is the region between the n and p contacts when the system is biased. However, *dead layers* can be present on the surface of the crystal. These are inactive regions through which radiation may have to pass, and are usually a result of natural or induced passivation, or due to the thickness of the electrical contacts. The electrical contacts between metal and the semiconductor material are an important component of the detector.

In intrinsic silicon and germanium, in order to provide current conduction from a metal to a semiconductor and vice-versa, the intrinsic region will be connected to n and p type surface contacts; one *Ohmic* and one *rectifying*. Ohmic contacts allow electrical charge to be conducted easily to the external electronics whereas rectifying contacts act as diodes, allowing current to only pass in one direction.

These contacts are produced by a very thin layer of heavily doped material produced from ion-implantation or diffusion. Spring metal wires are able to connect with the surface of this heavily doped region. The contact thicknesses

used in the GRI+ system are less than 1 μm thick.

It can be found however, that some of the charge that is created within a dead layer is transported to the depletion region through diffusion [56]. If diffusion takes place, the drifting to the active contacts will contribute to signal formation by causing a larger rise time.

For the measurement of high-energy gamma rays, such as those being considered for this thesis, the effects of attenuation by dead layers is generally negligble. However, the presence of these layers can significantly effect low-energy gammas or X-rays.

Leakage Current

As explained earlier, a large operating voltage is required in planar configurations in order to efficiently collect electrons and holes. Even without the presence of ionising radiation, all detectors show some conductivity. Therefore a steady-state leakage current will be observed. The levels of leakage current must be kept within the order of nanoamps (nA), otherwise this will lead to degradation of the energy resolution.

Fluctuations in the leakage current can sometimes mask small, real signals produced from a gamma-ray interaction. Reducing the leakage current is therefore an essential consideration in semiconductors so as to not miss the peak-current produced from a radiation-induced event, which would be of the order of a few microamps (μA)

One method implemented in the manufacturing process to reduce leakage current is the passivation of the semiconductor surface. *Passivation* is a technique used to treat metallic surfaces to reduce their chemical reactivity. In silicon detectors, this is from the creation of an oxide layer (SiO_2) on the surface of the material. Certain areas of the oxide layer are then removed to create locations for the entrance windows. Compared to non-passivated detectors where the junction extends across the entire surface, this oxide-passivated surface helps reduce the leakage current as the junction edges are now deep within the semiconductor segment.

An additional method used to supress the leakage current is the inclusion of a guard ring. The guard ring is often incorportated to ensure that the applied $\vec{E}$ field is uniform throughout the semiconductor volume. However some semiconductor detectors include a guard ring electrode that suppresses the leakage current [57]. Any induced leakage current produced from the

applied voltage appearing over the side surfaces of the volume are conducted to ground through the guard ring. Therefore it can no longer directly influence the measured signal.

Signal Production

The interaction of a gamma ray within the sensitive volume of a semiconductor produces an electron (depending on the specific interaction process). The effect of this secondary electron produces an electron-hole pair which drifts under the influence of an applied $\vec{E}$ field towards the collecting electrodes, which induces a charge. The formation of the output pulse begins at the point of the interaction, and develops as the electrons and holes move towards the electrodes. The current pulse is fully developed when the last of the charge carriers reaches the electrode.

The study of the evolution of this current pulse over time can provide a fundamental understanding of the timing properties of detectors. How the shape of the pulses change and are affected at different interaction locations will also be invaluable for database pulse shape analysis techniques (see Section 4.4.4).

The buildup of net charge near the junction of the collecting electrodes forms an electric potential difference across the junction. The value of this electric potential, ψ, can be found by solving Poisson's equation (3.21).

$$\bigtriangledown^2\psi = -\frac{\rho}{\epsilon} \tag{3.21}$$

Here, ρ is the net charge density and ϵ is the dielectric constant of the detector medium. This electric potential difference across the junction means that an electric field, ξ exists, the magnitude of which is found by taking the gradient of the potential, ψ, shown in Equation 3.22. The vector electric field, ξ, extends over the width of the depletion region.

$$\xi = -\bigtriangledown\psi \tag{3.22}$$

Charge carriers that are generated in the detecting medium will follow the electric field lines from their point of formation, to their collecting electrode. By creating assumptions on the velocity of the charge carriers as a function of

electric field, the position of the charge as a function of time can be determined [58].

The *Shockley-Ramo theorem* can determine the amount of induced charge due to this movement of charge carriers [59, 60]. The theorem states that the instantaneous current induced on a given electrode is given by the following equation:

$$i = q\vec{v} \cdot \vec{E_0} \tag{3.23}$$

Here, q is the charge of the carrier, $\vec{v}$, is the carrier's velocity, and $\vec{E_0}$ is defined as the weighting field. The weighting field describes the electromagnetic coupling of a charge to the electrodes. The total induced charge, Q, on the electrode can be found with equation 3.24.

$$Q = q\Delta\varphi_0 \tag{3.24}$$

Here, φ_0 is the weighting potential, which describes the coupling of a charge at any position to a specific electrode. φ_0 can be found as a function of position if a Laplace equation is solved for the geometry of the detector. This can be solved if the following boundary conditions are met:

- The voltage on the collecting electrode is set to unity.
- The voltage on any other electrodes is set to zero.
- Any additional charges (trapped charges) are ignored.

By solving the equation under these conditions, the weighting potential can be determined, the gradient of which is defined as the weighting field. This field differs to the applied electric field. It instead simply allows a method to determine the induced charge through the difference of weighting potentials at the start and end of carrier path.

Preamplifiers

A preamplifier is a fundamental element at the beginning of a signal-processing chain, acting as the interface between the detector and the pulse-processing electronics that follow.

The current signals that are produced from incident radiation are very small in magnitude. It is impractical and difficult to try and process the signals that are produced directly from these interactions. Therefore the function of the preamplifier is to shape and amplify the produced signal so that it is suitable for further processing.

As the preamplifier acts as an interface, it is ideal to have it located as close as possible to the detector in order to minimise sources of noise. Having the preamplifier situated here allows a good signal-to-noise ratio by minimising the capacitance, and allows other components in the pulse-processing chain to be at a significant distance away.

Preamplifiers can either be *voltage-sensitive* or *charge-sensitive*. Voltage-sensitive are commonly used but are undesirable for semiconductor detectors. Semiconductor detectors require a proportionality of the output voltage pulse to the charge, Q, as shown in Equation 3.25, where C represents the input capacitance. In voltage-sensitive semiconductor-diode systems, different operating parameters can affect the input capacitance, and therefore can affect the fixed relationship shown in Equation 3.25 [61]. Charge-sensitive preamplifiers are therefore used to rectify this situation.

$$V_{MAX} = \frac{Q}{C} \tag{3.25}$$

Figure 3.10 shows the components in a charge-sensitive resistive-feedback preamplifier circuit. The charge, Q from the detector is first collected on the first capacitor, C_i. It is then integrated over a second capacitor, C_f and further discharged over a feedback resistor, R_f. The resistance of R_f is large in order to reduce the noise induced in the system. The operational-amplifier, A, is utilised to amplify the input signal.

The time constant given by the product of $R_F C_F$ determines the decay rate of the tailing edge of the output pulse. In order to keep the proportionality as described in Equation 3.25, the time constant must be larger than the charge collection time (risetime of the pulse). If this proportionality is kept, then the height of the pulse is proportional to the energy deposited in the detector volume, and becomes independent of the input capacitance, C_i, as shown in Equation 3.26.

$$V_{OUT} = -\frac{Q}{C_f} \tag{3.26}$$

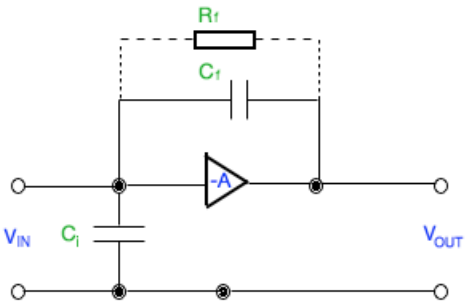

Figure 3.10: Simplified schematic of a charge-sensitive preamplifier circuit.

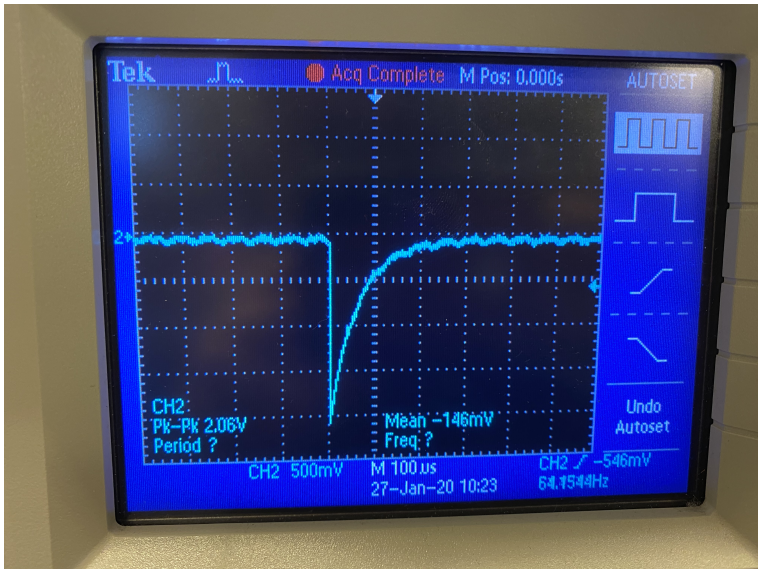

Figure 3.11: Image showing the observed pulse of a preamplifer on an oscilloscope.

Figure 3.11 shows a photograph of a negative preamplifier pulse obtained from a BEGe detector at the University of Liverpool using an oscilloscope. The vertical scale shows 500 mV per division, with the horizontal scale showing divisions of 100 μs. The preamplifier signal shown in Figure 3.11 shows the important properties of the pulse. The signal has a very fast fall time, of the order of a couple hundred ns, which is indicative of the charge collection time of the detector. The charge collection of inverted pulses are similarly described by the *risetime* of the pulse. The charge collection contributes to the energy resolution of the detector as described in Section 3.2.3 in Equation 3.28. The decay time of the falling tail end is purposely large, of the order of a few hundred μs and represents the time constant of the circuit.

An alternative approach to the inclusion of a feedback-resistor seen in the preamplifier circuit above, are *transistor-reset* preamplifiers. The feedback resistor, R_F, is a source of noise, so by removing the feedback resistor, any noise that is associated with the resistor is removed. Transistor-reset preamplifiers are also able to perform at very high pulse rates, compared to the resistive-feedback preamplifier where pile-up problems can occur.

Pile-up is a term used to describe the build-up of pulses. Due to the long tailing-edge of the preamplifier pulse, at high rates the pulses can overload the system. Rather than returning to the baseline, the pulses *pile-up* on top of one-another, as shown in Figure 3.12a. The amplitude of the pulses increase until it reaches a saturation point. At this point, the amplitude of the pulse, and its associated voltage information is lost. By removing the R_F resistor, the pulses are allowed to build until it reaches the defined limit as shown in Figure 3.12b. Once the threshold is reached, the voltage is rapidly reset to zero, and the process is able to repeat, with a smaller amount of information lost.

Whilst the preamplifier is being reset, it undergoes a period of *dead time*. Dead time is defined as the minimum time period between two consecutive counts so that they can be recorded as two separate events. If a system has a significantly large dead time, then there will be a large loss of events.

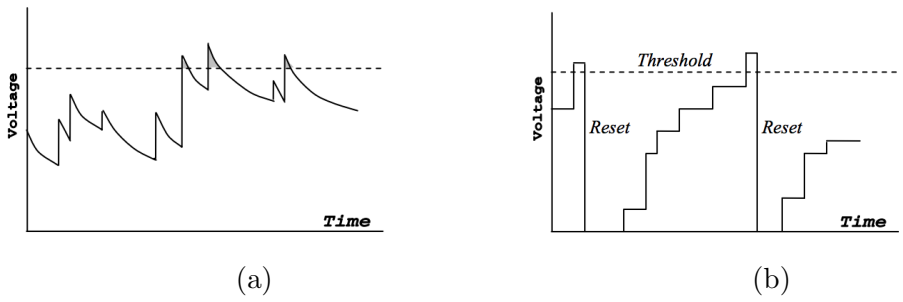

(a) (b)

Figure 3.12: Schematic representation of the pile-up of preamplifier pulses in (a) a Resistive-feedback and (b) Transistor-reset preamplifiers. The threshold is the saturation point, in which the information regarding the amplitude of the pulses is lost [62].

3.2.3 Properties of Radiation Detectors

Energy Resolution

In gamma-ray spectroscopy applications, the aim is to measure the energy distribution of the incident radiation. The energy resolution describes a detector's ability to resolve a particular energy. This is known as the *response function* of the detector for that particular gamma-ray energy [63].

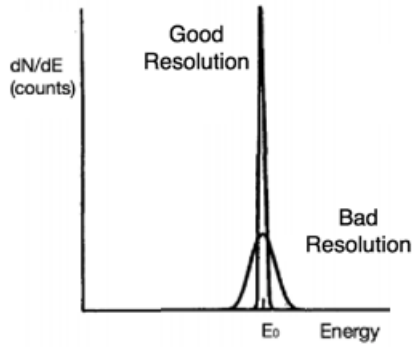

Figure 3.13: Example response functions for detectors with relatively good and relatively poor energy resolutions [63]

Figure 3.13 shows two examples of energy resolution values for the same energy, E_0. The difference in width is due to variations in the energy recorded from pulse to pulse. If this variation is reduced, then the width will be smaller. The response function is usually represented by a Gaussian peak. The net area under the peak would be the same if the same number of events are recorded in each case. The width of the peak describes the energy resolution, which can be quantified by the Full Width at Half Maximum (FWHM). The FWHM, as shown in Figure 3.14, is the width of the peak at half the maximum height. If the peak shape is Gaussian, then the $FWHM = 2.355\sigma$, with σ shown on the figure.

The numerical definition used to describe the energy resolution differs for scintillation detectors and for semiconductors. For scintillators, the energy resolution is typically described as a percentage, as shown in Equation 3.27. The smaller the value, the better the detector will be in being able to distinguish two full-energy peaks whose energies are close together.

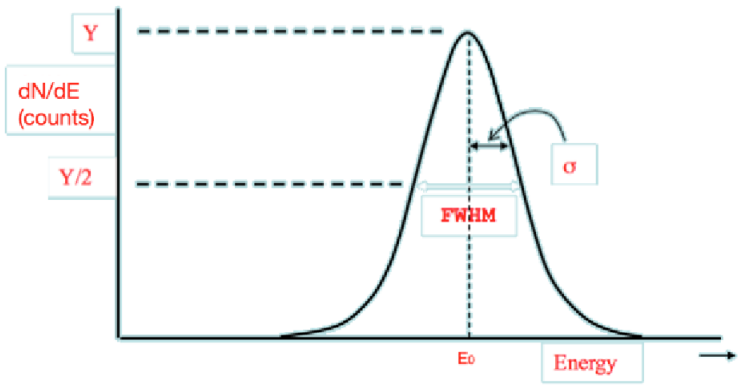

Figure 3.14: Definition of energy resolution, where the FWHM is defined as the Full Width at Half Maximum. [64].

$$Resolution, R\ \% = \frac{FWHM}{E_0} \times 100 \tag{3.27}$$

Where E_0 is defined as the peak centroid, and FWHM is found using Figure 3.14.

For semiconductors, the resolution is described as the FWHM of the full-energy peak in units of keV. This definition also assumes that the background radiation has been subtracted, or is negligible.

The FWHM of the peak can be affected by various factors, which all contribute together as shown in Equation 3.28.

$$(\delta r)^2 = (\delta e)^2 + (\delta s)^2 + (\delta c)^2 \tag{3.28}$$

Where δe is the contribution due to the electronics of the system, which could be due to random noise such as the detector's capacitance, input voltage, or the temperature of the system, which can cause drifting to occur. δs is due to statistical fluctuations and δc is due to incomplete charge collection.

The statistical fluctuations describes the number of charge carriers that are created with the interaction of radiation. These can be related by the following formula:

$$\delta s = 2.35\sqrt{\frac{F}{N}} \tag{3.29}$$

Where F is the Fano Factor, as described in Equation 3.30.

$$F = \frac{\sigma}{N} \tag{3.30}$$

Where σ describes the observed variance, and N is the number of charge carriers produced, as described by Poisson statistics.

It is the statistical fluctuations that contribute significantly to the energy resolution. As it is an intrinsic property of the detector material, it therefore can not be reduced, even with the improvement of the other contributions described in Equation 3.28.

Efficiency

Efficiency is a measure of the percentage of radiation that the detector is able to detect. An ideal system would have a *counting efficiency* of 100 %, where an event would be registered for all radiation that interacted within the volume. As uncharged radiation such as gamma rays have to interact first before any detection is possible, detectors are usually less than 100 % efficient.

Absolute efficiency is dependent on the detector properties, and how well it is able to measure the output signals produced from the interactions of incident radiation. It is defined by Equation 3.31 [65].

$$\epsilon_{ABS} = \frac{\text{Number of events recorded}}{\text{Number of radiation quanta emitted by source}} \tag{3.31}$$

The *Intrinsic efficiency* is defined as:

$$\epsilon_{INT} = \frac{\text{Number of events recorded}}{\text{Number of radiation quanta incident on detector}} \tag{3.32}$$

The intrinsic (Eq. 3.32) and absolute efficiency (Eq. 3.31) are related by the solid angle subtended by the source to the detector:

$$\epsilon_{INT} = \epsilon_{ABS} \cdot \left(\frac{4\pi}{\Omega}\right) \tag{3.33}$$

Where Ω is the solid angle of the detector as seen from the radioactive source position. The intrinsic efficiency is dependant on the type of material and thickness of the detector.

These counting efficiencies can be further divided into *total* and *peak* efficiencies.

The *total* efficiency describes all events that are detected, irrespective of energy. The *peak* efficiency only considers the interactions that deposit the photon's full energy, which can be observed by the prescence of a peak in the spectrum. Other events, which may deposit a proportion of that photon's energy, will be observed to the left of the full-energy peak. This value is the most significant when evaluating the performance of the detector system for a particular gamma-ray energy.

The absolute peak efficiency for a particular energy can be defined as:

$$\epsilon_{ABS} = \frac{\text{Net Peak Area}}{\text{Live Time(s)} \times \text{Gamma Emission Probability} \times \text{Source Activity (Bq)}} \tag{3.34}$$

The *live time*, as shown in Equation 3.34, is a term that describes the time that the detector is openly receiving data. This value subtracts the dead time of system from the real time, the length of time in which the measurement was performed.

The *Relative Efficiency* is an industry standard value and a point of comparison between radiation detectors. It compares the absolute efficiency of a gamma-ray detector to that of a $3'' \times 3''$ NaI(Tl) scintillation detector measuring the 1332 keV peak from a ^{60}Co source at a distance of 25 cm, under the same experimental conditions.

The **peak-to-total** ratio (P_T) is a way to relate the total and peak efficiencies. It is defined as the net counts in the full-energy peak area, against the gross total number of events in a spectrum. The gross counts are conventionally taken from above 100 keV so as to remove the contribution from X-rays. This ratio can help show the sensitivity to external effects such as scattering from nearby objects.

3.3 Compton Cameras

The use of the Compton effect on instrumentation was first considered in the 1950s [66], before it was applied as a Compton camera due to limitations of lead collimators in astronomy applications [67].

In medical and nuclear imaging, photon trajectories are being estimated by using directional information provided by lead collimators. Unfortunately, this does not give an accurate distance from the source to the detector. A new approach was outlined which looked to be a refined improvement on the conventional Anger Scintillation Camera [68]; a combination of a large area of a collimated scintillator and a photomultiplier system. This proposed gamma camera used the Compton effect to define the trajectory of the incident photon.

Compton cameras are not commonly used in nuclear decommissioning, with systems utilising mechanical collimators, as described in Section 2.3.1 usually being preferred.

3.3.1 Operation

A conventional Compton camera utilises two detectors to determine the energy and direction of an incoming gamma ray. Consider a radioactive source emitting a photon of energy E_I. In an ideal system, the photon will interact once in the first detector and once in the second detector. These events are known as *single-single* interactions.

As the gamma ray passes through the first detector, it Compton scatters and deposits a proportion of its energy E_{S1}. It is then fully absorbed in the second detector through photoelectric absorption, depositing the remainder of its energy E_{S2}. We can therefore express the incident energy as the sum of these values, such that $E_I = E_{S1} + E_{S2}$.

The Compton scattering formula, described in Equation 3.3, related the scattered photon E_S to the scattering angles. This equation can also be rearranged to find the scattering angle, θ, as shown in Equation 3.35. m_0c^2 is the rest mass energy of an electron.

$$cos\ \theta = 1 + m_0c^2 \left[\frac{1}{E_I} + \frac{1}{E_{S2}}\right] \tag{3.35}$$

This equation can provide the basis for Compton imaging, where θ in Equation 3.35 is the opening angle of a cone, the axis of which is the trajectory of the scattered photon between the two detector crystals projected back onto an image plane. More details on Compton imaging is detailed in Section 4.5.

3.3.2 Spatial Resolution

The response of a gamma-imaging system to the image reconstruction of a point source can be described by the *point spread function* (PSF), which ultimately describes the extent of blurring within an image [69]. Spectral line functions, such as a PSF, can be described by either a Lorentzian or Gaussian distribution.

Figure 3.15a shows the Compton image produced from the reconstruction of experimental data for a ^{137}Cs point source. Further details on how the image is reconstructed can be found in Section 4.5.

The Compton cones, created as described by Equation 3.35, overlap at highest intensity at the location of the radioactive source. These cone overlaps produce a distribution which can be described by a Lorentzian function, however, when applied to the profiles produced from the reconstructed image, it does not accurately describe the tails of the distribution.

Gaussian curves are used in measurements to describe random variables that are *normally distributed*. This can be used to help model curves which have additional broadening effects. In Compton images, these broadening effects produce large tailing observed in images due to the nature of overlapping cones.

Therefore, the fit applied to the image profile is a combination of a Gaussian and Lorentzian distribution; the Gaussian is able to account for the background contribution to the image, and the Lorentzian distribution can describe the profile. The FWHM of the fit applied to the distribution can also be referred to as the *spatial resolution*. This is a term that can be used to describe the quality of the Compton images produced.

For a high-quality Compton image, the spatial resolution produced from a point source should be small, in the range of a few pixels/millimetres. The broadening of the distribution can be attributed to the quality of the overlapping cones produced in the images, or additionally from poor energy resolution from the detector system, or due to a poor positional resolution, affecting the precision of the point of interaction.

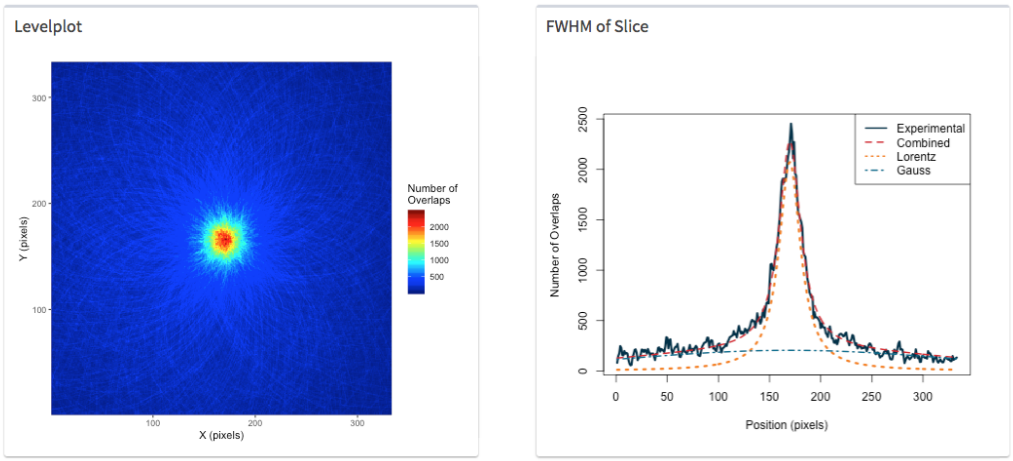

Figure 3.15: Screenshot showing the reconstructed image matrix and intensity profile produced of a ^{137}Cs point source, along with application of a combined Gaussian and Lorentzian fit to determine the FWHM of the intensity profile.

As described earlier, the total energy that is deposited into the detector system, E_I, and the initial energy deposited in the first detector, E_{S1}, are used in the creation of Compton cones as described by Equation 3.35. Any uncertainties on the amount of energy deposited in each interaction, or the precision in which an interaction can be localised, will affect the accuracy of the calculated scattering angle, θ. The larger these uncertainties, the poorer the spatial resolution.

3.3.3 Angular Resolution

Another term that can be used to describe the quality of an imaging system, is the angular resolution of the produced image as shown in Figure 3.16. The figure shows that whilst the spatial resolution of the images may increase with increasing distance away from the detectors, the angle subtended should be the same, i.e. an image at 2 m may have a very poor spatial resolution, but the angle subtended should be the same as an image produced 20 cm away.

By utilising the intensity profiles produced from the reconstructed images, the subtended angle shown in Figure 3.17, θ, can be calculated using basic trigonometry as shown in Equation 3.36. By doubling this value as shown in Equation 3.37, the angular resolution of the system can be determined, as shown in Figure 3.16. The source to detector distance is defined as the distance from the source to the centre of the detector crystal.

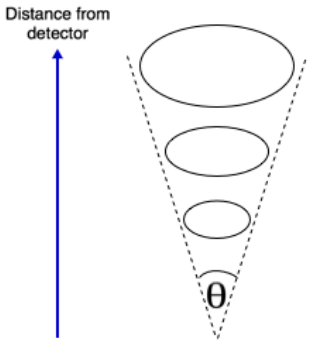

Figure 3.16: Diagram showing how the angular resolution should be the same as the distance from the detector increases.

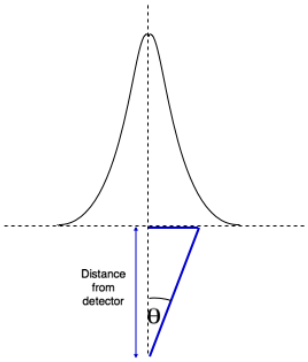

Figure 3.17: Diagram showing how the intensity profile of an image can be used to determine the angular resolution, by using half of the FWHM and the distance to the detector.

$$\theta = \text{Tan}^{-1}\left(\frac{\frac{1}{2}\text{ FWHM (mm)}}{\text{Source to detector distance (mm)}}\right) \tag{3.36}$$

$$\text{Angular Resolution} = 2\theta \tag{3.37}$$

Chapter 4

Experimental Set-Up and Methodology

The detector system which was used as the basis of the project was the GRI+ Compton Camera system at the University of Liverpool. As one of the main sources of contamination identified in nuclear decommissioning scenarios is ^{137}Cs, as detailed in Section 2.2.1, the system was optimised for the measurement of ^{137}Cs.

Data acquisition parameters that have been optimised in previous work will need to be re-investigated. This chapter will detail the experimental set-up for the measurements in this thesis. This includes the geometry and optimisation of the detector system and data aquisition parameters, and the decisions made for the data campaign.

4.1 GRI+

In 2009, the University of Liverpool proposed the development of a prototype semiconductor Compton camera with the aim of improving the efficiency and sensitivity of conventional medical imaging, such as SPECT, in the ProSPECTus project [4]. ProSPECTus was a two-tiered detector system, with the first detector a Canberra lithium doped silicon detector (Si(LI)), and the second a high-purity germanium (HPGe) detector.

The current GRI+ system is a development on this ProSPECTus system by the addition of a third detector tier. A coaxial HPGe detector has been placed behind the absorber detector to improve the efficiency of the system.

With portable data acquisition in mind for future in-situ measurements, the Computer Aided Design rendering shown in Figure 4.1 was a conceptual de-

sign to show how GRI+ could be transferred to a mobile cart. As shown in the image, the custom-designed cart would house the three detectors and their cooling systems. The cart also contains the digital data acquisition electronics and the power supply to allow for a fully portable gamma-ray imaging system.

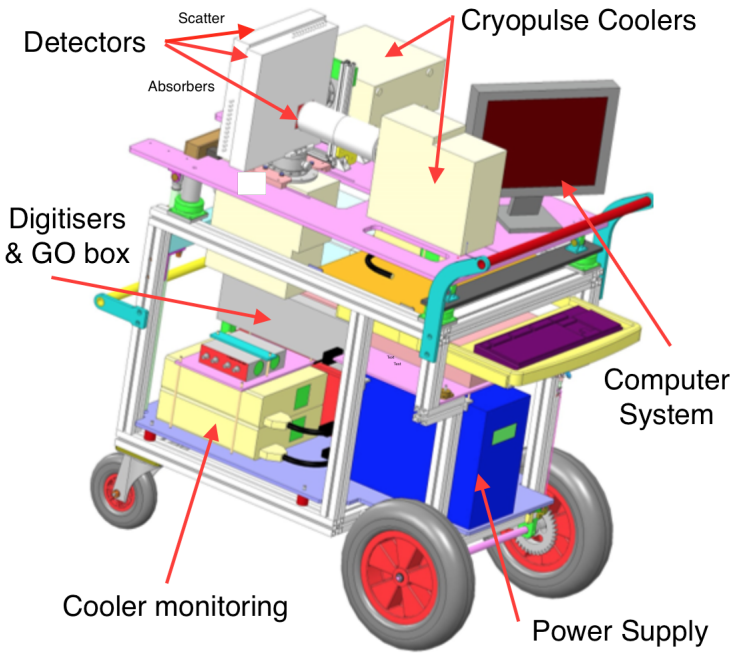

Figure 4.1: CAD drawing of the planned GRI+ detector system when transferred from its laboratory set-up to the portable cart.

The portability of the GRI+ system allowed for the first set of experimental data to be collected off-site (i.e. away from the departmental laboratory).

Scatterer

The first layer of the GRI+ detector system is a Canberra Si(Li) planar-strip detector (ESLXS 3500-8-13X-13Y). It is also referred to as the *scatterer* or *scatter* detector, due to its purpose within the Compton camera set-up to Compton scatter incoming photons.

The detector crystal is cylindrical, planar, Silicon doped with Lithium Si(Li) and electrically segmented using orthogonal strip contacts. It has an active diameter of 71 mm and a thickness of 8 mm, creating an active volume of 3500 mm^2.

The crystal is divided into 13 vertical n^+ contacts, coupled to AC charge-sensitive preamplifiers, whilst 13 horizontal p^+ contacts are coupled to DC charge-sensitive preamplifiers. These outputs provide the position of an event, and energy information obtained from the output voltage pulse. The AC and DC strips were labelled numerically as AC 01 - 13 and DC 14 - 26 on their respective faces, the AC face being the front-facing side of the detector when mounted on the cart.

The strip pitch is 5.5 mm with an inter-strip gap of 500 μm. With the double segmentation, this gives the Si(Li) a positional resolution of $(5.5 \times 5.5 \times 8.0)$ mm before the improvements with pulse shape analysis techniques (Section 4.4.4). All 26 strips are connected to a warm field-effect transistor (FET) and have a gain of 400 mV/MeV at 1 MΩ impedance.

The semiconductor detectors have to be cooled to cryogenic temperatures to improve the electron-hole mobility, as described in Table 3.1. At these temperatures, when a high reverse-bias is applied, semiconductors can operate as a diode [70]. The Si(Li) detector operates at $-175°$ Celsius. This temperature is achieved by using a Cryopulse CP5 cooler which can be seen on Figure 4.2.

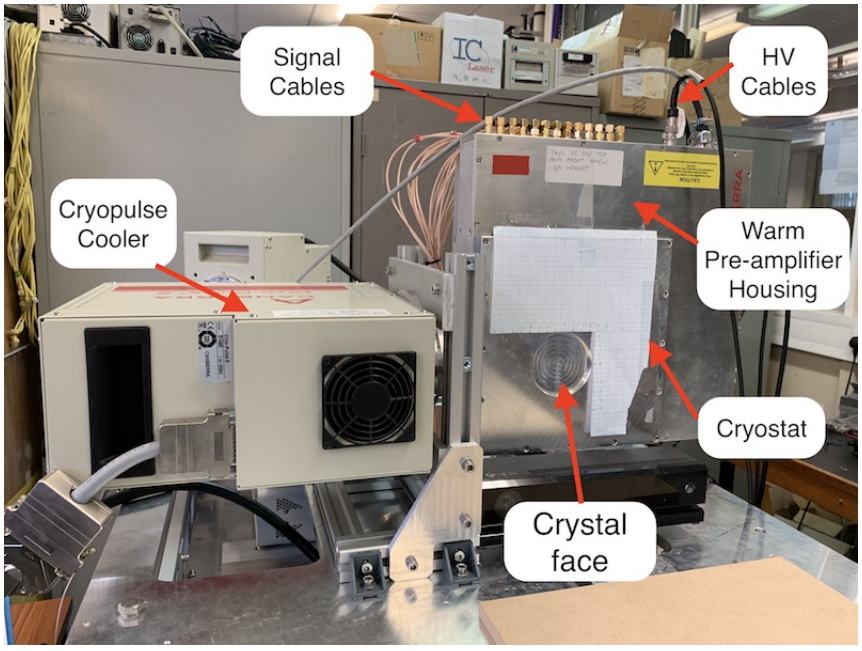

Figure 4.2: Photo of the AC side of the scatter detector when mounted on the cart within its cryostat, with the Cryopulse CP5 Cooler to the left of the image.

The Cryopulse cooler employs pulse tube technology, utilising a pressure wave rather than a mechanical piston to move the gas. It is seen as an ideal method for cooling the detector crystals due to the active reduction of vibrations within the cryostat [71] compared to other electronic coolers.

The cryostat that the Si(Li) crystal is housed in has dimensions of $(33 \times 33 \times 5)$ cm. The crystal is situated centrally in depth within the cryostat, and is surrounded by a 5 mm guard ring. Guard rings are usually implemented with silicon detectors to reduce leakage current and improve spectroscopic performance [72]. The charge collection performance of the detector is improved by ensuring a uniform electric field throughout the volume of the detector. As described by Equation 3.28, reducing the contribution from incomplete charge collection will improve the FWHM of a full-energy peak.

The scatter detector operates at a voltage of +600 V. Whilst the depletion voltage of the Si(Li) is +150 V, a bias of +430 V is required to saturate the velocity of the electron-hole pairs. This value can be checked by plotting the FWHM of the 60 keV peak from ^{241}Am as a function of the applied voltage for a few of the AC and DC strips. Edge and central strips were selected to get a suitable account of the detector. The observed noise levels on the AC side were also investigated as a function of applied bias voltage. The bias was increased from 0 V in increments of 10 V, with the FWHM and noise levels measured. As the voltage is raised from +150 V to a bias of +430 V, the resolution improves. Increasing the bias up to a value of +600 V, the FWHM is nearly constant in value. Beyond the bias of +600 V, the resolution once again degrades due to the increased levels of noise due to an increase in leakage current, as described in Section 3.2.2.

The positive polarity is applied to the AC side (n-type) of the detector, with the DC side grounded, therefore the AC side will collect the electrons and the holes will be collected at the DC side. The AC strips have a positive preamplifier output with the DC strips having a negative output, as the pulses are inverted in the preamplifers.

To verify the detector performance and check the energy resolutions matched the detector specification, the energy resolution of every strip was measured through analogue electronics and digitally. The preamplifier outputs were connected sequentially to an ORTEC 671 spectroscopy amplifier with a shaping time of 3μs, and collected using an Ortec *EASY-MCA-8k* Multichannel Analyser. The output from the MCA was analysed using the software program *Maestro* [73]. The FWHM of the peak is determined by converting the FWHM value in channels to keV based on the user's initial calibration of the software.

Data was collected using an ^{241}Am source to investigate the resolution at 60 keV. The source was placed a few centimetres away from the scatter detector face, with a count rate in the central strips of at least 100 counts per second, and a smaller value of 30 counts per second in the edge strips. The resolutions were recorded after achieving at least 3000 net counts in the 60 keV peak region for edge strips, and at least 10,000 net counts for the central strips. A full comparison of each strip with the manufacturer specification can be seen in Figure 4.3.

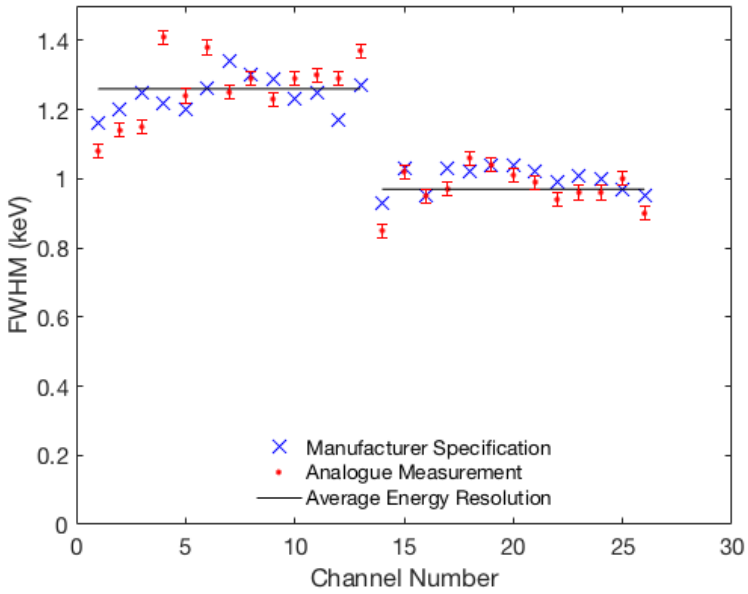

Figure 4.3: Graph to show how the analogue energy resolution compares to the manufacturer's specification across all scatter detector channels at 60 keV. The solid black line represents the average energy resolution for the analogue measurements for both the AC and DC channels. It can be seen that the channels on the DC side (14 - 26) have a better energy resolution in comparison to the AC channels (01 - 13).

As can be seen from the graph, the analogue energy resolution measurements are consistent with the expected manufacturer's resolution values, with no significant deviations from the specification resolutions. It can also be observed that the DC side of the scatter detector has a superior energy resolution in comparison to the AC side. The average analogue resolutions was found to be 1.26 $\pm$ 0.10 keV for the AC channels, and 0.97 $\pm$ 0.06 keV for the DC channels (errors calculated by finding the standard error of the mean). This is because the AC side of the detector has an increased level of noise due to the HV coupling capacitor. This difference in resolution led to the decision that the energies collected from the DC strips were to be utilised for the Compton

image reconstruction.

As well as the energy resolution, the noise level was also measured to check the detector's performance. Using a MS074104B Agilent oscilloscope with a 1 MOhm impedance, the Root Mean Square (RMS) noise level was measured from the amplified pulses for a select few strips. These checks are repeated before any significant set of measurements, using the same strips to make sure there are no significant changes to the detectors over time. The RMS noise level in the AC strips was found to be 1.02 ± 0.07 mV, and 1.15 ± 0.20 mV for the DC side before the measurements in this thesis were taken. These values were consistent with previously collected RMS noise measurements.

Further characterisation of the Si(Li) detector has been previously investigated [74] to assess the detector's performance.

Absorber

The second detector is a high-purity germanium crystal manufactured by Canberra (EGPS60×60×20-12X-12Y). Depending on what set-up the user requires, this can be seen as secondary scattering material in a 3-tier set-up, or the absorber detector in the 2-tier set-up.

The HPGe crystal is square-faced which is also electrically segmented using orthogonal strip contacts, and has dimensions of $(60 \times 60 \times 20)$ mm. The crystal is divided into 12 horizontal 'X' strips with n^+ amorphous germanium contacts, coupled to DC preamplifiers, whilst 12 vertical 'Y' strips with p^+ boron implanted contacts are coupled to AC preamplifiers. The AC and DC strips were labelled numerically as AC 01 - 12 and DC 13 - 24 on their respective faces (the AC face being the front-facing side of the absorber).

Each strip has a pitch of 5 mm and is separated by a distance of 500 μm. With the double segmentation, this gives the HPGe a positional resolution of $(5 \times 5 \times 20)$ mm before the improvements with pulse shape analysis techniques. All 24 strips are equipped with resistive feedback charge-sensitive preamplifiers connected to a warm FET, and a gain of 200 mV/MeV at 1 MΩ impedance. The DC strips have a positive preamplifier output with the AC strips having a negative output.

Figure 4.4 is a labelled photograph of the DC side of the absorber detector when mounted on the cart, with the AC side facing the scatter detector. The HPGe cryostat also has dimensions of $(33 \times 33 \times 5)$ cm and is similarly cooled with a Cryopulse CP5 cooler to a temperature of $-185°$ Celsius. At the en-

trance window to the detector, there is a thin piece of aluminium 0.8 mm thick on each side.

The absorber detector operates at a voltage of −1800 V, and its depletion voltage is −1300 V. Similar to the scatter detector, the negative polarity is applied to the AC side (p-type) with the DC side therefore grounded, and the corresponding pulses are inverted by the preamplifers. The AC side therefore collects holes and the DC side collects electrons.

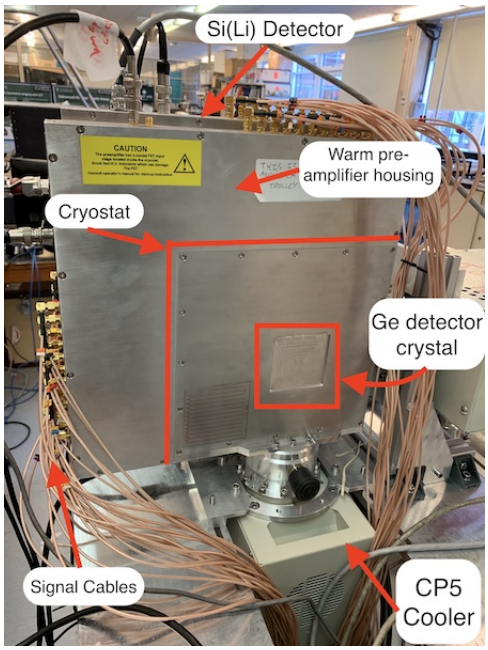

Figure 4.4: Photo of the DC side of the absorber detector when mounted on the cart within it's cryostat. Due to the design of the cart, the Cryopulse Cooler is positioned below the cryostat.

The analogue energy resolution of each individual strip was investigated using the same techniques as the scatterer, connecting each strip sequentially to an ORTEC 671 spectroscopy amplifier with a shaping time of 3 μs and an Ortec *EASY-MCA-8k* Multichannel Analyser. Using *Maestro*, the FWHM of the 122 keV peak from a Cobalt-57 point source placed approximately 10 cm away from the DC face of the absorber crystal was recorded, achieving a count rate in the region of 50 - 60 counts per second. The measurement of each strip was close to 3 minutes in length in order to collect approximately 10,000 counts in the net area of the 122 keV peak.

Figure 4.5 shows a full strip-to-strip comparison of the measured analogue energy resolutions to the manufacturer's specifications. Overall, the measured

resolutions were slightly higher than the specification resolutions, but consistent across the strips, with the exception of the AC 02, AC 11, DC 01 and DC 11 strips, which are significant outliers. The average energy resolution of the strips was found to be 2.14 ± 0.49 keV for the AC channels and 1.94 ± 0.49 for the DC channels.

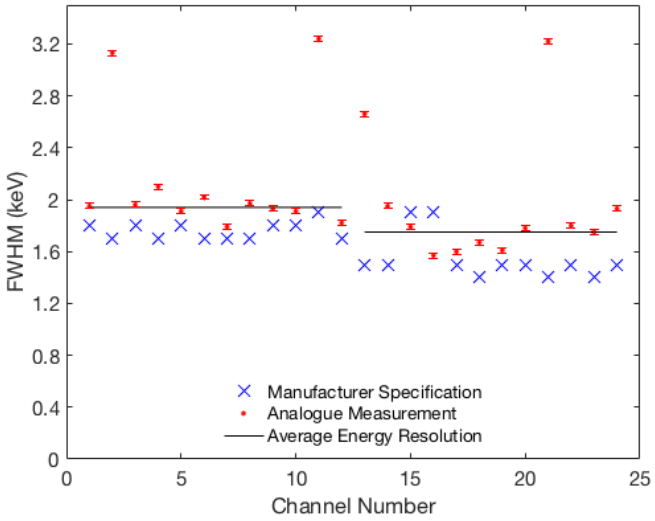

Figure 4.5: Graph to show how the analogue resolution compares with the manufacturer's specification against channel number for the absorber detector at 122 keV. The solid black line represents the average energy resolution, ignoring the outliers, for the analogue measurements for both the AC and DC channels. It can be seen that the DC channels (13 - 24) have a better energy resolution in comparison to the AC channels (01 - 12).

Similar to the scatter detector, the DC side has superior energy resolution in comparison to the AC side. In order to produce the optimum performance for Compton imaging, the DC energies were used alongside the scatter DC energies.

The resolution values shown in Figures 4.3 and 4.5 were recorded in March 2019. In a set of measurements taken in December 2018, there were no significant outliers found in the absorber strips [75] and the values were consistent with the manufacturer's specification.

The causes for the change in resolution in strips AC 02, AC 11, DC 01 and DC 11 is believed to originate from the presence of surface contamination on these strips, caused from a potential vacuum leak in the cryostat. This can be attributed to a known vacuum issue with the detectors. Significant problems were observed when the cooling power required for the CP5 units were reaching their limit.

For the HPGe detector, the standard operating power for the CP5 is around 100 W to keep the detector at cryogenic temperatures. The cooling power limit for the CP5 units is at 175 W. If the cooling power exceeds this limit, then this would cause the CP5 units to shutdown, and cause the temperature of the detectors to return to room temperature. This could seriously damage the detector crystals. It was observed that the cooling power for the HPGe detector's CP5 was steadily increasing from the 100 W value over a period of a few months, and was quickly approaching the limit of 175 W.

Within the cryostat there is a molecular sieve that can absorb any residual gas within the vacuum chamber [76]. A small amount of air is expected as all vacuum chambers will leak slightly, and this sieve can maintain the vacuum by absorbing the small amount of air that may leak in. However, there comes a point when it can no longer absorb any of the air as it only has a limited capacity. Due to an increasing amount of air entering the cryostat that is not being absorbed, the vacuum degrades and the detector warms up.

As the temperature increases, gases that were previously absorbed are re-released into the cryostat. The still cold detector crystal allows the escaped molecules to 'stick' to the crystal surface. This surface contamination can degrade the performance of the detector system.

In order to correct this issue, once the detector has warmed to room temperature, both the molecular sieve and the detector crystal can be heated to a temperature of 65° C by applying a voltage to an internal resistor within the cryostat. By heating both, the residual gases can be eliminated and any contamination that was present on the crystal surface is also released. To prevent any further contamination, the detector is simultaneously pumped to fully remove the outgassed gases. This process of annealing the detector continues for a duration of almost 100 hours until the contamination is removed. This process 'resets' the molecular sieve so that it is able to absorb any leaking gases, until it inevitably saturates again. Once complete, the detector is cooled again for operation.

As detailed earlier, significant degradation within strips AC 11, DC 01 and DC 11 (the problem with AC 02 was an anomaly that looked to be corrected in the digital measurements, as shown Figure 4.20) was found because of the thermal cycling of the absorber detector.

Due to time constraints, and the possibility that further contamination or mechanical damage could occur through persistent thermal cycling and pumping, it was decided to continue with the faulty strips for the measurements in this thesis. On completion of the data taking, the absorber detector was once again

pumped and the issue with the energy resolution on these specific strips were resolved.

Further characterisation of the absorber detector has been previously investigated here [77] to assess the detector's performance.

Coaxial

In a 3-tier set-up, the final absorber is a standard electrode coaxial germanium (SEGe) detector also manufactured by Canberra (GC4018 b.15105). It is a p-type detector, with the n-type contact on the outer surface, and a p-type contact on the inner electrode.

It has a diameter of 66.5 mm and a length of 50 mm, with a 6 mm offset distance from the aluminium entrance window. The outer assembly housing is also made out of aluminium (Figure 4.6a) and the system is also mechanically cooled using a Cryopulse CP5 cooler (Figure 4.6b).

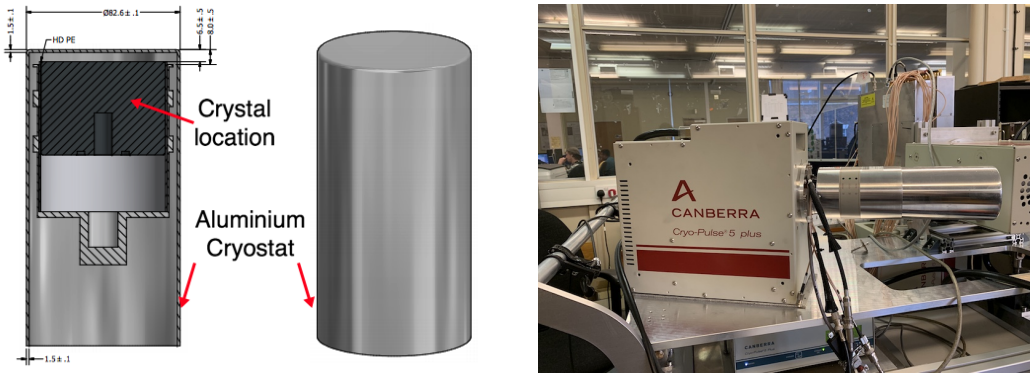

(a) (b)

Figure 4.6: Images to showing the coaxial detector (a) Schematic diagram of the crystal in it's aluminium housing (b) Coaxial detector with connected Cryopulse Cooler.

It operates at a bias voltage of +3000 V, and depletes at +2500 V. There is just one single signal output from the coaxial detector, which is connected to a charge-sensitive preamplifier and cold FET, and has a gain of 100 mV/MeV at 1 MΩ impedance. It has an energy resolution of 0.68 keV at 122 keV energy, increasing to 1.74 keV at 1332 keV energy.

Detector Geometry

Another significant improvement of GRI+ from the ProSPECTus system was the upgrade from the laboratory based frame to the custom designed cart system. As described earlier, Figure 4.1 showed how GRI+ could be transferred to a portable cart system. The cart system would allow GRI+ to work as a fully standalone system, with data aquisition electronics, cryopulse coolers and power systems self-contained on the cart. Figure 4.7 shows a photograph of the GRI+ cart system with the detectors and DAQ electronics mounted on the cart as it was transferred to an area on the University of Liverpool campus for measurements.

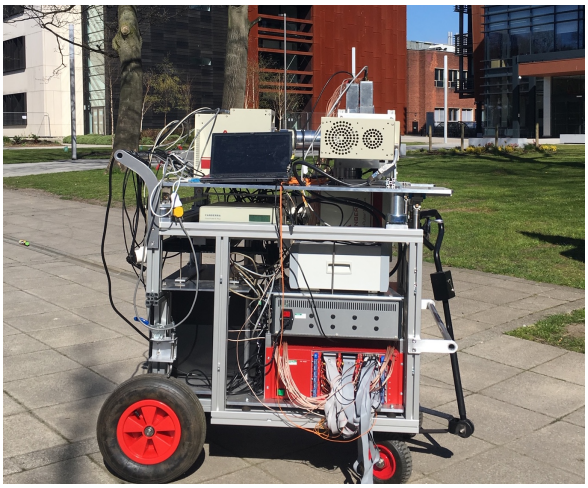

Figure 4.7: Image of the GRI+ cart system taken on the University of Liverpool campus.

As shown in the image, the three detectors along with the CP5 coolers are secured to the cart. These are not permanently fixed to one position, but can allow for minor alignments to take place such as changing the separations between detectors. The power-supply keeps the detectors at cryogenic temperatures during transportation to a new location. The image also shows the wiring of the detectors to the DAQ electronics.

When mounting the detectors, a cryostat separation between the scatterer and absorber detector had to be decided for measurements. Unlike the laboratory frame used previously, which allowed a minimum cryostat separation of 10 mm between the scatterer and absorber, the cart allowed a minimum separation of 4 mm. Previous measurements on the cart had been taken with a cryostat separation of 4 mm to optimise efficiency. However, it was found that microphonic noise was induced to the system with the two cryostats being in close proximity, caused by vibrations caused from the CP5 coolers. Because of this,

the cryostat separation was increased to 5.5 mm for the two data campaigns. The front of the coaxial detector was placed 6 mm from the DC face of the absorber detector.

Once mounted onto the cart system, it is important that the centre of each detector crystal aligns correctly to maximise the efficiency of the system. The centre of the HPGe detector is approximately 10.4 cm away from the cryostat edge nearest to the mechanical cooler. Based on the specifications of each detector and depending on which way each detector was orientated in order to place the cryostats on the cart, it meant that the Si(Li) detector had to be offset by approximately 8 mm both vertically and horizontally in order for the centre of each detector to align. The cart was specifically designed for the detectors and their cryostats to be permanently mounted, shown earlier from the CAD design in Figure 4.1, meaning the alignment of the coaxial to the absorber could be done with a rough visual inspection.

Alignment between the scatter and absorber detector can be confirmed with a quick reconstruction of a source that is placed centrally to the scatter detector face. In the reconstructed imaging space, the X-Y coordinates of the centre of the scatter face is defined as (0, 0). If a source is placed at this position, at any distance away from the detector face, any misalignments can be observed in the reconstructed image if the source is not located at (0, 0). Any misalignments can be corrected manually through minor corrections to the detector offsets, or if measurements have already taken place, can be amended with an offset correction post-analysis.

Once aligned, the separation of the cryostats at each of the four corners was measured with a vernier caliper to assess if there was any deviation due to the mounting of the detectors on the new frames. Table 4.1 shows how the separation of the cryostats deviate slightly at the bottom-right corner of the cryostat, opposite the frame support for the detector.

Table 4.1: GRI+ Cryostat separation (mm) at 4 different points in mm as measured with a vernier caliper (error of ± 0.1 mm)

Top-Left	Bottom-Left	Top-Right	Bottom-Right [mm]
5.5	5.5	5.5	7.7

The distance between the bottom-right corners of the two cryostats could not be reduced without altering the other three separations, so it was decided to keep the separations as detailed in Table 4.1, with the importance that the separation across the crystal faces would be close to uniform.

4.2 Signal Evaluation

GRI's data acquisition (DAQ) system allows for the post-processing of information that has been collected. The key features that must be obtained from pulses to evaluate the data are the amplitude of the pulse (i.e. the energy) and the *fold*. The fold defines the number of strips that a photon has interacted with, and is detailed in Section 4.2.3. The amplitude of the pulse can be acquired from two methods; the *Moving Window Deconvolution* algorithm or the *Baseline Difference* method.

4.2.1 Moving Window Deconvolution

A moving window deconvolution (MWD) algorithm is applied to evaluate the height of the pulse. The initial preamplifier pulse is the initial stage of the algorithm, as shown in Figure 4.8a. As described in Section 3.2.2, the sharp risetime and very long exponential decay of the tail, makes it difficult to precisely obtain any height information of the pulse. The MWD algorithm converts the signal into a step function, by removing the exponential tail of the pulse, whilst importantly maintaining the pulse height.

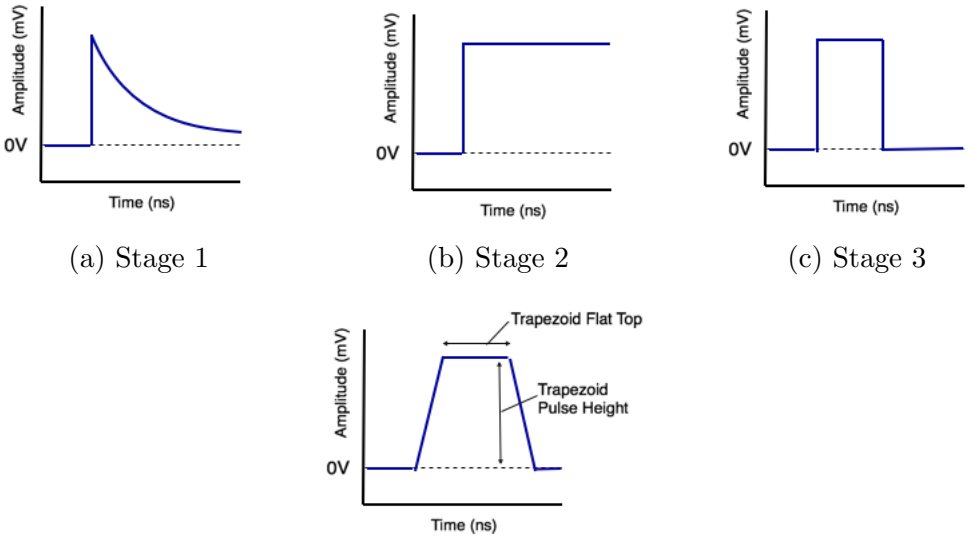

(a) Stage 1 (b) Stage 2 (c) Stage 3

(d) Stage 4

Figure 4.8: Schematic diagram showing the multiple stages of the Moving Window Deconvolution (MWD) algorithm used in shaping a preamplifier pulse. The four stages are described in the text.

By differentiating the step function, a square pulse can be created. This however can contain significant noise, so a *moving average window* of a user defined width is applied to remove any significant noise contributions, and ultimately leaves a trapezoidal shape as shown in Figure 4.8d.

Certain user defined parameters can affect how the MWD algorithm is implemented:

- Baseline Averaging Window - Takes an average of samples within the baseline over a defined number of samples.
- Decay Time - This is the time constant of the exponential decay to the preamplifier pulse.
- Peaking Time - The initial position on the flat top to collect samples for the peak averaging window.
- Peak Averaging Window - Takes an average of samples on the trapezoidal flat top over a defined width to calculate the peak amplitude.
- Trapezoid Flat Top - The duration of the trapezoid flat top.
- Trapezoid Rise Time - The rise time of the trapezoid leading edge.

The height of the trapezoidal flat top corresponds to the energy deposited by an interacting gamma ray. The application of these parameters ultimately affects the energy resolution of the system. The optimised values for the MWD parameters can be found in Table 4.2.

Table 4.2: Detector settings for the scatter and absorber detector to optimise the MWD algorithm.

Parameter	Scatterer	Absorber
Baseline Averaging Window*	4096	4096
Decay Time (μs)	50	50
Peaking Time (μs)	6.55	7.75
Peaking Averaging Window*	64	16
Trapezoid Flat Top (μs)	5.0	10.0
Trapezoid Rise Time (μs)	6.50	7.50
**Note: The units of Baseline and Peaking Averaging Window is based on a number of samples, as the number represents an arbitrary list position*		

Table 4.3: Detector settings applied for the measurements in this thesis.

Parameter	Scatterer Absorber Coaxial
Baseline Averaging Window*	4096
Decay Time (μs)	50
Peaking Time (μs)	6.5
Peaking Averaging Window*	64
Trapezoid Flat Top (μs)	2.5
Trapezoid Rise Time (μs)	5.5
**Note: The units of Baseline and Peaking Averaging Window is based on a number of samples, as the number represents an arbitrary list position*	

Whilst these settings led to an improvement in the energy resolution of the system, a problem with the data aquisition led to the system regularly crashing when there was a high throughput of events (above 1 kHz). A compromise was therefore found on the peaking time, peaking averaging window, trapezoid flat top and rise time parameters, which allowed long data sets to be taken without crashing or a loss of data, at just a slight degradation to the energy resolution by an average of 0.2 keV. These settings were applied across all three detectors and can be seen in Table 4.3.

4.2.2 Baseline Difference Method

An alternative method to determine the amplitude of a signal from the preamplifier pulse is the baseline difference (BLD) method. The BLD method is used in conjunction with the MWD method to help distinguish between what is a real signal and what is noise. The main three signals that can be processed are the following:

1) Real Signals

   Are the pulses that are created from a gamma-ray interaction within a strip and corresponds to the charge collected at the electrical contacts.

2) Transient Signals

   Also known as image charges. These are pulses found in neighbouring strips to those where a gamma-ray interaction has taken place.

3) Noise Signals

Products of electronic noise within the detector system.

The entirety of the preamplifer pulse is not required to determine if a pulse is a real signal or not. Instead, just 1280 ns of the signal is stored as shown in Figure 4.9 (approximately 600 ns either side of the pulse risetime).

Figure 4.9 shows the 1280 ns sample of a preamplifier signal that is obtained from the DAQ system. The sample focuses on the sharp risetime of the pulse. Two sampling periods, 300 ns in size, are selected of the digitised signal either side of the risetime, as shown in Figure 4.9. If the average value of the latter period is found to be three times greater than the standard deviation of the initial period, then it will be considered a real signal.

The average of the second sampling period is calculated to determine the amplitude of the pulse after correcting for the baseline offset. A baseline restoration algorithm is applied to the preamplifier signals to correct pile-up issues, and for the effect of crosstalk. The averages of the sampling periods are determined after this baseline offset has been removed, and is implemented in the digital data processing stage (see Section 4.4) and is not done in the digital electronics.

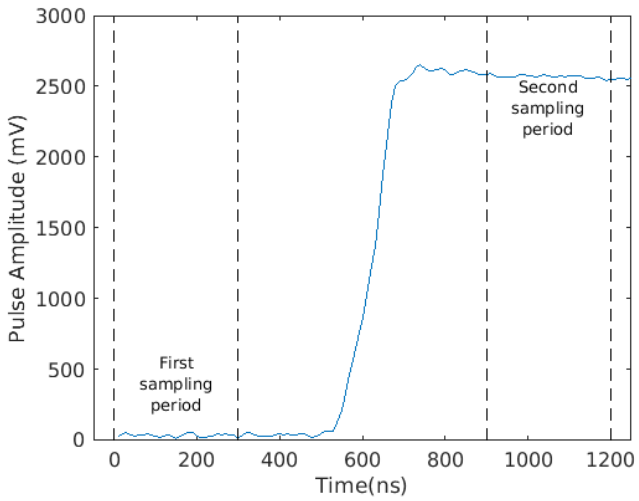

Figure 4.9: Preamplifier signal showing the two 300 ns sampling periods to determine if a pulse is a real signal. The average of the second sampling period is used to determine the deposited gamma-ray energy.

This method is less precise in calculating the pulse amplitude as only a small sample of the preamplifier pulse is utilised. Therefore it is unable to identify

small variances compared to alternative methods such as the MWD method, which utilises the entire pulse. The decaying edge is also not removed when analysing the second sampling period, which produces an uncertainty in the calculation. This imprecision leads to a slight degradation in energy resolution.

The MWD algorithm is an ideal technique to determine the energy of interacting photons, as it utilises the entirety of the pulse in comparison to the BLD method. The conversion of the exponential decay to a step function also leads to a higher precision of determining the height of the pulse.

However, the MWD algorithm is a poor method for determining the number of interacted strips (defined as fold - see below). This is because transient or even noise signals will have some energy as interpreted by the MWD algorithm, so the total number of interacted strips could be incorrectly classified. Therefore, energies are determined by the MWD algorithm after they are confirmed to be real events by the BLD algorithm. Going forward with digital processing, the MWD algorithm calculates the energies for the image reconstruction, and the BLD algorithm determines the fold of the event.

4.2.3 Event fold

Fold is a term used in this thesis to describe the number of strips that a photon has interacted with, within each face of the detectors. The interaction has to provide a *real* signal that exceeds any applied user-defined thresholds.

A single interaction is defined as an event that has activated one AC strip and one DC strip in one detector. A fold-1 event considers single-single interactions within each detector. This can also be described in the format of fold [1 1 1 1 1]. Each number in the fold format describes the number of strips activated in each detector as follows [AC_{Scat} DC_{Scat} AC_{Abs} DC_{Abs} Coaxial]. This fifth *coaxial* variable can define if it is a 2-tiered or 3-tiered event. Due to the coaxial not being electrically segmented, this value can either be 0 or 1.

A fold-2 event considers multiple interactions within one face of a detector. This is not constrained to neighbouring strips, meaning there is a multitude of different possible interactions within the two detectors.

Figure 4.10 displays the number of strips that were triggered in the scatterer and absorber detectors from the measurement of two ^{137}Cs point sources at a standoff distance of 45 cm. The significant number of fold 0 events is due to a known phenomenon with the DAQ system, where in *output all masked*

channels mode (details of acquisition modes are found in Section 4.3.1), not all 47 strips will be recorded. Once this issue is resolved, additional events will be available to utilise in image reconstruction.

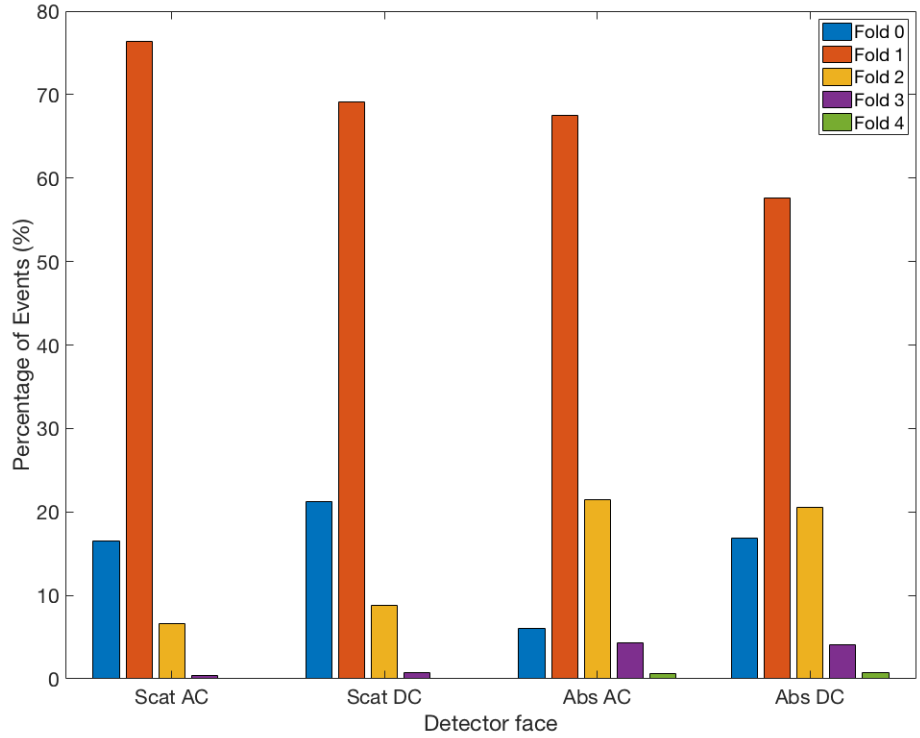

Figure 4.10: Chart showing the fold distributions in each of the faces of the scatter and absorber detectors from the measurement of two ^{137}Cs point sources placed at a standoff distance of 45 cm. Fold 1 interactions dominate.

As it can be seen in Figure 4.10, the detector faces are largely dominated by fold 1 interactions in both AC and DC. For the absorber detector however, there is a significant increase in the amount of multifold events. From this measurement alone, by summing the fold 2 - 4 events shown in Figure 4.10 an additional 25.3 % of useable events could be utilised from multifold interactions in the DC faces of the absorber detector, and an additional 9.5 % from the scatterer.

4.3 Data Acquisition System & Detector Optimisation

For a multi-channel detector system, digital electronics are usually preferred over analogue electronics. Digital systems have:

- Superior gain stability.

  Analogue systems need to be calibrated more often due to unwanted gain shifts within the electronics that can cause the pulse sizes to change.

- Superior capabilities at higher count-rates.

- Ability to store preamplifier pulses for online and offline analysis.

  This is advantageous in these applications for post-processing purposes, such as improving the position resolution of an interaction through pulse shape analysis (PSA) techniques.

A schematic diagram of the digital electronics used in the GRI+ set-up is shown in Figure 4.11.

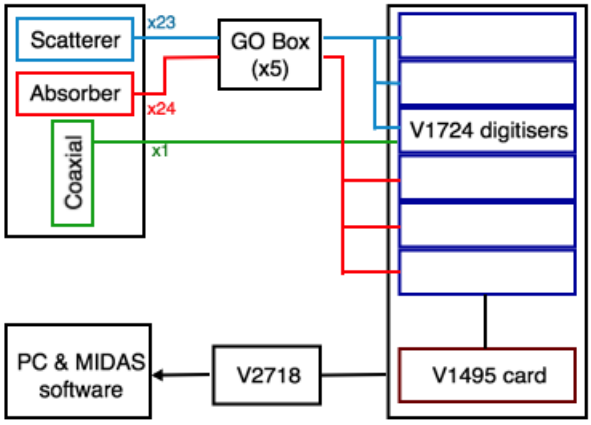

Figure 4.11: Schematic diagram of the electronics in the data acquisition system, from detectors to PC.

At the beginning of the chain shown in Figure 4.11, the outputs from the scatter and absorber detectors are first inputted into a Gain and Offset (GO) box using lemo coaxial signal cables of approximately 150 cm in length, before

connecting to the digitisers. The output from the coaxial detector goes directly to the V1724 digitiser card.

The GO box can amplify the signals by a factor of 2, 5, 10 or 11, and is chosen by the user depending on what energy gamma rays the system will be analysing. For the energies of interest for nuclear decommissioning, the GO box amplified preamplifier signals of the scatter and absorber detectors by a factor of 5.

A 60 keV gamma ray from ^{241}Am would have an original signal height of $\sim$ 10 mV in the scatterer and $\sim$ 6 mV in the absorber detectors (measured at 50 Ohms), which after amplification of the signals by a factor of 5 from the GO box, would have a signal height of approximately 60 mV and 30 mV respectively. The signal input of a 662 keV photon will be approximately 130 mV or 65 mV in the respective detectors. Due to the different polarity of preamplifier signals, the full use of the dynamic range of the digitiser cards (2.25 V) can be utilised.

The GO box also allows for a manual correction of the baseline offset for each channel. The amplitude of the pulse is measured relative to the baseline. The baseline is usually restored to zero for ease of extracting the amplitude of the pulse. Pile-up observed at higher rates, or capacitive coupling from neighbouring strips [78] could lead to a possible shift to the baseline. Therefore, to prevent the broadening of peaks from the misreading of the pulse amplitude, it is important that the baseline is restored to zero.

The outputs of the GO box are split across six 14-bit CAEN V1724 digitisers [79] that create the link between the detector and the computer. Lemo coaxial cables are used to connect the GO box outputs to the digitisers. The same length of cable, of approximately 60 cm, was used for all connections between the GO box and the digitisers to prevent any avoidable signal delays which may occur, which on average is approximately 1 ns/30 cm of cable.

As a maximum of six slots were available for the V1724 digitisers within the VME crate, the sytem was limited due to the total number of inputs available on the GO box (47) and the digitisers (48) compared to the total number of channels available from the three detectors (51). With 8 channels available on each digitiser card, the first three cards are assigned to the scatterer, with the final channel on the third card being used for the coaxial, and the remaining three cards using all the channels from the absorber detector.

A decision was made to not connect scatter detector strips AC 13 and DC 14 and 26. These strips were chosen as they were edge strips and were small in

size due to the circular shape of the crystal, as shown in Figure 4.12. The loss of recorded events from these strips doesn't largely affect the efficiency of the system. Therefore, 23 inputs were used for the scatterer, 24 for the absorber, and 1 for the single coaxial input.

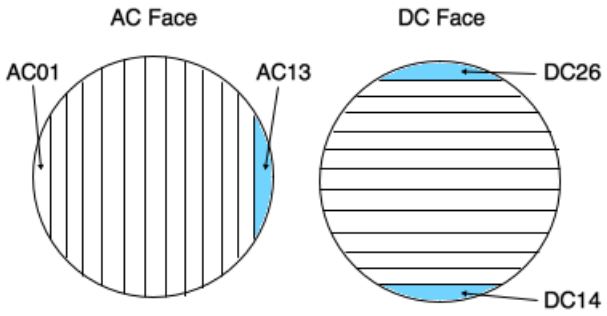

Figure 4.12: Schematic diagram of the scatter detector strips. The strips unused for the data acquisition are shown in blue.

A V1724 digitiser uses a flash ADC (analogue-to-digital converter) which allows for a sampling frequency of one sample every 10 ns (100 MHz) and a field-programmable-gate-array (FPGA) with digital pulse processing (DPP). The FPGA is where the latest version of firmware is installed. The height of a pulse is determined through the implementation of a Moving Window Deconvolution (MWD) algorithm in the CAEN V1724 cards, leading to the calculation of the energy that has interacted in the detector.

As shown in Figure 4.11, the V1724 digitisers are connected to a CAEN general purpose VME board, otherwise known as a V1495 card via 6 ribbon cables. A universal clock that is generated by the first V1724 digitiser card keeps the 6 units in sync with each other. The V1495 card controls and resets this universal clock once the acquisition has taken place, and will then return a 'valid' signal should all the user-specified criteria be successfully met after the processing of the signal.

4.3.1 User interface - MIDAS

The Multi Instance Data Acqusition System (MIDAS) [80], is a piece of software that controls the DAQ system. Commands can be issued from MIDAS to start and stop the data acquisition process, as well as allow parameters such as MWD energy algorithm criteria to be optimised and selected for mea-

surements to be taken. The MIDAS interface window also allows the user to control settings on the V1495 card.

In order for an event to 'trigger', the interaction must pass a hardware threshold. It is defined by the digital constant fraction discriminator (CFD) on the V1495 card and implemented on the V1724 cards. These thresholds are defined to ensure that a signal can be distinguished from electronic noise. The thresholds are set above what is measured for RMS electronic noise. For the Si(Li) the threshold was approximately 4.0 keV and for the Ge it was 8.0 keV. The CFD thresholds can be optimised for the different strips, the precision of which is determined through a trial and error process to allow the threshold to be as low as possible to allow for low energies to be measured and filtering out any noise, increasing the efficiency of the system.

On receipt of a validated trigger (an event that matches the user input criteria), a signal is sent to the V1724 cards to write out a preamplifier pulse sequence that is 1280 ns in duration. This event can also be time-stamped by the V1495 card, which provides a time reference point for the interaction of that event within the system. The timestamp of the V1495 clock is a 31-bit 'word', which means it has a *wrap around* frequency of 21 seconds (a scenario where the earlier event has a later timestamp value than the second event).

Figure 4.13 shows the screenshot of the MIDAS user interface, particularly the display which includes the options for the V1495 card to be applied. The three main settings of interest are; the detector coincidence, the coincidence window and the readout mode. These settings are highlighted in the figure.

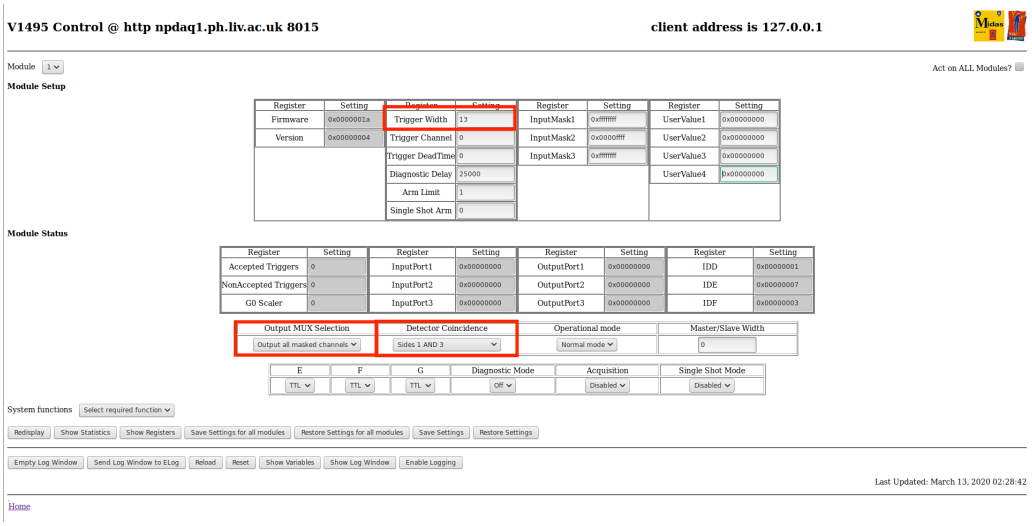

Figure 4.13: Screenshot of the MIDAS user interface. The highlighted red areas are where the user can alter the coincidence window, the detector coincidence, and the readout mode.

Due to the double-sided nature of the detectors, the face at which an event is triggered can be defined. These can either be triggered from the two AC faces, or from the DC faces. As the AC sides of the detector are the two 'front-facing' sides of the detectors when facing a source, interactions will occur closer to the AC face, leading to shorter charge collection times. Utilising these shorter charge collection times leads to a superior timing performance of the system, and therefore the AC sides are what is used for triggering. However, there is no evidence that there is a loss of efficiency from triggering from the DC faces of the detector. In Figure 4.13, sides '1 and 3' are representative of the AC sides of the two detectors. When collecting coincidence data, the two triggers from the scatterer and absorber must occur within the defined coincidence window.

The coincidence window is the time between interactions that occur between the scatter and absorber detector. This window helps define if scattering events are coming from true Compton scattered events from the incident gamma ray. The optimum coincidence window was investigated here [81] using ^{22}Na in a timing coincidence circuit, which determined the timing resolution of the detectors was 25 ns. The coincidence window was set to 325 ns to optimise the efficiency of the system, whilst reducing the number of false, or undesirable coincidences. In Figure 4.13, the trigger width is a value that is multiplied by 25 ns to obtain the coincidence window; for a coincidence window of 325 ns, the trigger width is set to 13.

The readout mode is defined as what signals are to be output from the detector when there is a gamma-ray interaction. The three main modes of operation include:

1) Output as Input Masked

   Only the signal from the strip in which the gamma ray interacted with is outputted.

2) Output as All Masked Channels

   When a photon interacts within a strip, then the readouts from all the other strips are provided at that particular time.

3) Output Nearest Neighbour

   When a photon interacts within a strip, the readouts from that strip

and its two neighbouring strips are included.

The three different modes have different benefits depending on what the user requires.

Output as input masked can be beneficial when there is high rates, however the output of single strips mean that further post-processing and use of parametric PSA techniques cannot be utilised. However, parametric and database PSA techniques could still be employed to determine the depth of interaction (see Section 4.4.4).

In order for a full parametric PSA technique to be utilised, the *Output as All Masked Channels* mode allows the user to observe the image charges across neighbouring strips. However, the DAQ system can struggle at high rates (above 10^3 counts per second) due to the amount of data being recorded, as it is very I/O intensive. If the 1280 ns information from a single preamplifier pulse is approximately 50 kB in size, some measurements can record over several MB/s of data.

Limiting the size of the coincidence window could help with the high I/O rates from the DAQ, by reducing the number of validated triggers. This means that any measurements that span a few days, with average rates of $\sim$100 kB/s, that requires to be ran in *Output as All Masked Channels* mode, can take place without fear of a system crash and loss of data. A balance must be found however, as having an incorrect timing window can lead to false coincidence events which will degrade the image quality.

The *output nearest neighbour* mode provides a good balance if some PSA techniques are required, and having to deal with rates over 10^3 cps. However, the inability to see how charge is shared across all the strips limits the PSA techniques which can be used for events with multiple interactions.

The information from signals that match the criteria implemented in the V1495 card, such as the raw preamplifer pulse, uncalibrated energy and time stamps, are sent to a CAEN V2718 card. This information is then transferred to a PC using a VME to PCI optical link bridge. The connections between the digitiser cards and the external circuitry such as the PC's is done optically, in order to provide electrical isolation. Through this, the information can be used for instantaneous online analysis, or stored offline for further processing.

4.4 Digital Data Processing

The relevant data, once collected, is processed using software developed at the University of Liverpool called MTsort ([82]). MTsort is used in conjunction with the MIDAS analysis package software.

MTsort interprets the collected data that has been stored on disk, and can produce user relevant spectra and matrices. It uses a custom programming language and can also encorporate C-algorithms.

Its primary use is selecting events that are suitable to produce Compton images from image reconstruction algorithms (see Section 4.5) in a sortcode. The sortcode is a set of code that is utilised for digital data processing, that interprets the data that was collected and *sorts* through it to extract user-defined relevant information. It can optimise the data by applying calibration coefficients, crosstalk corrections, and define parameters to help with pulse shape analysis. Conditions on the imaging data can be applied such as defining single-single interactions.

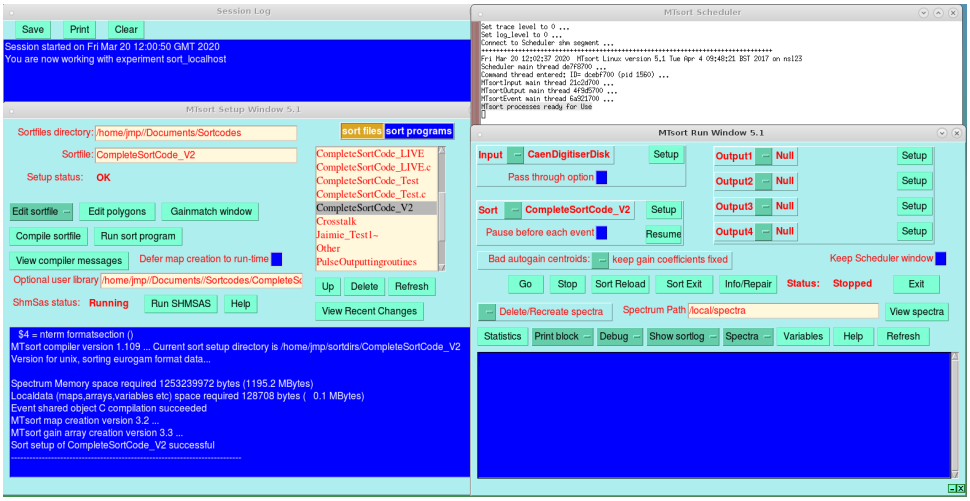

Figure 4.14: Screenshot of the MTsort software used for the digital processing of data.

MTsort can combine the spectra produced from the individual AC or DC channels to create an **addback spectrum**. An addback spectrum is defined as the summed energy deposited from single pixel events across a detector face. These can include scatter AC or DC addback and absorber AC or DC addback. Utilising coincidence events from both AC or DC sides of the two detectors are known as **sum energy** or **coincidence energy** spectra.

Measurements took place at the start of the campaign to calibrate the detectors. Individual strips are first calibrated in singles mode, and then the system is utilised in coincidence mode to observe if the calibration has been correctly applied over a large range of energies. To calibrate the scatter detector, the energies from a ^{133}Ba and ^{152}Eu source is used.

^{133}Ba decays via electron capture to two excited levels of ^{133}Cs, producing 437 and 383 keV gamma rays as they deexcite to two minor branches, with 160 and 81 keV gamma rays produced when returning to the ground state. K-shell ($K_{\alpha,\beta}$) X-rays of 30 keV and 35 keV are also emitted from this process.

^{152}Eu can decay via either electron capture to excited states of Samarium-152 (^{152}Sm) or via β^- decay to Gadolinium-152 (^{152}Gd). A large majority of the gamma emissions used in calibration such as 121.8, 244.7, 1112 and 1408 keV, arise from the ^{152}Eu to ^{152}Sm decay scheme. The 121.8 keV decay in ^{152}Sm leads to the production of K-shell ($K_{\alpha,\beta}$) X-rays of 40 and 45 keV energy, coincident with the 244 keV transition from internal conversion. Other key energies, such as 344 and 778 keV arise from the ^{152}Eu to ^{152}Gd decay scheme.

For the scatter detector, only the X-rays and lower-energy gamma rays will be utilised. The energy deposited in a single strip in the scatter detector (DC17) is shown in Figure 4.15. The figure shows the difference in the number of counts of various full-energy peaks when in singles or coincidence mode.

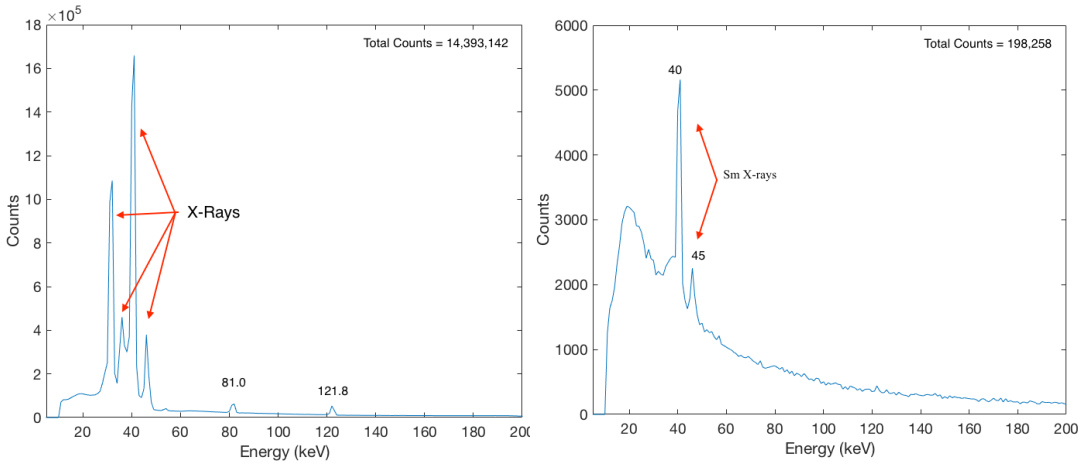

(a) (b)

Figure 4.15: Figure showing spectra from a single strip in the scatter detector in (a) singles mode of ^{133}Ba and ^{152}Eu and (b) coincidence mode of a ^{152}Eu source. Labelled are some full-energy peaks of interest.

In singles mode, each strip acts as though it is its own individual detector. Figure 4.15a shows the measurement used for calibrating the scatter detector using both sources. More low-energy peaks are present in this spectrum as photoelectrically absorbed interactions are more likely to be recorded in singles mode.

Figure 4.15b shows the strip in a measurement of ^{152}Eu in coincidence in *output all masked channels* mode. Here, a continuum is observed due to the amount of Compton scattered events that will be occurring in coincidence with events in the absorber detector. Only the ^{152}Sm X-rays are present as they will also be interacting in coincidence with gamma rays in the absorber, and will lead to unwanted true coincidences and summed peaks in the coincidence energy spectra.

For the absorber detector, a measurement of ^{152}Eu was taken in singles and coincidence (*output all masked channels*) mode. The energy spectrum of the recorded energy in a single absorber strip (DC 05) is shown in Figure 4.16. Figure 4.16a shows the spectrum when the detector is in singles mode, recording the numerous gamma-ray peaks produced from the ^{152}Eu decay to excited states in ^{152}Sm and ^{152}Gd, with the presence of the higher-energy peaks observed.

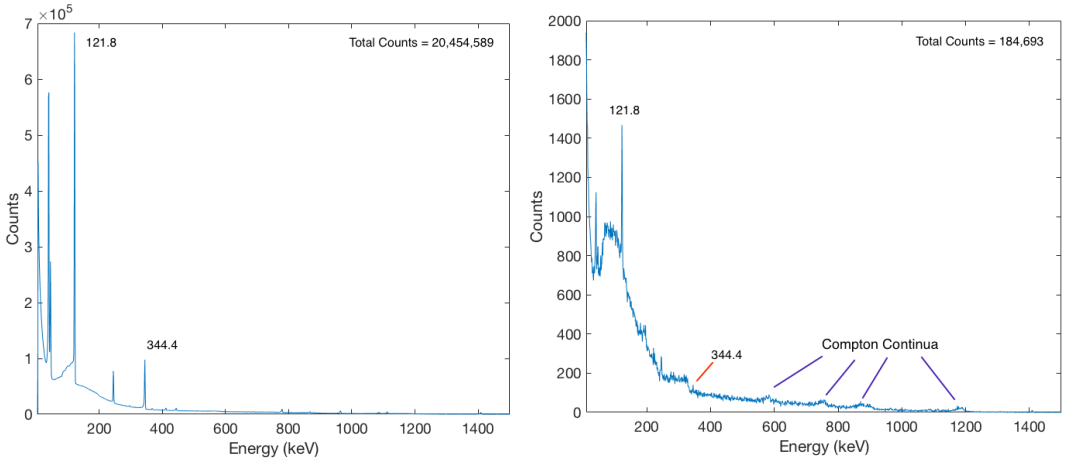

(a) (b)

Figure 4.16: Figure showing spectra from a single strip in the absorber detector in (a) singles mode of ^{152}Eu and (b) coincidence mode of a ^{152}Eu source. Labelled are some full-energy peaks of interest.

Figure 4.16b shows the same strip when the system is in coincidence mode. In comparison to the singles spectrum, the 121.8 keV full-energy peak is present

from photoelectrically absorbing in the absorber detector, but the ^{152}Sm X-rays are no longer observed. It is unlikely that the X-rays would pass through the scatter detector uninteracted to react with the absorber detector, and to deposit an energy higher than the defined energy threshold.

The rest of the energy spectrum shows additional peaks absorbing in the detector, from energies such as 244.7 and 344.3 keV, up to 1408 keV. There are also a few broader areas which do not match energies from the ^{152}Eu source. These are small Compton continua for the scattering of the various gamma rays.

The sum of the AC and DC strips on either detector leads to the addback spectra as shown in Figure 4.17. The scatter addback spectrum now includes the presence of the 121.8 keV full-energy peak. The absorber addback spectrum includes the Compton continua associated with the most prominent gammas from ^{152}Eu, but also some full-energy peaks are observed. This is due to the undesired coincidences of the X-rays. This feature can be prevented with the inclusion of a thin copper sheet in front of the ^{152}Eu source to shield the X-rays.

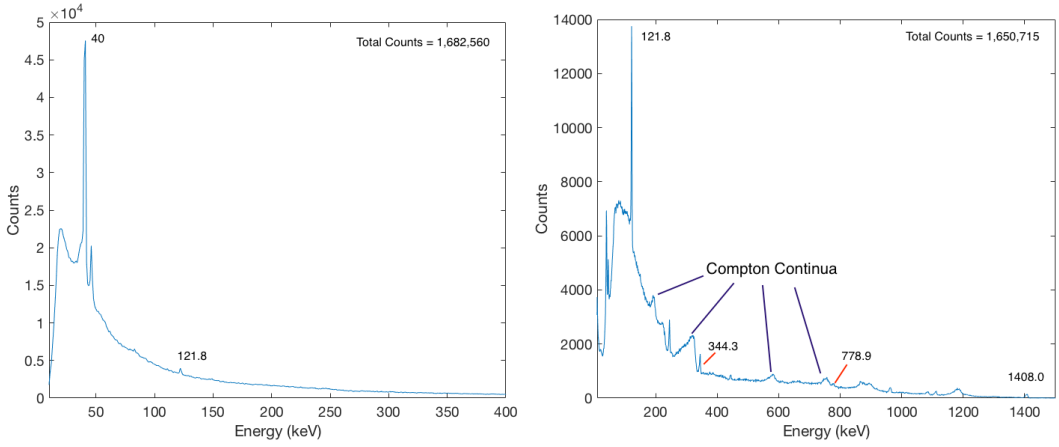

(a) (b)

Figure 4.17: Figure showing the addback spectrum for all events in the (a) scatter DC face and (b) absorber DC face of a ^{152}Eu source collected in *Output all masked* coincidence mode.

The influence of the X-rays can also be seen in Figure 4.18. Here, how the energies from the scatterer and absorber are summed on an event-by-event basis can be seen.

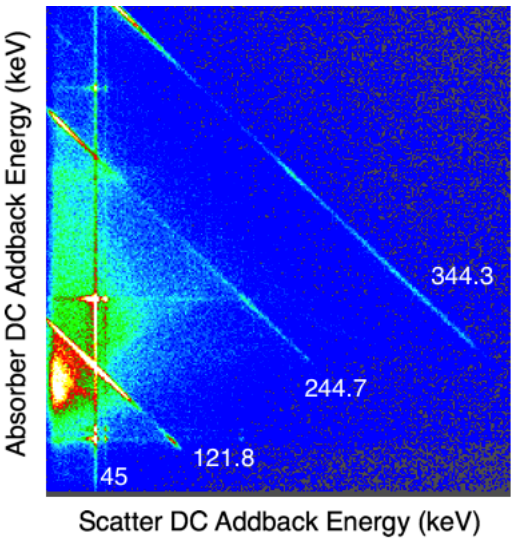

Figure 4.18: Matrix showing the scatterer DC addback energies against the absorber DC addback energies from a ^{152}Eu source in *Output all masked* coincidence mode. The diagonal lines show how the summed energies from the scatterer and absorber detectors total some full-energy peak energies. The vertical line at 45 keV is undesirable coincidences with the X-ray.

Figure 4.18 shows the scatterer DC energies plotted against the absorber DC energies in a matrix from the data shown in the previous spectra. The high-intensity areas on the matrix are representative of the gamma-ray interactions in both detectors. The diagonal lines show how the summed energies from the scatterer and absorber total the gamma-ray energies from the decay of ^{152}Eu. The lower-energy vertical line represents the 45 keV X-ray and its coincidence with events in the absorber detector.

The energies shown in this matrix, if they fall under the criteria of a fold [1 1 1 1] event, are displayed in a coincidence energy spectrum shown in Figure 4.19. The 162 keV peak to the right of the 121.8 keV peak is the result of a coincidence event between the 121.8 keV photon and a 40 keV X-ray. The energies present in this spectrum are what is utilised for image reconstruction. Additional thresholds were applied for the energies that appear in the coincidence spectrum, with the sum low-energy threshold at 100 keV, and the high sum-energy threshold at 1500 keV.

Once the data has been processed, a text file is produced stating the x, y and z positions of an event that deposited energy in the scatter and absorber detectors. It is written in a format that can be interpreted by the image reconstruction algorithm. The position of an interaction is considered centrally within a strip unless PSA is applied (Section 4.4.4).

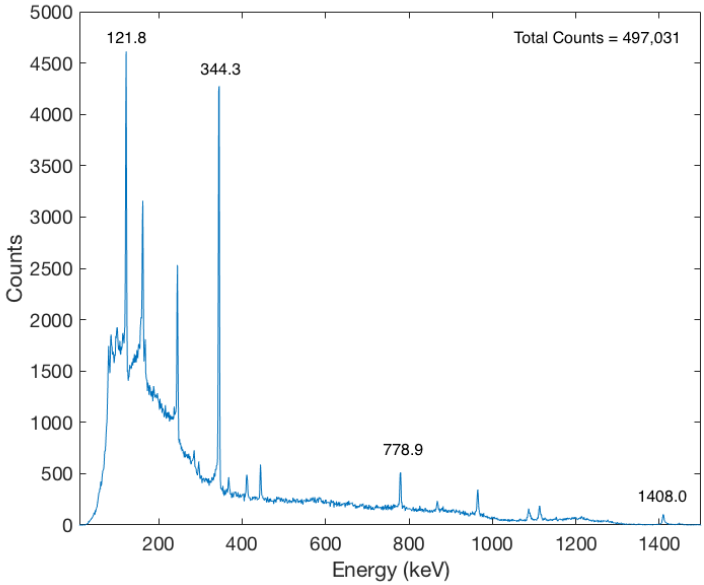

Figure 4.19: Figure showing the sum energy spectrum of two tier fold [1 1 1 1] events. This is an event by event sum of the spectra shown in Figure 4.17.

4.4.1 Energy Calibration

Due to the segmentation of the scatter and absorber detectors, each channel has to be individually calibrated for energy in order for the coincidence spectra to be accurately calibrated. Figures 4.15(a) and 4.16(a) show the example spectra used for calibration in the scatter and absorber.

Due to the thickness of the Si(Li), low-energy gamma rays are needed as a statistically significant amount of counts must be collected in order to confidently state the presence of a full-energy peak. Any gamma rays of an energy over 300 keV can take several hours to collect, and that is just on the central strips. If there was no restriction on time for a measurement, then it would be beneficial to have an additional full-energy peak for calibration. However, as it can take several hours or almost a day to collect a few hundred counts, as well as the computational strain of the numerous other events taken during singles mode acquistion, then the focus is to utilise gamma rays of energy below 300 keV.

Because of this, the 60 keV peak from ^{241}Am, 80 keV peak from ^{133}Ba and the low energies and X-rays from ^{152}Eu decay were used. The sources were placed approximately 20 cm away from the scatter detector face, with count rates of

over 2000 CPS achieved, leading to over 2 MB/s of data being stored for both calibrations.

Due to the numerous energies used in the calibration, it is not required to utilise a few higher energies (such as 244 and 344 keV from ^{152}Eu decay) for calibration of the scatter detector. The higher energies of ^{152}Eu up to 1408 keV were used to calibrate the absorber and coaxial detectors.

The centroids of the defined peaks were identified, and the channel numbers of a spectrum were reassigned to an energy by using a quadratic equation in the form $E = ax^2 + bx + c$, where x is the channel number and a, b and c are coefficients that can be determined. These coefficients can be utilised in a sortcode to calibrate the individual channels. Good linearity was observed for both individual channels and addback spectra, with a conversion of approximately 0.2 keV/channel.

4.4.2 Energy resolution

Through the optimisation of the MWD algorithm from the parameters found in Table 4.3, the digital energy resolution per channel was found for 60 keV photons for the scatter detector, and 122 keV photons for the absorber detector.

The calibrated spectra were exported and fitted using the *GF3* program [83]. GF3 is a least-squares peak-fitting program which is used primarily to fit gamma-ray spectra from semiconductor detectors. It will try and fit a Gaussian curve to a full-energy peak, the FWHM of which will represent the resolution of the energy peak. Due to the affect of background radiation or Compton scattering, this may be fit as a *skewed Gaussian* or a *smoothed step function* due to the possible asymmetrical nature of a peak from a higher background level on the low-energy tail of the full-energy peak. This fit also allows additional information from the peak to be obtained, such as the net peak area, which is used for other measurements in this thesis.

Figure 4.20 shows the digital energy resolution for both detectors for campaigns A and B. These represent the measurements that took place in the Oliver Lodge Laboratory (OLL), University of Liverpool (A) and the Central Teaching Laboratory (CTL), University of Liverpool (B). The majority of strips are within a 0.5 keV difference between the two sets of measurements.

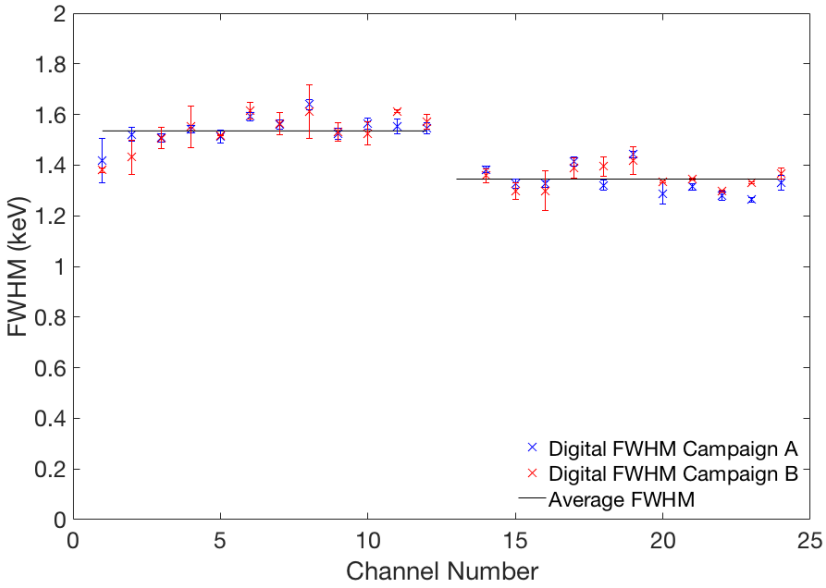

(a)

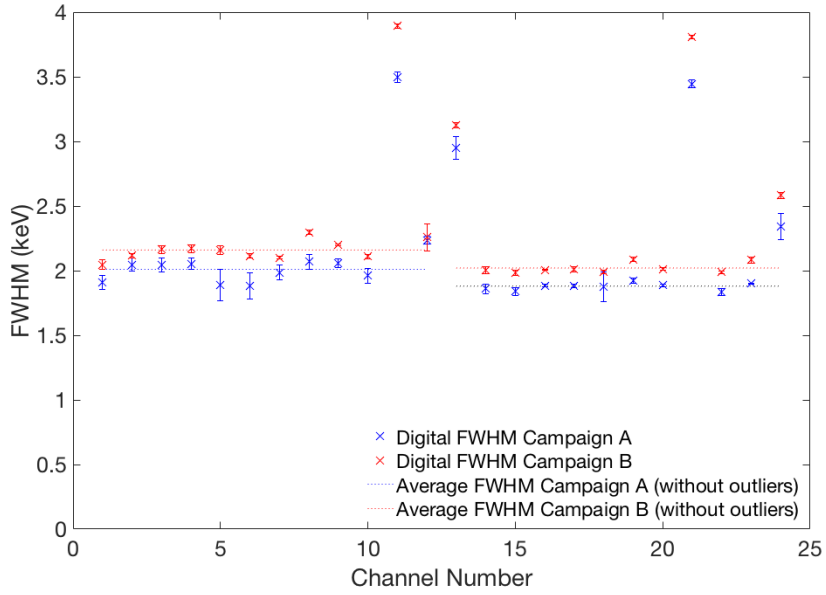

(b)

Figure 4.20: Graphs to show how the digital resolution varies with channel number in both data campaigns (a) for the scatter detector at 60 keV and (b) for the absorber detector at 122 keV.

Table 4.4: Table showing the average energy resolutions at 60 keV in the scatter detector.

Scatter Detector at 60 keV	Average AC Resolution	Average DC Resolution
Campaign A	1.54 ± 0.05	1.34 ± 0.06
Campaign B	1.53 ± 0.07	1.35 ± 0.04

The average digital FWHM values for the scatterer strips is found in Table 4.4 calculated from the values shown in Figure 4.20a. These values show an overall increase from the analogue average FWHM of 1.26 ± 0.10 keV for the AC strips and 0.97 ± 0.06 keV for the DC strips, which is to be expected when moving to digital electronics and the implementation of the MWD parameters. The uncertainties shown in Tables 4.4 & 4.5 were first obtained from the quality of the fit applied in GF3 for each strip, with the standard error of the mean then calculated for the average AC and DC resolutions.

The average digital FWHM values for the absorber strips is found in Table 4.5. A number of the faulty strips found in the analogue measurements found in Figure 4.5 were consistent with the digital measurements. The energy resolutions with and without the inclusion of the outlying faulty strips (AC 11, DC 01 and DC 11) is included in the table. These values are also greater than the analogue average FWHM of 2.14 ± 0.49 keV for the AC strips and 1.94 ± 0.49 keV for the DC strips.

The absorber detector shows that the digital resolution degraded slightly when transferred to the CTL, unlike the scatter detector with the two values within error.

Table 4.5: Table showing the average energy resolutions at 122 keV in the absorber detector.

Absorber Detector at 122 keV	Average AC Resolution	Average DC Resolution
Campaign A	2.14 ± 0.44	2.13 ± 0.52
A - without outliers	2.01 ± 0.10	1.88 ± 0.03
Campaign B	2.30 ± 0.51	2.30 ± 0.61
B - without outliers	2.16 ± 0.07	2.02 ± 0.04

Proportional Crosstalk

Crosstalk is a phenomenon caused by the capacitive coupling between neighbouring strips. This causes transient signals to appear in neighbouring strips, which the MWD algorithm may incorrectly interpret as a real event.

This affects the energy resolution of full-energy peaks due to an undesirable

affect that arises from charge-sharing across adjacent strips. Transient signals in neighbouring strips can show small baseline offsets that can be interpreted as real energies. These baseline offsets can also be summed with real signals, leading to a higher signal and an incorrectly calculated energy. With proportional crosstalk, the baseline shift increases linearly with energy.

When mulitple fold events are analysed, crosstalk effects become prominent. Energy peaks on a spectrum show a 'double-peaking' effect where a single energy full-energy peak should be present. This double-peaking can be seen in Figure 4.21 and is more prominent at higher energies. As can be seen in the figure, which shows the summed energy spectrum from ^{152}Eu, three prominant energies have been shifted to a higher energy due to crosstalk on the absorber AC face.

To correct for this, adjacent and non-adjacent strips are compared for multifold events. With non-adjacent strips, the crosstalk effect is not observed, and the peak is observed at the correct position after calibration. The adjacent strips will show the peak shifted at a higher energy. The difference between the centroid positions of these two peaks is taken for a range of energies.

A graph of the *energy shift* against the literature energy of the gamma rays will show a linear relationship as shown in Figure 4.22. The values from the gradient and the intercept of the straight line are applied to the shifted energy through the following equation:

$$E_C = E(1 + m) - c \tag{4.1}$$

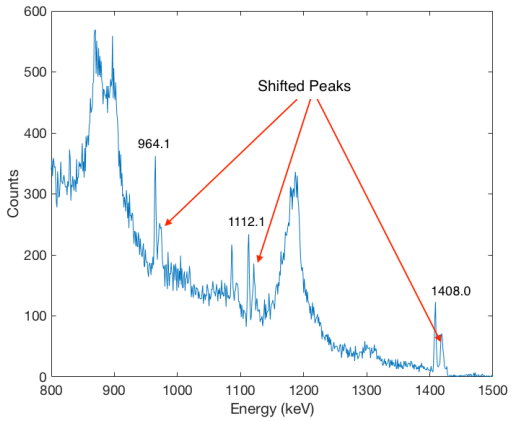

Figure 4.21: Spectrum showing the affect of proportional crosstalk on the absorber AC face from a measurement of ^{152}Eu in *output all masked* coincidence mode.

Where E_C is the corrected energy after the coefficients have been applied to the energy, E, and m and c represent the gradient and y-intercept respectively. Values will be applied to fold 2 events both in the scatterer and absorber for both AC and DC, and for fold 3 events in the absorber AC and DC sides. If the values are applied incorrectly, this can still lead to a broadened energy peak. The crosstalk correction for higher-fold events is implemented in the sortcode.

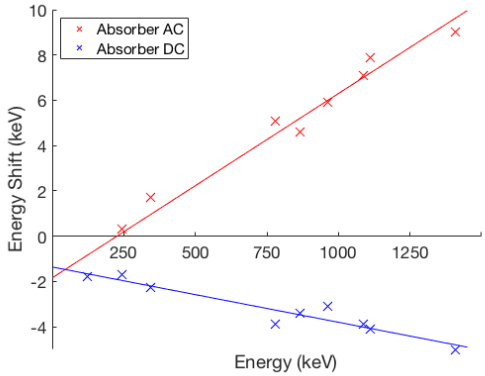

Figure 4.22: Graph showing how the crosstalk correction factors can be determined from analysing the gradient and y-intercept of the energy values plotted against the shifted energy, due to proportional crosstalk observed in the absorber AC and DC faces.

4.4.3 Event Processing

During the digital data processing of a measurement, pulses have to pass certain conditions in the sortcode in order for events to be selected for imaging. The breakdown of interactions from the measurement of two ^{137}Cs point sources at a standoff distance of 45 cm (the same measurement used for Figure 4.10) is shown in Table 4.6.

The first line of Table 4.6 shows the total number of interactions that take place within the detectors that initially pass the CFD thresholds set in the V1495 card, and is assigned an energy as governed by the MWD algorithm. If a signal exceeds the CFD threshold, then all the signals from the channels are recorded.

The second line compares the MWD values with the BLD algorithm to confirm if the registered interaction is classed as a real fold, i.e. a true interaction. This value is inclusive of interactions in all three detectors, with the breakdown of the number of real interactions in each individual channel within a detector

shown in Table 4.6. For example, the value of 1 737 231 interactions in the scatter detector could be broken down further into 879 244 real interactions on the AC channels, and 857 987 interactions on the DC channels. Similarly with the absorber detector, the 2 333 240 interactions in the absorber detector could be divided into 1 220 640 real interactions on the AC channels, and 1 112 600 on the DC channels.

Table 4.6: Breakdown of the number of events used at each stage leading to image reconstruction.

Parameter	Number	Percentage (%)
MWD interactions passing an energy threshold	4 719 403	100.0
Real fold interactions (Total)	4 119 979	87.3
Real Interactions - Scatterer	1 737 231	
Real Interactions - Absorber	2 333 240	
Real Interactions - Coaxial	49 508	
Total number of two tier events	912 268	19.3
Total number of three tier events	49 508	1.0
Fold [1 1 1 1] two tier events	258 941	5.5
Imageable Events	245 330	5.2
Energy gated events for image reconstruction	11 605	0.3

An *event* considers a number of interactions that occur between the scatter and absorber detectors within a defined amount of time. The interactions that deposit energy in both the scatter and absorber detector only, within the defined coincidence window and regardless of fold, are considered as two-tier events. It can be seen in the table, that this is just 19.3 % of the original number of MWD interactions that passed the energy threshold. However, these events are incorporating the AC and DC interactions that are included in the real events of both detectors, so it is not exactly an 80 % loss of useable events.

Two tier events that interact with one AC and DC strip on each detector are broken down further into Fold [1 1 1 1] events. These Fold [1 1 1 1] events will be utilised in the image reconstruction (the process of which is described in Section 4.5). The difference between these events and the *Imageable Events* shown in Table 4.6, is the addition of an energy gate applied by the user in the sortcode when the data is being processed.

The data that is suitable for Compton imaging is then filtered through an additional energy gate during the image reconstruction process to observe full-energy peak events in the reconstructed image. The larger the energy gate, the larger percentage of events that can be used, however this can affect the

quality of the image. As can be seen in Table 4.6, these events only amass to 0.3 % of the initial interactions that initially passed the threshold criteria. The ratio between the gated events and the imageable events is also comparable to the peak-to-total value in the energy spectrum.

Another way of increasing the number of events that can be used in the final image reconstruction is to utilise multifold events. However, being able to successfully classify an event that has interacted multiple times is difficult and could lead to the incorrect positioning of the gamma ray to be used in image reconstruction. Methods to include fold-2 events are currently being investigated to increase the efficiency of the GRI system.

For this reason, only fold [1 1 1 1] events are considered in this thesis. It will be detailed if the coaxial has been enabled for it to be a 2-tier or 3-tier event. Tables such as the one shown above will be included for each measurement in this thesis, and a further breakdown of the interactions is shown in Appendix B.

4.4.4 Pulse Shape Analysis

Recent data campaigns with GRI+ have implemented the use of Pulse Shape Analysis (PSA) techniques. Before PSA techniques were introduced, interactions were assumed to take place centrally within voxels in the front two detectors. With the size of each voxel, $5.5 \times 5.5 \times 8$ mm^3 for the scatterer and $5.0 \times 5.0 \times 20.0$ mm^3 for the absorber, assuming a central interaction leaves a large degree of positional uncertainty.

Section 3.3 describes how the energy deposited in detectors can be used to reconstruct a cone in Compton imaging. The points of interaction between detectors form the vertex of the cone (see Section 4.5.1 on image reconstruction). Where these cones overlap leads to the location of the radioactive source. The positional uncertainty will therefore affect the reconstruction of these cones and result in a significant error in cone overlaps.

Two different PSA techniques have been used with measurements involving GRI+; parametric and database. Parametric PSA is what is described in this section for improving the XYZ positions. It is used in this thesis as it is an efficient and quick method to improve the positional resolution. For the measurements taken in this thesis, the quick obtaining of values is ideal in possible offsite scenarios where knowledge of the source location would be required quickly.

Database PSA is a new method that is currently being implemented. This offline technique matches preamplifer signals from interactions to an online database, which includes simulated pulses from a large number of known positions. However, depending on the amount of data that is collected, the time it takes to compare all the signals can be as long as days. Therefore the method, whilst offering improved position resolution, is too time consuming for this work.

Parametric XY-PSA

In Section 3.2.2, the Shockley-Ramo theorem introduces how charge can be induced through the movement of charge carriers. By analysing the amplitude of these induced charges, the position resolution can be improved. As the scatterer and absorber detectors have orthogonal strips, the position can be improved in both X and Y.

In Section 4.2.2, the three signals that can be processed in data acquisition were described. Consider an interaction that occurs centrally within a strip, producing a sample of the real signal over 1μs. The induced transient signals on the neighbouring strips over the same period should amount to charges of equal amplitude, as shown in Figure 4.23a. However, if the interaction is closer to one neighbouring strip than the other, as seen in Figure 4.23b, then the collected image charges will be asymmetrical in nature.

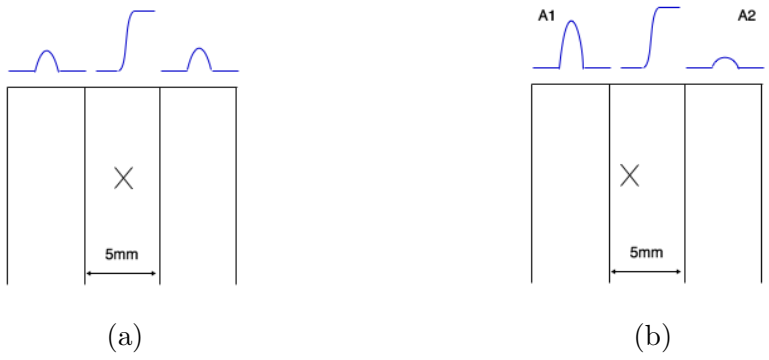

(a) (b)

Figure 4.23: Figure describing how the image charges are induced on neighbouring strips when a gamma-ray interaction occurs (a) centrally or (b) shifted to a neighbouring contact.

The difference in the magnitudes of the area of the image charges can be described by an *asymmetry* term, A, and can be represented by the following equation [84]:

$$A = \frac{A_1 - A_2}{A_1 + A_2} \tag{4.2}$$

In Equation 4.2, A_1 and A_2 represent the areas of the induced charges to the left and right of the real signal respectively, as shown in Figure 4.23b. The value of A will fall between 1 and -1. The closer it is to 0, the more central the point of interaction was within the strip (these values are scaled to be used with the MTsort codes).

Figure 4.24 shows an example distribution of asymmetry parameters for one strip. The distribution can be divided into 5 segments of equal area to improve the lateral position resolution by 5, reducing the scatterer resolution to 1.1 mm from 5.5 mm, and the absorber resolution to 1.0 mm from 5.0 mm . The uncertainty associated with this technique has been investigated in previous work, [84], and found that over 78 % of events are either identified correctly or within error of one sub-strip.

The asymmetry terms can vary from strip-to-strip. Similar to how energy calibration is required due to the small variations in the gain of the preamplifiers, the asymmetry parameters must also be calibrated in order to produce a distribution unique to that strip. To calibrate the two detectors, the readout mode of *output all masked* must be applied in order to observe the signals from neighbouring strips. A ^{152}Eu source was placed approximately 10 cm away from the scatter detector face. Only Fold 1events are used for the calibration.

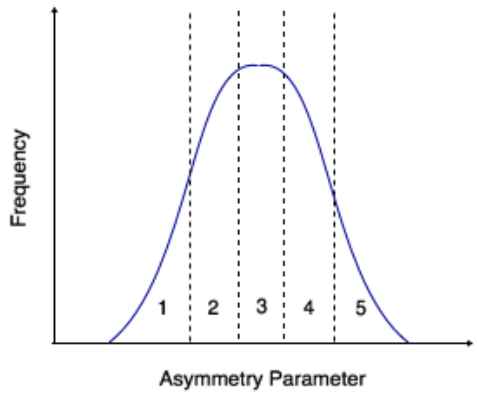

Figure 4.24: Figure describing the distribution of asymmetry values. The dashed lines show how the distribution can be segmented and represent a specific position on a strip.

For each strip, 4 values are defined which represent the boundaries observed

in Figure 4.24 to separate the distribution into 5 sections. These values are implemented in the .C code, which is called by the MTsort codes. In further measurements, the position of interaction can be determined by comparing against these values. Figure 4.25 shows the asymmetry distributions in the DC absorber strips collected from the calibration measurement. The slight variations between strips can be observed in the figure.

As can be seen from Figure 4.25, strips DC01 and DC12 do not show an asymmetry distribution. This is because they are edge strips. Edge strips don't have a parameter as they do not have two adjacent strips, therefore the point of interaction can be assumed to be central. A different approach can be adopted however by looking at the single induced image charge on the one neighbouring strip following the equation 4.3 [84]:

$$A_{single} = \frac{A_{L/R}}{E_\gamma} \tag{4.3}$$

In this equation, $A_{L/R}$ represents the area of the single image charge found on the left (L) or right (R) of the hit strip. E_γ is the energy deposited by a gamma ray in that interaction. As detailed here, [84], this technique provides approximately the same uncertainty as the original asymmetry approach.

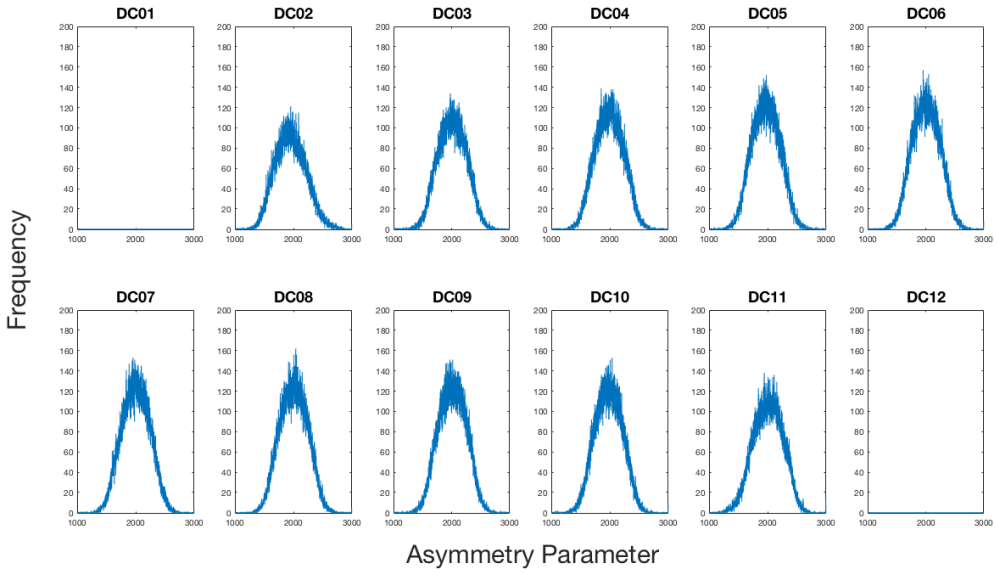

Figure 4.25: Figure showing the asymmetry distributions for the absorber DC strips. DC01 and DC12 have no distributions as they are edge strips.

Parametric Z-PSA

Unlike XY-PSA, Z-PSA utilises the time it takes for the charge carriers to traverse to the detector electrodes to produce the real signal. The time it takes to reach the electrode will vary depending on the location of the interaction within the crystal. This difference in time will be reflected in the induced signal.

Z-PSA was only implemented for the absorber detector, as the 20 mm depth leads to the largest degree of positional uncertainty. Z-PSA for the scatterer is currently in development to further improve the position sensitivity. It is currently difficult to implement these techniques in the scatter detector due to its smaller depth in comparison to the absorber detector. Because of this, it is difficult to identify significant differences across the depth of the scatterer, and therefore it can't be divided accurately into smaller sections.

Z-PSA is largely dependent on the *risetime* of a preamplifier pulse. The rise-time is a term which describes the time it takes for a signal to reach a particular percentage of its amplitude. A 1 μs sample of the preamplifier pulse is taken focusing on the area of the pulse where it reaches its full amplitude. The preamplifier pulse is shown in Figure 4.26. Only 0.5 μs of the sample is shown in this figure to improve the clarity of the image.

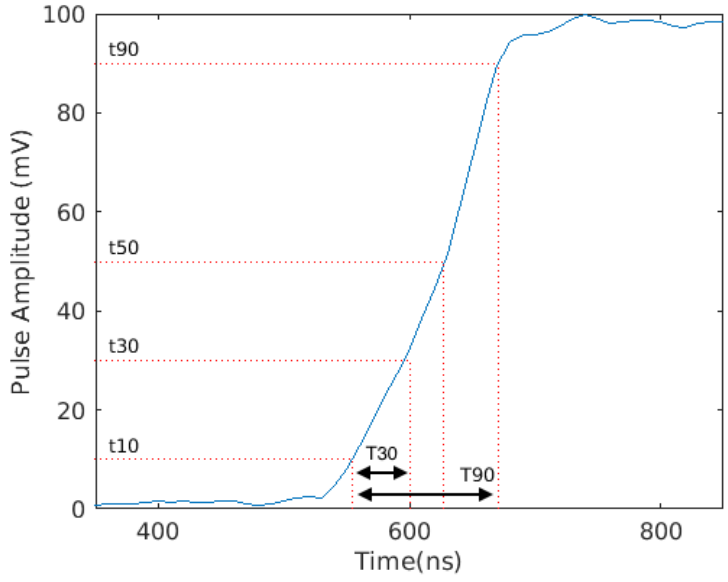

Figure 4.26: Diagram of the risetime of a pulse reaching 10 %, 30 %, 50 % and 90 % of its full amplitude. The time it takes for the pulse to rise from t10 to t30 is referred to as T30, likewise the time it takes to rise from t10 to t90 is referred to as T90.

From this sample, the time it takes for a pulse to reach 10 %, 30 %, 50 % and 90 % of its full amplitude can be determined, also shown by Figure 4.26. This 1 μs segment of the pulse is also what is utilised for the BLD algorithm as stated in Section 4.2.2.

The difference between 90 % of the pulse amplitude (t90) and 10 % of the pulse amplitude (t10) is chosen over the true beginning and end of the pulse. This is because these values provide a better reflection of the true signal, allowing the charge collection time to be determined with less uncertainty, and reducing the signal-to-noise found at the baseline and magnitude of the signal. Other risetimes are calculated relative to t10, as shown:

$$T90 = t90 - t10 \tag{4.4}$$

$$T50 = t50 - t10 \tag{4.5}$$

$$T30 = t30 - t10 \tag{4.6}$$

Three techniques for determining the Z-position of the interaction were investigated to find which produced the greatest improvement in image resolution [85], with the methodology of the three techniques explicitly detailed. A summary of the three techniques is found below.

Z-PSA1 - T30 vs T90 gates

The absorber detector can be divided into volumes dependant on the risetime values. The depth of the absorber could be split into three discrete sections, with a gamma-ray interaction of an unknown position localised to one of the three sections by analysing the risetime of the preamplifier signal.

The T30 risetimes across each mm depth were determined, however, it was difficult to divide it further due to the similarity of signals and a lot of overlap between depths. Therefore, rather than utilising a single risetime to represent a single mm position, grouped distributions could allow for segmentation.

From this, the three sections of the detector depth were segmented into 1 - 4 mm, 5 - 13 mm and 14 - 20 mm. Further precision could be deduced from applying the same technique to the T90 risetimes. The three sections were segmented to 0 - 7 mm, 8 - 14 mm and 15 - 20 mm.

Using these gates for the T30 and T90 risetimes, a plot of the T30 risetimes against the T90 times produces a characteristic 'tick' distribution from the areas of higher intensity, as shown in Figure 4.27 for both the AC and DC faces. The figure shows four plots of the T30 v T90 risetimes for a single

absorber AC strip. The first plot shows the full set of T30 vs T90 risetimes across the entire depth of the absorber detector. The additional three show how the risetimes can be segmented into regions which represent a grouped depth position, shown by the areas of higher intensity. An interaction in an unknown position within the absorber can therefore be compared to the various regions shown in Figure 4.27 to determine an interaction position.

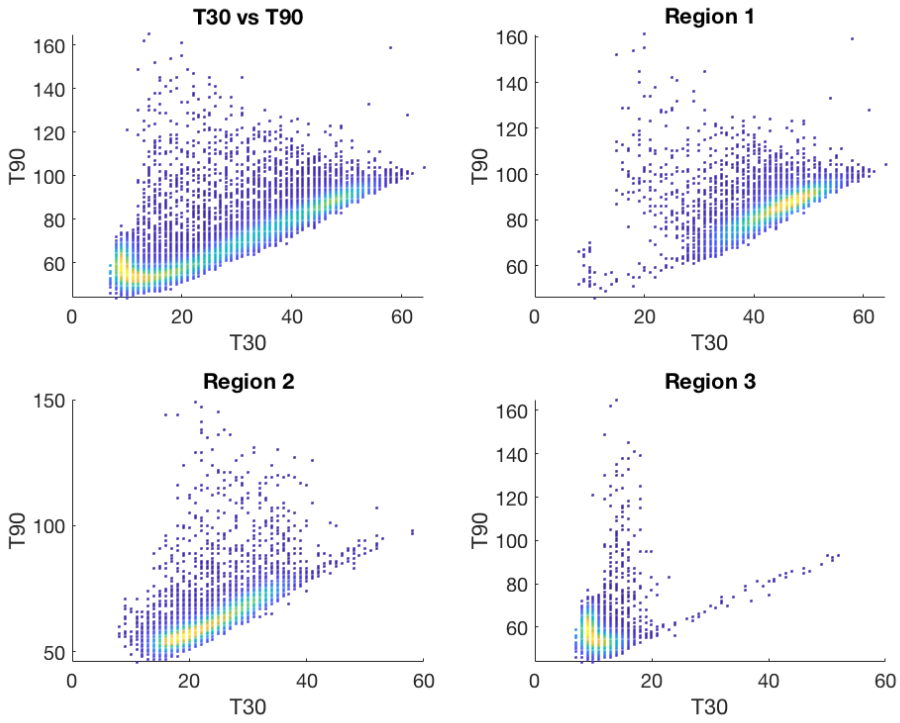

Figure 4.27: Plots of the T30 vs T90 risetimes for a single absorber AC strip, reproduced from [85]. The first plot shows the full set of risetimes across all depth distributions, with the additional three comparing the regions of risetimes that represent three detector depth locations.

Z-PSA2 - Risetime correlation

A disadvantage to Z-PSA1 is the ability to only segment the absorber depth to three different segments due to the imprecision of separating risetimes at smaller depths. If the absorber depth could be divided into more sections, improving upon the three determined by the Z-PSA1 technique, this would further improve the position sensitivity of an event.

To try and improve upon this method, the risetimes collected on one face of

the absorber detector were compared to the risetimes collected on the opposite face. If an interaction occurs closer to one face than the other, there will be a difference in the charge collection time due to the amount of distance travelled within the crystal. This will be reflected in the T30 and T50 values.

The T50 values measured at the DC side were subtracted from the T50 values measured at the AC side, and likewise with T30 values on an event by event basis. A correlation was observed between the subtracted values and the depth of the absorber detector as shown in Figure 4.28. The figure shows two plots of the T30 subtracted values and the T50 subtracted values. This correlation can be gated upon to segment the absorber into five different sections; 1 - 4 mm, 5 - 8 mm, 9 - 12 mm, 13 - 16 mm and 17 - 20 mm. This method allows for a more equal segmentation of the absorber detector compared to Z-PSA1.

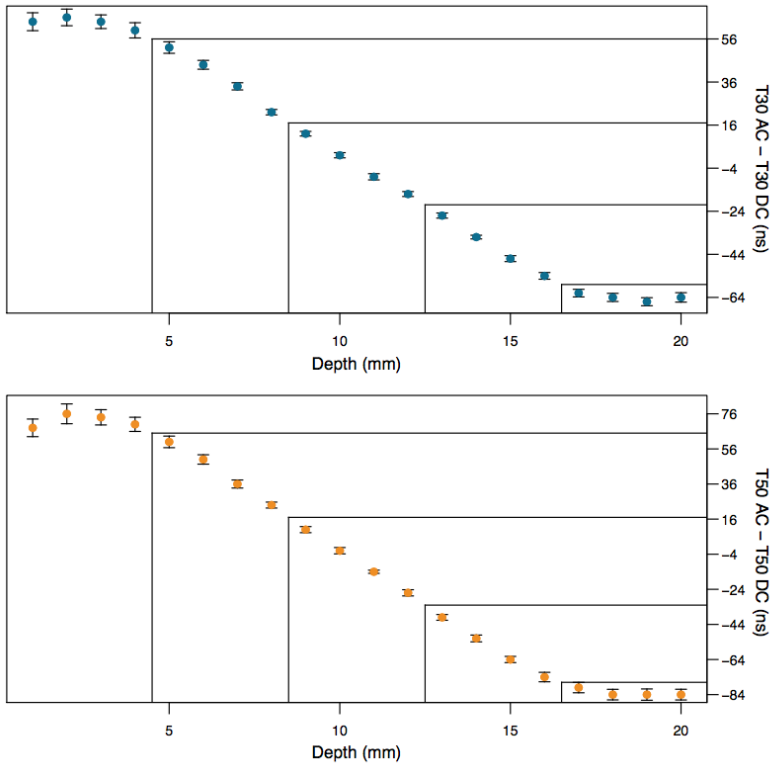

Figure 4.28: Plots showing the T30 AC -T30 DC (top) and the T50 AC - T50 DC (bottom) distributions. Reproduced from [85]. Due to the correlation between the values and the absorber depth, the plot can be divided into five sections as shown by the additional lines.

Z-PSA3 - Chi-squared Minimisation

The final method estimates the position of an interaction by comparing the risetime of the event to known risetimes at each depth in the detector. The absorber detector had been previously mounted on a scanning table, utilising a 1 GBq collimated ^{137}Cs source to create a $60 \times 60 \times 20$ matrix at 1 mm increments of known detector responses, to create a relationship between interaction position and the signal risetime produced [77].

The average risetimes, including T30, T50 and T90 values on the AC and DC faces, could be plotted at 1 mm increments as determined from the scan. The average AC and DC risetimes for the different depth positions is shown in Figure 4.29.

When an interaction takes place in an unknown position, the risetime of the signal is then compared to the average values as shown in Figure 4.29 using a chi-squared minimisation method. From this method, a best estimate can be determined to identify the depth of the interaction. This method is able to provide a position resolution of 1 mm in the z-depth as the pulses arise from the 20 increments from the collimated scan.

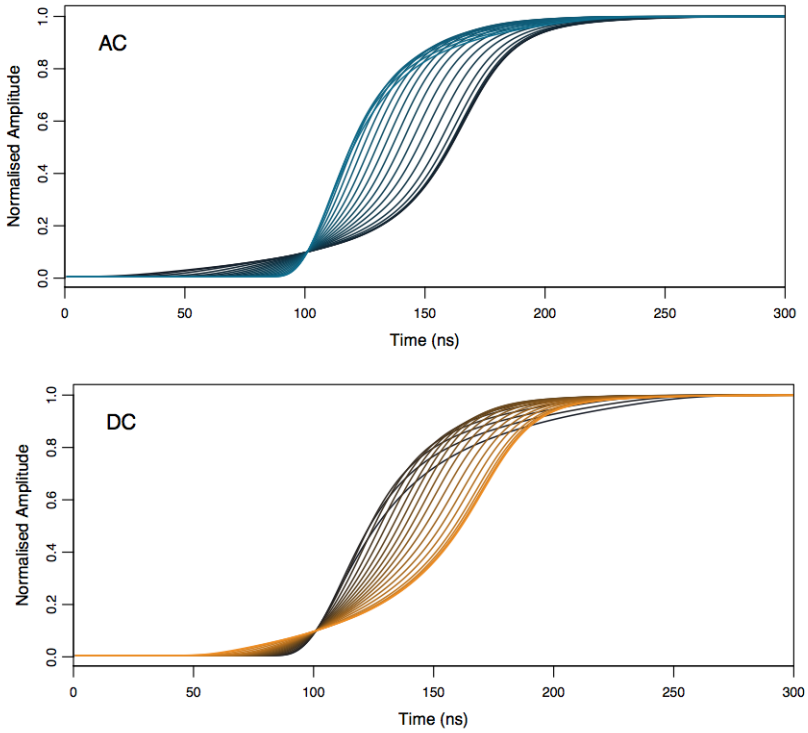

Figure 4.29: Figure showing the average AC and DC pulses from each 1 mm step through the detector depth. Reproduced from [85].

This method was found to be more sensitive within the main bulk of the detector crystal. The interactions that occur close to the AC or DC faces (1 - 3 mm and 18 - 20 mm depths) have slight deviations in the risetimes, and are therefore difficult to differentiate, as can be seen from the thicker lines shown on Figure 4.29 showing the overlap of depths.

The effect of the three different PSA techniques on the quality of the produced images is found in Section 5.2.

4.5 Image Reconstruction

After the experimental data has been processed, the sortcode used in Section 4.4 produces text files which detail the x, y and z positions of interactions within the two detectors, and the energy deposited at those interactions. These positions are described on the Z-coordinate plane, where Z = 0 is the back of the absorber crystal (as seen in Figure 4.30a).

These parameters are what is required for image reconstruction. Two image reconstruction algorithms are utilised which interpret the data collected from GRI+ to produce Compton images. The analytical code is a filtered back-projection technique which is the basis of the majority of reconstructed images used in this thesis. The second is a maximum-likelihood expectation maximisation (MLEM) iterative code.

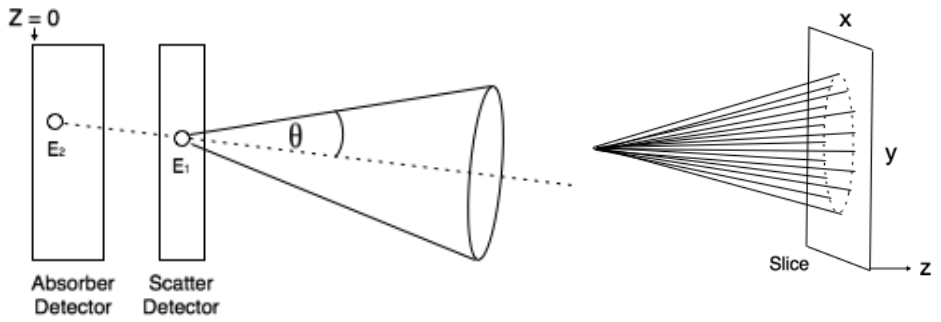

Figure 4.30: Schematic diagrams showing (a) how a Compton cone is produced from the points of interaction between the two detectors and (b) Projection of the Compton cone onto a slice. The cone is divided into a given number of points per angular degree of the cone.

4.5.1 Analytical Code

An analytical image reconstruction algorithm designed at the University of Liverpool [86] was utilised for the reconstruction of Compton data from simulations or experiment, utilising the methodology of back projection of cones.

Using the positions from the text file, the analytical code uses trigonometric relationships to produce a cone, which is projected into the imaging space. The two points of interaction between the two detectors forms the vertex of a cone as shown in Figure 4.30a and the angle θ representing the angle from Compton scattering as described by Equation 3.32, and E_1 and E_2 represent the energy deposited in the respective detectors.

As can be seen from Figure 4.30a, inaccuracy on the position of interactions within the detectors will lead to the incorrect reconstruction of the Compton cone. Any significant uncertainties on the x, y and z positions will therefore degrade the image quality. This is why the development of PSA techniques as detailed in the previous section is important for Compton imaging.

Once the cone has been constructed, the radioactive source can be identified anywhere along the annulus of the cone. With multiple interactions, more cones are produced. The location of the radioactive source can be located where the cones overlap. Cones can either be projected into a 3D imaging space, such as a cube, or alternatively onto a spherical surface [87] as shown in Figure 4.31.

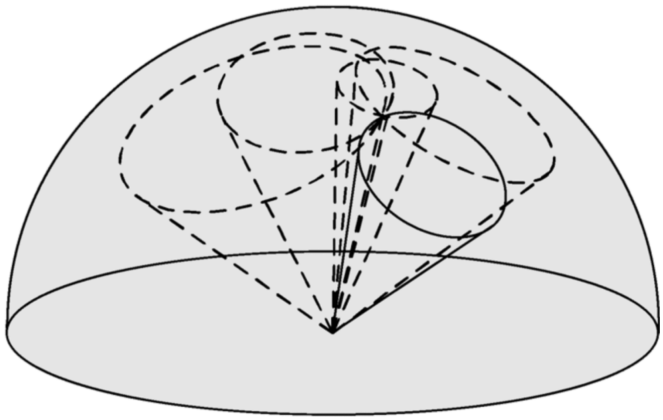

Figure 4.31: Figure showing multiple Compton cone projections onto a unit sphere [88].

The disadvantages of the previously mentioned techniques are that the 3D cube imaging space is very intensive computationally, and is therefore a time-consuming process. Projecting onto the spherical surface does not provide

any information on the distance of where the source is located, which is a requirement in decommissioning scenarios.

Therefore for the analytical reconstruction code, the cones are projected into a 2D cartesian imaging space of which a *slice* can be taken at a given Z-position, as shown by Figure 4.30b. The Z-position of a slice differs from the source-to-detector distance. Whereas the source-to-detector distance measures the distance between the source and the face of the scatter detector, the Z-position is relative to the back of the absorber crystal. This Z-position will therefore change if the separation between the cryostats is altered.

In this work, the source-to-detector distance is known from the experimental set-up of the measurements. This distance is then translated into a Z-position based on the information detailed earlier. However, in scenarios where the location of the source is unknown, then a different technique can be utilised to determine the optimum Z-slice to use for imaging. The maximum number of cone overlaps in individual slices can be analysed over a range of distances, with slices being analysed at 1 mm precision. The location of the greatest overlap can provide an indication of an estimated source location. This method does not work at standoff distances of more than 30 cm however [89].

The images are reconstructed using a Filtered Back Projection (FBP) algorithm. FBP utilises a combination of unfiltered backprojection and ramp filtering procedures. Standard backprojection of profiles leads to blurring or the prescence of artefacts within an image. The ramp filter is a type of high-pass filter that is able to remove blurring from an image by removing low-frequency statistics. Therefore, the filtering of each profile modifies the information to produce a sharper image [90]. The profiles received from data acquisition are referred to as *forward projections*.

If a slice through imaging space is taken, according to the Z-position or the source-to-detector distance, then a 2D image will be produced showing the number of cone overlaps. This image is known as the *Compton Image* (Figure 4.32a).

The quality of the data shown in Figure 4.32 can be improved by altering parameters that can be varied in the imaging application interface [91]. Figure 4.33 shows a screenshot of the user interface.

Firstly, as shown in Figure 4.33, is which type of reconstruction algorithm the user would like to use. This gives the option of the analytical reconstruction or alternative iterative reconstruction algorithms.

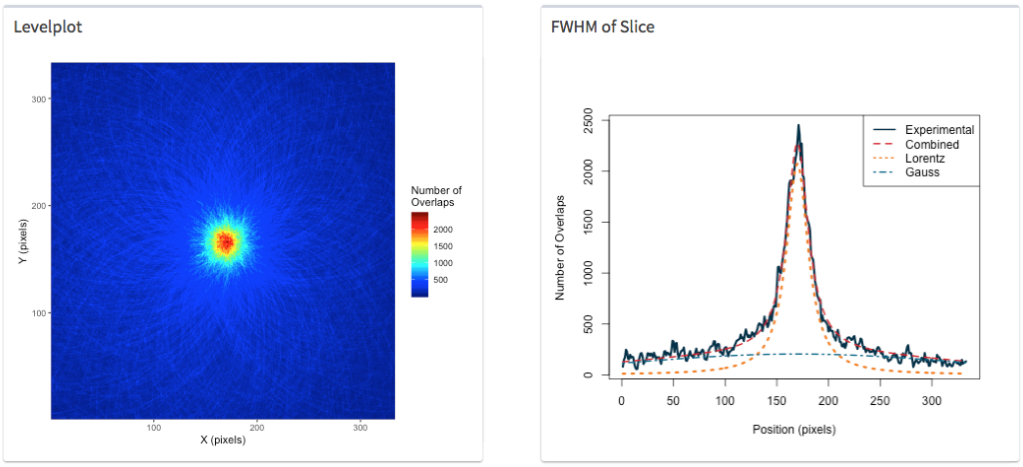

Figure 4.32: Screenshot showing the reconstructed image matrix and intensity profile, along with application of a combined Gaussian and Lorentzian fit to determine the FWHM from the imaging application.

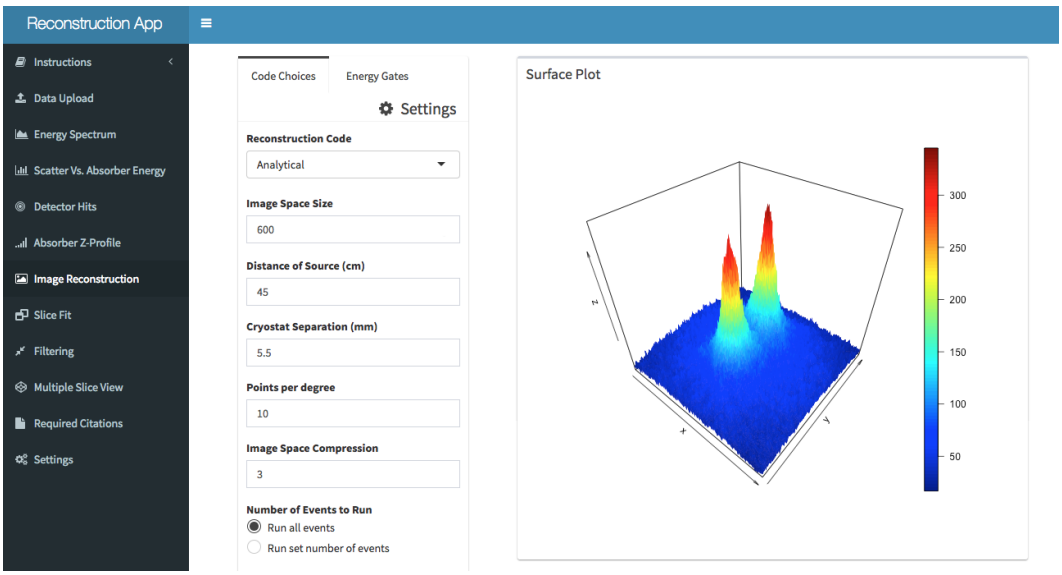

Figure 4.33: Screenshot of the application used to implement the analytical image reconstruction code [91].

The **image space size** defines the size in pixels in the X and Y directions for the reconstructed image. The larger the image size, whilst taking slightly longer in time to reconstruct, provides a better description of the background.

The **distance of source**, if known by the user, is also input here. As described earlier, this is then translated to a Z slice in which the reconstructed image is shown.

The **cryostat separation** is also known by the user, based on the geometrical set-up of the detector system as described in Section 4.1. This value is set as 5.5 mm for the measurements in this thesis, based on Table 4.1.

The following parameters can help improve the quality of the reconstructed image:

Points per degree - The algorithm moves around the cone in 1 degree increments (Figure 4.30b). At short standoff distances, these points look like a continuous line, but at larger standoff distances, then the separation between points is clear, and therefore the point of overlap between cones can be difficult.

Image Space Compression - Also known as compression factor. The number of mm per bin can be changed to help group events

Energy Gate - An upper and lower-energy threshold can be applied to the 'sum energy' which is the total energy deposited in the system (whether it is two or three tiers).

The imaging application also allows the user to see a slice through the 2D image, through the point in which the maximum number of cone overlaps is found in X and Y. Depending on the source being imaged, a fit can be applied to the slice to determine the FWHM of the image. Producing this fit is important as the point with the maximum number of cone overlaps should occur where the source position is. This can allow the identification of the source position in X and Y. As described in Section 3.3.2, a combined Lorentzian and Gaussian fit is applied to the image slice as shown in Figure 4.32.

The imaging application can also implement the use of additional frequency filters to the reconstructed image. High-pass and low-pass filters are commonly used in image processing to reduce noise and enhance the quality of the image.

The filter of most benefit to the reconstructed Compton images is the high-pass filter (HPF). This is because the true source will have a high-frequency of cone overlaps, whereas the lower number of cone overlaps are seen as low-frequency. The HPF can therefore remove these low-frequency overlaps to focus on the true signal. This must be optimised to avoid the presence of any artefacts

within the image. This is achieved by the user applying a cutoff frequency. Signals that pass this cutoff frequency value will be included in the image, with any signals with frequencies lower than this value attenuated.

The optimum parameters to be used for the image reconstruction are described in Chapter 5. The effect of the HPF on the quality of the reconstructed images is also found in Section 5.2.1.

4.5.2 Iterative Code

Similar to the analytical code, the iterative code analyses the output text file produced from MTSort. The parameters that are described in the previous section are again defined by the user before reconstructing the image.

The iterative reconstruction code used is a Maximum Likelihood Expectation Maximisation (MLEM) method [92]. It is implemented in C++ and uses ROOT. ROOT is an open-source data analysis software that can allow for the evaluation of large sets of data [93]. Its principle is to find the ideal image through sucessive estimates.

The first step of the MLEM code is to produce an initial primary image which is comparable to the image reconstructed using the analytical code. This is considered to be the first estimate. A sequence is then started for the first iteration. The iterative code can include the physics of the detector system through a system matrix. The initial estimate is given by allocating, with equal likelihood across the system matrix, a set of forward-projected cones through the imaging-space to create artificial data. The sytem matrix describes the relationship between the image space and the projection space. Each element of the system matrix is given equal probability of detecting the incoming photon. The uniform system matrix could be problematic when investigating sources of the same activity, or distributed samples. These problems will be explored in this thesis in Section 5.2.2.

This data is then correlated to the measured data and subsequent corrections are made by calculating the difference between the previous estimate, and the true projection data. This difference is also included in the new estimate and repeated for all events in the user assigned array (for example $500 \times 500 \times 500$ pixels). Successive estimates are then taken to give a projection of the initial object.

The user can define the number of iterations to take place, however this can take a lot of computational time. The total number of events and the defined

imaging space can also largely affect the time it takes for the iterations to be constructed.

Unlike the imaging application which has been created for the analytical code, there is no direct image output from the iterative algorithm. The outputs from the iterative code does not provide a detailed image matrix nor intensity profiles. Instead, the files are read by the ImageJ software [94], which can produce a version of the output that can used with Matlab for further analysis and visualisation.

Chapter 5

Results and Analysis

In industrial measurement environments, such as those detailed in Section 2.3.1, Gamma Imaging systems are required to collect data at large standoff distances (1 - 5 m) and in the presence of scattering material such as concrete. This thesis will investigate the feasibility of using the GRI+ Compton Camera in measurements similar to those described earlier, and identify if there are any limitations from imaging and analysing ^{137}Cs data with scattering media or at large standoff distances.

As stated in Section 4.4.2, the measurements were split across two locations on the University of Liverpool Campus. The measurements summarised below took place at the Oliver Lodge Laboratory, University of Liverpool, as a basis for measurements due to the low levels of background radiation.

^{137}Cs Point Source Measurements

A set of measurements with two ^{137}Cs point sources of similar activity at varying separations, and two ^{137}Cs point sources of different activity at varying separations took place to evaluate the imaging performance of GRI+ at a defined distance, and the response of the system where the extended source will be located.

^{137}Cs Extended Source Measurements

Measurement of a ^{137}Cs non-uniform distributed sample at a defined distance, with and without the presence of scattering material in the form of a concrete wall. Industrially relevant for contamination scenarios.

Ingress of radiation in concrete

Measurements with a high-activity ^{137}Cs point source with varying thicknesses of concrete material, to determine if the thickness of material the radiation has attenuated through can be identified. Industrially relevant for contamination

scenarios.

The benefit of having GRI+ on a cart system allowed for the first set of measurements to be taken 'offsite'. This was to test the ability of GRI+ to work as a fully standalone system, as well as to assess how the system would perform after transferring to a new location. The new location was at the Central Teaching Laboratory, University of Liverpool, in a room which contained a significant amount of background radiation due to the presence of two high-activity AmBe neutron sources and multiple laboratory-standard gamma sources. The measurements that took place in this campaign are summarised below:

^{137}Cs Point Source Measurements at a large standoff distance

Point source measurements at varying standoff distances allowed for the angular resolution of GRI+ to be investigated, as well as the overall ability of GRI+ to measure radioactive sources at a maximum distance of 2.5 m.

Effect of background radiation on measurements

Repeat of a selection of the measurements taken in the first data campaign to identify if the larger level of background radiation has had a significant affect on the quality of results, by comparing them with the previous set of data.

Detailed descriptions of each measurement will be explained further in the relevant sections of this chapter.

5.1 Experimental Procedure

The response of the detector system over a range of positions was investigated, due to the requirement of gamma imaging systems being able to collect data at a large range of standoff distances. The measurements detailed in this thesis involved the positioning of point and extended ^{137}Cs sources between the range of 44 cm and 250 cm away from the scatter detector face. Due to the frame of the cart system, if it was pushed against something, such as a wall in an offsite measurement, then 44 cm is the minimum achievable source-to-detector distance to measure a source of contamination. This set-up is shown in Figure 5.1.

A platform was used as the basis for measurements in the campaign. The cart was pushed as close to the platform as possible, allowing for the edge of the platform to align with the source-to-detector distance of 44 cm. The platform was also used as a stable stand to support multiple concrete bricks for the scattering experiments, and to also help align sources to the y = 0 position. Sources were positioned 20.7 cm above the surface of the platform to allow it to align with y = 0 as shown in Figure 5.1.

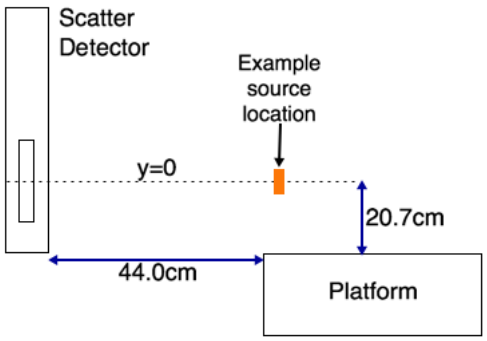

Figure 5.1: Schematic diagram of where sources are positioned relative to the scatter detector face.

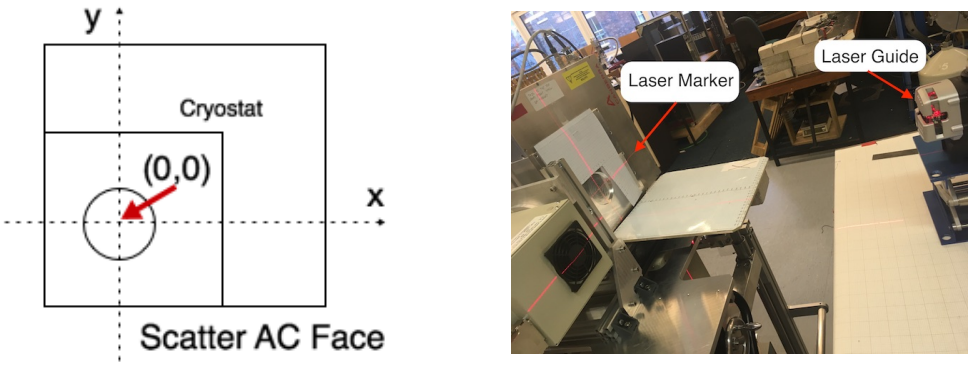

(a) (b)

Figure 5.2: (a) Schematic diagram showing the cartesian co-ordinate system relative to the scatter detector face (b) Photograph of the laser guide in the intended position of a point source, and aligning it to the central axis of the scatter detector.

In the reconstructed imaging space, the (x, y) coordinates of the centre of the scatter detector face are defined as (0, 0) as shown in Figure 5.2a. Reconstructed images are then created with the centre of the image also being (0, 0). This central position of (0, 0) is found to produce the maximum imaging

efficiency [95], so sources are usually positioned at (0, 0) for this reason. Positioning sources here also has the added benefit for allowing the inclusion of additional objects on the reconstructed images by positioning them relative to (0, 0). This is seen in images where the scatter detector face, or the concrete wall have been overlaid onto the image.

Due to measuring at a minimum standoff distance of 44 cm, aligning to the central axis could lead to a significant positional uncertainty. Therefore a laser guide was used to make sure any sources were placed as close to the origin of (0, 0) as possible (Figure 5.2b).

Once the sources were in position, the MIDAS data aquisition parameters were set. Firstly, the MWD parameters that were detailed in Table 4.3 are applied to the V1724 digitisers to provide the energy in data collection. The V1495 settings are also applied, with the coincidence window of 325 ns set, the AC sides for the two detectors were defined as the triggers, and the readout mode was set as *output as all masked channels*.

Once the measurement has started, the data collection can be monitored through an online, live analysis of the data. Through this live analysis, the measurements can be supervised to check that nothing is going wrong with the data acquisition. To check that the DAQ system is functioning as it should be, the readout of all 48 strips (if utilising the coaxial detector) is checked. In *output as all masked channels* mode, all 48 strips should be recording data. If this number is less than 48, then an issue during the data acquisition can be identified.

If the data acquisition is running smoothly, we can obtain a realtime readout of spectra. By observing the coincidence energy spectra, identification of radioactive sources present in the measurement can be achieved in a short space of time, depending on the activity of the source (a couple of minutes for kBq sources). Determining if there is a sufficient amount of events to be used for image reconstruction can also be done by observing the net areas of full-energy peaks of interest in these coincidence spectra. An amount of 10, 000 counts in the 662 keV full-energy peak region was required for all the measurements recorded in this thesis, as a minimum statistical value in order to obtain high-quality reconstructed images

Post-analysis of the data through the MTSort program produces output text files which contain the x, y and z positions of interactions, and the energy deposited at those interactions. This can then be inserted into the analytical image reconstruction application (Figure 4.33).

Knowledge of the source-to-detector distance is required in order to reconstruct the image. The distance is translated to a Z-slice from the sortcodes, as Z = 0 is the back of the absorber detector crystal, and source-to-detector distances are measured from the front of the scatter detector face. For the measurements described in this chapter, the source-to-detector distance is known. This can be an issue however for characterisation scenarios when there is radiation in an unknown location.

As mentioned in Section 4.5.1, this can be resolved my taking multiple slices across a range of distances where the source is predicted to be. This method was first discussed here [89], where the optimium slice in the Z-direction can be determined through observing the pixel with the maximum number of cone overlaps for each slice. This method is implemented in the imaging application and has been tested for near-field measurements. However, this method has not been investigated for extended sources, or through the attenuation through material.

A quick investigation of this method at large standoff distances found that the estimated position was always a significant underestimation that fell within the region of 25 - 35cm, no matter the source-to-detector distance. Further optimisation of the process is therefore required before this method can be used to determine the source-to-detector distance for image reconstruction in an industrial setting.

As stated in Section 4.5.1, the following parameters can affect the quality of the image produced; the applied energy gate, compression factor and points per degree.

Figure 5.3 shows the coincidence energy spectrum produced from a 15.7 MBq ^{137}Cs source positioned 68 cm away from the scatter detector face. The coincidence spectrum shows all the fold [1 1 1 1 0] events which can be utilised in the image reconstruction of a ^{137}Cs source, without any PSA techniques implemented. By applying an energy gate around the full-energy peak of interest, in this case the 662 keV full-energy peak from ^{137}Cs, the source can be located.

The width of the applied energy gate is important, as having it too narrow ($\pm$ 1 keV) around the energy of interest can lead to a lack of statistics and a poor quality image as there will be fewer cone overlaps. Alternatively, having too wide a gate ($\pm$ 20 keV) can lead to events that are not of interest in the reconstructed image, leading to a larger image resolution. By observing the coincidence energy spectrum, a sensible energy gate can be applied which incorporates the events within the full-energy peak of interest.

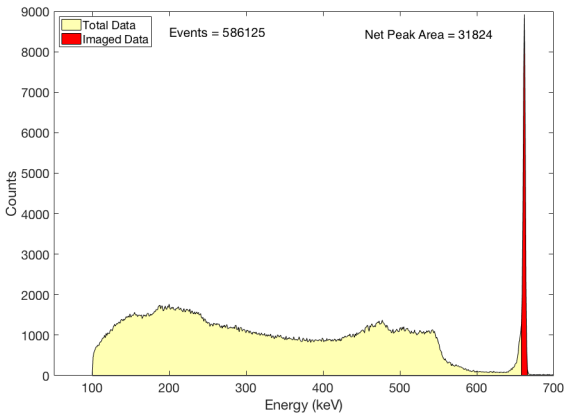

Figure 5.3: Spectrum showing what events are used in a reconstructed image when an energy gate is applied to the sum energy. The red part shows what events are selected for the image, where the lower and upper energy thresholds were 658 and 666 keV respectively.

Figure 5.4a shows the reconstructed image produced when no energy gate is applied and all the events in the spectrum are used. As can be seen, there is a lack of clarity in the image that is produced. Whilst a source can be observed, it is not truly localised. If a profile of this image slice was to be found, it would be difficult to state the source location due to a large signal-to-noise, making it difficult to discriminate the true source position.

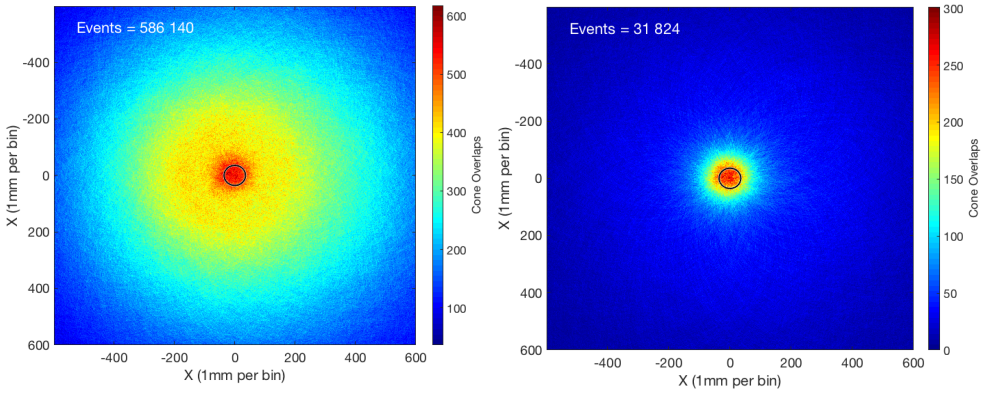

Figure 5.4: Comparison of the analytical image produced from a ^{137}Cs point source positioned at a distance of 68 cm, utilising fold [1 1 1 1] events and without any PSA techniques applied. The images show (a) without and (b) with an energy gate applied between the energies 658 - 666 keV for a 662 keV full-energy peak. The number of events used for each reconstruction is shown in the top-left of each image. The black circle in the centre of each image represents the size of the scatter detector face relative to the image. The compression factor is 1 mm/bin.

As shown in Figure 5.4b, when the energy gate is applied the events selected in the image reconstruction are solely from the full-energy peak. The upper and lower thresholds for the energy gate where chosen to utilise as many full-energy events as possible. Because of this, the lower and upper energy thresholds applied were 658 and 666 keV respectively. Applying an energy gate is also beneficial when multiple different radioisotopes are present.

For image reconstruction, the default compression factor of 1 mm/bin is usually assigned for measurements at a short standoff distance (less than 30 cm). At these larger standoff distances however, a compression factor of 1 mm/bin is undesirable as there is a limited number of statistics available for image reconstruction. With multiple sources, this can make the data too dispersed, and therefore difficult to distinguish the presence of multiple sources.

Whilst we can discern from Figure 5.4b that a source is present, the number of counts divided across the multiple pixels can leave a noisy image slice, as shown in Figure 5.5a. The large fluctuations in the slice can make it difficult to determine where the true centroid position is located, and as a result, the location of the radioactive source relative to x and y.

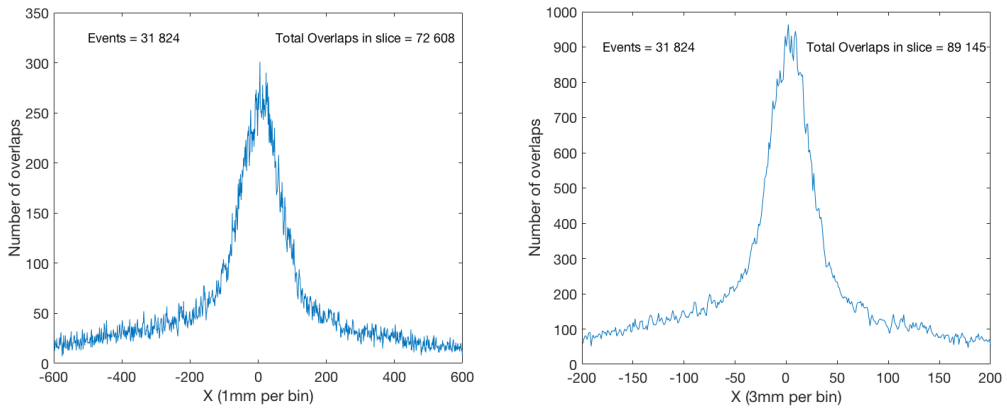

(a) (b)

Figure 5.5: Intensity profile produced from a slice of an analytically reconstruced image of a ^{137}Cs point source, utilising fold [1 1 1 1] events and without any PSA techniques applied. a) The slice with a compression factor of 1 mm/bin b) The slice with a compression factor of 3 mm/bin.

By increasing the compression factor value, data points will be assigned to wider bins. This causes a smoothing to the profile, as shown by Figure 5.5b, which shows the difference when the compression factor is increased to 3 mm/bin. The number of events for the image remains the same, however

there is an increase in the number of cone overlaps found in that image slice, shown by the y-axis values in Figure 5.5.

Figure 5.6 shows how the maximum number of cone overlaps found in an image slice, such as those seen in Figure 5.5, varies with the percentage of events used to reconstruct the image. The graph is a result of changing the percentage of gated events shown in Figure 5.4b. How the number of cone overlaps change with the compression factor of the image is also observed. As can be seen from Figure 5.6, a linear relationship can be observed between the two.

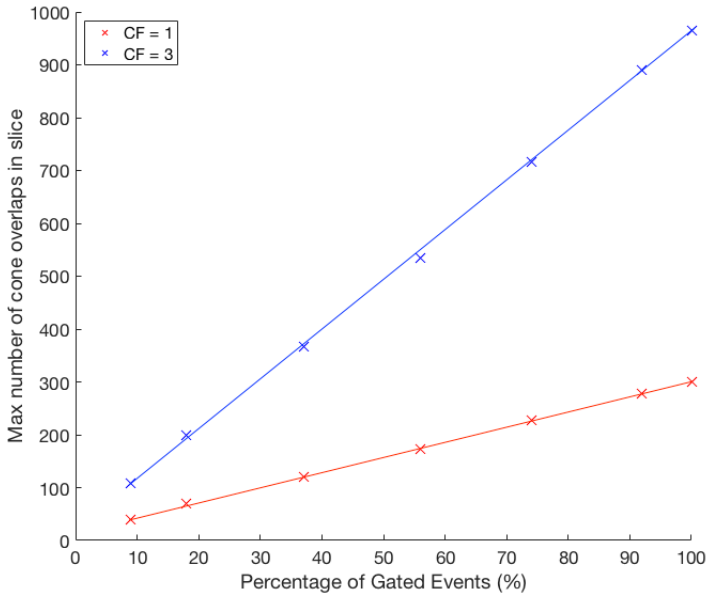

Figure 5.6: Graph showing the linear relationship between the number of events used in the analytical image reconstruction, and the maximum number of cone overlaps found in that image slice for compression factors of 1 and 3 mm/bin. The results were obtained from the analytical reconstruction of a ^{137}Cs point source positioned 68 cm away from the scatter detector face. Fold [1 1 1 1] events were used without any PSA techniques applied.

Therefore, it can be assumed that the more full-energy peak events that are obtained during a measurement, the increased number of cone overlaps will be seen in the reconstructed image. By having a higher number of cone overlaps, a higher quality reconstructed image will be produced.

As explained in Section 4.5.1, the number of points per degree (PPD) can also affect the quality of the image resolution. At larger standoff distances, the overlaps of cones when set to the default parameter of 1 PPD is rare, resulting in an imprecise representation of where the radiation 'hotspot' is. Therefore, by assigning more points per degree of the cone, there is an increased

probability that overlaps of cones will be observed at large stand off distances, as shown by Figure 5.7.

There reaches a point however, where increasing the PPD beyond a value of 10 makes little difference to the quality of the image. Similarly, at shorter standoff distances, increasing the PPD does not have a significant affect on the quality of the image. Therefore, it is recommended to use a value of 10 points per angular degree for measurements beyond 30 cm.

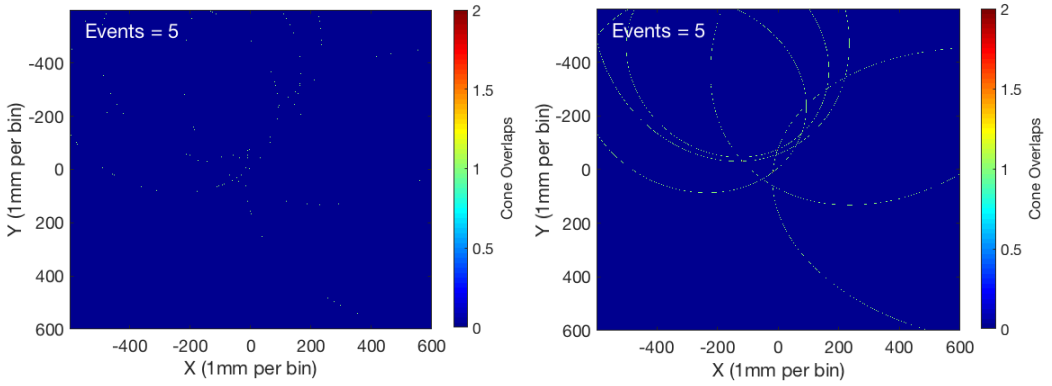

(a) (b)

Figure 5.7: Image reconstructions showing the same 5 events but with a PPD values of a) 1 point per degree and b) 10 points per degree. The more points per angular degree of the cone leads to an increased chance of a cone overlap at large standoff distances.

A summary of the parameters selected for the analytical reconstruction of data is shown in Table 5.1.

Table 5.1: Parameters applied for the analytical image reconstruction through the imaging application.

Parameter	Value
Distance of source (cm)	68
Cryostat separation (mm)	5.5
Points per degree	10
Compression Factor (mm/pixel)	3
Image Space Size (pixels)	400×400
Lower Energy Threshold (keV)	658
Upper Energy Threshold (keV)	666

Apart from the *Distance of source* parameter observed in Table 5.1, the remaining variables remain unchanged for the other analytically reconstructed

images in this chapter, unless stated otherwise. The source to detector distance is translated to a Z co-ordinate value through defining the cryostat separation, as the software will define that Z = 0 lies at the back of the absorber crystal.

For each measurement, a table detailing the breakdown from the initial interactions recorded in the detectors to the events used in the image is included, similar to that seen in Table 4.6. The number of incident gamma rays on the scatter detector face is also incorporated in these tables. These are calculated by determining the solid angle of the source subtended onto the scatter detector face. The methods for calculating these values for multiple sources is described in Appendix C.

5.2 ^{137}Cs point source analysis

In an industrial setting, the radiation that is to be measured will follow a more complex distribution, compared to calibrated laboratory point sources as detailed in Section 2.3.1.

Because of this, a non-uniform ^{137}Cs extended source, of length 18 cm, was used to investigate the Compton Camera's ability to measure distributed radiation at larger standoff distances and with the presence of scattering material. Extended sources have been previously used with the ProSPECTus and GRI+ [75, 85, 96] . However these investigations have taken place within 30 cm of the scatter detector face and without scattering material. Therefore, it was important to evaluate the system's capability of not only measuring multiple sources of the same radioisotope, but also of different activity at larger standoff distances.

The response of the GRI+ Compton Camera at different positions away from the central position of (0, 0) was investigated using point sources before measurements with an extended source could take place. It has been demonstrated that the response function of the imaging system varies across the imaging space [95]. However, as this investigation was within near-field distances (less than 30 cm), it was necessary to evaluate the system's response at this new standoff distance.

- Two ^{137}Cs point sources of similar activity at varying positions.
- Two ^{137}Cs point sources of different activity at varying positions.

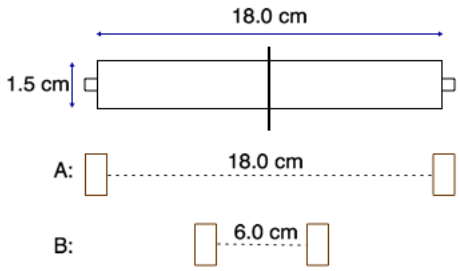

Figure 5.8: Schematic diagram showing the dimensions of the ^{137}Cs extended source, and the positioning of the two point sources for the measurements, relative to the length of the extended source. A and B show the positions of the sources for the different measurements.

With the central axis at x = 0, and the length of the extended source being 18 cm, the two point sources were first placed at x = -9 cm and x = 9 cm (Figure 5.8A), and then at a position closer to the central axis at x = - 3 cm and x = 3 cm for the second set of measurements as shown in Figure 5.8B at a standoff distance of 45 cm. By observing the response of the imaging system at these positions, it can provide confidence in GRI+ describing the geometry of extended sources.

5.2.1 Sources of similar activity

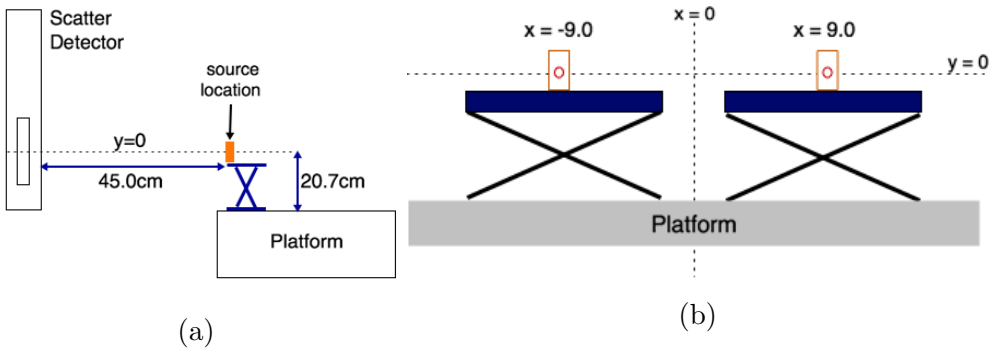

Figure 5.9: Schematic diagrams showing the experimental set-up of two ^{137}Cs sources of similar activity. (a) Side view showing the source-to-detector distance of 45 cm (b) View from the scatter detector face, with the sources positioned relative to x = 0.

Two ^{137}Cs point sources, of activity 0.23 and 0.27 MBq respectively were positioned as described in the schematic diagram shown in Figure 5.9, with the sources placed at x = ± 9 cm, with Figure 5.10 showing photographs of

where the sources were positioned. Figure 5.10a shows how the source was aligned to y = 0 as mentioned at the beginning of this chapter. The bottom of the red tape represented the height of 207 mm.

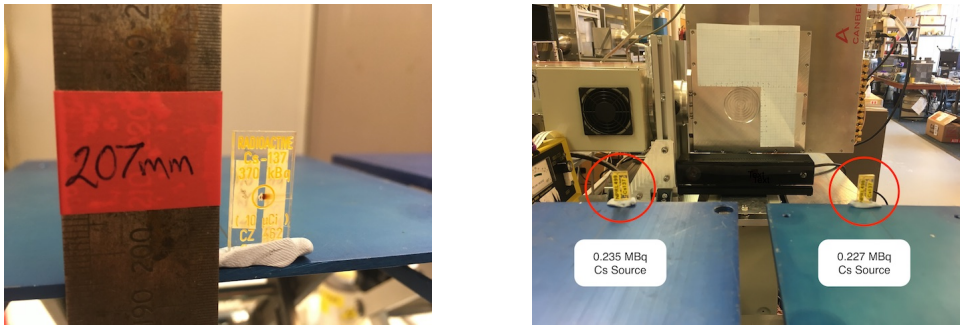

(a) (b)

Figure 5.10: Images showing the experimental set-up of two ^{137}Cs point sources, both with activity approximately 0.3 MBq. (a) Aligning the height of the source to y = 0 (b) Position of the two sources at x = - 90 mm and x = 90 mm to show the extremes of the soil sample at a distance of 45 cm.

Data[1] was collected over a period of almost 30 hours, with 1.09×10^9 gammas incident on the scatter detector face over that period of time. The DAQ system observed an event rate of 10 s^{-1}. The raw data is processed using the MTsort software as detailed in Section 4.4. A breakdown of the number of interactions recorded, to the number of events seen in the final image can be seen in Table 5.2.

Table 5.2: Breakdown of the number of events leading to the final analytically reconstructed image of two ^{137}Cs sources of 0.227 & 0.235 MBq placed at (± 90, 0, 450) mm.

Parameter	Frequency	Percentage (%)
Incident γs	1.01 $\times 10^9$	-
MWD Interactions Recorded	5 592 920	100
Real fold interactions	4 826 766	86.3
Number of 2 tier events	1 692 995	30.3
Fold [1 1 1 1] imageable events	217 070	3.9
Energy Gated imaged events	9 583	0.2

[1]Details of this measurement, and the other measurements described in this thesis are described in Appendix B

The number of *MWD interactions recorded* represents every time an interaction is registered in one of the strips that successfully passes the low-energy applied thresholds defined by the CFD, and has a defined energy as stipulated by the MWD algorithm. The *real fold interactions* is the total number of these interactions that have also been confirmed as a true signal as determined by the BLD algorithm. The total number of interactions which then deposit energy in both the scatter and absorber detectors within the defined coincidence window are considered as a *2 tiered event*. Multiple fold interactions are included in this value. By extracting the fold [1 1 1 1] events, these can then be considered as the imageable data. It is this data that is then exported into text files.

Different text files are produced which show the application of the different PSA techniques described in Section 4.4.4 on the x, y and z positions. The text file of choice is then input into the imaging application, where the user can then apply the parameters shown in Table 5.1, except with the source-to-detector distance set at 45 cm.

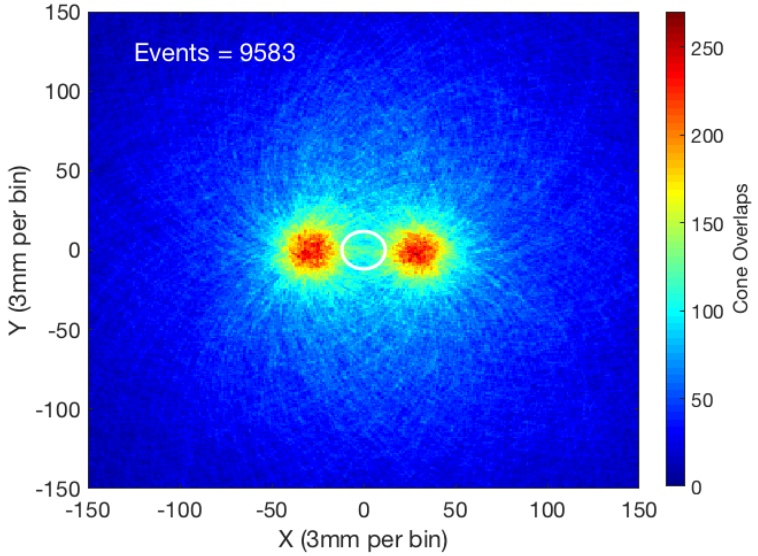

Figure 5.11: Analytical reconstruction of two ^{137}Cs point sources placed 9 cm either side of point (0, 0). The image slice was taken at Z = 54, 45 cm away from the scatter detector face. The compression factor was 3 pixels/mm. 9 583 events were processed without any PSA techniques applied. The white circle represents the size of the scatter detector face relative to the source positions.

Figure 5.11 shows the intensity matrix produced from the analytical reconstruction of the data. A visualisation of the image matrix is produced instantaneously by the imaging application, however the matrix shown in Figure

5.11 was exported and visualised using Matlab in order to include additional information. In Figure 5.11, a white circle has been included which shows the size of the scatter detector face relative to the source position. The centre of the circle is situated at (0, 0).

The energy gate was applied to focus soley on events within the 662 keV full-energy peak. The two sources can be clearly identified by the two regions of high intensity. By looking at a slice of the image through the row of maximum intensity, we can identify the position of the two sources by applying the combined Gaussian-Lorentzian fit, as described in Section 3.3.2.

This fit can be automatically applied to the reconstruction of a single point source, and two point sources, however it usually requires slight refinement with multiple sources. The parameters defining the Gaussian and Lorentzian peak position, amplitude and width can be applied manually. The peak positions can be estimated from a visual inspection of the produced intensity matrix and slice through the maximum y value. Once the values have been initially estimated, a chi-squared minimisation technique iterates to find a successful estimate of the Gaussian and Lorentzian fits. A *combined* fit will be applied through the summation of the Gaussian and Lorentzian fits, to see how well it matches with the experimental data. This is shown in Figure 5.12.

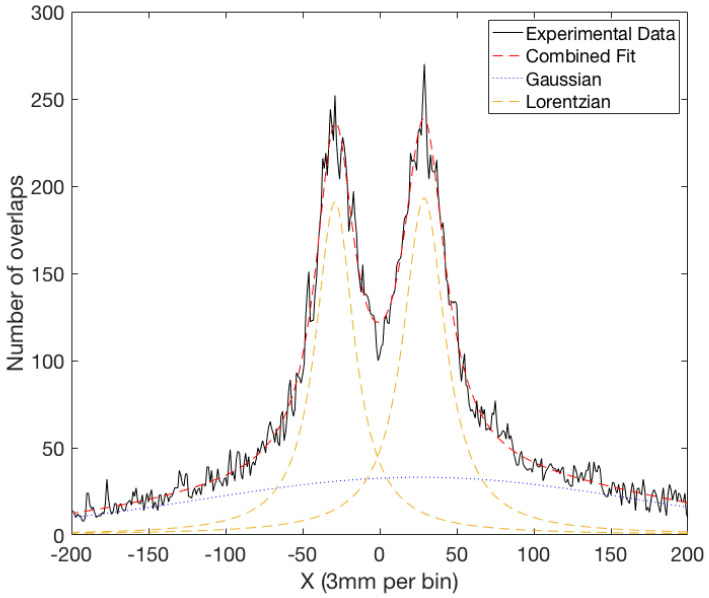

Figure 5.12: Intensity profile of two ^{137}Cs sources, placed 9 cm either side of point (0, 0). The compression factor was 3 mm/pixel. A combined fit has been applied through the summation of a manually applied Gaussian and Lorentzian profile.

The peak positions and their associated errors can be provided from the applied fit. The peak positions from the fit applied in Figure 5.12 were found to be -30.0 ± 0.2 and 27.9 ± 0.2. The separation between these two positions can be determined, with the value being tripled to account for the assignment of the binning (3 mm/bin). The separation between the two sources was found to be **173.7 ± 0.8 mm**. The final error was found through the calculation of errors in quadrature.

The true separation of the source based on their positions would have been **180 ± 1 mm**. If we look at the specific peak positions obtained from the applied distributions, these would translate to −90.0 and 83.7. Assuming that there are no significant experimental errors arising from where the two sources were positioned, then the applied distributions are likely to be the source of error between the calculated separations.

Slight manual corrections could be made to the applied fits to try and improve upon this value, whilst keeping the combined fit matching the experimental data, or future measurements could require a minimum number of cone overlaps to produce a high-quality Lorentzian fit to the peaks. This result shows that two sources can be resolved at this standoff distance, along with a reasonable estimation of the source separation, without PSA techniques being applied.

Positional Gating

Another reconstructed image produced from the measurement detailed above was created, but with no energy gates applied. The aim for this was to see if it was possible to back-project an energy spectrum based on positional gates applied to the image.

Figure 5.13 shows the reconstructed image, utilising all 205 458 events due to no energy gates being applied to the reconstruction. As can be seen in the figure, two localised hotspots can be identified representing the positioning of the two ^{137}Cs sources. Three position gates were then applied, as represented by the different coloured rectangles shown on the figure.

Once the areas had been selected, the analytical reconstruction code is rerun. Rather than ellipse points being added to the 2D image viewed in the matrix, separate slices are created for each energy. The slice is the size of the defined area [97]. Histogram plots can then be produced which show the number of overlaps produced in the slice area, as shown in the spectra in Figure 5.14.

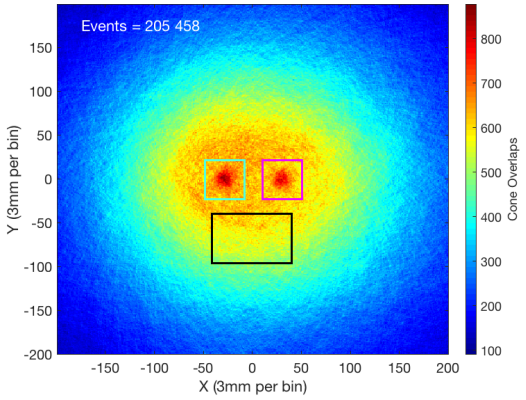

Figure 5.13: Analytical reconstruction of two ^{137}Cs point sources placed 9 cm either side of point (0, 0). The compression factor was 3 pixels/mm. 205 458 events were processed with PSA techniques applied. The coloured rectangles represent areas applied for positional gating.

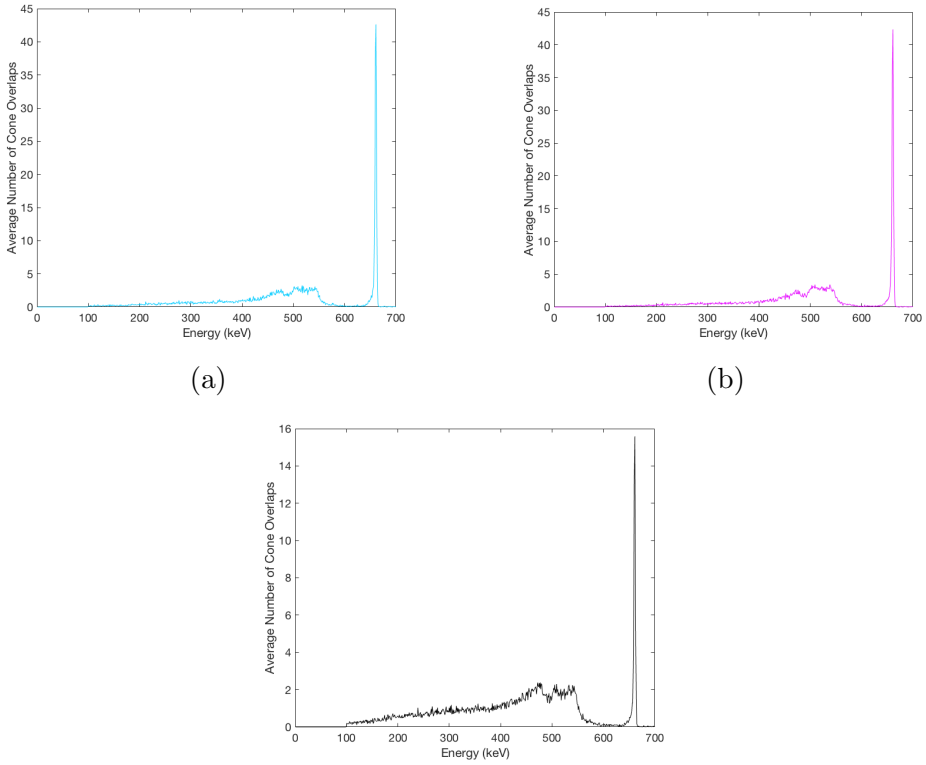

Figure 5.14: Histograms produced from the positional gates applied to the analytical reconstruction of two ^{137}Cs sources positioned at (± 90, 0, 450) mm. The graphs show the average number of overlaps found in the specified regions.

The different colour histograms represent the different colours of the position gates shown on Figure 5.13. The main conclusion obtained from the histograms shown in Figure 5.14 is that all the overlaps shown in each section are primarily caused by the ^{137}Cs 662 keV full-energy peak. Figure 5.14c, which represents the black area, shows how the 662 keV cones are influenced to a lesser degree, as shown by the fewer cone overlaps.

Near-Axis measurement

The two sources were then moved to a 60 mm separation, positioned at x = ± 30 mm, as shown in Figure 5.15b, whilst remaining at the 45 cm standoff distance (Figure 5.9a). The same parameters were applied to the analytical image reconstruction, and data was collected for nearly 25 hours. The breakdown of the number of events can be found in Table 5.3.

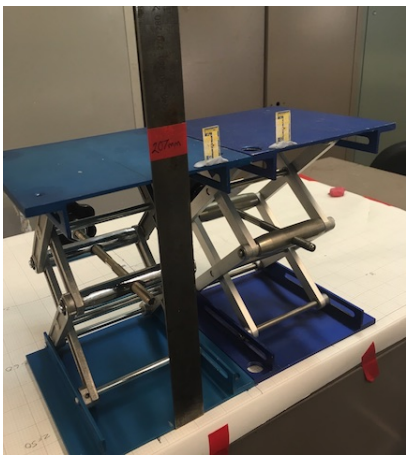

(a)

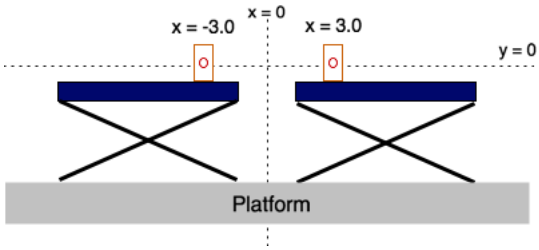

(b)

Figure 5.15: (a) Image showing the experimental set-up of two ^{137}Cs point sources both with activity of approximately 0.3 MBq at a standoff distance of 45 cm. (b) Schematic showing the separation of the two ^{137}Cs sources of 6 cm.

Table 5.3: Breakdown of the number of events leading to the final analytically reconstructed image for two ^{137}Cs sources of 0.227 and 0.235 MBq placed at (± 30, 0, 450) mm.

Parameter	Frequency	Percentage (%)
Incident γs	8.58 $\times 10^8$	-
MWD interactions recorded	4 719 403	100
Real fold interactions	4 119 979	87.3
Number of 2 tier events	912 268	19.3
Fold [1 1 1 1] imageable events	258 941	5.5
Energy Gated imaged events	11 605	0.2

The intensity matrix produced from the data at this separation is shown in Figure 5.16, as well as the slice through the point of maximum intensity in the x-direction.

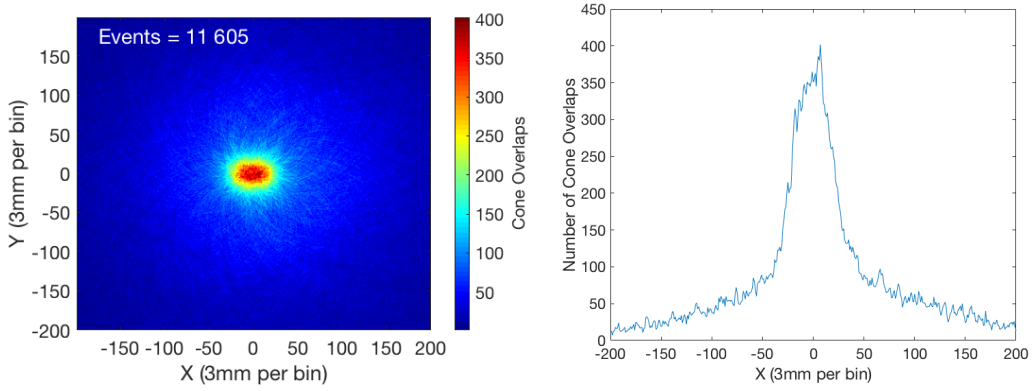

(a) (b)

Figure 5.16: (a) Analytical reconstruction of two ^{137}Cs point sources placed 3 cm either side of point (0, 0). The image slice was taken at Z = 540, 45 cm away from the scatter detector face. The compression factor was 3 mm/bin. 11 605 events were processed without any PSA applications. (b) Intensity profile at the point of maximum intensity.

The data presented in Figure 5.16 shows an elongation of the profile in the x-direction, leading to the assumption that this could possibly be from a distributed source. As it can be seen from Figure 5.16, the sources can not be distinguished in neither the intensity matrix nor the intensity profile. The precision of the interaction position is affecting the quality of the reconstruction, leading to the inability to identify multiple sources. This could be improved by applying parametric pulse shape analysis techniques, or a high-frequency filter.

It is unlikely that utilising the iterative MLEM code as described in Section 4.5.2 would improve the image. Previous work using the iterative imaging code [81] showed that multiple sources cannot be individually separated. Due to each element of the system matrix being given equal probability of detecting an incoming gamma-ray, the counts are assigned to the more intense regions of activity as the number of iterations increase. As a result, the lower-activity source will lessen in intensity with each increased iteration. This problem can be fixed if a true detector response function was described. This would then be reflected in the system matrix and can accommodate sources of different activity. Similarly, refining the quality of the input data will lead to improvements using the iterative MLEM code.

For different isotopes, this could be adapted by applying individual energy gates, which are then iterated separately and a final image is produced by combining multiple iterations in a time-consuming process. This process will not work with multiple sources of the same gamma-ray energy.

Improving the precision of the interaction position could lead to the identification of multiple sources. The three Z-PSA methods for determining the Z position in the absorber detector, as described in Section 4.4.4, will be compared. Parametric PSA techniqes were utilised for the X-Y positions in the scatterer and absorber, using the analysis of the asymmetry terms produced from the area of the induced image charges found on neighbouring strips. Providing an interaction exceeds the pre-defined energy thresholds, there is no minimum amount of energy that is required to be deposited in either detector in order for image charges to be induced on neighbouring strips. The effect of the PSA techniques on the analytical reconstruction were observed.

The number of events in the output text files are the same with and without PSA, meaning PSA is applied to the same events that are used in the original analytical reconstruction. The same number of events are also used even when the energy gate is applied (as long as the width of the gate is not varied between measurements). No statistical information is therefore lost through the application of PSA or through the inclusion of the user defined energy gate.

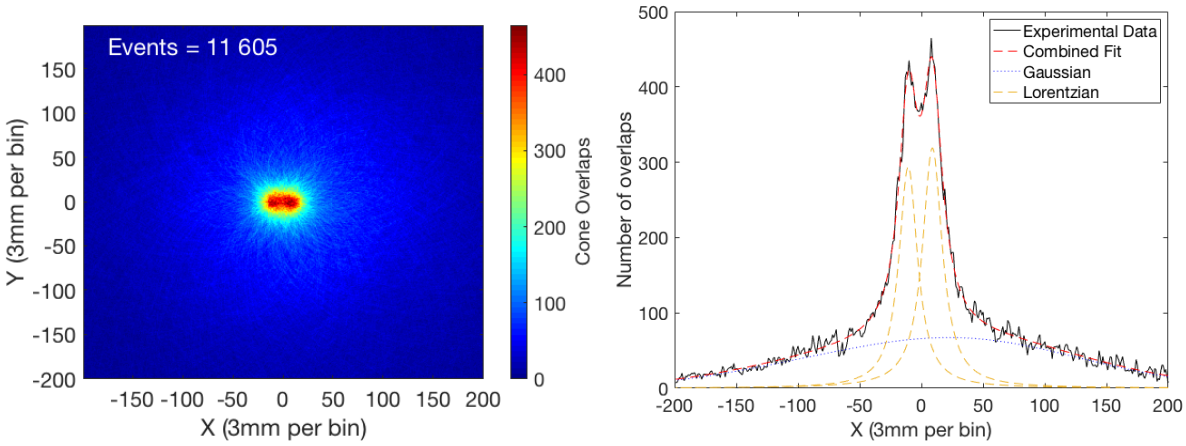

(a) (b)

Figure 5.17: (a) Analytical reconstruction of two ^{137}Cs point sources placed 3 cm either side of point (0, 0). The compression factor was 3 mm/bin. 11 605 events were processed with XY and Z-PSA1 applied. (b) Intensity profile at the point of maximum intensity with the combined Gaussian and Lorentzian fits.

Each image was reconstructed using the same parameters as detailed in Table 5.1. Only the manual fit parameters were altered in order to obtain an accurate combined fit to the experimental data.

Figure 5.17 shows the intensity matrix and profile with the use of Z-PSA1, with the reconstructed image displayed in (a) showing that 11 605 full-energy peak events were used. From an initial visual inspection of the image, the suggestion of the prescence of two sources could be supported by two weak hotspots on the image. Whilst the two sources can not be distinguished fully, the intensity profile shown in (b) suggests that two sources are present with the presence of two peaks.

The figure shows the applied Gaussian and Lorentzian fits, which combine to successfully fit the double-peaked profile. By using the information provided by the applied combined fit, the peak centroid positions can be determined. By calculating the difference between the peak centroids, and accounting for the compression factor of 3 mm/bin, the separation of the two sources for the three Z-PSA methods can be found.

The centroids of these peaks are located at -11.7 ± 0.1 and 7.9 ± 0.1. This leads to a calculated source separation of $\mathbf{58.8 \pm 0.6}$ **mm** (a comparison of calculated source separations can be found in Table 5.4). The difference in height between the two peaks even alludes to a possible difference in activity between the two sources.

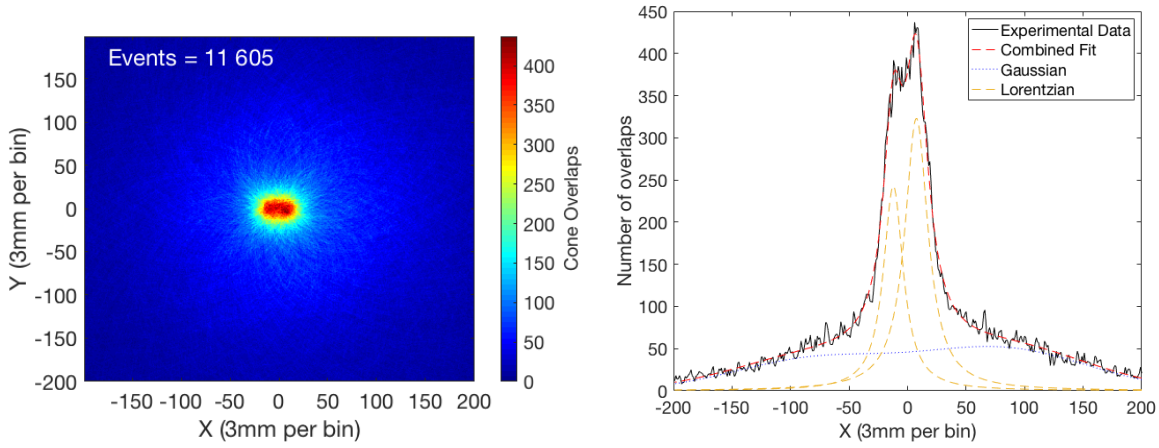

(a) (b)

Figure 5.18: (a) Analytical reconstruction of two ^{137}Cs point sources placed 3 cm either side of point (0, 0). The compression factor was 3 mm/bin. 11 605 events were processed with XY and Z-PSA2 applied. (b) Intensity profile at the point of maximum intensity with the combined Gaussian and Lorentzian fits.

Figure 5.18 shows the analytically reconstructed image and the intensity profile of the application of the Z-PSA2 method to the data. As can be seen from this image, the same number of events (11 605) are used in the reconstruction, reaffirming the earlier point that the different techniques are applied to the same events. The image suggests the presence of a distributed source, compared to two separate sources due to the region of high-intensity in the image.

When the slice through the point of maximum intensity is produced, as shown in Figure 5.18b, it shows that the two sources cannot be distinguished from the intensity profile. The profile is of a poorer quality compared to the one produced from the Z-PSA1 method, despite the assumption from the description of the method in Section 4.4.4 that Z-PSA2 would lead to more accurate results due to increased segmentation of the absorber detector for positional information.

The inclusion of the Lorentzian peaks allows the peak centroids to be obtained, which could not be easily estimated solely from the intensity profile. The centroids of these peaks are located at -13.2 ± 0.2 and 6.6 ± 0.2. This leads to a calculated separation of $\mathbf{59.4 \pm 0.9\ mm}$. Similar to the Z-PSA1 method, a difference in height of the two peaks suggests a difference in activity.

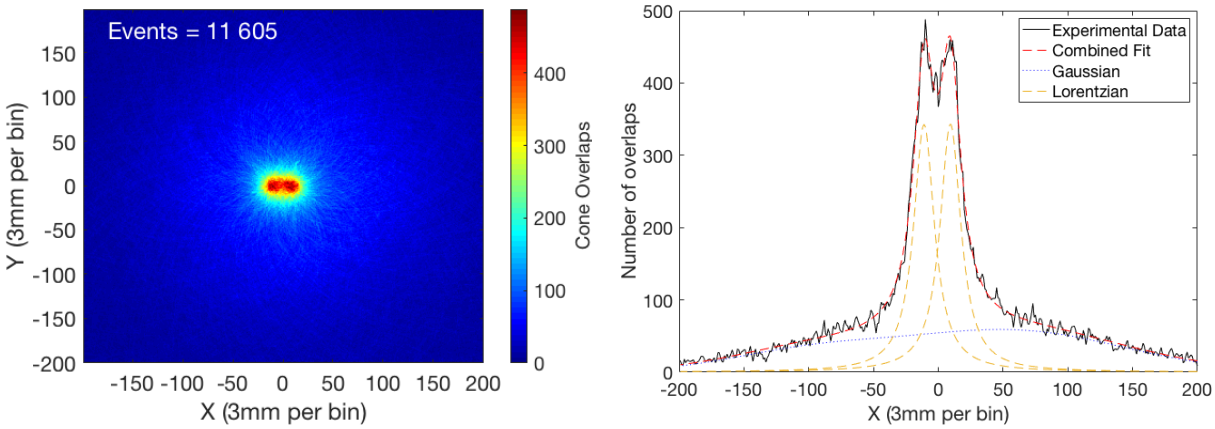

(a) (b)

Figure 5.19: (a) Analytical reconstruction of two ^{137}Cs point sources placed 3 cm either side of point (0, 0). The compression factor was 3 mm/bin. 11 605 events were processed with XY and Z-PSA3 applied. (b) Intensity profile at the point of maximum intensity with the combined Gaussian and Lorentzian fits.

Figure 5.19 shows the reconstructed image through the application of the Z-PSA3 technique. From an initial visual inspection, the presence of two

sources can be identified from both the reconstructed image and the intensity profile.

Figure 5.19b shows two defined peaks, similar to the profile produced from Z-PSA1 technique. Whilst the peaks seem to be more defined compared to the other Z-PSA methods, the heights of the Lorentzian peaks are relatively equal, unlike the difference in heights shown in Figures 5.17b & 5.18b. The peak centroids can be determined from the Lorentizan peaks, and found to be at -12.0 ± 0.1 and 8.4 ± 0.1, leading to a source separation of $\mathbf{61.2 \pm 0.6}$ **mm**.

Table 5.4 shows a comparison for the different separations that were calculated from the applied fits shown in Figures 5.17b - 5.19b.

Table 5.4: Separations calculated from the difference between peak centroids produced from the applied fits.

PSA Method	Peak Position 1	Peak Position 2	Separation (mm)
Z-PSA1	-11.7 ± 0.1	7.9 ± 0.1	58.8 ± 0.6
Z-PSA2	-13.2 ± 0.2	6.6 ± 0.2	59.4 ± 0.9
Z-PSA3	-12.0 ± 0.1	8.4 ± 0.1	61.2 ± 0.6

The two sources were placed at x = $\pm$ 30 mm, leading to an experimental source separation of 60 ± 1 mm. Performing a consistency check with the separations found in Table 5.4 found them to all be consistent with the true separation.

Comparing the images and slices from Figures 5.17 - 5.19, it can be seen how the different Z-PSA techniques can affect the ability to resolve multiple sources and improve upon the quality of the reconstructed images. It is clear that the x, y and z positional information is limiting the ability to resolve the two sources when you compare Figure 5.16, when no PSA is applied, to the images shown in Figures 5.17 - 5.19. Any previous assumptions of a distributed sample from initial observations are corrected through resolving the image to two point sources, with a separation calculated for each through the application of PSA.

The capability of imaging multiple sources was investigated in previous work [85] at separations of 2 cm, 4 cm and 8 cm at a maximum standoff distance of 30 cm. At this distance, the 2 cm separation was the only one where the two sources could not be identified with the use of XYZ PSA.

The quality of the images could be further improved through application of

the high-pass filter, and it can be seen if there is any further improvement upon the calculated separation of the two sources.

High-Pass filter

As described in Section 4.5.1, the high-pass filter (HPF) is able to produce a more precise indication of point sources. This is done by focusing on the areas with a higher number of cone overlaps, which are representative of the location of the source, and by filtering out the lower number of cone overlaps, which will be representative of the background. The HPF can only be applied to a previously reconstructed image slice.

In order to modify the reconstructed image slice to produce an optimised image, the user can define a *cutoff frequency* on the imaging application. Signals with a frequency higher than this defined *cutoff frequency* will be allowed to pass in the new reconstructed image, with anything below this cutoff frequency supressed.

This value can be optimised in order to avoid any low-frequency background events appearing as artefacts on the image. On the imaging application, the cutoff-frequency value for any of the filters available can be set between thresholds of 0 and 300. For the HPF, this value should be set at a threshold of between 15 and 30 in order to successfully filter out the background events and reduce the number of artefacts observed in the filtered image [85].

Choosing a value between 15 and 30 is specific to the image, and is optimised by the user to produce the highest-quality image. It was found for these measurements that the reconstructed images were optimised with a cutoff-frequency value of 30. For consistency and comparison purposes, this value was kept the same when comparing the different Z-PSA methods. This value may change for other filtered images in this chapter.

Figure 5.20 shows the intensity matrix and profile of the image after application of the HPF. Compared to the earlier profile found in Figure 5.17b, the two sources are more clearly defined, with the relative heights of the two peaks comparative to the slight difference in the activity of the two sources.

Due to the filtering of the background, the shape of the profile has changed from one that required a combined Lorentzian and Gaussian distribution, to one that can be well described by a two-term Gaussian fit. The small fluctuations observed to the left and right of the peaks are due to low intensity artefacts that could not be filtered out. These artefacts are at a minimum level due to the selection of the specified cutoff frequency.

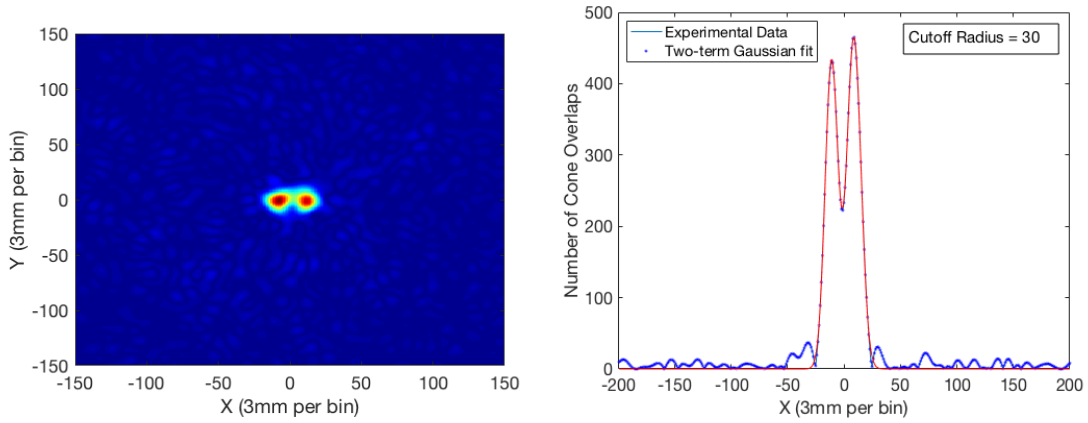

(a) (b)

Figure 5.20: The intensity matrix (a) and image slice through the point of maximum intensity (b) produced from applying a HPF to the reconstructed image produced from Z-PSA1 of two ^{137}Cs sources separated by 60 mm. The cutoff radius applied to the HPF was 30. A two-term Gaussian fit was applied to the profile to identify the peak positions. R-Square = 0.991.

The two-term Gaussian fit was applied to the image profile that was created from producing a slice through the point of maximum intensity in the x-direction. The Gaussian fit can be shaped to the two peaks using Matlab, but does not account for the low intensity artefacts in the profile. Through analysis of the Gaussian fit, the two peak centroid positions can be extracted and the separation between the sources calculated. These values were found to be -10.9 ± 0.2 and 8.9 ± 0.1, with a separation of $\mathbf{59.4 \pm 0.7}$ **mm** . This compares to the experimental source separation of 60.0 ± 1.0 mm, and a change from calculated source separation of 58.8 ± 0.6 mm. (A comparison of these results can be found in Table 5.5).

Matlab is able to produce a R-Square value that describes the *goodness-of-fit*, a quantifiable way of measuring how successful the fit is to the experimental data by providing a value between 0 and 1. The closer the value is to 1, the more successful the fit. The R-Square value for the fit shown Figure 5.20b was 0.991.

By analysing the relative heights of the two peaks, it can be determined if there is a relationship between the relative heights and the relative intensities of the sources used. The amplitude of the two peaks, as obtained from the Gaussian fit, were found to be 430.8 ± 6.9 and 464.7 ± 7.2. The ratio of the two heights is 0.927 ± 0.021, compared to the ratio of source activities of 0.966. A summary comparison of the relative heights for the different Z-PSA

techniques can be found in Table 5.6.

The improvement with the introduction of the high-pass filter is evident with the first Z-PSA technique. This is also distinct in Z-PSA2. In Figure 5.17b, it was difficult to discern that two sources were present, and it was only through the application of the combined Lorentzian and Gaussian fit that the two source positions could be estimated.

By applying the high-pass filter, the two sources are now clear in both the image and the intensity profile. The image quality isn't as high as that shown compared to Z-PSA1, but the ability to be able to recognize two sources is a massive improvement. The ability to resolve the peaks clearly allows for the peak centroids to be found at -11.1 ± 0.2 and 9.1 ± 0.2, with a calculated source separation of $\mathbf{60.6 \pm 0.8\ mm}$. This is in comparison to the previously calculated separation from the unfiltered image of 59.4 ± 0.9 mm, and true separation of 60.0 ± 1.0 mm.

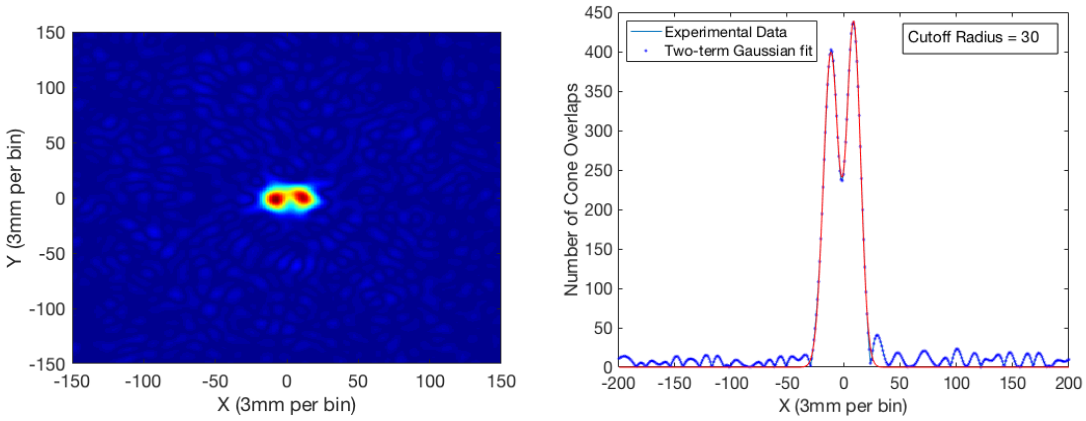

(a) (b)

Figure 5.21: The intensity matrix (a) and image slice through the point of maximum intensity (b) produced from applying a HPF to the reconstructed image produced from Z-PSA2 of two ^{137}Cs sources separated by 60 mm. The cutoff radius applied to the HPF was 30. A two-term Gaussian fit was applied to the profile to identify the peak positions. R-Square = 0.988.

Similar to Figure 5.20(b), the heights of the two peaks are consistent with reflecting the differences in the two sources activity, however the relative heights of the peaks differ the most in comparison to the other Z-PSA techniques. The amplitudes of the two peaks were found to be 396.9 ± 7.5 and 435.1 ± 7.7, with the relative height found to be 0.912 ± 0.024.

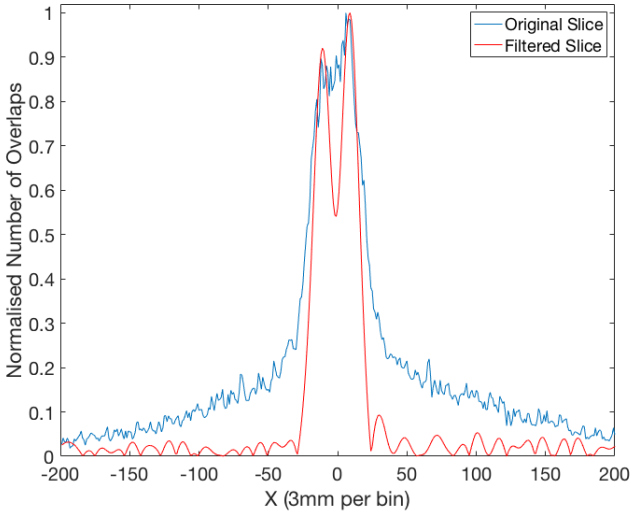

Figure 5.22: A comparison of the normalised profiles of the images reconstructed from Z-PSA2, with and without the use of the high-pass filter.

A normalised profile of the original intensity slice and the filtered slice is shown in Figure 5.22 to demonstrate how the filtered profile compares to the original slice, as the slice produced from Z-PSA2 was the most difficult to determine the presence of two sources.

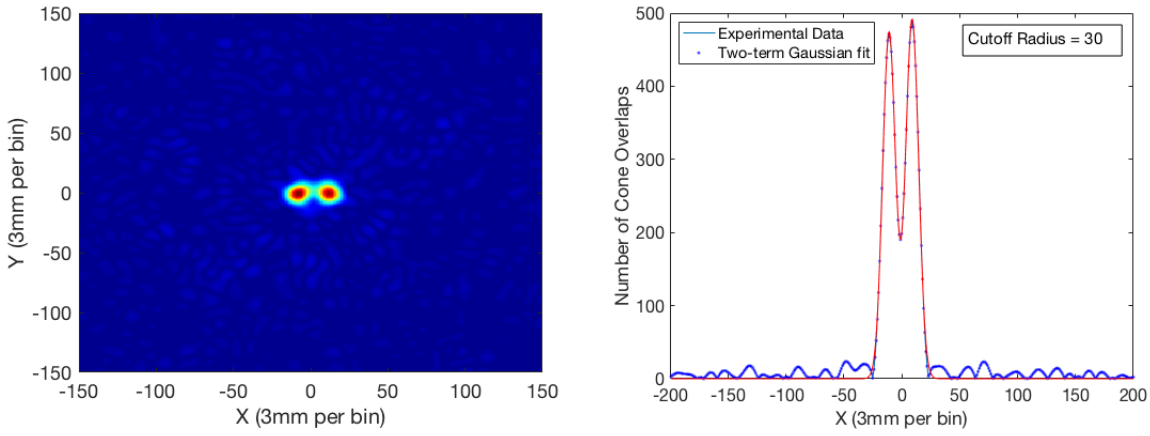

(a) (b)

Figure 5.23: The intensity matrix (a) and image slice through the point of maximum intensity (b) produced from applying a HPF to the reconstructed image produced from Z-PSA3 of two ^{137}Cs sources separated by 60 mm. The cutoff radius applied to the HPF was 30. A two-term Gaussian fit was applied to the profile to identify the peak positions. R-Square = 0.992.

Finally the high-pass filter was applied to the image produced from Z-PSA3, with the results shown in Figure 5.23.

The intensity matrix shows a very clear definition of two point sources, and the separation between the peak centroids in Figure 5.23b could be determined using the two-term Gaussian fit, with a R-Square value of 0.992. The peak centroids were located at -10.9 ± 0.1 and 9.0 ± 0.1, giving a calculated source separation of **59.7 ± 0.4 mm** .

Compared to the original reconstructed image through application of Z-PSA3, the heights of the two peaks looked relatively equal, as shown in Figure 5.19b. Through the HPF, there is a now a difference to the heights, with the larger peak now indicative of the higher-activity source. The amplitudes of the two peaks from the Gaussian fit were found to be 474.0 ± 7.1 and 491.7 ± 7.0, giving the relative heights between the two peaks 0.964 ± 0.020, compared to the relative intensity of the two sources of 0.966.

At extreme positions (x = ± 90), the sources can be easily identified where the separation of the peak centroids is approximately the distance between the sources (18 cm). However, at near-axis positions (x = ± 30), the application of PSA and the high-pass filter is required to realise there are two sources present.

Table 5.5 shows how applying the HPF allows the positions of the peaks to be identified clearly and source separations to be calculated with their associated errors. Improvements can be observed for the Z-PSA methods 1 and 3, with the separation closer to the true separation of 60 mm. Whilst the improvements are less than 1 mm, being able to accurately locate the position of two sources will be hugely beneficial in nuclear decommissioning scenarios.

Table 5.5: Table showing the separations calculated from the difference between peak centroids produced from the applied two-term Gaussian fit, compared to the previous values shown in Table 5.4 for measurements of two ^{137}Cs sources placed at (± 30, 0, 450) mm.

PSA Method	Peak Pixel Position 1	Peak Pixel Position 2	Separation (mm)	Previous separation (mm)
Z-PSA1	-7.9 ± 0.1	11.9 ± 0.1	59.4 ± 0.4	58.8 ± 0.6
Z-PSA2	-6.6 ± 0.2	12.1 ± 0.2	60.6 ± 0.9	59.4 ± 0.9
Z-PSA3	-10.9 ± 0.1	9.0 ± 0.1	59.7 ± 0.4	61.2 ± 0.6

The two ^{137}Cs sources used in these measurements had activities of 0.227 and 0.235 MBq respectively. The relative heights of the two peaks found in Figures 5.17b-5.19b, and 5.20b-5.23b could be compared to the relative intensity of the two sources, to see if one of the Z-PSA methods gives an

accurate representation of the possible activity of the measured sources. The summary comparing the values of these results for the different Z-PSA methods can be found in Table 5.6.

Table 5.6: Table showing the relative heights of the peaks of the Lorentzian fits for the original Z-PSA methods (no errors provided), and of the relative heights produced from the two-term Gaussian fit in the filtered images. The heights are from reconstructed images of two ^{137}Cs sources placed at (± 30, 0, 450) mm.

PSA Method	Relative Height
Z-PSA1	0.921
Z-PSA2	0.751
Z-PSA3	0.999
Filtered Z-PSA1	0.927 ± 0.021
Filtered Z-PSA2	0.912 ± 0.024
Filtered Z-PSA3	0.964 ± 0.020
Relative intensity of 0.227MBq and 0.235MBq	0.966 ± 0.006

As it can be seen from Table 5.6, only the relative heights from the Filtered Z-PSA3 slice closely match the relative intensity of the two ^{137}Cs sources.

Another method that could be used to compare against the relative intensity is by considering the area under each peak. For the reconstructed images before the HPF was applied, the area under the Lorentzian peaks was considered. For the slices produced after the application of the HPF, the image slice was divided into two individual Gaussians as shown in Figure 5.24. The areas under the two separate Gaussians were considered for the relative area calculation.

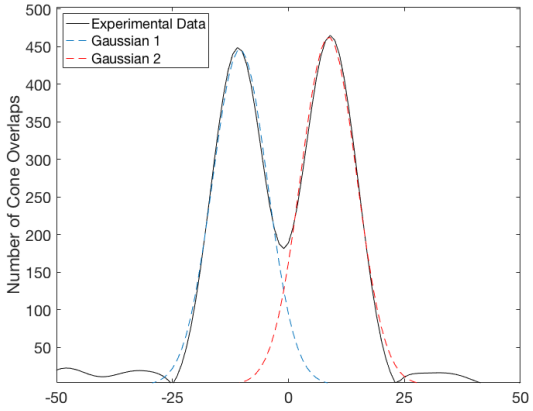

Figure 5.24: Figure showing how the experimental data was split into two separate Gaussians from the image slice produced after the application of the HPF on the Z-PSA1 data.

The areas under the Lorentzian and Gaussian curves were found by computing the approximate integral using the trapezoid method through Matlab. This function does not provide a numerical uncertainty on the areas. A summary of the calculated relative areas for the different Z-PSA methods and application of HPF is shown in Table 5.7.

Table 5.7: Table showing the relative areas of the peaks of the Lorentzian fits for the original Z-PSA methods (no errors provided), and of the relative heights produced from the two-term Gaussian fit in the filtered images. The areas are from reconstructed images of two ^{137}Cs sources placed at (± 30, 0, 450) mm.

PSA Method	Relative Area
Z-PSA1	0.873
Z-PSA2	0.645
Z-PSA3	0.999
Filtered Z-PSA1	0.883
Filtered Z-PSA2	0.964
Filtered Z-PSA3	0.954
Relative intensity of 0.227 MBq and 0.235 MBq	0.966 ± 0.006

As can be seen in Table 5.7, the filtered images provide a more accurate estimation of the relative intensity, with the Z-PSA2 method providing the closest approximation. The Z-PSA3 method gives a more consistent indication of the intensity of the sources from both the relative heights and areas of the peaks in the filtered profile.

Applying the high-pass filter to all images has shown its ability to distinguish the presence of multiple sources, which could not be done previously at these standoff distances or separations.

Going forward, the Z-PSA3 method will be used for the reconstruction of the other images produced for the remainder of this thesis. Despite the quality of the analytically reconstructed image, the Z-PSA3 method gave a suitable estimation of the separation of the two sources, as well as the previously mentioned approximation of the relative intensity. Images with the high-pass filter will also be included to be compared against the original images (no PSA).

5.2.2 Sources of different activity

Similar to the experimental set-up previously shown in Figure 5.9, two point sources of ^{137}Cs were placed at a distance of 45 cm away from the scatter detector face, with two measurements taking place with different source separations; 18 cm (Figure 5.25) and 6 cm. One of the sources included in this measurement had an activity of 0.041 MBq (left-hand source shown in Figure 5.25) compared to the second source of activity 0.235 MBq. The significant difference in activity of the two sources should help replicate the non-uniformity of the extended source, whilst investigating the quality of the images produced at these positions.

Figure 5.25: Image showing the experimental set-up of two point sources of ^{137}Cs of activities 0.041 MBq (left-hand side) and 0.235 MBq (right-hand side), placed with a separation of 18 cm.

The time it took to collect the data for the separation of 18 cm was just over 50 hours in order to collect the necessary statistics in the gated image, nearly 20 hours more than the measurement described in Section 5.2.1. This was due to a reduced count rate of 5 s^{-1} on account of the lower activity source. A breakdown of the number of events used in the image can be found in Table 5.8.

The output file without the application of any PSA methods to the x, y and z positions was first reconstructed using the analytical image algorithm. As expected, with the separation of 18 cm the two sources can be distinguished as shown in Figure 5.26, with 12 813 full-energy peak events used in the image reconstruction. With this image and slice, whilst no PSA is applied, it can be seen from visual inspection that two sources are present.

Table 5.8: Breakdown of the number of interactions leading to the final analytically reconstructed image for two ^{137}Cs sources of 0.041 and 0.235 MBq placed at (± 90, 0, 450) mm.

Parameter	Frequency	Percentage (%)
Incident γs	1.04 $\times 10^8$	-
MWD interactions recorded	6 462 759	100.0
Real fold interactions	5 531 630	85.6
Number of 2 tier events	1 359 722	21.0
Fold [1 1 1 1] imageable events	322 265	5.0
Energy Gated imaged events	12 813	0.2

From a visual estimation, determining the location of the peak centroids could lead to a large positional uncertainty due to the inability to accurately determine which point is the true centroid. However, through applying the combined Lorentzian and Gaussian fit to the data, as shown in Figure 5.26b, the peak centroids could be located and the separation calculated using the method described earlier. The separation was calculated to be **181.5 ± 1.9 mm**, compared to the experimental separation of 180.0 ± 1.0 mm.

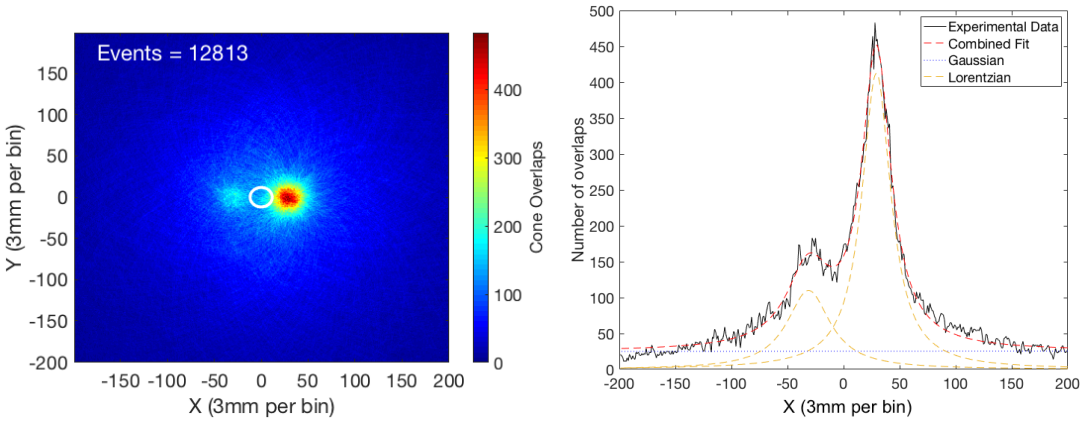

(a) (b)

Figure 5.26: (a) Analytical reconstruction and (b) image slice of two ^{137}Cs point sources of different activity placed 9 cm either side of the point (0, 0). The sources were placed 45 cm away from the scatter detector face. The compression factor was 3 mm/bin. 12 813 events were processed without any PSA. The white circle represents the size of the scatter detector face relative to the source positions. A combined fit has been applied to the profile through the summation of a manually applied Lorentzian and Gaussian fit.

For comparison, the output file which utilised the application of XY PSA and Z-PSA3 methods to the x, y and z positions was reconstructed analytically, as shown in Figure 5.27.

When applying PSA to the data, the points of intensity are more localised and there is less fluctuation with the X-slice. This is specifically noticeable with the smaller peak. Whilst from a visual inspection the peak centroids are more easily identified, the difference between the centroids was calculated using the peak positions obtained from the Lorentzian fits shown in Figure 5.27b. The separation was found to be **174.0 ± 0.7 mm**.

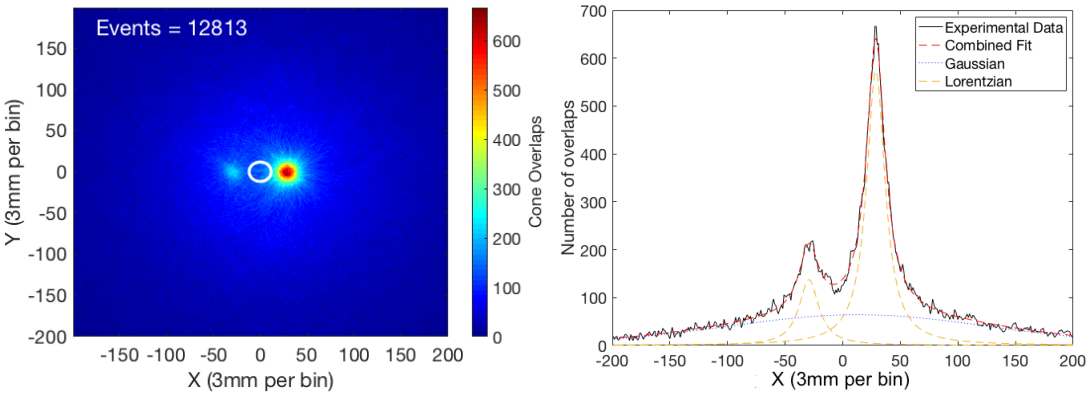

(a) (b)

Figure 5.27: (a) Analytical reconstruction and (b) intensity profile of two ^{137}Cs point sources of different activity placed 9 cm either side of the point (0,0). The sources were placed 45 cm away from the scater detector face. The compression factor was 3 mm/bin. 12 813 events were processed with PSA applied to the x, y, z positions. The white circle represents the size of the scatter detector face relative to the source positions. A combined fit has been applied to the profile through the summation of a manually applied Lorentzian and Gaussian fit.

The high-pass filter was then applied to the reconstructed images shown previously to see if, like in Section 5.2.1, there would be a significant improvement upon the image quality and the separation between the two sources. The cutoff frequency was optimised to a value of 30. As stated previously, this is optimised based on a visual judgement of the filtered image and reducing the number of large artefacts present in the image.

Figures 5.28 and 5.29 shows the affect the HPF has on the image quality, showing a very clear improvement with sharper points of intensity in the reconstructed image, and more well-defined peaks in the image slice. Using the same method as in Section 5.2.1, a two-term Gaussian fit was applied to the filtered profile using Matlab to determine the peak centroids and determine the separation of the two sources. The separation without any PSA techniques applied was calculated to be **178.2 ± 1.2 mm**. The R-Square value for the fit applied in Figure 5.28b was 0.995.

Similarly, the reconstructed PSA image was filtered using the HPF as shown in Figure 5.29a. The R-Square value of the two-term Gaussian fit as shown in Figure 5.29b was 0.995. The separation was found to be **171.0 ± 0.7 mm**.

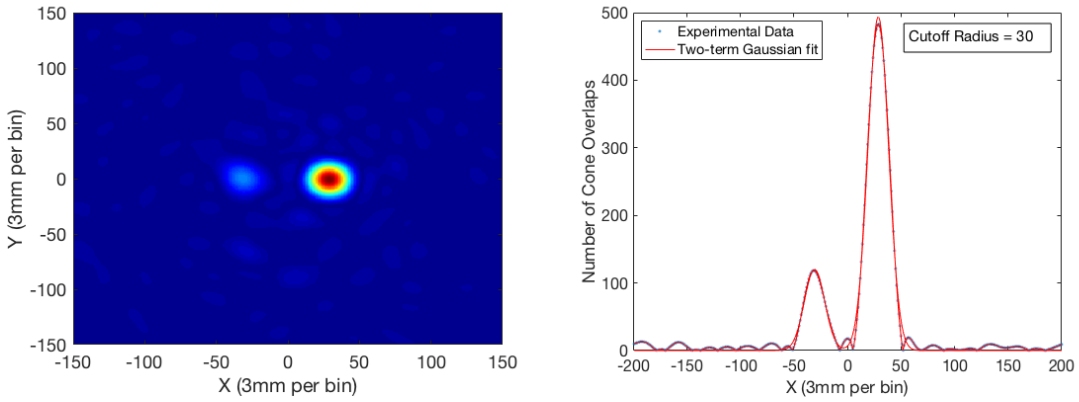

(a) (b)

Figure 5.28: High-pass filter reconstruction, with the intensity matrix (a) and image profile (b) of two ^{137}Cs sources of different activity placed at a separation of 18 cm without any applications of PSA. Cutoff radius of 30. A two-term Gaussian fit has been applied to the profile to determine the peak positions. R-Square = 0.995.

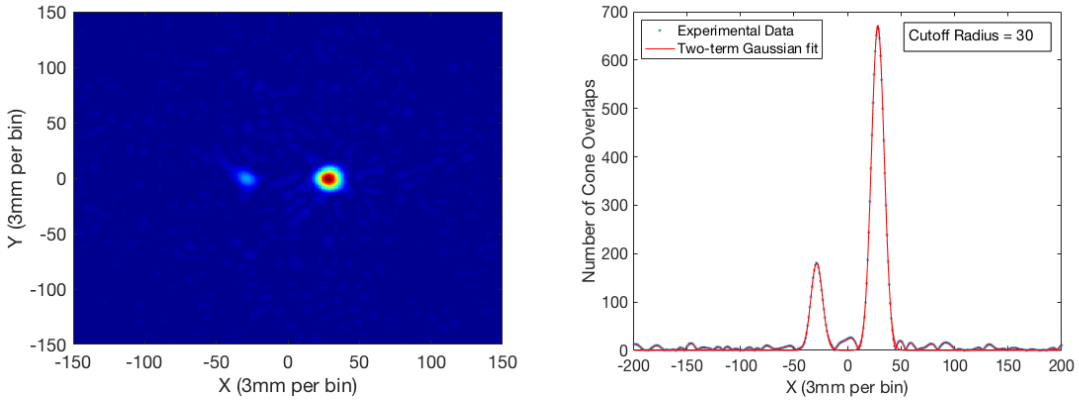

(a) (b)

Figure 5.29: High-pass filter reconstruction, with the intensity matrix (a) and image profile (b) of two ^{137}Cs sources of different activity placed at a separation of 18 cm with PSA applied to x, y and z. Cutoff radius of 30. A two-term Gaussian fit has been applied to the profile to determine the peak positions.

Unlike the results shown in Section 5.2.1 with the sources of similar activity, the separation calculated from the filtered profile is less accurate than the

unfiltered value. This could be due to the HPF localising on an incorrect pixel of intensity, due to the poor positional information initially given for the image reconstruction due to no PSA being applied to the x, y or z positions. However, the result obtained from the inclusion of x, y and z PSA leads to a result further away than the expected separation of 180 mm. Due to the significant improvement in the position resolution from applying PSA, and as shown by the results from Section 5.2.1, it would be expected that applying the HPF would improve the accuracy of the result.

Whilst the raw data is showing a less accurate result, the precision of the separation is improved through applying the HPF. Therefore, it could be possible that due to the different geometry of the lower activity source, there is a larger positional uncertainty when it was placed close to the position of $x = -9.0$, and that the calculated separation produced from the fits shown in Figures 5.27b & 5.29b was an accurate representation of the source separation.

The results shown in Tables 5.6 & 5.7 determined that through the analysis of the relative heights and areas of the two peaks, a comparison could be made to the relative intensity of the activities of the two measured sources. Therefore the relative heights and areas of the peaks found in the image slices above were compared to the relative intensities of the 0.235 MBq and 0.041MBq sources. Table 5.9 shows a comparison of the relative heights and areas obtained from the Lorentzian and two-term Gaussian fits of the data.

Table 5.9: Table showing the relative heights and areas (no errors provided) of the peaks of the Lorentzian and Gaussian fits from the analytically reconstructed images with and without the application of Z-PSA3 and HPF. The values are from reconstructed images of two ^{137}Cs sources of different activity placed at (± 90, 0, 450) mm.

PSA Method	Relative Height	Relative Areas
No PSA	0.267 ± 0.130	0.387
Z-PSA3	0.240 ± 0.136	0.255
Filtered NoPSA	0.243 ± 0.009	0.240
Filtered Z-PSA3	0.269 ± 0.009	0.247
Relative intensity of 0.041 MBq and 0.235 MBq	0.174 ± 0.006	

As can be seen from Table 5.9, the proportions of the relative heights and areas are considerably higher than the relative intensity of the two sources, 0.174. It can be seen from the table that there are also no overall statements of improving the precision. Whilst it seems like the inclusion of PSA improves the precision of the relative heights and areas, this is not the case when the HPF is applied. This significant difference between the values would mean that the method of comparing the relative heights or areas of the two peaks is

unreliable when trying to quantify the activity of the two sources.

Previous methods to estimate the activity of a measured source utilised a function that described the imaging efficiency across a selected part of the detector's field of view [99]. From this imaging efficiency, the activity of the measured source could be estimated by analysing the number of imaged events. Both point and distributed sources were taken into consideration, but all measurements were within 35 cm of the scatter detector face.

Iterative Reconstruction

Whilst the analytical reconstruction of these images produced reasonable estimatations of the location of the sources, the data was also reconstructed iteratively to observe the effect on two points of different intensities.

Section 4.5.2 describes how the MLEM iterative reconstruction code can produce an image through successive iterations. The same output text file used for the analytical imaging application is used, along with the definition of similar parameters, such as energy gates, compression factor, and points per angular degree of the cone. These parameters (as detailed in Table 5.1) were kept the same for the iterative reconstruction.

The number of iterations can be defined by the user. Iteration 0 represents the same image that is produced from the analytical reconstruction, with iteration 1 providing the first set of estimates. Due to the computational time it takes for iterative reconstruction, over an imaging space size of 400×400, six iterations were chosen. It was found here [81, 85] that the fifth iteration leads to the most promising results, so six iterations would have allowed for the predicted optimum iteration, whilst minimising computational time.

The iterative reconstructions of the two ^{137}Cs sources of different activities with the application of parametric XY PSA and Z-PSA3 was achieved. Figure 5.30 shows the images that were reconstructed using the ImageJ software from the first four iterations, and reproduced using Matlab. A function was utilised to convert the image to values between 0 and 1, as represented by the colourbar scale. This has to be done as the information regarding source intensity is lost through the iterative reconstruction.

Whilst six iterations had been reconstructed, as can be seen in Figure 5.30, by the third iteration the second source is almost indistinguishable. This is understandable because of the uniform system matrix (as mentioned in Section

4.4.2). The more intense points will be favourable to the less intense and the algorithm will iterate to a single point source.

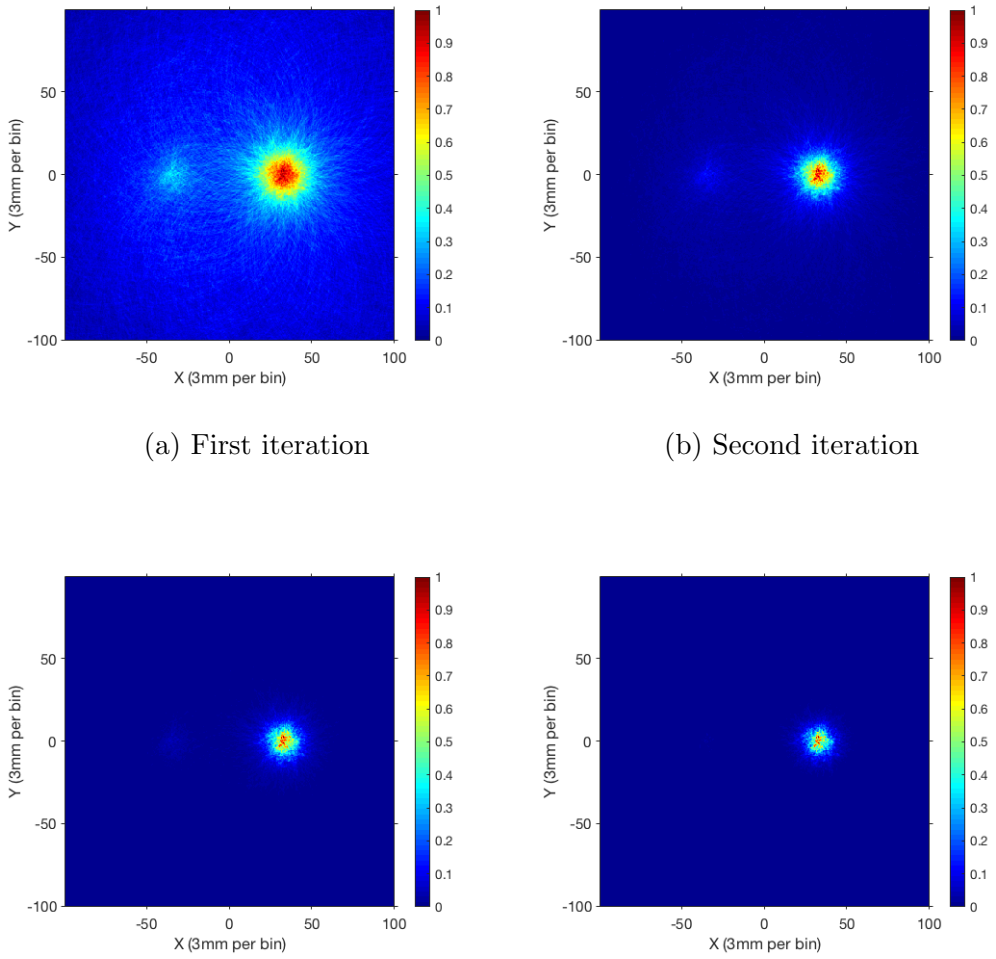

(a) First iteration

(b) Second iteration

(c) Third iteration

(d) Fourth iteration

Figure 5.30: Iterative reconstructions 1(a) - 4 (d) of two ^{137}Cs point sources of different activity placed with an 18 cm separation with the application of XY and Z-PSA3. All images are reconstructed with a compression factor of 3.

This can be seen more clearly in the image slices of the four iterations, as shown in Figure 5.31. Whilst the background events are being removed, the intensity of the left-hand peak is reducing, due to the MLEM algorithm focusing on the more intense right-hand peak. After further iterations, the left-hand peak will be removed entirely. Therefore, it is not ideal to use the iterative reconstruction code for non-uniform sources, unless the weighting of the system matrix can be altered.

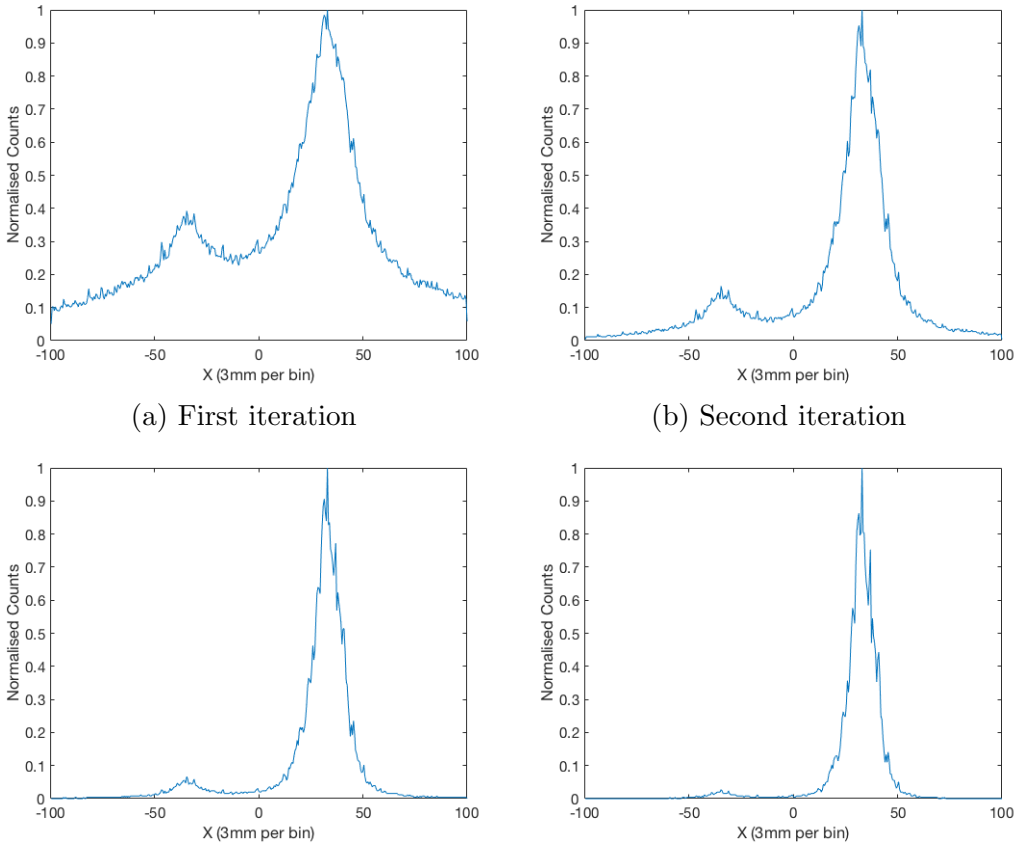

(a) First iteration

(b) Second iteration

(c) Third iteration

(d) Fourth iteration

Figure 5.31: Image slices produced from iterative reconstructions of two ^{137}Cs point sources of different activity placed with an 18 cm separation with the application of XY PSA and Z-PSA3 techniques. All slices are normalised due to scaling of images.

Positional Gating

The positional gating described in the previous section was also implemented to an ungated reconstruction of this measurement. The positional gates were applied to specific areas as shown on Figure 5.32.

As with the previous results, the histograms produced show that it is largely the 662 keV full-energy peak that is influencing the different regions in the image. Unlike the measurement with sources of similar activity, the histograms shown in Figures 5.33a and 5.33b allude to the difference in source activity. The higher number of cone overlaps observed in the blue spectrum, compared to the background events in the black spectrum, can also show that it arises from another source, and is not background. The relative heights of the two peaks observed in the blue and pink spectra (35.9 and 73.9 respectively) are

not comparable with the relative intensities of the source activities.

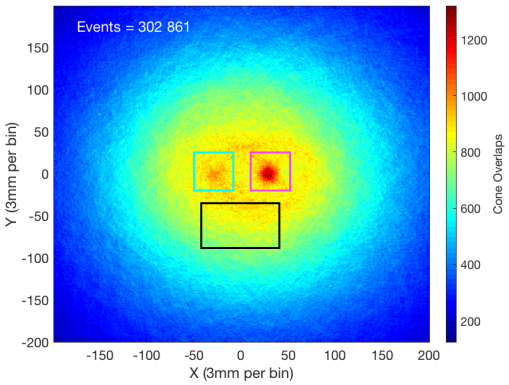

Figure 5.32: Analytical reconstruction of two ^{137}Cs point sources of different activity placed 9 cm either side of point (0,0). The compression factor was 3 pixels/mm. 302 861 events were processed with PSA techniques applied. The coloured rectangles represent areas applied for positional gating.

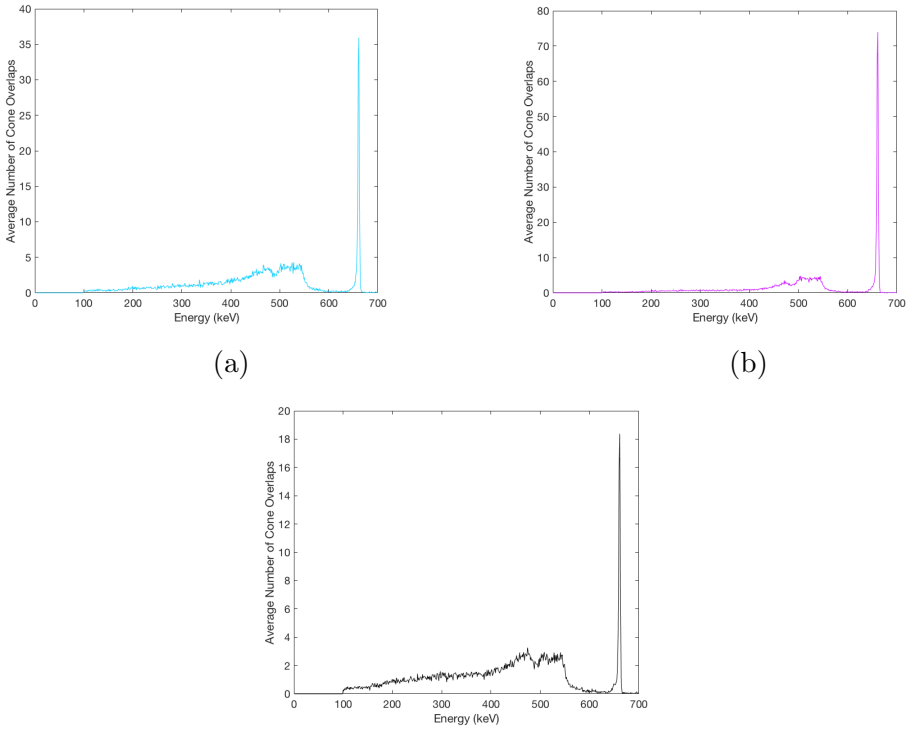

Figure 5.33: Histograms produced from the positional gates applied to the analytical reconstruction of two ^{137}Cs sources of different activity positioned at (± 90, 0, 450) mm. The graphs show the average number of overlaps found in the specified regions.

Near-axis Measurement

Similar to the measurement described earlier in Section 5.2.1, the two sources were moved to positions of x = ± 30 mm as described by Figure 5.15b. Data was measured over a period of nearly 28 hours, with a breakdown of the useable events found in Table 5.10.

Table 5.10: Breakdown of the number of interactions leading to the final analytically reconstructed image for two ^{137}Cs sources of 0.041 and 0.235 MBq placed at (± 30, 0, 450).

Parameter	Frequency	Percentage (%)
Incident γs	5.83 $\times 10^8$	-
MWD interactions recorded	3 670 237	100.0
Real fold interactions	3 155 557	86.0
Number of 2 tier events	754 235	20.6
Fold [1 1 1 1] imageable events	210 668	5.7
Energy Gated imaged events	8238	0.2

The data was reconstructed analytically with and without the applications of XYZ PSA, using the same image application parameters that had been defined for the previous measurements. Figure 5.34 shows the reconstructed image utilising 8238 gated full-energy peak events, and the intensity profile across the X-direction without any PSA implemented. As it can be seen in the Figure, it is difficult to separate the two sources without the application of PSA.

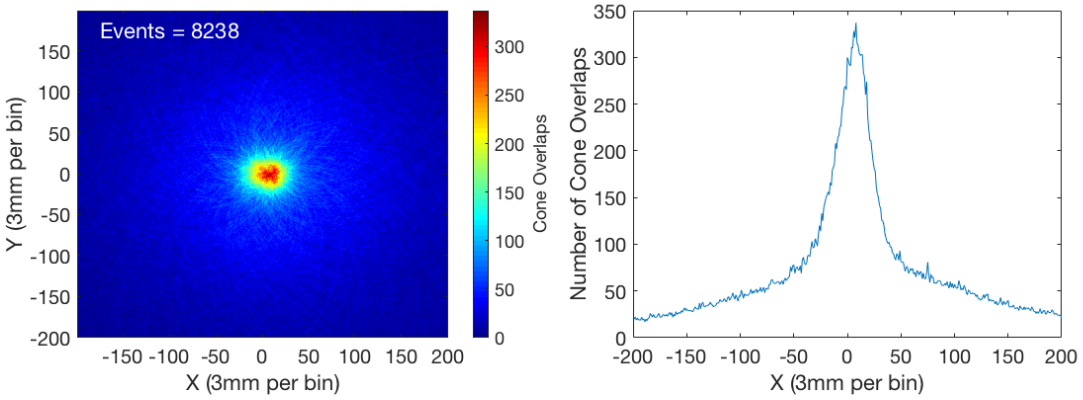

(a) (b)

Figure 5.34: (a) Analytical reconstruction and (b) intensity profile of two ^{137}Cs point sources of different activity placed 3 cm either side of the point (0, 0). The sources were placed 45 cm away from the scater detector face. The compression factor was 3 mm/bin. 8 238 events were processed without any PSA.

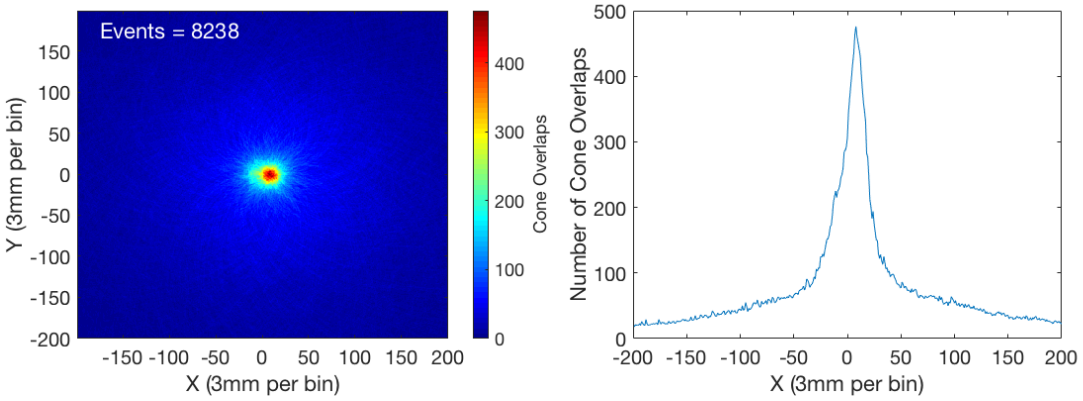

(a) (b)

Figure 5.35: (a) Analytical reconstruction and (b) intensity profile of two ^{137}Cs point sources of different activity placed 3 cm either side of the point (0, 0). The sources were placed 45 cm away from the scater detector face. The compression factor was 3 mm/bin. 8 238 events were processed with XY and Z-PSA3.

Figure 5.35 shows the analytical reconstruction of the same data but with the application of XY PSA and Z-PSA3. Whilst the application of PSA was successful with the same separation of 6 cm with two sources of the same activity, from what is observed in Figure 5.35 it cannot be stated with confidence that two sources are observed. It is only through the knowledge of the location of the sources that a possible estimation could be made by interpreting the image slice. However this is not suitable when in a real scenario the location of the sources would be unknown.

A fit is not applied to the image profiles shown in Figure 5.34b or 5.35b due to the fact the fitting used on the imaging application assumed that it is one peak produced from a single source. Therefore the combined Lorentzian and Gaussian distribution poorly fits the profile, and so cannot be used to determine the FWHM or peak centroid position. Even when the user defines that two peaks are present, which has been used in previous figures, it is unable to apply the fit correctly.

The high-pass filter was then applied to the reconstructed images shown in Figures 5.34a & 5.35a. The cutoff frequency was optimised for each one separately, with values of 15 and 25 for Figures 5.34a & 5.35a respectively.

It is through applying the HPF to the reconstructed images that we are able to identify the presence of two sources. Figures 5.36 and 5.37 show the filter applied to the data with and without PSA applied. The asymmetrical nature of the slice and matrix shown in Figure 5.36 alludes to the distribution of

differing activity. It is only through PSA that we are able to observe two clear peaks representing the positioning of the two sources.

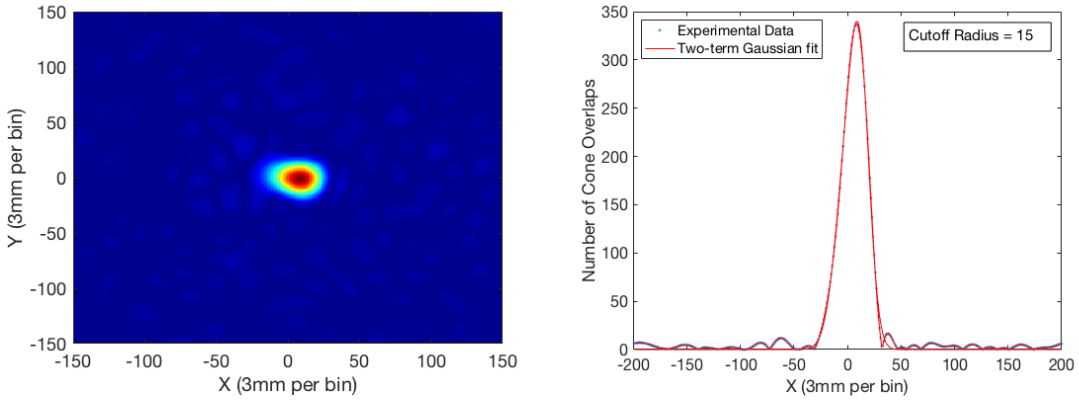

(a) (b)

Figure 5.36: High-pass filter reconstruction, with the intensity matrix (a) and image slice (b) of two ^{137}Cs sources of different activity placed at a separation of 6 cm without any applications of PSA. Cutoff radius of 15.

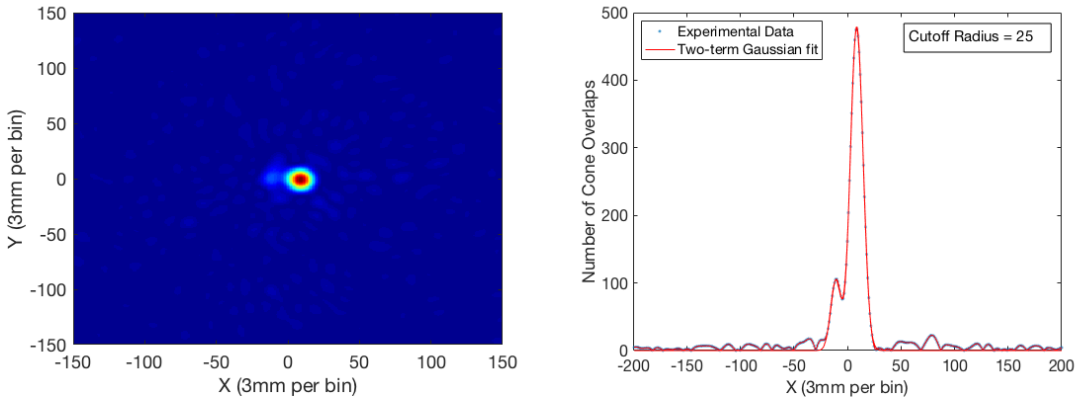

(a) (b)

Figure 5.37: High-pass filter reconstruction, with the intensity matrix (a) and image slice (b) of two ^{137}Cs sources of different activity placed at a separation of 6 cm with the application of XY and Z-PSA3. Cutoff radius of 25.

Whilst the two peaks cannot be clearly observed in the image slice, the two-term Gaussian is able to represent the extended profile, as shown in Figure 5.36b, with an R-Square value of 0.996. The centroid positions can be extracted from the Gaussian fit coefficients, albeit with larger errors on the position of the lower-activity source compared to previous fits, with centroid

positions of 1.5 ± 6.3 and 12.8 ± 0.8, leading to a calculation of **33.9 ± 6.4 mm** .

Figure 5.37a shows two clear peak centroids, and therefore the two-term Gaussian fit can be applied to the data to obtain the source separation. The peak positions were found from the Gaussian fit shown in Figure 5.37b, with a R-Square value of 0.992, and the separation calculated to be **59.4 ± 0.9 mm**. This is consistent with the experimental separation of 60 mm.

To show how the filtered profile compared to the original profile produced from the analytical image reconstruction, the two profiles were normalised and compared with each other. This is shown in Figure 5.38. The asymmetrical side to the profile corresponds to the position of the lower-activity source. The relative heights of the two peaks in Figure 5.38 were inconsistent with the relative intensities of source activities, with a value of 0.218 compared to 0.174.

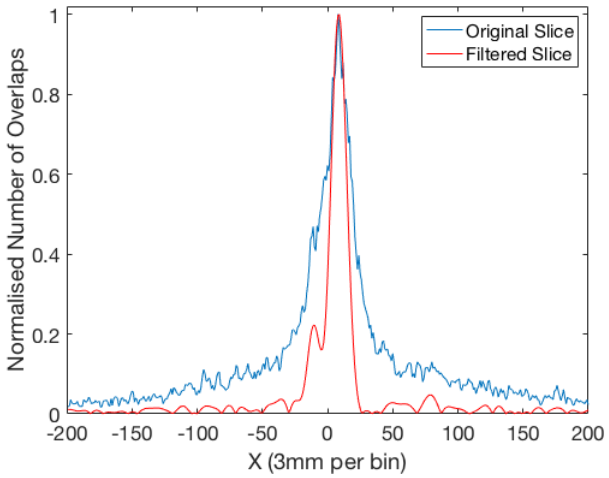

Figure 5.38: Comparison of the normalised intensity profiles from the original reconstruction and after the high-pass filter has been applied, after application of Z-PSA3. Measurement is of two ^{137}Cs sources of activities 0.041 & 0.235 MBq positioned at ($\pm$ 30, 0 , 450) mm.

5.3 ^{137}Cs Extended source measurement

Once the resolving power of the detector, and its imaging capability at this distance had been observed with point sources, the measurements with the extended source took place. Through these measurements, the affect of scattering material on the quality of imaging a distributed sample can be analysed through the use of a 'concrete wall'. Measurements in the laboratory consisted of:

- Extended source without the presence of scattering material.
- Extended source placed within a 'concrete wall'.

The extended source to be used in these measurements was from a soil sample created for a previous experiment, of length 18 cm and diameter 1.5 cm, as shown earlier in Figure 5.8. Liquid ^{137}Cs was fed through a vial containing soil, which was then sealed for the use in future measurements. The source has an activity of approximately 1.2 MBq.

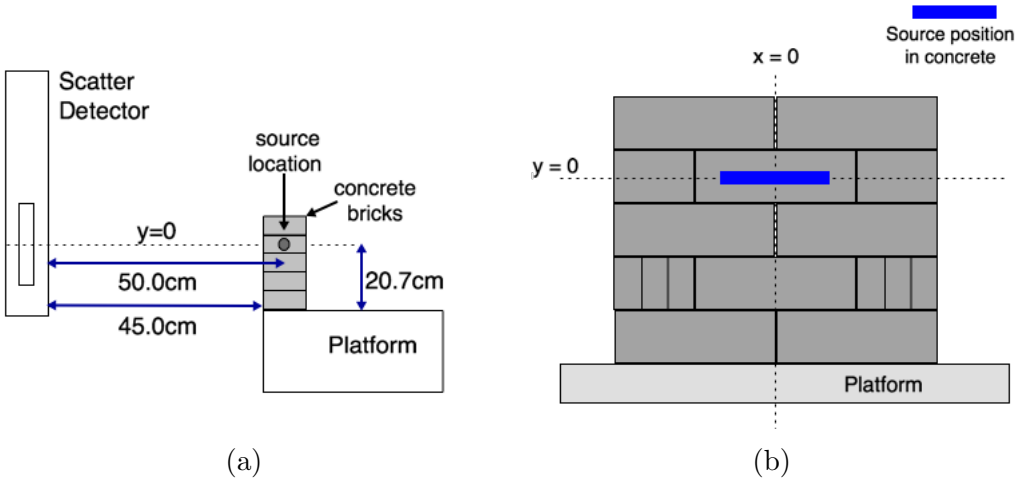

Figure 5.39: Schematic diagram showing the position of an extended ^{137}Cs source when placed within a concrete wall. (a) Side view showing the source-to-detector distance of 50 cm (b) View from the scatter detector face, with the brick containing the source positioned relative to x = 0 and y = 0.

When the concrete wall is included in the measurement, the edge of the bricks will be placed at the source-to-detector distance of 45 cm. This is the closest distance the cart can achieve when placed next to a wall, as shown in Figure 5.39. The extended source will be placed centrally within the brick, which

corresponds to a distance of 50 cm. When the concrete wall was not included in the experiment, the extended source was therefore placed at a distance of 50 cm for comparison.

The positions of sources in this section and Section 5.2 were placed with the positioning of the cart in mind for realistic measurement scenarios. Due to the separations considered in the previous section, the 5 cm difference in source-to-detector position should not significantly affect the overall quality of the results.

Due to the increased distance, there will be a reduction in imaging efficiency the further away from the detectors the sources are positioned. Also, as noted in previous work, the spatial resolution of the images and the ability to resolve multiple sources degrades at an increasing distance away from the detectors. If single point sources were to be investigated, then this change in source-to-detector distance would have a minor change on the quality of the images and suitable comparisons couldn't be made on detector response. Additionally, if the length of the extended source was shorter, then this change of distance could possibly have an affect on accurately noting the change in intensity across the sample.

Before the measurements with GRI+ began, the variation of activity through the sample was investigated to see how the distribution compared to the profiles that will be reconstructed once the measurements were taken. It was expected that the activity distribution within the soil sample would not be uniform, due to the nature of distilling liquid ^{137}Cs through the soil. A collimated scan of the soil sample showed the variation in activity through the vial.

A 3" $\times$ 3" NaI detector with a Voltage-Divider network across the photomultiplier tube, operating at a voltage of 900 V through a Canberra 3102 HV unit, was connected to a Canberra 2022 spectroscopy amplifier with a shaping time of 6 μs. Lead blocks were arranged to create a 1.5 cm slit-collimated scan of the sample, which allowed for 12 measurements to take place across the 18 cm length. It was not required to have a more precise collimation (1 cm or even a few mm) as the set collimation was sufficient to characterise the sample activity.

An energy spectrum was collected using the program ORTEC *Maestro*, with 4092 channels utilised across the energy spectrum. The net area of the 662 keV full-energy peak was recorded after a real-time period of 120 seconds. The count rate was then recorded against centimetre position of the sample as shown in Figure 5.40.

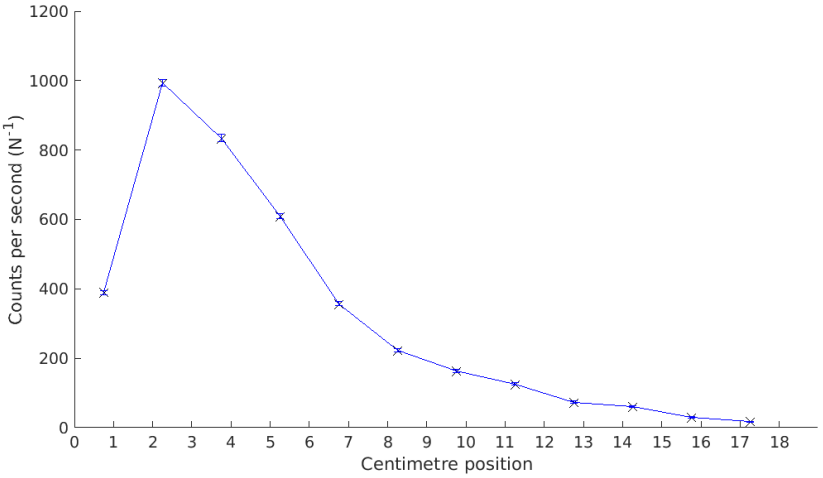

Figure 5.40: Graph showing the results of the collimated scan of the soil sample, showing the number of net counts per second relative to the detector's position along the source.

The non-uniformity of the sample was observed with a significantly 'hotter' end to the sample, as shown near the 3 cm position in Figure 5.40. This non-uniformity was the basis of the measurements detailed in Section 5.2.2.

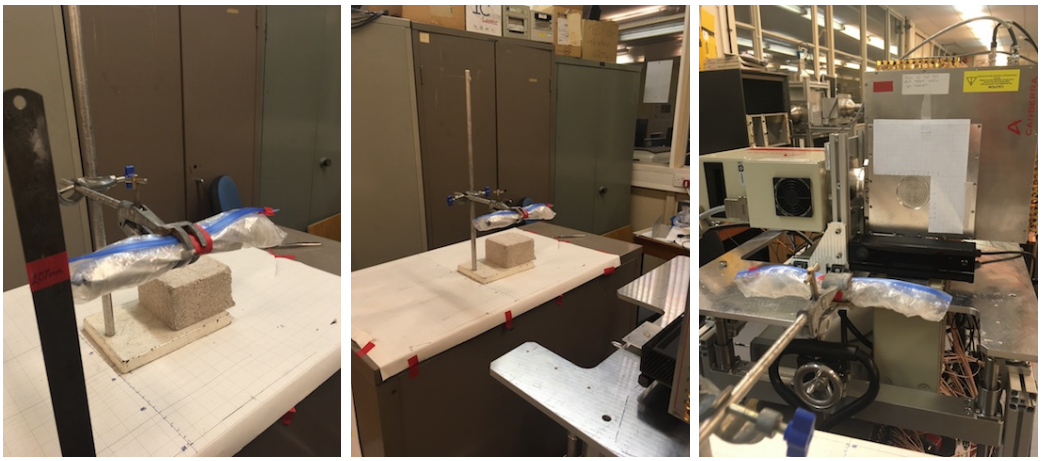

(a) (b) (c)

Figure 5.41: Images showing the experimental set-up of the ^{137}Cs extended source soil sample. (a) Aligning the height of the source to y = 0 (b) The source's position in Z to be used as a comparison when placed within the concrete brick (c) View in relation to the scatter detector face.

The extended source was first positioned relative to (0, 0), based on the position the source would be in the concrete wall as shown in Figure 5.39b. The source was held at this position using a clamp stand as shown in Figure 5.41,

at a standoff distance of 50 cm. Data was collected for almost 19 hours with a count-rate of 39 s^{-1}. A breakdown of the number of events used in the image reconstruction is found in Table 5.11.

Table 5.11: Breakdown of the number of events leading to the final analytically reconstructed image for an extended ^{137}Cs source of activity of approximately 1.2 MBq placed 50 cm away from the scatter detector face.

Parameter	Frequency	Percentage (%)
MWD interactions recorded	12 627 496	100
Real fold interactions	10 190 644	80.7
Number of 2 tier events	2 596 103	20.6
Fold [1 1 1 1] imageable events	629 780	5.0
Energy Gated imaged events	28 823	0.2

The data was reconstructed analytically with the use of XY PSA and the Z-PSA3 technique, using the same parameters defined in Table 5.1 (except for the source-to-detector distance). The high-pass filter was also applied to the reconstructed images to observe the improvement in image quality.

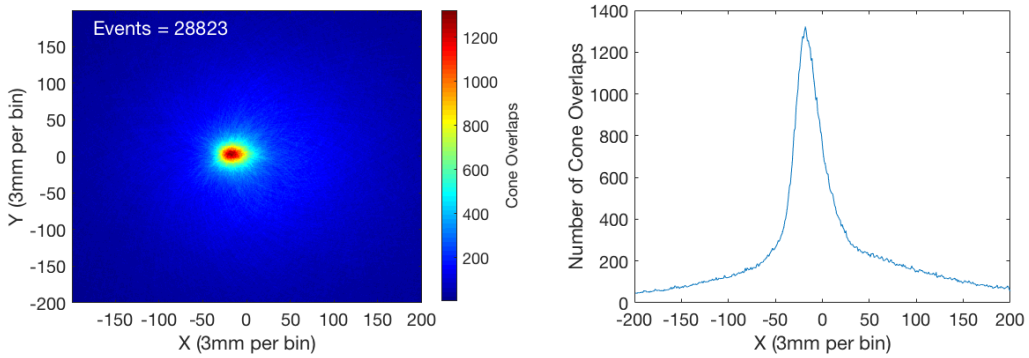

(a) (b)

Figure 5.42: (a) Analytical image reconstruction and (b) intensity profile of the ^{137}Cs extended source. The source was placed 50 cm away from the scatter detector face. 28 823 events were processed with use of XY PSA and Z-PSA3 techniques. Compression factor of 3 mm/bin.

Figure 5.42 shows the intensity matrix produced from the image reconstruction, and a slice through the point of maximum intensity in the X-direction. Similar to the images shown with the sources of differing activity, the profile is asymmetrical in nature. Comparitive to the collimated measurement of the sample, the profiles are similar, showing that the measurement provides a good

representation of the intensity of the radiation present in the sample. Due to the aysmmetry of the peak, and large background, a suitable fit of the peak could not be applied.

Once again, by filtering the image (Figure 5.43), a clearer definition of the extended source can be observed. A slice through the point of maximum intensity in the X-direction is seen in Figure 5.43b. The two-term Gaussian fit was applied to the profile to see if the peak centroid was consistent with the maximum count rate shown in Figure 5.40. The peak centroid obtained from the fit was found to be at -18.9 ± 0.1, which translates to -56.7 ± 0.3 mm after taking into account the compression factor of 3. The R-Square value for the fit was 0.994.

It can be deduced that the maximum count rate in Figure 5.40 is approximately 3 cm in to the 18 cm length. The center of the sample would have been positioned at (0, 0), 9 cm into the length of the source. The peak position obtained from the Gaussian fit shown in Figure 5.43b has the maximum -5.67 ± 0.03 cm away from the origin, which would be in close agreement with the location of the maximum point from the collimated profile.

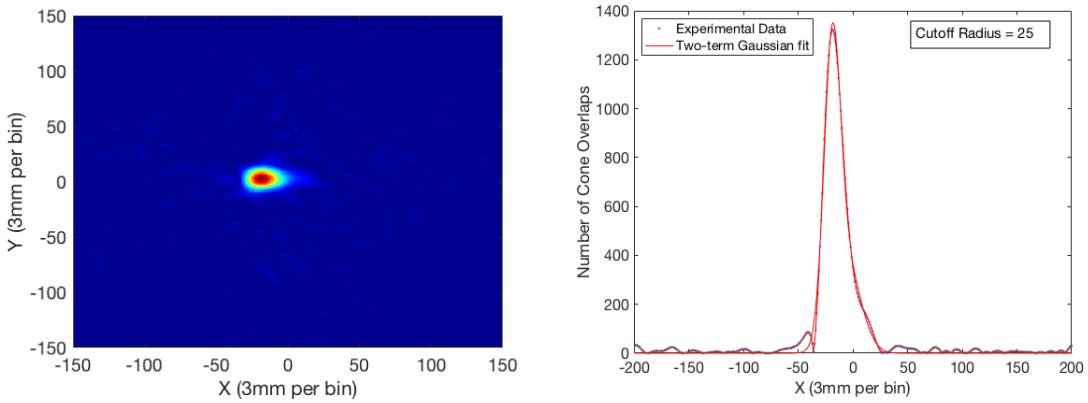

(a) (b)

Figure 5.43: High-pass filter reconstruction, with the intensity matrix (a) and image profile (b) of the extended ^{137}Cs source with XY PSA and Z-PSA3 techniques applied. Cutoff radius of 25. A two-term Gaussian fit was applied to the profile, with a R-Square value of 0.994.

The normalised profiles from Figures 5.42b & 5.43b were compared as shown in Figure 5.44. Additional vertical lines were included on the image to represent the length of the extended sample. It can be deduced that from the single, asymmetrical centroid present in Figure 5.43b, that there is a distributed source of radiation. The rising and falling edge of the filtered slice

also accurately matches with the length of the sample. These results can provide confidence that distributed radiation can be measured and the location identified.

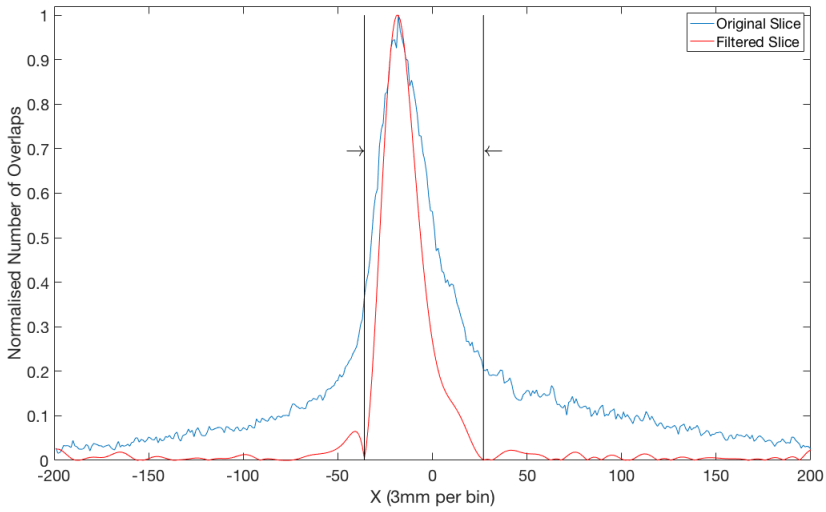

Figure 5.44: Comparison of the normalised intensity profiles from the original reconstruction of PSA data and after the high-pass filter has been applied for the distributed source. The additional vertical lines represent the length of the distributed source.

Whilst Figure 5.44 shows the ability of GRI+ to image distributed sources, the introduction of concrete will lead to increased scattering of photons, and the reduction of full-energy peak events used for imaging. In order to achieve the experimental set-up as shown earlier in Figure 5.39, the extended source would need to be placed within one of the concrete bricks. To accomplish this, a hole was drilled through the center of one of the bricks as shown in Figure 5.45.

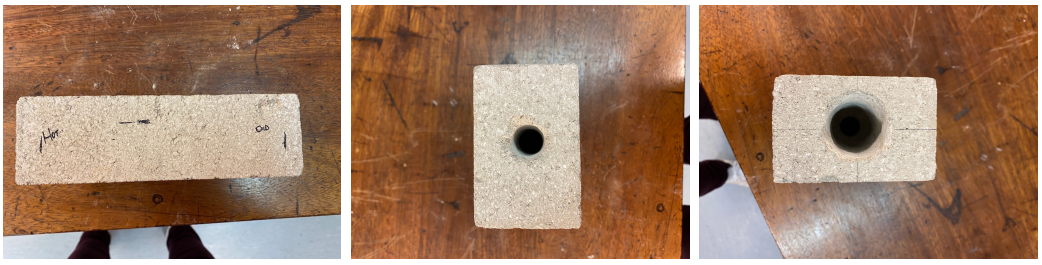

(a) (b) (c)

Figure 5.45: Images of the concrete brick that the ^{137}Cs extended source was placed in. (a) shows the estimation of where the source was placed within the brick, along with highlighting the 'hotspot' of the sample. (b) and (c) show the holes drilled within the brick.

Figure 5.45b shows the diameter of the sample (2 cm) so that it would be as close in contact to the brick as possible. Figure 5.45(c) was a larger hole drilled on the opposite side, of diameter 4 cm, to allow the full sample to be within the brick, due to a protuding 'lip' halfway through the sample, as shown earlier in Figure 5.8.

A concrete wall was set up based on the experimental schematic as shown in Figure 5.39b, with the bricks positioned to allow the midway point of the brick containing the extended source to fall at y = 0. Photos of the experimental set-up is shown in Figure 5.46.

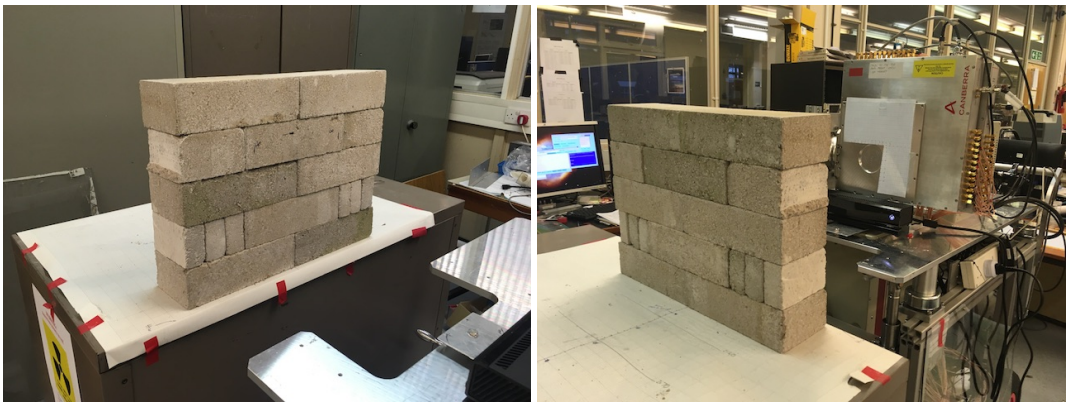

(a) (b)

Figure 5.46: Images showing the experimental set-up of the ^{137}Cs extended source soil sample placed within a concrete wall (a) Front-facing view (b) Rear-facing view.

Table 5.12: Breakdown of the number of events leading to the final analytically reconstructed image for an extended ^{137}Cs source of activity of approximately 1.2 MBq placed 50 cm away from the scatter detector face within a concrete wall.

Parameter	Number of Events	Percentage (%)
MWD interactions recorded	33 596 922	100.0
Real fold interactions	27 929 067	83.1
Number of 2 tier events	7 028 064	20.9
Fold [1 1 1 1] imageable events	1 918 063	5.7
Energy Gated imaged events	41 989	0.1

Due to the addition of the scattering material, data was collected for nearly 61 hours, nearly three times as long as the previous measurement. Even though the count rate for the measurement was 30 s^{-1}, the increased time for the

data to be collected was in order to collect more full-energy peak events for the image reconstruction. The breakdown of the events is shown in Table 5.12.

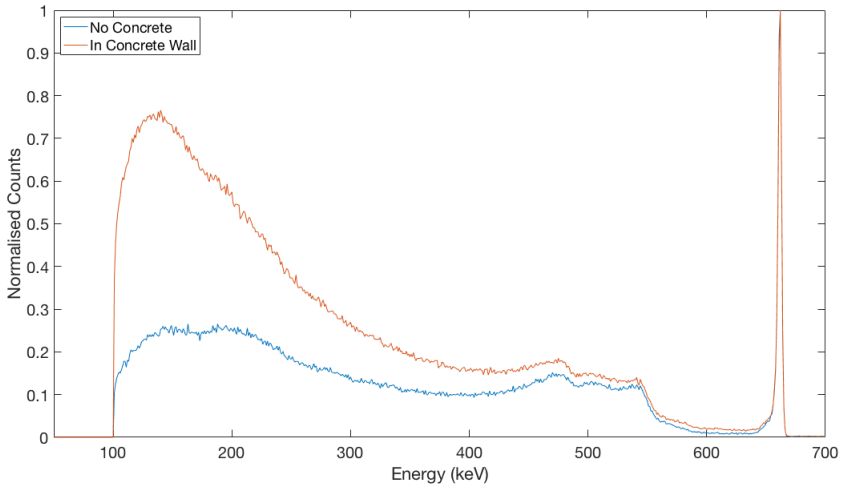

Figure 5.47: Normalised spectrum comparing the fold [1 1 1 1] coincidence data produced from a 1.2 MBq ^{137}Cs extended source with and without the presence of a concrete wall.

The coincidence spectrum of fold [1 1 1 1] events from the measurements with and without concrete is shown in Figure 5.47. Both spectra were normalised to the highest count in the 662 keV peak in their significant spectrum. The full-energy peak events in this spectrum are used for the analytical image reconstruction, as both reconstructions used the same energy gate of 658 - 666 keV. As can be seen, the inclusion of the concrete wall has led to a significant increase in the low-energy scattering aspect of the Compton continuum.

The analytical reconstruction of the energies shown in Figure 5.47, with the x, y and z positions from the application of PSA, is shown in Figure 5.48, with no energy gate applied, so 1 769 141 events are utilised in the image reconstruction. Despite the significant amount of lower-level background scattering, a hotspot is observed around the central brick. The reconstructed matrix includes the concrete brick set-up as seen in the schematic diagram of Figure 5.39b, which was added in separate analysis using Matlab. The positioning of each 'brick' was based on the distance between each length and cartesian image space co-ordinates of (0, 0). These were adjusted to the size based on the compression factor of the images.

Figure 5.49 then shows the image when the selected events for the image reconstruction fall between the defined energy gate of 658 - 666 keV, localising

the higher-intensity number of cone overlaps to the central brick, and removing the lower-energy scattering.

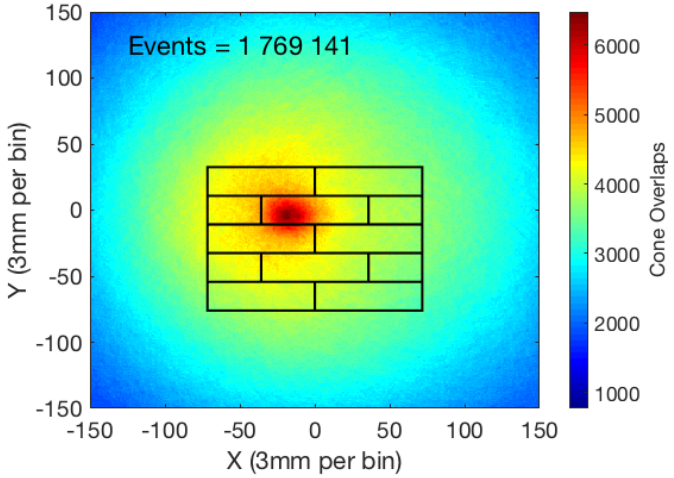

Figure 5.48: Analytical image reconstruction of the ^{137}Cs extended source placed within the concrete wall. The source was placed 50 cm away from the scatter detector face. 1 769 141 events were processed with use of XY PSA and Z-PSA3 technique. The experimental concrete set-up has been overlaid onto the matrix to show the positioning of all the bricks corrected for the compression factor of 3 mm/bin.

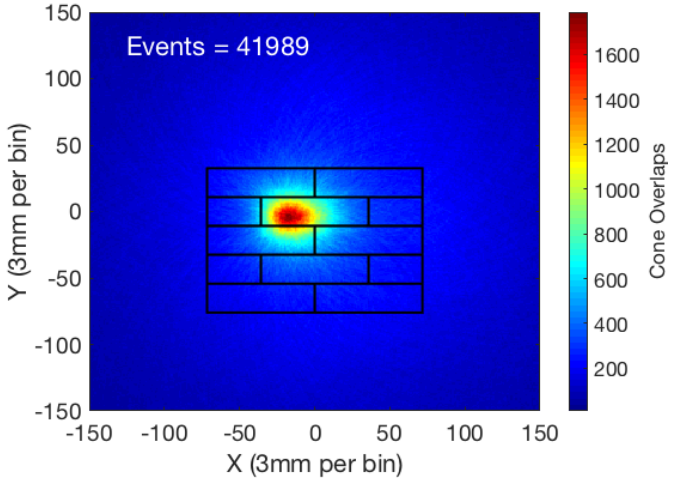

Figure 5.49: Analytical image reconstruction of the ^{137}Cs extended source placed within the concrete wall. The source was placed 50 cm away from the scatter detector face. 41 989 events were processed with use of XY PSA and Z-PSA3 technique. The experimental concrete set-up has been overlaid onto the matrix to show the positioning of all the bricks corrected for the compression factor of 3 mm/bin.

If the Compton continuum was gated upon (energies of 100 - 480 keV) rather

than the full-energy peak, the entire imaging space is filled with a large number of cone overlaps, with the most intense area encompassing the entire concrete wall and beyond. No information can be obtained from gating on the continuum, even though a significant amount of events are available due to the scattering of photons through the concrete. Section 5.5.2 investigates gating on different regions of the Compton continuum, and if it affects the quality of the image.

The high-pass filter was then applied to the reconstructed image and the image matrix was produced as shown in Figure 5.50. In this image, the positions of the concrete bricks were included again.

Figures 5.48, 5.49 & 5.50 locate the extended source to within the correct brick, as detailed in Figure 5.39b. The filtered image constrains the source to the one brick, unlike what is seen in the non-filtered figures. Some additional, low-intensity artefacts are observed within Figure 5.50, but could simply be down to the incorrect cut-off frequency assigned for the high-pass filter.

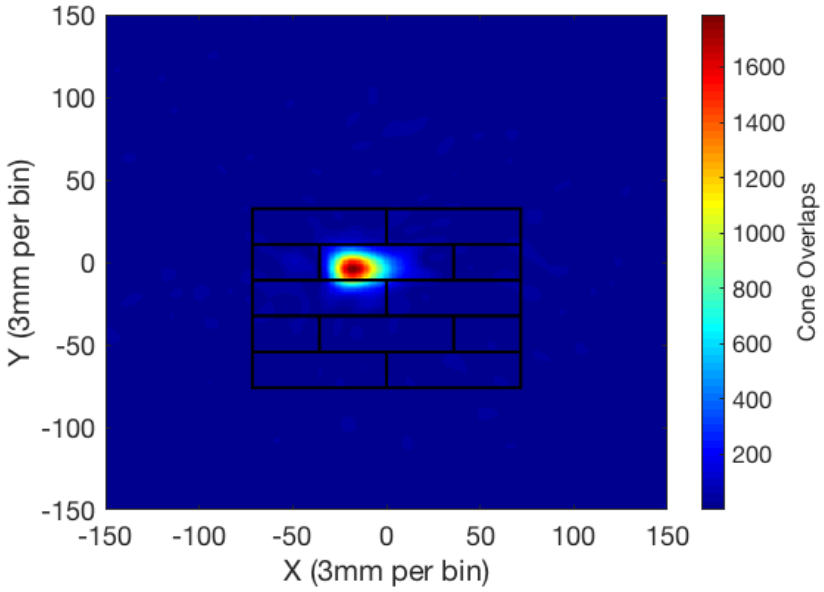

Figure 5.50: Intensity matrix produced after the application of the high-pass filter of the extended source placed within the concrete wall. The experimental set-up has been overlaid onto the matrix to show the positioning of all the bricks corrected for the compression factor.

A slice through the point of maximum intensity in the X-direction was produced from Figures 5.43a & 5.50, and the values were normalised so that they could be compared to each other. This is shown in Figure 5.51. Additional vertical lines are included on the figure to show the rising and falling edges of

the peak.

Despite a shift in the location of the falling edge of the slice from the concrete measurement, the overall shape of the two profiles is very similar. By calculating the separation between the two lines, an estimate can be determined for the length of the extended source.

The separation of the lines with and without concrete were 189 mm and 213 mm respectively. The inclusion of concrete has led to an increased estimation of the length of the extended source.

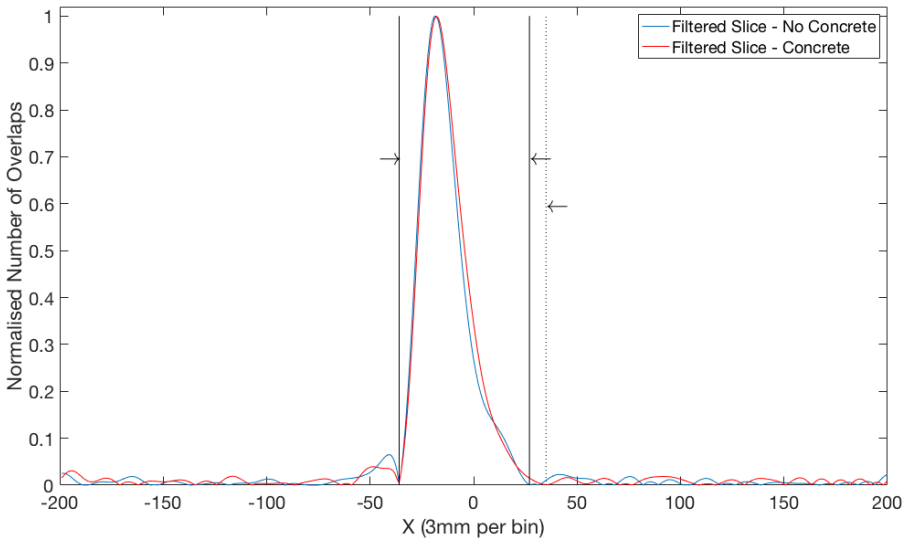

Figure 5.51: Comparison of the normalised intensity profiles from the high-pass filter image reconstruction for the distributed source, with and without the prescence of concrete. The additional vertical lines represent the length of the distributed source in the two mediums.

The measurement of the source within the concrete wall would have been measured over the same length of time that the measurement without the concrete wall had (19 hours) for a true comparison. However, due to a reduced number of full-energy peak events, it was decided to continue the data collection in order to increase the number of useable events for image reconstruction. The length of time for the measurement with the concrete wall (60 hours) would not be suitable in an industrial scenario.

A comparison of the total number of imageable events, to the number of imageable events that fall within the 658 - 666keV energy thresholds was made between the two measurements. The increased amount of imageable events available, and therefore the increased number of full-energy peak events, was

only due to the duration of the measurement. The percentage difference is shown in Table 5.13. It can be concluded from the table that the number of imageable full-energy peak events is reduced by nearly a factor of 2 with the introduction of scattering material.

Table 5.13: Table showing the percentage difference between the number of imageable events that fell within the applied energy gate of 658 - 666 keV, and the total number of imageable events produced from the text files in the measurement of the extended source with and without a concrete wall.

Run	Duration (h)	Full-Energy Peak Events	Total Imageable Events	Percentage (%)
No concrete	18.9	28,823	600,637	4.80
Concrete	60.8	41,989	1,769,141	2.37

The sample used however was approximately 1.2 MBq in activity, at a stand-off distance of 50 cm within a scattering medium. This sample was what was readily available in the laboratory as a distributed ^{137}Cs source. For measurements of sources of a higher activity, the length of time to collect a suitable number of full-energy peak events suitable for imaging would decrease.

5.4 Varying thicknesses of scattering material

A key area of interest in nuclear decommissioning scenarios is determining the thickness of material that a radioactive source has attenuated through. Assumptions are usually made over whether radioactive contamination is on the surface of a wall, or behind it. Cursory visual inspections of produced spectra take place or through examination of the ratio of the full energy peak compared to scattered components.

A near replication of the type of measurement done in industry is shown schematically in Figures 5.52 and 5.53. A collimated ^{137}Cs point source, of 15.6 MBq activity, was placed approximately 4 m away from a NaI scintillator detector and recorded over a period of 6 hours in a teaching laboratory in the Central Teaching Laboratories at the University of Liverpool. Directly in front of the source were several bricks of concrete of 21 cm thickness, to represent a wall scenario.

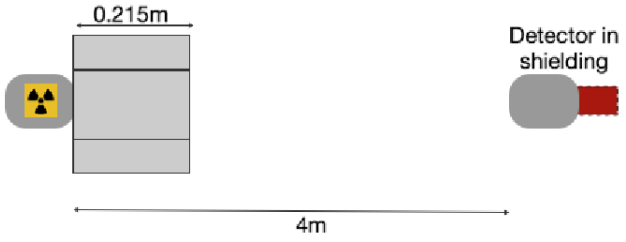

Figure 5.52: Schematic diagram (not to scale) of the experimental set-up to replicate a scenario at a nuclear facility to determine if a source of radioactivity is behind a concrete wall using a NaI scintillator detector.

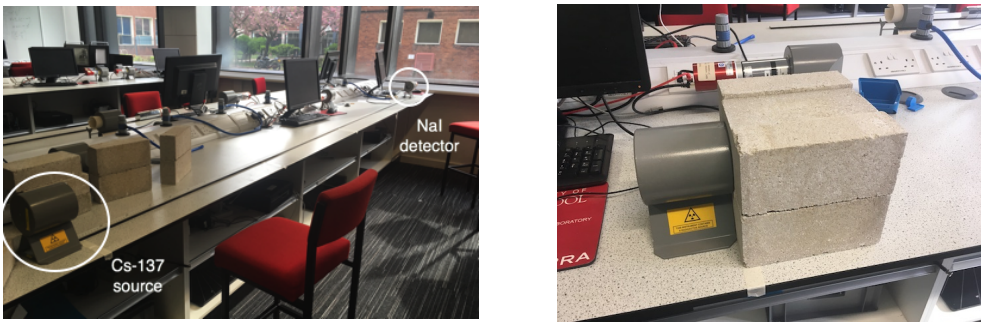

Figure 5.53: Images of the experimental set-up shown in the schematic diagram shown in 5.52.

The measurement was collected over a period of 6 hours to replicate the time of measurement observed in industry [32]. The spectrum was produced using ProSpect®, a gamma-spectroscopy software package used to analyse gamma-spectroscopy data [100].

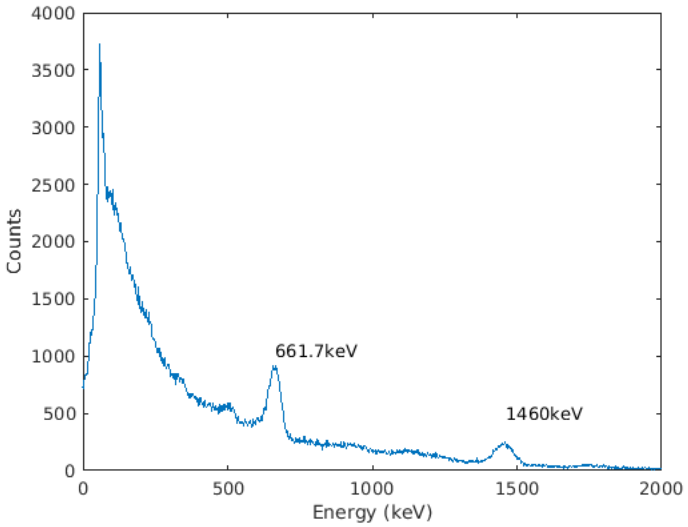

Figure 5.54: Gamma-ray energy spectrum produced using ProSpect software, from a 15.6 MBq collimated ^{137}Cs point source placed behind 21 cm of concrete material, at a standoff distance of 4 m using a NaI scintillator detector. The spectrum was collected over a period of 6 hours.

As it can be seen from the spectrum in Figure 5.54, the 662 keV full-energy peak can be observed, but there is a large region shown to the left of the peak due to the scattering of the photons through the concrete. The 1460 keV full-energy peak produced from the naturally occurring potassium-40 (^{40}K) radioisotope is also observed, which is likely present in the concrete bricks used during the measurement and the walls of the laboratory. This peak can be ignored as it is a characteristic background radiation source.

If no full-energy peak appears in the spectrum, it is usually concluded in [32] that the source of radiation is behind the wall. Whilst the 662 keV full-energy peak is present in the spectrum shown in Figure 5.54, the net peak area is largely reduced. The inclusion of the concrete would lead to a change in the peak-to-total ratio. The presence of the peak in this spectrum could be due to varying factors such as the stand-off distance, thickness of the concrete wall, or the activity of the source differing to those that may be present in a realistic nuclear facility scenario. These parameters were selected based on what was available in a laboratory setting.

Methods to determine the thickness of concrete a gamma ray has attenuated through has been investigated previously [101]. This method investigated the ratio between the 662 keV gamma-peak and 30 keV X-ray through varying thicknesses of concrete material to produce the following relationship with respect to the concrete thickness, d:

$$d = \frac{1}{\mu_X - \mu_\gamma} log_e \frac{R_0}{R_{X/\gamma}} \tag{5.1}$$

In Equation 5.1, R_0 and $R_{X/\gamma}$ represents the ratios of the intensities at zero depth and depth d respectively. μ represents the linear attenuation coefficients of the X- and γ radiation with concrete.

This method cannot be utilised with measurements taken for imageable data from GRI+ due to the inability to observe the ^{137}Cs X-ray in the coincidence energy spectra. This can be seen in Figure 5.55, which shows the coincidence energy spectrum of fold [1 1 1 1] events of a ^{137}Cs point source, and the lack of the 30 keV X-ray.

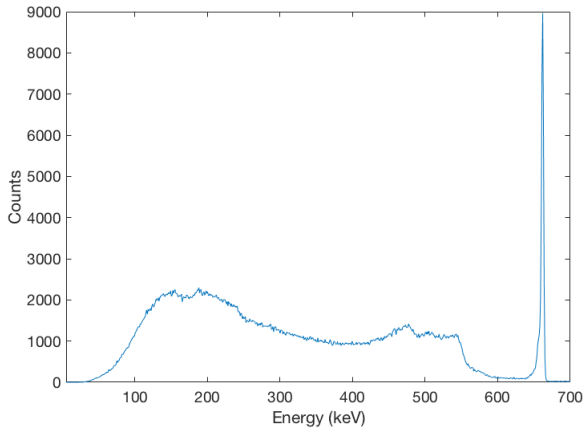

Figure 5.55: Coincidence energy spectrum of ^{137}Cs from fold [1 1 1 1] events collected with GRI+.

In the 2-tier Compton camera set-up, it is highly unlikely that the 30 keV X-ray will be observed. For this event to occur, the 30 keV energy will have to be divided across the scatterer and absorber detectors within the set coincidence window. Due to the low-energy of the X-ray, it is highly probable that it will be photoelectrically absorbed in the scatterer. Any observation of the ^{137}Cs X-rays is likely to be from additional summed photopeaks which arise from undesirable coincidence events with part of the 662 keV gamma ray. As well as

this, the low-energy thresholds of individual strips ($\sim$ 10 keV) means that any scattered photons from the 30 keV X-ray most likely fall below these defined thresholds, meaning the X-ray is not observed from the energy spectrum.

Therefore, in order to obtain additional information from a Compton image, an alternative method would need to be used which utilises the imageable data. With the increasing amount of concrete material present, more scattering would take place, therefore increasing the amount of data present in the Compton continuum of a spectrum. Therefore the peak-to-total ratio was investigated as the thickness of concrete material increased.

The **peak-to-total** ratio (P_T) is a way to relate the total and peak efficiencies. As mentioned earlier in Section 3.2, it is defined as the net counts in the full-energy peak area against the gross total number of events in a spectrum. The gross counts are conventionally taken from above 100 keV so as to remove the contribution from X-rays. This ratio can help show the sensitivity of external effects such as scattering from nearby objects. The peak-to-total ratio is primarily used for quantifying the performance of a gamma-ray detector, and it is not commonly used in decommissioning analysis. The priority is being able to map the contamination and to additionally quantify the radiation [29].

(a) (b)

Figure 5.56: Images showing a concrete divided into six relatively equal segments in relation to a standard concrete brick.

In general, the average thickness of a concrete wall is approximately 20.3 cm. The length of the bricks used in the measurements described in Section 5.3 measured at 21.5 ± 0.5 cm. One of these bricks was divided into six relatively equal segments to allow for a varying thickness of concrete to be measured up to the maximum thickness of 21.5 cm, a close approximation to the average thickness of a concrete wall used in construction. Figure 5.56 shows images

of the brick segmented into 6 pieces and placed in comparison to one of the untouched concrete bricks.

As with the previous measurements in this chapter, the surface of the concrete will be situated near the minimum distance that the cart can be pushed up against, to simulate a realistic scenario of measuring a wall. To allow for the maximum thickness of concrete to be situated infront of the source at the minimum defined distance of 45 cm, the source was placed at a distance of 65 cm away from the scatter detector face. This is shown in the schematic diagram in Figure 5.57.

Due to the increased distance, and the amount of scattering material that was used for the measurements, a higher-activity source was required. For these measurements, a 15 MBq ^{137}Cs point source was used. The point source was positioned close to the cartesian image co-ordinates of (0, 0). Figure 5.46b shows a photo of the source being aligned to y = 0.

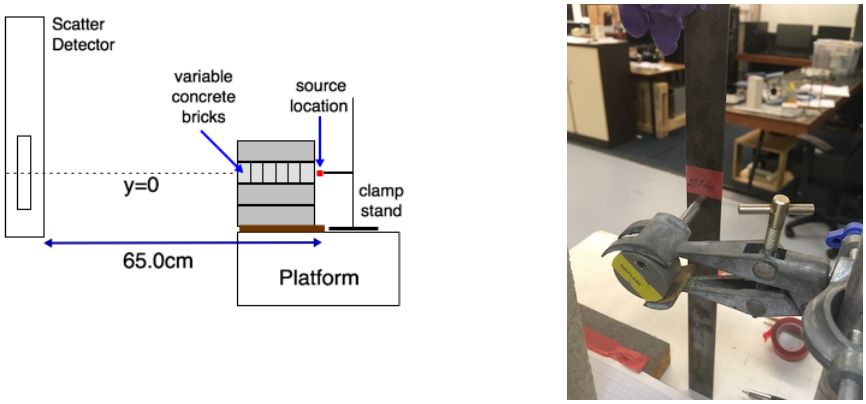

(a) (b)

Figure 5.57: (a) Schematic diagram showing the position of a ^{137}Cs point source at a source-to-detector distance of 65 cm, situated behind varying thicknesses of concrete bricks. (b) Image showing the setting of the source height to y = 0.

Additional concrete bricks were included to allow the source and the smaller bricks to be situated relative to the central axis of the detector system as shown in Figure 5.58. The extra bricks also create additional scattering for the source, something which helps create a more realistic scenario if trying to replicate an in situ measurement of a wall.

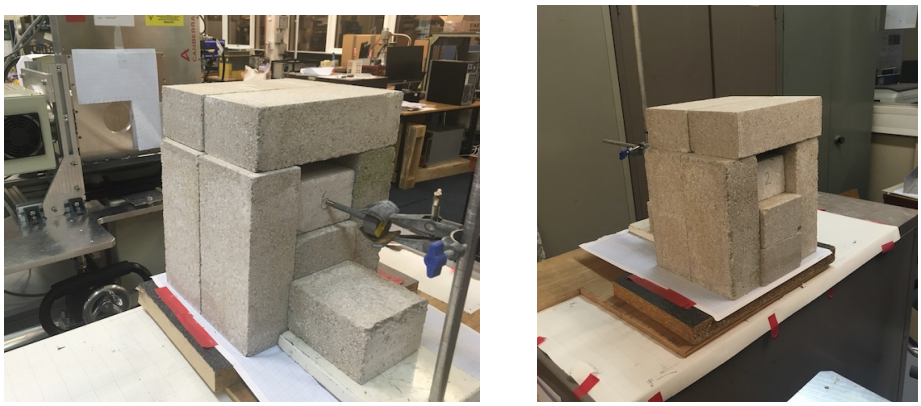

(a) (b)

Figure 5.58: Images showing the experimental set-up (a) The source aligned to the segmented concrete (b) Alternative view where one of the bricks has been removed.

Where possible, data was collected until the net counts in the 662 keV full-energy peak area was close to 10, 000 counts. A breakdown of the number of events for each measurement can be found in Appendices A and B. The net peak areas and the time it took to collect those events are shown in Table 5.14. The net peak areas were found utilising the GF3 program. The associated errors on the net peak areas were on account of the fit of the full-energy peak.

In Table 5.14, the 0 cm measurement represents that there was no concrete material directly infront of the ^{137}Cs point source, but the remaining bricks as shown in the experimental images in Figure 5.58 remained present.

Table 5.14: Table showing the net peak area of the 662 keV ^{137}Cs peak in a coincidence spectrum from fold [1 1 1 1] DC events, as a function of concrete thickness, and the time it took for the measurement to take place.

Concrete thickness (cm ± 0.1 cm)	Net Peak Area	Time (hours)
0.0	9146 ± 109	4.60
3.5	9016 ± 107	5.31
7.0	10770 ± 118	8.06
10.5	8295 ± 104	7.43
14.0	10069 ± 145	12.91
17.5	8147 ± 119	15.32
21.0	8643 ± 300	28.10

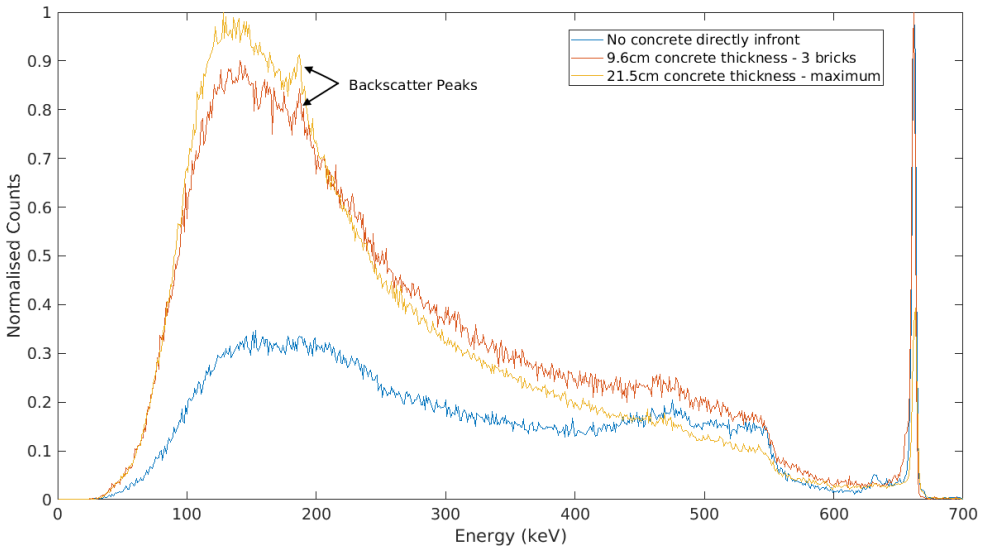

Figure 5.59: Figure showing three different normalised coincidence spectra of a 15.6 MBq ^{137}Cs source passing through varying thicknesses of concrete material.

The coincidence energy spectra from fold [1 1 1 1] DC events were analysed for the peak-to-total values. A comparison of the spectra from three different thicknesses of concrete is shown in Figure 5.59.

As can be seen in Figure 5.59, the low-energy part of the Compton continuum increases due to more photons scattering with the increased thickness of concrete placed infront of the source. It shows that there is not a significant amount of additional scattering between the half-thickness of three bricks, and the maximum thickness of concrete. The backscatter peaks are also more prominent in the spectra involving concrete, as labelled on Figure 5.59. The spectrum also shows that at the maximum thickness, the higher-energy region of the Compton continuum, representing the forward-scattered 662 keV events, reduces in comparison to the other two distributions.

The net areas of the 662 keV full-energy peaks produced from each thickness of concrete were compared to the gross area of the spectra above 100 keV to determine the peak-to-total (P_T) ratio. The natural log of the P_T ratio of these two values was plotted against the thickness of concrete as shown in Figure 5.60.

As shown in Figure 5.60, a linear relationship is observed. A linear regression was computed against the linear model shown in Figure 5.60. An R-square value of 0.9937 was obtained for the linear equation of $-0.066x + 1.339$. This

relationship could provide the basis for future in situ measurements which is discussed in Chapter 6.

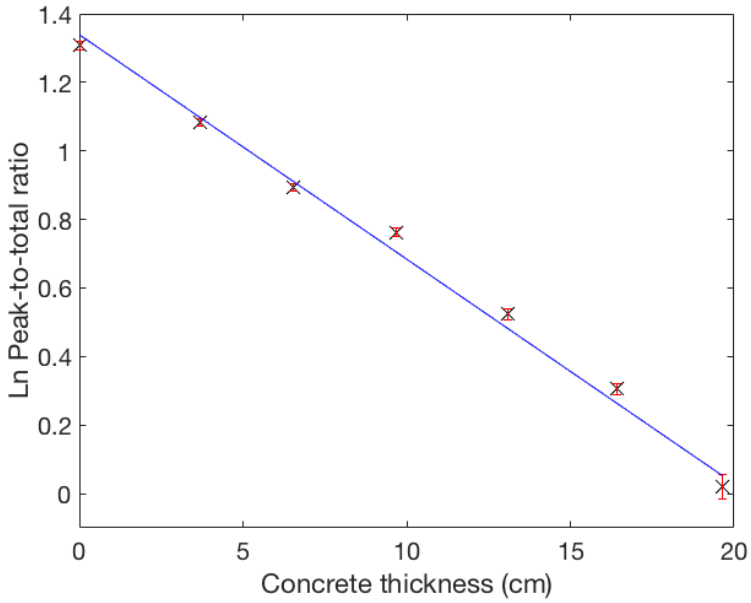

Figure 5.60: Graph showing the relationship between the Ln of the peak to total ratio and the thickness of concrete material.

5.5 ^{137}Cs point source analysis at large standoff distances

A high-activity 15.6 MBq ^{137}Cs point source was used for measurements to assess the Compton camera's imaging capability at large standoff distances. These distances varied upto a maximum standoff of 2.5 m. The point source was also used as a basis for measurements including scattering material as described below:

- Point source at large standoff distance
- Point source placed behind a 'wall'
- Point source placed infront of 'wall'

5.5.1 Angular Resolution

Previously, the angular resolution was investigated here [102] with GRI+ to see how the affect of applying different PSA techniques to the absorber detector improved the resolution. An angular resolution of approximately 11 degrees in the X direction was obtained with parametric XYZ PSA applied to the absorber detector, and without any PSA applied to the scatterer. In comparison to other industrial systems that were detailed in Section 2.3.1, the other Compton Camera, the Polaris-H detector, had an angular resolution of 30 degrees during real-time measurements, which could be improved to 20 degrees through post-processing of the data.

By including parametric PSA techniques to the scatterer detector as well as the absorber, the angular resolution should improve from the 11 degrees investigated previously. The angular resolution was calculated for three measurements that had been collected during the data campaign. All measurements involved a 15.6 MBq point ^{137}Cs source situated without the presence of any scattering material present. The distances that were used were 68 cm, 100 cm and 250 cm. These measurements could not be compared to the results found previously due to variations in the experimental set-up, such as a larger cryostat separation.

The data was reconstructed analytically, with the use of X-Y PSA for the positions of interactions in both the scatter and absorber, and Z-PSA3 for the absorber detector. The parameters used for the previous images in this

chapter were kept the same.

Another parameter that can be defined in the reconstruction is the image space size. A 400 × 400 matrix, (set as a value of 1200 in the application) was used in the reconstructions in the earlier sections to this chapter. In order to get a suitable Gaussian fit on the background events on the image, the image space size was increased from 1200 to 1600 for the measurements. The angular resolution value can vary if the space size is set too small.

Table 5.15: Breakdown of the number of interactions leading to the final analytically reconstructed image for a 15.6 MBq ^{137}Cs source placed at distances of 68 cm, 100 cm and 250 cm.

Parameter	68 cm		100 cm		250 cm	
	Events	Percentage (%)	Events	(%)	Events	(%)
Number of incident γ	2.38×10^{10}	-	1.12×10^{10}	-	2.44×10^{10}	-
MWD interactions recorded	46 202 981	100.0	31 149 382	100.0	31 612 113	100.0
Real fold interactions	20 397 360	44.1	21 252 184	68.2	28 200 338	89.2
Number of 2 tier events	8 329 901	18.0	23 504 740		6 663 082	21.0
Fold [1 1 1 1] imageable events	725 819	1.6	38 461	0.1	2 115 615	6.7
Energy Gated imaged events	31824	0.07	1 679	0.01	94 601	0.30

As can be seen in Table 5.24, the breakdown of interactions and events for the measurement at 100 cm shows an error of arising from the data acquisition, which is stating that there are more 2-tier events than there are real fold interactions. The 38 461 imageable events were collected when the DAQ system was successfully reading out all 48 strips during the measurement. A condition in the sortcode is that an imageable event won't be printed unless all 48 strips have been read out. However, part-way through the measurement, the DAQ system crashed and it continued to read out information from random combination of strips. These random interactions have lead to false coincidences observed in the 2-tier system, and hence the additional number of observed 2-tier events compared to real fold interactions. Due to time limitations, this measurement could not be repeated for a sufficiently long measurement.

Figures 5.61 - 5.63 show the intensity matrices and image profiles for the measurements at these three distances, along with showing the applied fits to the profiles. The quality of Figure 5.62a is largely due to the lack of events in the reconstructed image. As there are only 1679 full-energy peak events that are used for the image reconstruction, there is only approximately 70 cone overlaps in the point of maximum intensity in the image. The lack of events leads to the particularly noisy image, despite the compression factor of

all images being 3 pixels/mm. This will likely contribute to the slightly larger error in Table 5.16 compared to the other two values. A full breakdown of events from the three measurements can be found in Table 5.24.

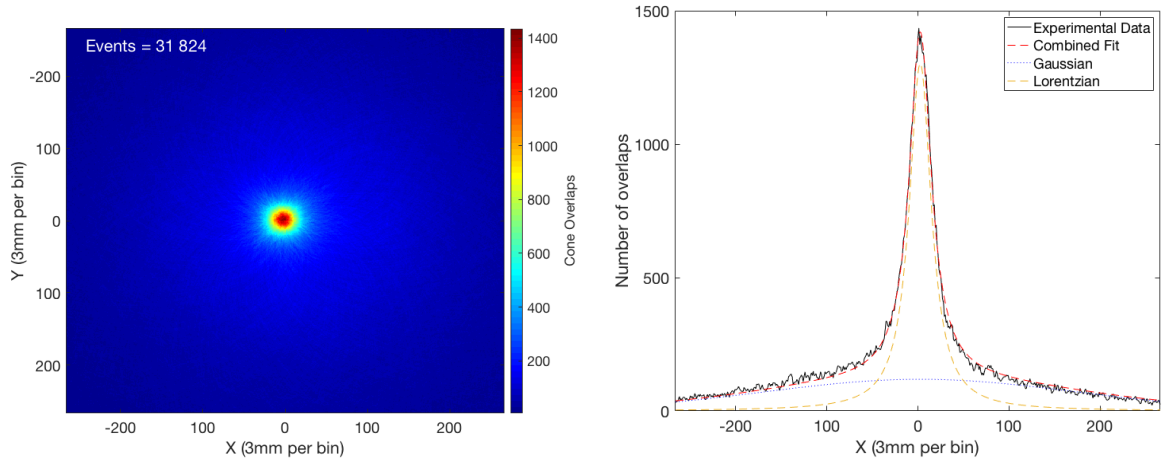

(a) (b)

Figure 5.61: Analytical reconstruction (a) and intensity profile with applied combined Lorentzian and Gaussian fit (b) of fold [1 1 1 1] coicindence events with the application of XY PSA and Z-PSA3, from a ^{137}Cs point source placed 68 cm away from the scatter detector face. 62 018 full-energy peak events were used in the reconstruction, with a compression factor of 3 mm/bin.

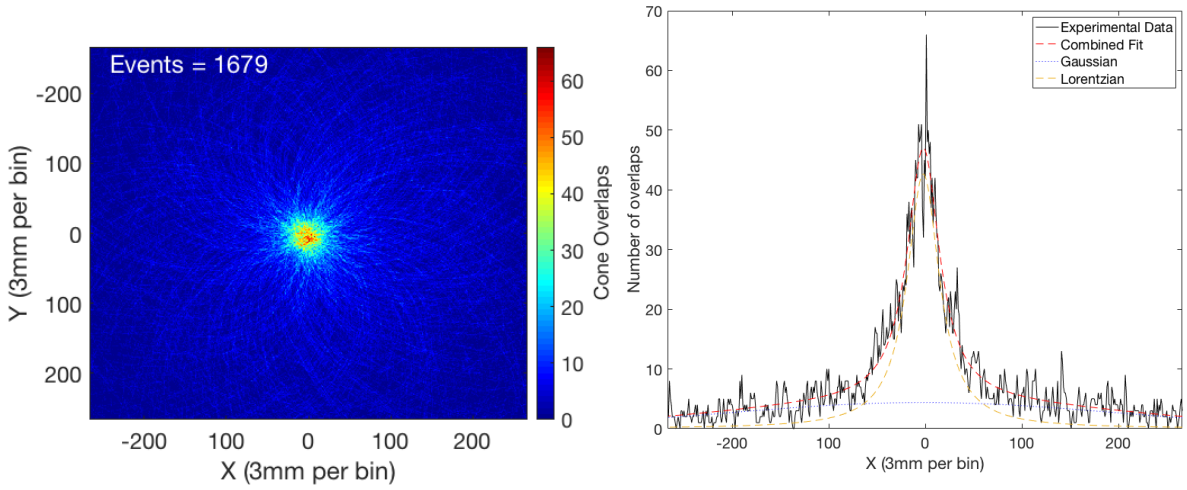

(a) (b)

Figure 5.62: Analytical reconstruction (a) and intensity profile with applied combined Lorentzian and Gaussian fit (b) of fold [1 1 1 1] coicindence events with the application of XY PSA and Z-PSA3, from a ^{137}Cs point source placed 100 cm away from the scatter detector face. 1 679 full-energy peak events were used in the reconstruction, with a compression factor of 3 mm/bin.

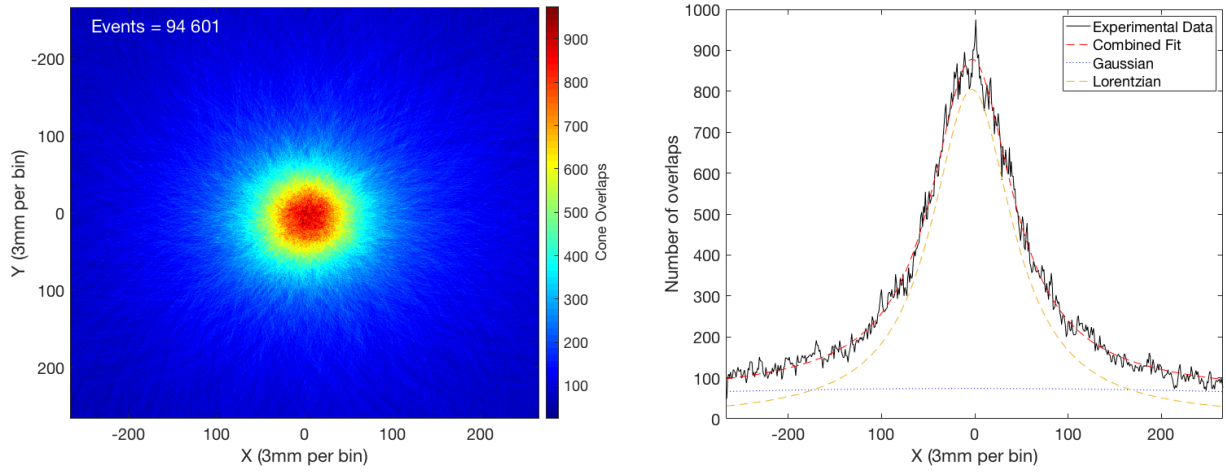

(a) (b)

Figure 5.63: Analytical reconstruction (a) and intensity profile with applied combined Lorentzian and Gaussian fit (b) of fold [1 1 1 1] coicindence events with the application of XY PSA and Z-PSA3, from a ^{137}Cs point source placed 250 cm away from the scatter detector face. 94 601 full-energy peak events were used in the reconstruction, with a compression factor of 3 mm/bin.

The FWHM calculated from these fits are used in Equations 3.36 & 3.37 to determine the angular resolution, the results of which are shown in Table 5.16. The errors shown in Table 5.16 were calculated based on the errors on the FWHM from the fit and the solid angle from the distance from the source to the detector.

The results shown in Table 5.16 show how the inclusion of the scatterer parametric XY PSA has improved the angular resolution from the previously obtained 11 degrees [102] to an average value of 7.19 ± 0.26 degrees from the results above, which included a run in which the number of statistics was limited due to a DAQ failure.

Table 5.16: Angular Resolution of GRI+ at various standoff distances with PSA applied

Distance (cm)	Resolution (degrees)	FWHM (mm)
68	7.35 ± 0.05	87.91 ± 0.63
100	6.96 ± 0.23	122.13 ± 3.96
250	7.25 ± 0.10	317.14 ± 4.29

An angular resolution of approximately 7 degrees, evaluated at distances of up to 2.5 m, is a promising characteristic demonstrated by the GRI+ system,

especially in comparison to other gamma-imaging system. This value could even be improved upon further with the use of database PSA.

5.5.2 Effects of concrete

The purpose of this measurement was to investigate the effects scattering material would have on the quality of the image, and if it was possible to restore any lost events due to the effects of scattering.

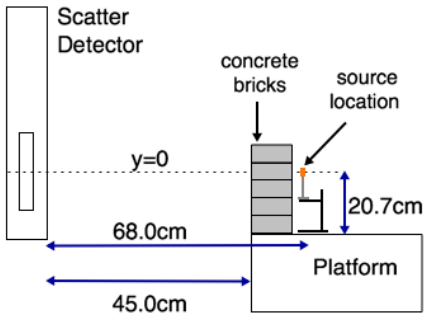

Figure 5.64: Schematic diagram of the measurement of a high-activity ^{137}Cs point source at a standoff distance of 68 cm, behind a concrete wall.

Section 5.4 showed that a relationship between the thickness of scattering material and the peak-to-total ratio of the coincidence energy spectra can be achieved. However, when measuring contamination in decommissioning scenarios, an image of the source of radiation is required to identify the location. The introduction of a scattering medium, as shown in Sections 5.3 & 5.4, will reduce the number of full-energy peak events which will be used for image reconstruction. Therefore a lot of useable events could be lost in the image reconstruction when a gate is applied over the full-energy peak of interest. It is not feasible to simply increase the duration of the measurement taken in situ. Therefore, this section will explore if any additional events from the coincidence spectra can be used in the image reconstruction without degrading the quality of the image.

The 15.6 MBq ^{137}Cs point source was imaged at a stand-off distance which allowed the set-up of a concrete wall, as shown in Figure 5.64. The ^{137}Cs source was first measured without any concrete material present at a distance of 68 cm. This measurement was to provide a basis for the images to be compared to when concrete was placed in between the source and the detector. This

distance also allowed the edge of the brick to be 48 cm away from the scatter detector face. It wasn't placed at the closest feasible distance of 45 cm due to an additional measurement taken place (not described in this thesis), where the point source was placed in front of the wall (Figure 5.65).

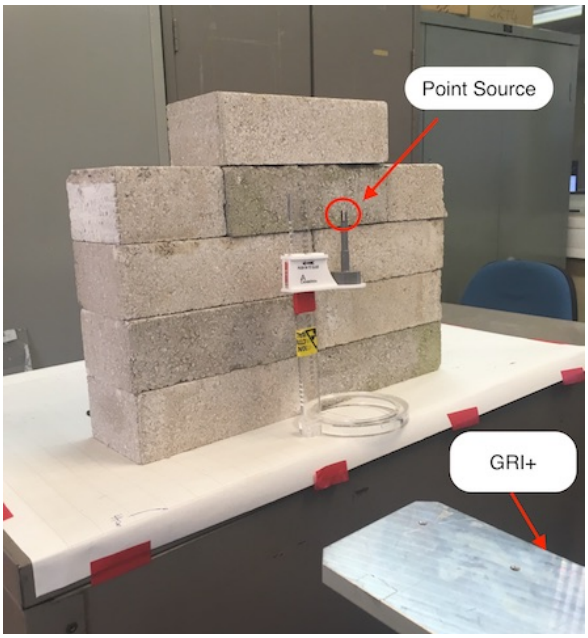

Figure 5.65: Photo showing the experimental set-up of a 15.6 MBq ^{137}Cs point source placed in front of a concrete wall. The Compton Camera is situated to the right of this image (off-photo), part of the metal cart is seen in the bottom-right of the image.

Fold [1 1 1 1] coincidence data was collected with a count rate in the DAQ of 160 s^{-1}, and the text files produced from MTSort were analytically reconstructed using X-Y PSA and Z-PSA3 and DC-face energies. The breakdown of the events used in the image can be seen in Table 5.17.

Table 5.17: Breakdown of the number of interactions leading to the final analytically reconstructed image for a 15.6 MBq ^{137}Cs source placed 68 cm away from the scatter detector face.

Parameter	Frequency	Percentage (%)
Number of incident γ	1.15 $\times 10^{10}$	-
MWD interactions recorded	46 202 981	100.0
Real fold interactions	20 397 360	44.1
Number of 2 tier events	8 329 901	18.0
Fold [1 1 1 1] imageable events	725 819	1.6
Energy Gated imaged events	31 824	0.06

Similar to the previously reconstructed images in this chapter, the parameters defined for the imaging application remained the same (Table 5.1), except for the source-to-detector distance and the image space size was increased from 1200 to 1600 to obtain a more accurate background fit. The combined Lorentzian and Gaussian fit was applied to the profile produced at an X-slice through the point of maximum intensity. The FWHM of the peak from this fit was recorded to show the image resolution. The reconstructed image and the profile can be seen in Figure 5.61a.

The measurement was then repeated with the inclusion of the concrete wall, as shown in the experimental images in Figure 5.66 utilising the same parameters. The inclusion of the concrete wall reduced the observed count rate to 70 s^{-1}. A breakdown of the number of events used in the image reconstruction can be seen in Table 5.18.

(a) (b)

Figure 5.66: Images showing the experimental set-up of a 15.6 MBq ^{137}Cs point source placed behind a concrete wall.

Table 5.18: Breakdown of the number of interactions leading to the final analytically reconstructed image for a 15.6 MBq ^{137}Cs source placed 68 cm away from the scatter detector face, behind a concrete wall.

Parameter	Frequency	Percentage (%)
Number of incident γ	2.38 $\times 10^{10}$	-
MWD interactions recorded	57 896 783	100.0
Real fold interactions	40 193 281	69.4
Number of 2 tier events	11 211 235	19.4
Fold [1 1 1 1] imageable events	2 052 513	3.5
Energy Gated imaged events	33 040	0.06

A comparison of Tables 5.17 & 5.18 shows how the number of energy gated events reduces to 0.06 % of those recorded by the sortcode when concrete is included, despite the percentage of fold [1 1 1 1] imageable events increasing by an additional 1.9 %.

Figure 5.67 shows the normalised spectrum comparing the two fold [1 1 1 1] coincidence energy spectra with and without the presence of the concrete wall. By looking at the coincidence spectra of the two measurements, as shown in Figure 5.67, it can be observed how the low-energy part of the Compton continuum changes with the inclusion of scattering material. The normalised spectra shown in Figure 5.67 show a similar profile through the Compton continuum, which could be beneficial when selecting additional energy gates. A small peak is present in the spectrum involving concrete at 632 keV. The presence of this peak could be due to ballistic deficit; a loss of the pulse amplitude due a problem with the shaping process. However, the cause for this peak is due to a gain-shift from a strip during this measurement, leading to a miscalibration.

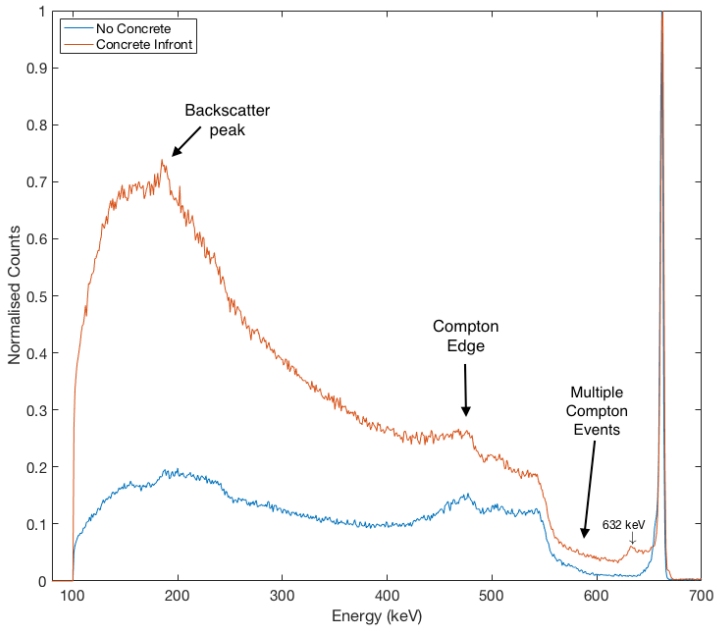

Figure 5.67: Figure showing the fold [1 1 1 1] coincidence spectra produced of a 15.6 MBq ^{137}Cs source positioned at (0, 0, 68) cm with and without the presence of a 10 cm thick concrete wall.

The key features of a gamma-ray energy spectrum can be identified on Figure 5.67. The backscatter peak, Compton edge and region of multiple Compton events leading up to the full-energy peak can all be identified. There is an

additional feature shown in the figure, which is not attributed to the inclusion of concrete as it is present on both spectra, as well as other spectra shown in this thesis. The Compton edge from a 662 keV gamma ray should be seen around 480 keV, where a photon has scattered by an angle of 180°, which is labelled on Figure 5.67. This additional region, between 500 - 550 keV, also seems to have a Compton edge. This feature could arise from summed coincidence events from scattering photons, which are observed more prominantly due to the increased standoff distance.

The text files produced from the coincidence spectra shown in Figure 5.67 were analytically reconstructed with energy gates of 658 - 666 keV, and the FWHM of the peaks produced in the image slices were recorded. Table 5.19 shows the effect the concrete wall has on the image resolution.

The increased percentage of fold [1 1 1 1] events can be explained by the increased number of scattered events that are present in the large Compton continuum, as seen in Figure 5.67. The table also shows the percentage of full-energy peak events from the total number of fold [1 1 1 1] imageable events that were used for the coincidence spectrum shown in Figure 5.67, which can also be represented by the peak-to-total ratio.

Table 5.19: Image Resolution of GRI+ at 68 cm with and without concrete, and the percentage of events used in the image from the total number of useable imageable events.

	FWHM (mm)	Peak-to-Total
Without concrete	87.93 ± 0.62	5.43
With concrete	87.91 ± 0.63	2.10

Table 5.19 shows that even with the inclusion of the concrete wall, the image resolution barely changes, despite a significant loss of full-energy peak events due to scattering, as shown by the peak-to-total values for the two measurements.

Both measurements had nearly 30 000 full-energy peak events in the reconstructed images as shown in Tables 5.17 & 5.18, which can explain the similarity between resolutions. By increasing the number of full-energy peak events, the combined Lorentzian-Gaussian fit can be applied to a statistically relevant amount of data, reducing the level of uncertainty on the quality of the fit, and consequently the FWHM values obtained from the fit. As stated earlier, increasing the duration of the measurement is not feasible, therefore more events need to be selected that are used within the image reconstruction, not solely those that fall within the full-energy peak energy gate (658 - 666 keV).

The inclusion of concrete leads to additional small angle scatters before the gamma rays reach the scatter detector. These photons, should they interact in the detector system, are now contributing to specific regions of the Compton continuum. In principal, by restoring some additional events from these regions of the Compton continuum which are a direct result of the 662 keV gamma ray, the image resolution should improve. These additional regions will account for the loss of full-energy peak events due to the inclusion of concrete.

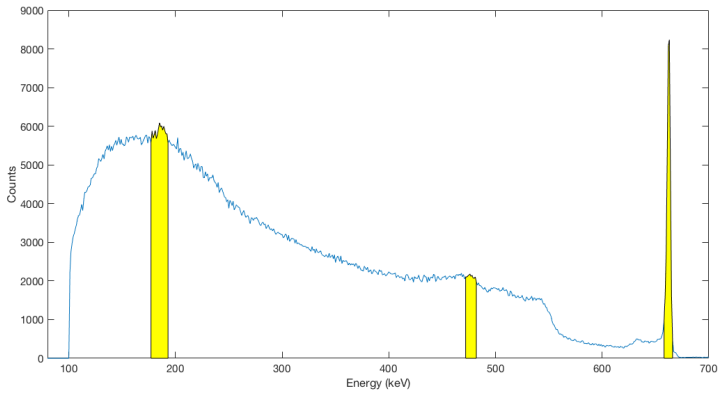

Figure 5.68: Two-tier coincidence energy spectrum from fold [1 1 1 1] events produced from a ^{137}Cs point source behind a 10 cm thick concrete wall. The yellow highlighted areas represent energy gates applied to the image reconstruction.

Figure 5.68 shows the coincidence energy spectrum from the measurement including concrete. The highlighted regions show the additional energy gates encompassing the backscatter peak, 177 - 193 keV, and the Compton edge, 472 - 482 keV. These additional energy gates were also applied to the original measurement without concrete, to observe if the image resolution also improves with that measurement.

Narrow and wide energy gates were applied to the data. Selected energy gates are usually kept narrow in order to isolate the key features of the spectrum (such as the full-energy peak). By increasing the width of the defined gates, the increased number of events used in the image can originate from background events. These can be detrimental to the quality of the image, having a larger influence on the Gaussian shaped background to the image, rather than the Lorentzian peak. This affect can be observed when larger gates are applied around the Compton edge.

Tables 5.20 - 5.22 show how the image resolution varies with the different energy gates applied. It also shows how the angular resolution changes, and the percentage of events that are available for image reconstruction that are

used.

Table 5.20: Comparison of image and angular resolution from measurements of a ^{137}Cs source placed at (0, 0, 68) cm, with and without the presence of a concrete wall, with the following energy gates applied across the full-energy peak and the backscatter peak.

Energy Gate	FWHM (mm)		Angular Res (deg)		Percentage of Events (%)	
(keV)	No Concrete	Concrete	No Concrete	Concrete	No Concrete	Concrete
658 - 666 177 - 193	90.61 ± 0.64	85.35 ± 0.56	7.62 ± 0.05	7.18 ± 0.05	10.17	8.43
615 - 666 160 - 200	87.41 ± 0.56	86.79 ± 0.56	7.35 ± 0.05	7.30 ± 0.05	18.14	18.20

Table 5.20 shows how gating on the backscatter peak, as well as the photopeak, affects the image resolution. The results shown in this table highlight the importance of selecting additional regions and how they can potentially degrade the quality of the image. Gating over the backscatter peak has increased the spatial resolution of the original measurement without concrete from 87.93 ± 0.62 mm to 90.61 ± 0.64 mm. The opposite occurs with the concrete measurement, with an improvement in the image resolution from 87.91 $\pm$ 0.63 mm to 85.35 ± 0.56 mm.

This is understandable, as the introduction of the concrete leads to more backscattered events, so it can be confidently stated that the events in this region arise directly from the 662 keV photon. However, in the original image, including this additional region has lead to a larger influence from background events. Increasing the width of the two energy gates only improves the resolution of the original image minutely, and it degrades once again in the concrete measurement.

An energy gate was then applied around the Compton edge, which is identified near 480 keV in Figure 5.51. A narrow energy gate was first selected, 472 - 482 keV. For the wider energy gates, two separate regions above and below the Compton edge were selected. The first energy gate, 460 - 490 keV, aimed to utilise the higher-angled Compton scattered events from the 662 keV photon. The second region, between 482 - 544 keV, was to utilise the events in this additional feature observed in the Compton continuum, as mentioned earlier. If the image resolution improves, then it can be concluded that the events observed in this feature originate from the 662 keV full-energy peak.

Figure 5.69 shows the larger gated regions on the spectrum. The orange region represents the 482 - 544 keV region to be investigated. The yellow regions show

the wider energy gates for the full-energy peak and the backscatter peak, as demonstrated in Table 5.20.

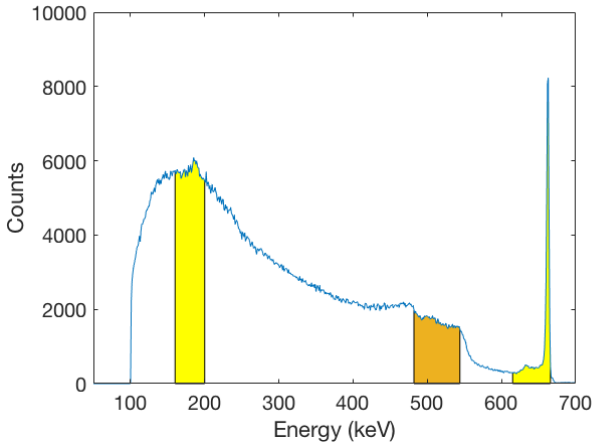

Figure 5.69: Two-tier coincidence energy spectrum from fold [1 1 1 1] events produced from a ^{137}Cs point source behind a 10 cm thick concrete wall. The highlighted areas represent wide energy gates applied to the image reconstruction.

Table 5.21 shows how the image and angular resolution changes with the inclusion of the Compton-edge energy gates. The first narrow energy gate applied shows further improvement to the resolution values compared to the energy gate selected across the backscatter peak. When the gates are widened to incorporate the high-angle Compton scatters, there is significant improvement to the non-concrete measurement. However, utilising these same events for the concrete measurement shows a slight degradation.

Table 5.21: Comparison of image and angular resolution from measurements of a ^{137}Cs source placed at (0, 0, 68) cm, with and without the presence of a concrete wall, with the following energy gates applied across the full-energy peak and the Compton edge.

Energy Gate	FWHM (mm)		Angular Res (deg)		Percentage of Events (%)	
(keV)	No Concrete	Concrete	No Concrete	Concrete	No Concrete	Concrete
658 - 666 472 - 482	84.24 ± 0.74	86.59 ± 0.82	7.09 ± 0.06	7.29 ± 0.07	7.83	3.57
615 - 666 460 - 490	77.11 ± 0.93	87.49 ± 1.15	6.49 ± 0.08	7.36 ± 0.10	13.56	7.31
615 - 666 482 - 544	92.08 ± 1.42	110.76 ± 1.79	7.75 ± 0.06	9.31 ± 0.15	18.88	10.00

When the higher-energy region above the Compton edge is used, a significant worsening of the image and angular resolutions is observed. Therefore, it can be concluded that the events that occur within the region of 482 - 544 keV are background events which negatively contribute to the quality of the image and leave a larger level of uncertainty on the FWHM value.

It can also be noted from Table 5.21 that a smaller percentage of the imageable events is used when gating on the Compton edge. This shows that it is not always necessary to include as many events as possible to improve the image quality, but the importance of choosing the correct region from the spectrum.

Table 5.22 shows the quality of the image resolution when energy gates are applied across all three regions. Comparing the results between the three tables, it can be seen that for measurements that involve scattering material, it is beneficial to apply additional narrow energy gates across the backscatter peak, Compton edge, and the full-energy peak. The events used from these supplementary regions can account for the loss of full-energy peak events from scattering through the concrete, but the increase of scattering from concrete will lead to undesirable events in the spectrum, therefore it is best to keep the applied energy gates narrow.

For standard measurements, with minimal amount of scattering however, it can be seen that including wide energy gates across the same regions significantly improves the image and angular resolutions. Incorporating high-angle Compton scatters and the leading edge of the full-energy peak utilises events which have come directly from the 662 keV photon.

Table 5.22: Comparison of image and angular resolution from measurements of a ^{137}Cs source placed at (0, 0, 68) cm, with and without the presence of a concrete wall, with the following wide energy gates applied.

Energy Gate	FWHM (mm)		Angular Res (deg)		Percentage of Events (%)	
(keV)	No Concrete	Concrete	No Concrete	Concrete	No Concrete	Concrete
658 - 666						
472 - 482	84.26 ± 0.73	85.39 ± 0.73	7.09 ± 0.06	7.19 ± 0.07	12.57	9.89
177 - 193						
615 - 666						
460 - 490	77.49 ± 0.93	86.21 ± 1.05	6.52 ± 0.08	7.25 ± 0.09	24.64	22.24
160 - 200						
615 - 666						
482 - 544	92.68 ± 1.38	110.22 ± 1.53	7.80 ± 0.12	9.27 ± 0.13	29.96	24.92
160 - 200						

The importance of selecting the correct region on the spectrum has also been highlighted from the results in these tables. Figure 5.70 shows the analytical image reconstruction and image slice of the concrete measurement, with the wider energy gates applied which incorporated the events from the region between 482 - 544 keV. As can be seen from the figure, the large number of overlaps observed are originating from background events, leading to a large Gaussian background. The FWHM obtained from Figure 5.70b was 110.2 ± 1.5 mm, a signifcant increase on the FWHM values found in Table 5.19.

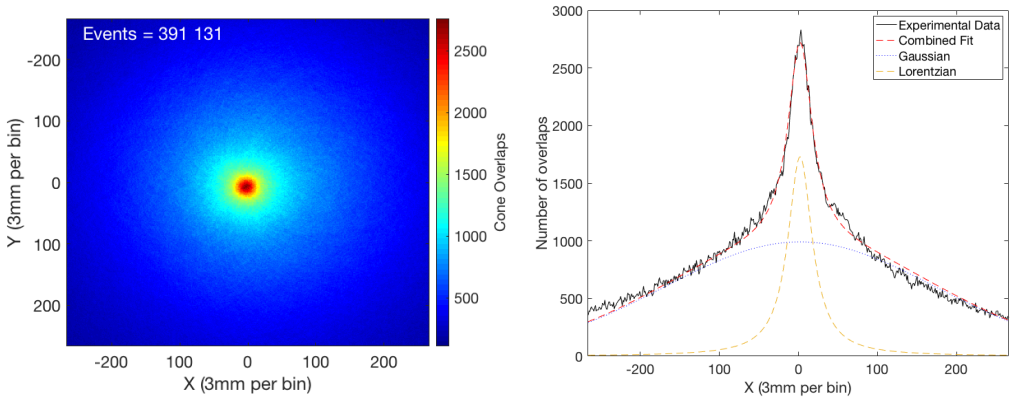

Figure 5.70: Figures showing how the increased energy gates on the coincidence spectrum (a) leads to an analytically reconstructed image (b) with a large Gaussian background as shown in the image slice (c). The FWHM of the Lorentzian peak was 110.2 ± 1.5 mm.

It can be concluded from these results that no defined set of energy gates can be applied for each measurement, due to the differences to the FWHM values observed between the measurement with and without concrete. However, all tables show the advantages and disadvantages to using additional regions of the energy spectra. As long as the events being used are directly from the interacting 662 keV photon, then they can be beneficial in providing additional information, otherwise undesired background events will be used which will reduce the quality of the Compton images.

The values described in Tables 5.19 - 5.22 were determined from spectra which originated from the two-tier system. A comparison of the coincidence spectra produced from the three-tier system (fold [1 1 1 1 1]) was made to see if there were any significant features that could be used as additional gates for image reconstruction. Events that are used in this spectrum have to have also interacted in the coaxial detector. Figure 5.71 shows the fraction of three-tier events with and without the presence of concrete.

As can be seen from Figure 5.71, there are no other discernable features to the spectra apart from the 662 keV full-energy peak. Regions that were gated upon previously, such as the backscatter peak and Compton edge, are not observed on this spectrum. Therefore, there is no advantage to using the three-tier system for imaging if scattering material is present, as additional spectrum features cannot be utilised. Also, there is only a small amount of full-energy peak events in comparison to two-tiered data.

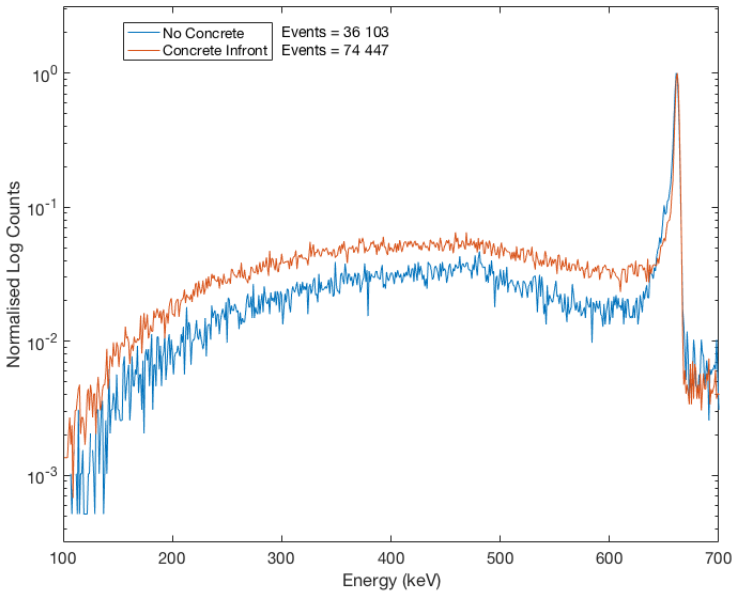

Figure 5.71: Figure showing the fold [1 1 1 1 1] coincidence energy spectra of a ^{137}Cs source with and without the presence of a concrete wall, measured using the three-tier GRI+ system. The total number of events in each spectrum is also detailed.

5.6 High Background measurements

GRI+ was transferred to a room on the University of Liverpool campus that contained two neutron sources, along with additional low-activity gamma sources, to replicate a more realistic setting that may be seen in a nuclear facility. The cart was situated as shown in Figure 5.72 to allow for large standoff measurements to be taken, which couldn't have been achieved in the previous laboratory set-up.

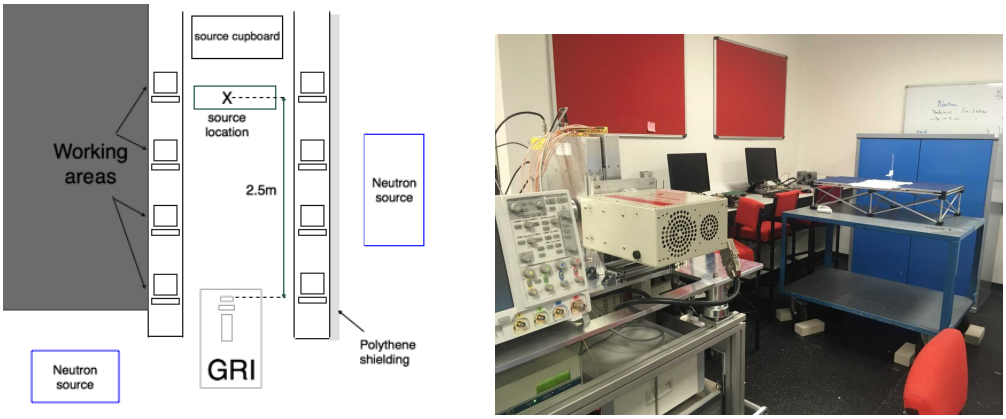

(a) (b)

Figure 5.72: (a) Diagram showing the layout of the laboratory containing the two neutron sources, and the placement of GRI+ for the second set of measurements. Items are not to scale. (b) Photo of the experimental set-up of a source placed 2.5 m away from the scatter detector.

The focus of measurements in this room would be to observe if there were any significant contributions from background radiation to the quality of the measurements and images collected by GRI+. Separate to common background gamma-peaks such as ^{40}K at 1460 keV, is the presence of prompt-gamma rays from neutron interactions, as shown in Figure 5.73.

The spectrum shown in Figure 5.73 shows the prompt-gamma rays as a result of the presence of two high-activity Americium-Berylium (AmBe) sources. The alpha-emitting Americium reacts with the Berylium source to produce neutrons, but also produces ^{12}C in an excited state. When ^{12}C* deexcites, it releases a 4.4 MeV photon.

The broad nature of the peak compared to the other peaks present in the spectrum is due to Doppler broadening. Due to the high-energy of the 4.4 MeV peak, the single and double-escape peaks are observed at 3.4 and 3.9

MeV. Neutron capture reactions with the material in its enclosure, H(n,γ)D produces a prominent 2.2 MeV peak. Additional background peaks observed in Figure 5.73 also includes photons from ^{214}Bi, including the 0.77, 0.93, 1.1 and 1.7 MeV photons, and a 2.6 MeV peak from ^{208}Tl. High-energy neutrons can also react with ^{16}O to produce ^{16}N which rapidly decays emitting a 6.1 MeV peak. The single and double-escape peaks can be observed on the higher-energy part of the spectrum. The lower-energy peaks around 0.4 MeV arise from ^{228}Ac, a naturally occurring decay product from the ^{232}Th decay chain. Similarly, the lead X-rays could be from the natural decay chain of ^{238}U or from any possible lead shielding present near the detector whilst the measurement was being taken.

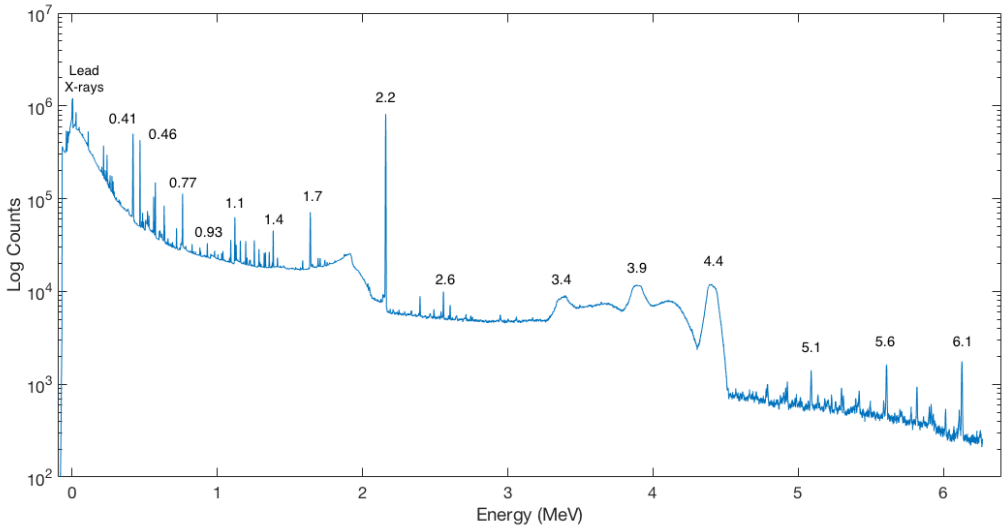

Figure 5.73: Spectrum showing the most prominent background gamma-ray peaks collected using a HPGe detector [103].

The detector live-time for the spectrum shown in Figure 5.73 was 21.3 hours (24.2 hours real-time). The count rates for some of the different energies observed in the spectrum can be seen in Table 5.23. The gammas of most significance that could potentially affect the measurements are those arising from the prompt gammas emitted from the neutron sources.

As stated in Section 2.3.1, current gamma imaging systems deployed in industry use collimators to reduce the effects seen from background radiation. These collimators will only shield against low-energy background events however, as higher-energy gammas will likely pass through the collimators.

In the previous laboratory measurements, the scenarios that were considered

included point sources with no scattering material, and sources with induced scattering, leading to a Compton background were the energies registered in the continuum would have originated from the incoming 662 keV gamma ray.

Table 5.23: Count rates from the presence of the background gamma rays in the neutron room.

Energy (MeV)	Count Rate (counts/s)
1.1	1.946 ± 0.008
1.7	3.397 ± 0.009
2.2	3.375 ± 0.012
2.6	0.282 ± 0.004
3.4	6.598 ± 0.062
3.9	10.824 ± 0.074
4.4	18.016 ± 0.024

However, due to the high-energy of the emitted prompt gammas, it is unlikely that full-energy peak events would be measured and observed on the coincidence energy spectra. Partial energy deposition of these prompt gammas from scattering with the detectors may lead to false coincidence events, creating a more complicated scenario.

As seen in the previous section, additional areas of the Compton continuum were gated upon to try and improve the image resolution, which would help identify the location of the source. If the background events were gated upon again, the inclusion of these false-coincidence events could lead to incorrectly reconstructed Compton cones for those energies. These cones could lead to fewer overlaps observed in the reconstructed image, affecting any possible analysis of the source location.

Three measurements that have been discussed previously in this thesis were repeated in the high-background environment. These measurements were as follows:

- Two ^{137}Cs sources placed at a standoff of 45 cm, and a separation of 18 cm - Measurement A.
- Two ^{137}Cs sources placed at a standoff of 45 cm, and a separation of 6 cm - Measurement B.
- Extended source placed within the concrete wall set-up - Measurement C.

Table 5.24: Breakdown of the number of interactions leading to the final analytically reconstructed image for a 15.6 MBq ^{137}Cs source placed at distances of 68 cm, 100 cm and 250 cm.

Parameter	Measurement A		Measurement B		Measurement C	
	Frequency	Percentage (%)	Frequency	(%)	Frequency	(%)
MWD interactions recorded	7 842 514	100.0	4 366 312	100.0	51 940 515	100.0
Real fold interactions	7 137 303	91.0	3 983 963	91.2	44 544 780	85.8
Number of 2 tier events	1 631 056	20.8	907 972	20.8	11 041 194	21.3
Fold [1 1 1 1] imageable events	522 745	6.7	292 143	6.7	3 321 571	6.4
Energy Gated imaged events	21 193	0.3	11 960	0.3	71 887	0.1

The coincidence energy spectra produced from DC energies from fold [1 1 1 1] interactions were compared for the three measurements. The measurements in the neutron laboratory were recorded for at least the same period of time as the original measurements, but the times varied due to the accessibility of the lab at certain times of the day. Figure 5.74 shows the coincidence spectra from these events, normalised to account for the different measurement times.

As can be seen from the normalised spectra in Figures 5.74a - c, there is no significant deviation between the two profiles, although it can be seen that there is an increased amount of counts in the lower-energy part of the Compton continuum for the three measurements in the neutron laboratory.

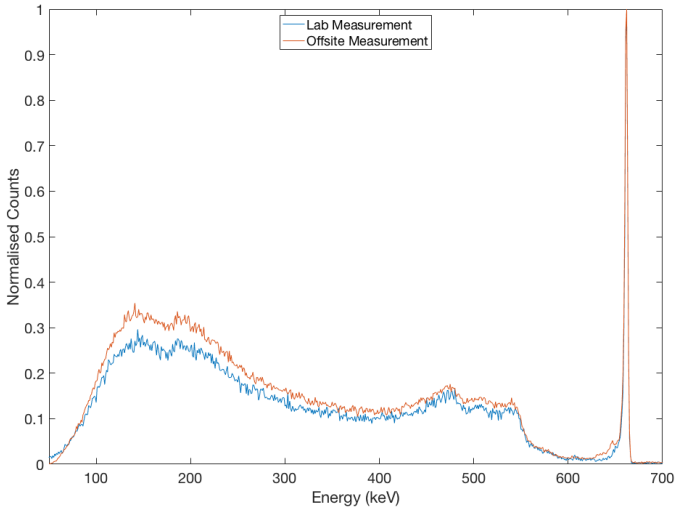

(a) Measurement A

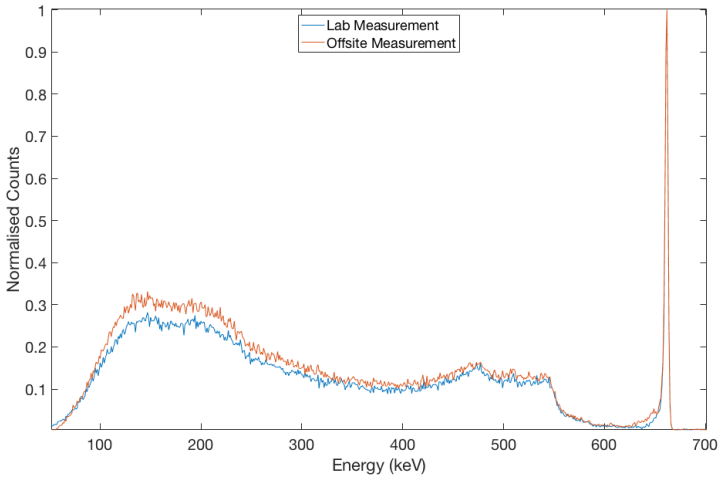

(b) Measurement B

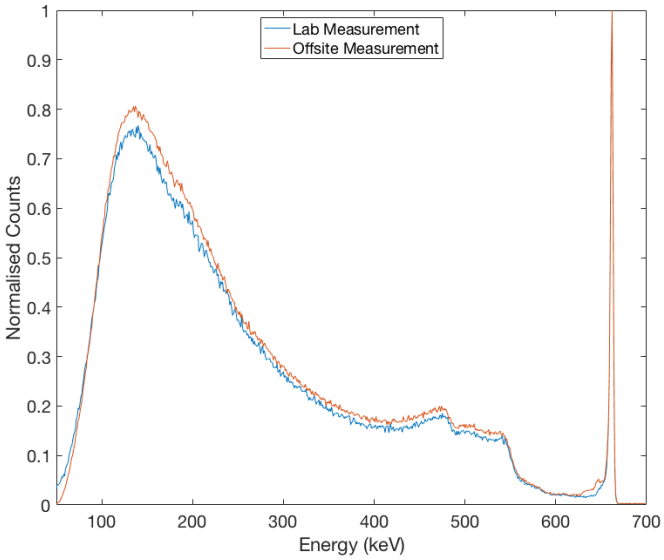

(c) Measurement C

Figure 5.74: Normalised coincidence spectra from three measurements taken from the Oliver Lodge Laboratory to a room with high-background radiation. The energies of the events were recorded from the DC face of the detectors from fold [1 1 1 1] interactions.

To quantify the affect that this additional scattering could be having, the peak-to-total values were calculated from these coincidence spectra using a method similar to that detailed in Section 5.4. These results can be found in Table 5.25.

The results shown in Table 5.25 across the two locations show that the higher-background environment has a very small affect on the measurement.

Table 5.25: Peak-to-Total values for coincidence addback spectra from single interactions in the scatter and absorber detectors.

Measurement	Peak-to-Total ratio	
	Laboratory	High-Background room
A	5.128 ± 0.052	4.534 ± 0.031
B	5.203 ± 0.047	4.563 ± 0.041
C	2.580 ± 0.012	2.442 ± 0.009

Summary

The performance of the GRI+ system from the University of Liverpool has been assessed for industrially relevant experimental scenarios. The results detailed in this chapter demonstrate how GRI+ is able to produce high-quality images at large stand-off distances, with an average angular resolution across a range of distances obtained. A non-uniform source of distributed activity was measured, with the localisation of the source achieved within a concrete wall setup, and an accurate representation of the distribution of activity within the sample observed. GRI+ also showed a sensitivity to the introduction of scattering materials, with a relationship determined with the thickness of scattering material, and an understanding of what events can be used for image reconstruction. Further discussion on the results achieved in the chapter are detailed in Chapter 6.

Chapter 6

Conclusions and Future Work

In this thesis, the capability and performance of GRI+ for possible future in-situ measurements was investigated by assessing data collected from industrially relevant scenarios. These scenarios focused on measurements of ^{137}Cs at large standoff distances and in the presence of concrete scattering material.

Optimising the quality of analytically reconstructed Compton images was done by investigating previously-developed PSA techniques, optimisation of the imaging parameters, and the use of the high-pass filter. The range of measurements included high-activity and relatively low-activity point sources, as well as analysis of an unevenly distributed, extended source.

This thesis also describes the first set of offsite measurements that GRI+ has undertaken to replicate in-situ measurements in a room with high-levels of background radiation. The impact of the higher-levels of background radiation was evaluated to observe if it had a significant influence on the quality of the results.

6.1 Conclusions

From the work in this thesis, some overall conclusions could be made over the performance of the GRI+ system.

The parametric Z-PSA3 technique for the absorber detector, in conjunction with the parametric X-Y PSA techniques currently implemented in data analysis, was determined to produce the optimum Compton images. The HPF applied to analytically reconstructed images could allow for the separation of near-axis measurements to be calculated from the images.

For each measurement, a table which detailed the breakdown of events that were used in the energy gated Compton images was shown. A comparison of the tables showed the amount of full-energy peak events that were used in the final image fell within the range of $0.1 - 0.2\%$ of the total number of interactions that were recorded by the DAQ system. This value can be increased by utilising more multi-fold events, and therefore increasing the efficiency of the system.

High-quality Compton data and reconstructed images have been produced over varying standoff distances, providing further knowledge of the performance of the GRI+ system beyond what has been previously measured with the system.

A sensitivity to measurements involving concrete material allowed for a further understanding of what additional imageable events from the Compton continuum can be used to improve the quality of images.

The main conclusions from the separate investigations are shown below:

^{137}Cs Point Source Analysis

The performance of GRI+ with two ^{137}Cs point sources, first of similar activities and then with differing activities, was investigated at a distance of 45 cm. This is the minimum achievable distance a source of radioactive contamination could be measured from in an in-situ measurement.

The separation of the two sources of similar activity, positioned 180.0 ± 1.0 mm from each other, without any PSA techniques applied was calculated to be 173.7 ± 0.8 mm.

The separation of the two sources positioned 60.0 ± 1.0 mm from each other was calculated to be 61.2 ± 0.6 mm, and this value was improved to 59.7 ± 0.4 mm with the application of the HPF.

The measurements were then repeated with one of the sources changed to that of a much lower activity, 0.041 MBq. The separation with the application of PSA and the HPF was found to be 171.0 ± 0.7 mm. This seemed significantly far from what was believed to be a true separation of 180 mm, however a positional error on one of the sources could mean the true separation value was different, and actually to a value closer to the obtained 171.0 ± 0.7 mm. Positional uncertainties on the sources is possible due to the nature of the experimental set-up. When the sources were moved to a separation of $60.0 \pm$

1.0 mm, the PSA and HPF applied image calculated a separation of 59.4 ± 0.9 mm.

Analysis of the relative heights and areas of the peaks in the reconstructed images were compared against the relative activities of the two sources, to try and provide a method of quantifying the activity from the measurements. Neither technique provided an accurate, consistent representation of the activity of the sources. Quantifying the activity of the sources from these Compton images is a technique that needs to be refined.

Extended Source Measurement

The imaging capability of point sources at a standoff distance of 45 cm allowed for the investigation of an extended source of uneven distribution, with and without the presence of concrete material. The inclusion of the concrete did not largely affect the analysis of the Compton image in determining the length of the distribution.

However, the introduction of the concrete severely reduced the collection of imageable full-energy peak events, meaning a larger measurement time was required in order to produce a high-quality image of the radioactive source, the position of which was accurately located to the concrete brick in which it was situated.

Varying thicknesses of scattering material

Due to the operation of the GRI+ Compton Camera, a method was suggested to determine the thickness of concrete material that is place in front of a radioactive source. By varying the thickness of concrete positioned in front of a high-activity ^{137}Cs point source, the peak-to-total (P_T) ratio was evaluated from the coincidence energy spectrum; the energies from which are used for image reconstruction.

A linear relationship was observed between the natural log of the P_T and the thickness of concrete, with a linear equation of $0.066x + 1.339$ obtained. This relationship could potentially be the basis for future in-situ measurements, and provide an estimation on the amount of concrete material that is in front of a radioactive source of contamination, rather than the previous methods of assuming it is on the surface of a wall.

Far-field measurements

The angular resolution was determined and compared for three measurements at large standoff distances; 68 cm, 100 cm and 250 cm. An average angular resolution of 7.19 ± 0.26 degrees was calculated. This value is a promising characteristic for a gamma-ray imaging system, especially in comparison to the imaging systems currently used in decommissioning.

Through a re-analysis with an improved parametric PSA algorithm, or with the use of database PSA techniques, the spatial resolution of these images at these distances could be improved upon further.

High Background measurements

The data presented in this thesis shows the first set of measurements of the GRI+ system in an 'offsite' location, in a room with a significant level of background radiation on the University of Liverpool campus. This tested the system's ability to work as a fully standalone system. There were no significant degradations in the performance of the individual detector strips, as shown in Figures 4.20a & 4.20b.

Three measurements taken under the standard laboratory conditions were compared to replicated measurements in this high-background environment. A comparison of the P_T ratios from each measurement showed that, whilst there was a slight reduction in each of the P_T ratios, the background radiation has not significantly affected the quality of the results.

6.2 Future Work

This thesis has showed that there is potential for the GRI+ Compton Camera to be used in decommissioning environments, however, work is still required before it can be fully considered for in-situ measurements.

The following suggestions describe what is recommended for changes directly related to the work detailed in this thesis, as well as possible work to expand the potential of GRI+.

6.2.1 Improvements to the Data Campaign

Superimposing Compton Images

As described in Section 2.3.1, imaging systems are required to produce a visualisation of the location of contamination during in-situ measurments, and this is usually completed post-processing. Previous work [85] has visualised point sources by combining Compton image reconstructions with a mapping of the surrounding area completed by a FARO X330 LIDAR system. This initial investigation was only considered for near-field point sources however.

All the measurements detailed in this thesis included a real-image of the environment taken with an XBox Kinect. This was with the focus of being able to superimpose the reconstructed Compton images onto a real image to help identify the location of the radioactive source.

A disadvantage of simply overlaying the two images on top of the other is that it does not provide a true, accurate representation of the distribution of radiation, especially if the radiation is distributed across multiple surfaces.

As seen from Section 5.1, a distributed sample was located within a concrete brick through recreating the environment after knowing the specifications of what was being measured. Through post-analysis, the location of the sample was determined. However, this was achieved after some time, therefore this method is not suitable for larger settings and for a quick turnaround of results.

Projecting the Compton cones through a real, imaging space and overlaying the cones onto specific surfaces would be a proposed next step. This imaging modality can then be compared with the measurements taken in this thesis with the data collected with the XBox kinect, to see if the radiation can be accurately mapped to its true location.

Varying thicknesses of concrete

The linear relationship shown in Figure 5.60 shows that further information can be deduced from the data taken by GRI+. However, due to the physical limitations of what was feasible for laboratory measurements, and what could be disclosed by industrial partners for security reasons, the amount of concrete material used for the experiments was based on estimations on what the average thickness of a concrete wall was.

Therefore in a realistic scenario, the amount of scattering material that is present will increase. This will in turn affect the peak-to-total ratio by affecting the lower-energy part of the Compton continuum. The source-to-detector distance will also affect the values of the peak-to-total. The gradient of the linear relationship shown in Figure 5.60 will change as the distance from the detector increases.

It is unrealistic to complete a set of experimental measurements to replicate what is present in an industrial setting. Utilising validated simulations to provide a database of measurements for varying thicknesses of concrete would prove to be a better alternative.

GAMOS and Geant4 simulations of GRI+ have been validated previously. By demonstrating an agreement with the experimental data taken in this thesis, a potential database of peak-to-total values for varying thicknesses of concrete and standoff distances could be created, which could then be utilised for in-situ measurements, and be highly invaluable for decommissioning purposes.

Additional improvements

Further suggestions to how the data described in this thesis could be improved upon is listed below:

- Fixing the DAQ system so that a higher rate of events can be sucessfully recorded.
- Increase the efficiency of the system by using multifold events in the imaging process.
- Due to the equal weighting of the phase space, an improvement to the current MLEM algorithm, or implentation of a new code should be investigated which can alter the phase space balance, and therefore be used for the measurements of extended sources.
- Use of database PSA to observe improvements to the image resolution.
- Create a detailed efficiency equation for the extended field-of-view, allowing for the quantification of activity or surface dose from the reconstructed images.

6.2.2 Further considerations

One of the measurements taken at the CTL involved an off-axis ^{60}Co source. This was to replicate one of the test scenarios set forward by Sellafield [29], to observe how the presence of a high-activity, off-axis source would effect the measurements. However, the activity of the ^{60}Co source (0.3 MBq) was too weak to make any significant contribution to the measurement. Repeating this measurement, but with a higher-activity source could allow for a suitable investigation of the presence of off-axis radiation on the images.

The next major test for the GRI+ system will be for the trialling of the cart in a true in-situ measurement. Discussion with one of the industrial partners to this project, *Mirion Technologies*, lead to the planning of a set of in-situ measurements in a test contamination scenario. Due to the disruption caused by the COVID-19 pandemic however, these measurements have been postponed.

The transport of a liquid radionuclide such as ^{137}Cs through a dense medium such as a concrete block could also be investigated. The production of a concrete phantom was initially considered for the work in this thesis, but various limitations delayed the manufacturing indefinitley.

The measurements in this thesis have assumed that any radioactive contamination is on the surface or behind a defined thickness of concrete material. A true investigation of the ingress of radiation within concrete would be highly beneficial for the nuclear industry. Observing the uptake of liquid ^{137}Cs through a concrete brick, and imaging over a long period of time could provide invaluable information. However, the logistics of performing an experiment such as this safely, and with minimal risk would be difficult in a University laboratory setting.

It is hoped that the research and findings detailed in this thesis will provide a basis for the further development of the GRI+ Compton Camera, with the knowledge of the experimental procedures and analysis to be implemented for any future in-situ waste characterisation scenarios.

Appendix A

List of Publications

This appendix details some published works as author and co-author on the GRI+ Compton Camera.

Author

Feasibility study of a Compton Camera for nuclear contamination scenarios with varying thicknesses of concrete material.

Jaimie Platt et al. IEEE Conference Proceedings. 2019 IEEE Nuclear Science Symposium and Medical Imaging Conference (NSS/MIC), Manchester, United Kingdom, 2019, pp. 1-3, doi: 10.1109/NSS/MIC42101.2019.9059767.

Co-Author

Characterisation of the charge collection properties in a segmented planar HPGe detector

E. Rintoul et al. Nuclear Inst. and Methods in Physics Research, A 987 (2021) 164804

A semiconductor triple-layered Compton camera for Proton Therapy verification

S. Kalantan et al. 2019 IEEE Nuclear Science Symposium and Medical Imaging Conference (NSS/MIC), Manchester, United Kingdom, 2019, pp. 1-3, doi: 10.1109/NSS/MIC42101.2019.9059654.

Creation and Validation of Calculated Pulse Databases for Pulse Shape Analysis in the Planar Semiconductor Detectors of a Triple-Layered Compton Camera System

E. Rintoul et al. IEEE Conference Proceedings, 2018 IEEE Nuclear Science Symposium and Medical Imaging Conference (NSS/MIC), Sydney, Australia, 2018, pp. 1-4, doi: 10.1109/NSSMIC.2018.8824595.

Awaiting Publication

Gamma-Ray Imaging Performance of the GRI+ Compton Camera

A. Caffrey et al. Submitted to Nuclear Inst. and Methods in Physics Research, A November 2020

Appendix B

List of Measurements

Table B.1 is a complete list of the measurments described in this thesis. Details of each measurement includes the duration of the measurement, the count rate (s^{-1}) received by the data aquisition system and the tape rate, the amount of data recorded (kBytes) per second.

A breakdown of the number of events is also included in Table B.1, beginning with the total number of events the MWD code was used with a registered event. The *selected* events are the those that have successfully passed the low-energy threshold set by the user. The number of 2 tier events are interactions which fell within the defined coincidence window. Imageable events are Fold [1 1 1 1] interactions which are written to .txt files which can be used with the Imaging Application [91].

The imaged events are the events shown in the final reconstructed images shown in this thesis. This value can vary depending on the user parameters defined in the Imaging application, such as the image space size, or the Z slice to be observed. The energy gate applied for all measurements is between 658 - 666 keV.

Measurements R328 - R329 are listed in order of increasing concrete thickness as described in Section 5.4.

* - Concrete was involved in the measurement.
** - Measurements were taken 'offsite' in the Central Teaching Laboratories, University of Liverpool.

N/A - Values were not obtained during the measurement.

Table B.1

Run Name	Activity (MBq)	Position (mm)	Duration (h)	Event rate (s^{-1})	Tape Rate (kBytes/s)	Number of MWD interactions	Number of real fold interactions	Number of 2-tier events	Fold [1111] imageable events	Energy gated imaged events
R6	0.227 & 0.235	(-90|90, 0, 450)	29.80	10	89	5 592 920	4 826 766	1 692 995	217 070	9 583
R7	0.227 & 0.235	(-30|30, 0, 450)	24.25	15	83	4 719 403	4 119 979	912 268	258 941	11 605
R8	0.041 & 0.235	(-90|90, 0, 450)	51.14	5	59	6 462 759	5 531 630	1 359 722	322 265	12 813
R10	0.041 & 0.235	(-30|30, 0, 450)	27.6	10	60	3 670 237	3 155 557	754 235	210 668	8238
R11	$\backsim$1.2	(-90|90, 0, 450)	18.90	39	300	12 627 496	10 190 644	2 596 103	629 780	28 823
R13*	$\backsim$1.2	(-90|90, 0, 500)	60.79	30	243	33 596 922	27 929 067	7 028 064	1 918 063	41 989
R328*	15.695	(0, 0, 650)	4.60	N/A	1 649	17 928 099	6 908 087	3 282 863	247 456	-
R15*	15.695	(0, 0, 650)	5.31	120	1318	16 828 329	7 593 854	3 359 253	305 318	-
R18*	15.695	(0, 0, 650)	8.06	N/A	930	17 816 175	10 076 806	3 609 848	440 893	-
R20*	15.695	(0, 0, 650)	7.43	80	636	11 110 606	7 485 409	2 301 896	387 210	-
R19*	15.695	(0, 0, 650)	12.91	55	439	13 078 418	9 869 789	2 733 369	596 308	-
R16*	15.695	(0, 0, 650)	15.32	42	317	11 153 450	8 974 841	2 333 509	600 787	-
R329*	15.695	(0, 0, 650)	28.09	N/A	200	15 466 772	12 823 426	3 081 030	847 092	-
R5	15.695	(0, 0, 680)	14.47	160	1243	46 202 981	20 397 360	8 329 901	725 819	31824
R300*	15.695	(0, 0, 680)	42.48	70	621	57 896 783	40 193 281	11 211 235	2 052 513	33 040
R404	15.695	(0, 0, 1000)	20.67	N/A	664	31 149 382	21 252 184	23 504 740	38 461	1 679
R12**	15.671	(0, 0, 2500)	113.85	15	137	31 612 113	28 200 338	6 663 082	2 115 615	94 601
R19**	0.227 & 0.235	(-90|90, 0, 450)	41.88	12	100	7 842 514	7 137 303	1 631 056	522 745	21 193
R20**	0.227 & 0.235	(-30|30, 0, 450)	22.50	11	96	4 366 312	3 983 963	907 972	292143	11 960
R21* **	$\backsim$1.2	(-90|90, 0, 500)	95.60	33	269	51 940 515	44 544 780	11 041 194	3 321 571	71 887

Appendix C

Solid Angle Calculation

Gamma rays are emitted isotropically from a radioactive source. This 4π spherical projection of gamma rays emitted per second, based on the activity of the source used, means we can determine the number of gamma-rays that are emitted onto a small surface-area of a sphere.

This is usually determined by the solid angle subtended at the centre of a sphere to produce a cone as shown in Figure C.1. The base of the cone can be represented by the scatter detector face. Using trigometric relationships, the angle Ω can be found in relation to the 4π spherical projection.

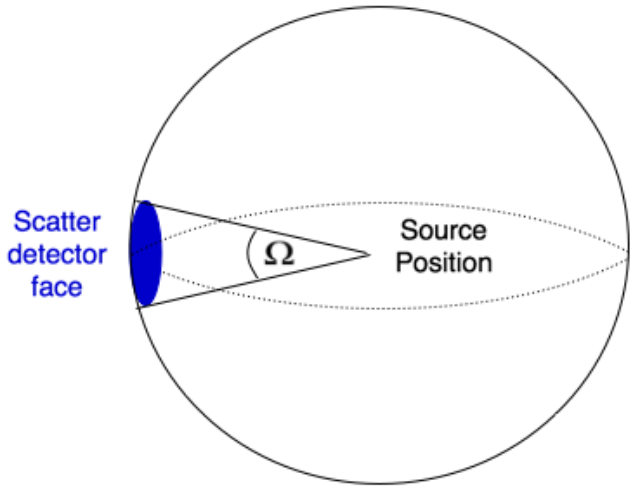

Figure C.1: Schematic showing the solid angle, Ω subtended by a radioactive source onto the scatter detector face.

However, this scenario works with a single source, with the height of the cone being the source-to-detector distance. However, with multiple sources, irregular cones are produced based on the positioning of the sources. This is shown

in Figure C.2.

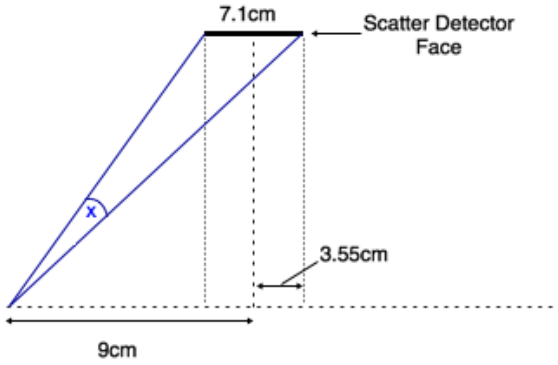

Figure C.2: Schematic showing the position of a source 9 cm away from the central x = 0, 45 cm from the scatter detector face, and the calculation to determine the angle x.

In this example, based on measurement R6 as described in Appendix A, two sources are positioned ± 9 cm from the central axis of x = 0. The axis of x = 0 falls centrally within the scatter detector face. To find the angle subtended onto the detector, x, we need to use two trigonometric relationships as shown in Figure C.3.

Figure C.3 shows two right-angled triangles, where the hypotenuses of these triangles represent the slant lengths of the irregular cone in Figure C.2. The vertical lengths are known from the source-to-detector distance of 45 cm, and the horizontal lengths can be determined by adding or subtracting the scatter detector face radius from the source position of 9 cm. Using the trigonometric function, *Tan*, the angles a and b can be calculated. By subtracting angle b from a, the angle subtended, x can be determined.

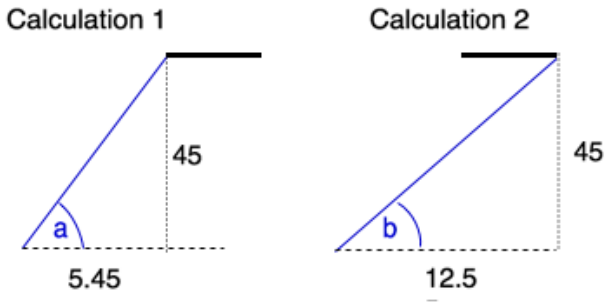

Figure C.3: Diagram showing the trigonometric calculations to find angles a and b, using the known source-to-detector distance, 45 cm, and the distance from the central x = 0 axis.

Once angle, x has been calculated, it can be used in the following relationship:

$$\frac{x}{2\pi} : \frac{gammas\ incident\ on\ detector}{total\ gammas\ emitted\ in\ 4\pi} \tag{C.1}$$

The number of incident gamma rays on the scatter detector face for each measurement is shown in Table C.1.

Any measurements involving the 18 cm distributed ^{137}Cs soil sample have not been calculated due to the complicated nature of the geometry. Measurements that this involves are: R11, R13.

Table C.2 shows the measurements that involved scattering material placed directly infront of the source. For these calculations, the estimated number of gamma-rays projected onto the scatter detector face will be reduced in intensity depending on the thickness of the concrete, as described by Eq. 3.12.

The values that have been calculated in these tables include only the gamma-rays that are emitted within that particular solid angle, Ω. These values do not include any additional photons that may have interacted in the detectors from scattering from nearby materials.

Table C.1

Run Name	Source Position (cm)	Duration (h)	γs emitted (s^{-1})	γ fraction correction	4π projected	Ω (rads)	Incident on detector
R6	(±9, 0, 45)	29.80	227000 235 000	193 177 199 985	2.072×10^{10} 2.145×10^{10}	0.151	1.01×10^{9}
R7	(±3, 0, 45)	24.25	227000 235 000	193 177 199 985	1.686×10^{10} 1.746×10^{10}	0.157	8.58×10^{8}
R8	(±9, 0, 45)	51.14	41 000 235 000	34 891 199 985	6.424×10^{9} 3.682×10^{10}	0.151	1.04×10^{9}
R10	(±3, 0, 45)	27.60	41 000 235 000	34 891 199 985	3.467×10^{9} 1.987×10^{10}	0.157	5.83×10^{8}
R328	(0, 0, 65)	4.60	15 695 000	13 356 445	2.212×10^{11}	0.109	3.84×10^{9}
R5	(0, 0, 68)	14.47	15 695 000	13 356 445	6.957×10^{11}	0.104	1.15×10^{10}
R404	(0, 0, 100)	20.67	15 695 000	13 356 445	9.939×10^{11}	0.071	1.12×10^{10}
R12	(0, 0, 250)	113.85	15 671 000	13 336 021	5.466×10^{12}	0.028	2.44×10^{10}

Table C.2: Experimental runs involving concrete.

Run Name	Concrete thickness (cm)	Position (cm)	Run Duration (h)	γs emitted* 0.851 (s^{-1})	4π projection	Ω (rads)	Incident	Attenuated
R15	3.37	(0, 0, 65)	5.31	13 336 021	2.553×10^{11}	0.109	4.43×10^{9}	3.95×10^{9}
R18	6.54		8.06		3.876×10^{11}		6.72×10^{9}	5.37×10^{9}
R20	9.67		7.43		3.573×10^{11}		6.20×10^{9}	4.45×10^{9}
R19	13.13		12.91		6.208×10^{11}		1.08×10^{10}	6.86×10^{9}
R16	16.44		15.32		7.366×10^{11}		1.28×10^{10}	7.27×10^{9}
R329	19.67		28.09		1.351×10^{12}		2.34×10^{10}	1.19×10^{10}
R300	10.3	(0, 0, 68)	42.48		2.043×10^{11}	0.104	3.38×10^{10}	2.38×10^{10}

Bibliography

[1] Nuclear Decommissioning Authority, June 2019, Corporate report, Nuclear Provision: the cost of cleaning up Britain's historic nuclear sites

[2] I. Macpherson & A. Dunlop, February 2016, Development of a Systematic Approach to Post-Operational Clean Out at Sellafield, *https* : *//inis.iaea.org/collection/NCLCollectionStore/_Public/47/061/47061295.pdf*

[3] World Nuclear Association, August 2020, Decommissioning Nuclear Facilities, *https* : *//www.world−nuclear.org/information−library/nuclear−fuel−cycle/nuclear−wastes/decommissioning−nuclear−facilities.aspx*

[4] L. Harkness *et al*, 2009, Development of the ProSPECTus Semiconductor Compton Camera for Medical Imaging, 2009 IEEE Nuclear Science Symposium Conference Record

[5] INTERNATIONAL ATOMIC ENERGY AGENCY, TECDOC 1579, New Developments and Improvements in Processing 'Problematic' Radioactive Waste, IAEA Vienna 2007

[6] G.B National Grid Service, *https* : *//www.gridwatch.templar.co.uk/*

[7] S. Ling, J. Sanny *et al*, 10.3: Nuclear Binding Energy, *https* : *//phys.libretexts.org/Bookshelves/University_Physics/Book%3A_University_Physics_(OpenStax)/Map%3A_University_Physics_III_−_Optics_and_Modern_Physics_(OpenStax)/10%3A__Nuclear_Physics/10.03%3A_Nuclear_Binding_Energy*

[8] C.F. Weizsäcker, July 1935, On the Theory of Nuclear Masses, Phys. 96 (1935) 431

[9] H.A. Bethe & R.F. Bacher, April 1936, Stationary States of Nuclei, Rev. Mod. Phys. 8 (1936) 82

[10] B. T. Geilikman, November 1960, The Asymmetry of Nuclear Fission, The Soviet Journal of Atomic Energy volume 6, pages178–183

[11] K. Deyman, S. Biegalski, D. Haas, February 2015, Determination of short-lived fission product yields with gamma spectrometry, J Radioanal Nucl Chem 305:213–223

[12] T. England & B. Rider, October 1994, Evaluation and Compilation of Fission Product Yields, Los Alamos National Laboratory

[13] INTERNATIONAL ATOMIC ENERGY AGENCY, 1998, Radiological Characterisation of Shut Down Nuclear Reactors for Decommissioning Purposes, Technical Report Series 389

[14] National Institute of Standards and Technology, Sept 2009, Radionuclide Half-Life Measurements, URL: *https* : *//www.nist.gov/pml/radionuclide−half−life−measurements−data*

[15] D. Almond *et al*, May 2007, Chernobyl's legacy: Prenatal exposure to radioactive fallout and school outcomes in Sweden

[16] Y. Onda *et al*, January 2015, Soil sampling and analytical strategies for mapping fallout in nuclear emergencies based on the Fukushima Dai-ichi Nuclear Power Plant accident, Journal of Environmental Radioactivity, Volume 139, Pages 300-307

[17] Y. Sato *et al*, 2018, Radiation imaging using a compact Compton camera inside the Fukushima Daiichi Nuclear Power Station building, Journal of Nuclear Science and Technology, 55:9, 965-970, DOI: 10.1080/00223131.2018.1473171

[18] INTERNATIONAL ATOMIC ENERGY AGENCY, 2009, Classification of Radioactive Waste, IAEA SAFETY STANDARDS SERIES No. GSG-1

[19] Managing Radioactive Waste Safely: A Framework for Implementing Geological Disposal. Food & Rural Affairs Great Britain. Dept. for Environment. Cm Series.132, 2008. ISBN 9780101738620. URL: *https* : *//assets.publishing.service.gov.uk/government/uploads/system/uploads/attachment_data/file/*228903/7386.*pdf*

[20] Radioactive Waste Management, Release of Radioactive Materials and Buildings from Regulatory control, OECD 2008 NEA No. 6403

[21] Nuclear Decommisioning Authority, 2016, How much Radioactive Waste is there? *https* : *//nda.blog.gov.uk/*2017/04/03/*how − much − radioactive − waste − is − there/*

[22] Radioactive Waste Management, December 2016, Geological Disposal: Waste Package Accident Performance Status Report, NDA Report no. DSSC/457/01

[23] S.J. Singledecker *et al*, March 2012, Radioactive Waste Characterization Strategies; Comparisons Between AK/PK, Dose to Curie Modeling, Gamma Spectroscopy, and Laboratory Analysis Methods, Los Alamos National Laboratory, WM2012 Conference

[24] Mirion Technologies, Radiagem^{TM} 2000 Personal Portable Dose Rate and Survey Meter, PDF: *https* : *//mirion.s*3.*amazonaws.com/cms*4_*mirion/files/pdf/spec − sheets/c*38559_*radiagem*_2000_2.*pdf*?1562763748

[25] INTERNATIONAL ATOMIC ENERGY AGENCY, 1986, *Methodology and Technology of Decommissioning Nuclear Facilities*, Technical Reports Series No. 267, IAEA, Vienna

[26] van der Ende, B. M *et al*, April 2019, Stand-off nuclear reactor monitoring with neutron detectors for safeguards and non-proliferation applications, Nature Communications volume 10, Article number: 1959 (2019)

[27] Kromek, TN15TM High Sensitivity Ultra-compact Thermal Neutron Scintillation Detector, 2018, URL: *file* : *///Users/admin/Downloads/TN*15 − *A*4*E* − *Rev*3 − 180614.*pdf*

[28] Ortec, Comparison of Gamma-ray Nondestructive assay measurement techniques *http* : *//www.ortec − online.com/ − /media/ametekortec/technical*%20*papers/waste*%20*assay/comparison − gamma − ray − nondestructive − assay − measurement − techniques.pdf*?*la* = *en.*

[29] Sellafield Report - Active demonstration and benchmarking of gamma imaging technology, November 2017, Sellafield LTD, J. Revill, C. Mathieson, RTD-008-50-002, Nuclear Decommissioning Authority

[30] Technology Demonstration Workshop on Gamma Imaging IAEA Headquarters, October 2015, Vienna and IAEA Laboratories, Seibersdorf

[31] INTERNATIONAL ATOMIC ENERGY AGENCY, 2010, Technological Implications of International Safeguards for Geological Disposal of Spent Fuel and Radioactive Waste, Nuclear Energy Series No. NW-T-1.21

[32] John Revill, Sellafield Ltd, Private Communication, April 2018

[33] L. Harkness-Brennan, 2018. An introduction to the physics of nuclear medicine. Morgan & Claypool Publishers

[34] Cavendish Nuclear, October 2019, RadScan ®:900, *https* : *//www.cavendishnuclear.com/assets/uploads/*2019/10/*RadScan*−900−*Products*−*and* − *Services* − 2019_10.*pdf*

[35] CREATEC, N-Visage Gamma Imager, *https* : *//www.createc.co.uk/case_study/n* − *visage* − *gamma* − *imager/*

[36] N. Owen, November 2018, N-Visage: Innovation in Radiation and Contamination Mapping, CREATEC

[37] J.A. Mason, *et al*, July 2012, Development and Testing of a Novel Gamma ray Camera for Radiation Surveying, Contamination Measurement and Radiation Detection, Proceedings of INMM12, Orlando, Florida (12-A-409-INMM)

[38] Mirion Technologies, iPIX Ultra Portable Gamma Ray Imaging System, *http* : *//canberra.com/products/hp_radioprotection/pdf/ipix*−*ultra*−*portable*−*gamma*−*ray* − *imaging* − *system.pdf*

[39] K. Amgarou *et al*, August 2016, A comprehensive experimental characterization of the iPIX gamma imager, Journal of Instrumentation 11(08):P08012

[40] Innovative Physics, Hot Spot Location Products, *http* : *//www.activeradsys.com/tp/images/AC_HSL_Lite_Web*2.*pdf*

[41] C.G Wahl *et al*, 2015, Polaris-H Measurements and Performance, H3D, *https* : *//instrumentation.lanl.gov/local_resources/polarish*2.*pdf*

[42] H3D, Polaris-H, Gamma-Ray Imaging Spectrometer Specification Sheet

[43] Radiation Interactions, Chapter 2, Radiation Detection & Measurement 4th edition, Glenn F Knoll, 2010, John Wiley & Sons, Inc., New York

[44] R.D. Evans, 1955, The Atomic Nucleus, Copyright 1955 by the McGraw-Hill Book Company

[45] V. Valković, 2019, Measurements of Radioactivity, Chapter 4, Radioactivity in the Environment (second edition)

[46] X-Ray Mass Attenuation Coefficients, National Institute for Standards and Technology, *https* : *//www.nist.gov/pml/x* − *ray* − *mass* − *attenuation* − *coefficients*

[47] II: Gamma-Ray Interactions, Chapter 10, Radiation Detection & Measurement 4th edition, Glenn F Knoll, 2010, John Wiley & Sons, Inc., New York

[48] Signal Generation in Radiation Detectors, Chapter 1, p57, Signal Processing & Radiation Detectors 1st edition, Mohammad Nakhostin, 2018

[49] II: The Photocathode, Chapter 9, Radiation Detection & Measurement 4th edition, Glenn F Knoll, 2010, John Wiley & Sons, Inc., New York

[50] IV: Properties of Scintillation Gamma-Ray Spectrometers, Chapter 10, Radiation Detection & Measurement 4th edition, Glenn F Knoll, 2010, John Wiley & Sons, Inc., New York

[51] III: Semiconductors as Radiation Detectors, Chapter 11, Radiation Detection & Measurements, 4th edition, Glenn F. Knoll, 2010, John Wiley & Sons, Inc., New York

[52] H. Spieler, 2005, Semiconductor Detector Systems, Physics Division, Lawrence Berkeley National Laboratory

[53] G. Bertolini & A. Coche, 1968, Semiconductor Detectors

[54] T.E. Schleslinger & R.B James, Semiconductors for Room Temperature Nuclear Detector Applications, Vol. 43, 1995

[55] G Yang *et al* 2015 J. Phys.: Conf. Ser. 606 012014

[56] B.L. Wall *et al*, Oct 2013, Dead layer on silicon p-i-n diode charged-particle detectors, $arXiv : 1310.1178v2[physics.ins - det]$

[57] II: Configurations of Germanium Detectors, Chapter 12, Radiation Detection & Measurement 4th edition, Glenn F Knoll, 2010

[58] The Shockley-Ramo Theorem for Induced Charge, Radiation Detection & Measurement 4th edition, Glenn F Knoll, 2010

[59] W. Shockley, Currents to conductors induced by a moving point charge. Journal of applied physics, 9(10):635–636, 1938

[60] S. Ramo, Currents induced by electron motion. Proceedings of the IRE, 27(9):584–585, 1939

[61] Voltage and Charge Sensitive Configurations, Chapter 16, Radiation Detection & Measurement 4th edition, Glenn F Knoll, 2010

[62] Pulse Processing: Preamplifiers and Noise. Nuclear Physics Graduate School, University of Liverpool Physics Department

[63] V: Energy Resolution, Chapter 4, Radiation Detection & Measurement 4th edition, Glenn F Knoll, 2010

[64] High-Resolution Gamma Spectroscopy Lecture, University of Liverpool Physics Department, 2015

[65] VI: Detection Efficiency, Chapter 4, Radiation Detection & Measurement 4th edition, Glenn F Knoll, 2010

[66] R. Hofstadter & J.A. McIntyre, April 1950, Measurement of Gamma-Ray Energies with Two Crystals in Coincidence, Phys Rev 78: 619-620

[67] L.E. Peterson & R.L. Howard, September 1961, Gamma-Ray Astronomy in Space in the 50 keV to 3 MeV Region, University of Minnesota

[68] R.W. Todd, J.M. Nightingale & D.B. Everett, April 1974, A proposed camera, Nature Vol. 251

[69] R.S. Lawson, 2013, The Gamma Camera: A Comprehensive Guide, Institute of Physics and Engineering in Medicine

[70] Operating Manual of SILICON Strip Planar Detector, Canberra, Chemin de la Roseraie 67384 Tanneries Cedex

[71] Cryo-Pulse® 5 Plus Electrically Refrigerated Cryostat, Mirion Technologies, $https : //mirion.s3.amazonaws.com/cms4\_mirion/files/pdf/spec - sheets/c0514\_cryo - pulse\_5\_plus\_spec\_sheet\_1.pdf?1557862973$

[72] V Mishra *et al*, August 2005, Role of Guard Rings in improving the performance of silicon detectors, Pramana - journal of Physics, Vol. 65 No. 2 pp259-272

[73] MAESTRO-Pro Advanced Spectroscopy, ORTEC, AMETEK

[74] L. Harkness *et al*, 2013, Characterisation of a Si(Li) orthoganal-strip detector, Nuclear Instruments and Methods in Physics Research A 726 52–59

[75] T. Woodroof, February 2020, Quantitative Compton Imaging of Caesium-137 in Porous Media, PhD thesis s.l. : University of Liverpool Physics Department

[76] D. Judson, University of Liverpool, Private Communication, 2020

[77] E. Rintoul *et al*, 2020, Characterisation of the Charge Collection Properties in a Segmented Planar HPGe Detector, Awaiting Publication

[78] J. Dormand *et al*, October 2008, Charge collection performance of a segmented planar high-purity germanium detector, Nuclear Instruments and Methods in Physics Research A, 595(2), 401-409

[79] CAEN, $https://www.caen.it/caen-digitizer-whitepaper/$, Date Accessed: June 2019

[80] V. Pucknell, 1995, The MIDAS multi instance data acquisition system, Daresbury Laboratory

[81] A. Patel, 2016, An Experimental Investigation to Assess the Feasibility of Imaging Medical Radioisotopes with the ProSPECTus Compton Camera. PhD thesis s.l. : University of Liverpool Physics Department

[82] J. Cresswell & J. Simpson, 2010, MTsort language-edoc033

[83] GF3, D. Radford, May 2000, Oak Ridge National Laboratory, $https://radware.phy.ornl.gov/gf3/gf3.html$

[84] R. Cooper, October 2007, Performance of the SmartPET Positron Emission Tomography System for Small Animal Imaging, PhD thesis s.l. : University of Liverpool Physics Department

[85] A. Caffrey, 2019, The Development and Evaluation of a Compton Camera for Imaging Spent Fuel Rod Assemblies. PhD thesis s.l. : University of Liverpool Physics Department

[86] D. Judson, A Novel Image Reconstruction Code, Awaiting Publication

[87] R. Basko *et al*, 1998, Application of spherical harmonics to image reconstruction for the compton camera, Phys. Med. Biol., vol. 43, no. 4, pp. 887-894

[88] D. Xu and Z. He, October 2006, Filtered Back-Projection in $4pi$ Compton Imaging With a Single 3D Position Sensitive CdZnTe Detector, IEEE Transactions on Nuclear Science, vol. 53, no. 5, pp. 2787-2796,

[89] L. Harkness, 2010, A Design Study of the Semiconductor Sensor Head for the ProSPECTus Compton Camera, PhD thesis s.l. : University of Liverpool Physics Department

[90] Webb's Physics of Medical Imaging, second edition, 2012, p277, Image Reconstruction Methods for SPECT, Series in Medical Physics and Biomedical Engineering, CRC Press Taylor & Francis Group

[91] A. Caffrey, Analytical Reconstrucion App, Private Communication

[92] D. Judson & A. Andreyev, University of Liverpool, Private Communication

[93] ROOT: Data Analysis Framework, CERN, *https* : *//ph − root − 2.cern.ch/*

[94] ImageJ software, *https* : *//imagej.nih.gov/ij/features.html*

[95] T. Woodroof, February 2020, Chapter 4, *Quantitative Compton Imaging of Caesium-137 in Porous Media*, PhD thesis s.l. : University of Liverpool Physics Department

[96] J. Dormand, July 2014, *The Proof of Concept of a Fused Radiometric and Optical Stereoscopic Imaging System*, PhD thesis s.l. : University of Liverpool Physics Department

[97] A. Caffey, Private Communication, July 2020

[98] D. Judson, University of Liverpool, *http* : *//ns.ph.liv.ac.uk/ dsj/web/Fitting.htm*

[99] T. Woodroof, February 2020, Chapter 5, Quantitative Compton Imaging of Caesium-137 in Porous Media, PhD thesis s.l. : University of Liverpool Physics Department

[100] Mirion Technologies, ProSpect® - Gamma Spectroscopy Software, *https* : *//mirion.s3.amazonaws.com/cms4_mirion/files/pdf/spec − sheets/c40022_prospect_v1 − 0_super_spec_3.pdf*?1560965724

[101] A. Shippen & M. Joyce, 2009, Applied Radiation & Isotopes (2010) 68(4): 631-634

[102] E. Rintoul *et al*, 2018, Creation and Validation of Calculated Pulse Databases for Pulse Shape Analysis in the Planar Semiconductor Detectors of a Triple-Layered Compton Camera System, IEEE Conference Proceedings, 978-1-5386-8495-5/18/ ©2018 IEEE

[103] S. Kalantan, University of Liverpool, Private Communication